

CHRISTIAN-ALBRECHTS-UNIVERSITÄT ZU KIEL
INSTITUT FÜR THEORETISCHE PHYSIK UND ASTROPHYSIK

TDDFT Study of the Charge and Energy Transfer of Ions Interacting with Solid Surfaces

DISSERTATION ZUR ERLANGUNG DES DOKTORGRADES DER
MATHEMATISCH-NATURWISSENSCHAFTLICHEN FAKULTÄT
DER CHRISTIAN-ALBRECHTS-UNIVERSITÄT ZU KIEL

VORGELEGT VON

Lukas Deuchler

KIEL, AUGUST 2021

Lukas Deuchler

*TDDFT Study of the Charge and Energy Transfer
of Ions Interacting with Solid Surfaces*

Dissertation zur Erlangung des Doktorgrades der
Mathematisch-Naturwissenschaftlichen Fakultät
der Christian-Albrechts-Universität zu Kiel

Erstgutachter:

Prof. Dr. Eckhard Pehlke

Institut für Theoretische Physik und Astrophysik,
Christian-Albrechts-Universität zu Kiel

Zweitgutachter:

Prof. Dr. Stefan Heinze

Institut für Theoretische Physik und Astrophysik,
Christian-Albrechts-Universität zu Kiel

Tag der mündlichen Prüfung:

22. November 2021

Zum Druck genehmigt:

17. Dezember 2021

یک چند به کودکی به استاد شدیم
یک چند ز استادی خود شاد شدیم
پایان سخن شنو که ما را چه رسید
از خاک در آمدیم و بر باد شدیم

With them the seed of Wisdom did I sow,
And with my own hand labour'd it to grow:
And this was all the Harvest that I reap'd—
"I came like Water, and like Wind I go."

THE RUBAIYATS OF OMAR KHAYYĀM
(Translation by E. Fitzgerald^[1])

CONTENTS

| | |
|---|------------|
| Deutschsprachige Zusammenfassung | i |
| Abstract | iii |
| Symbols, Units and Acronyms | v |

| | | |
|----------|---|----------|
| 1 | Fundamentals and State of the Area | 1 |
| 1.1 | The Study of Plasma-Surface Interactions and Related Physical Phenomena | 1 |
| 1.1.1 | Ion-Surface Scattering | 3 |
| 1.1.2 | Energy and Charge Transfer Channels | 4 |
| 1.1.3 | Electronic Excitations on Surfaces | 7 |
| 1.2 | Additional Theoretical Concepts and Computational Approaches | 9 |
| 1.2.1 | Classical Simulations for Scattering, and Energy Dissipation | 9 |
| 1.2.2 | Newns-Anderson Model | 12 |
| 1.2.3 | Wave Packet Propagation, TDDFTB-MD and TDDFT-MD | 14 |
| 1.3 | Overview of This Thesis and the Investigated Problems | 16 |

| | | |
|----------|--|-----------|
| 2 | Density Functional Theory and Computational Aspects | 19 |
| 2.1 | Density-Functional Theory | 19 |
| 2.1.1 | Hohenberg-Kohn Theorems | 20 |
| 2.1.2 | Kohn-Sham Equations | 21 |
| 2.1.3 | Approximations to Exchange and Correlation | 23 |
| 2.2 | Time-Dependent Density-Functional Theory | 27 |
| 2.2.1 | Runge-Gross Theorem | 27 |
| 2.2.2 | Van Leeuwen Theorem | 29 |
| 2.2.3 | Time-Dependent Kohn-Sham Equations | 30 |
| 2.2.4 | Adiabatic Approximation to Exchange and Correlation | 31 |
| 2.3 | Computational Aspects and Employed Software Packages | 32 |
| 2.3.1 | Creation of Atomic Pseudopotentials: fhi98PP | 32 |
| 2.3.2 | Time Propagation of the Time-Dependent Kohn-Sham Equations | 34 |
| 2.3.3 | Dynamics of the Nuclei | 37 |
| 2.3.4 | Model Systems with Non-Vanishing Net Charge | 39 |
| 2.3.5 | (TD)DFT-MD Simulations: Octopus | 40 |
| 2.3.6 | Attributing Electronic Charges to Atoms | 41 |

| | | |
|----------|--|------------|
| 2.3.7 | Additionally Employed Software Packages | 43 |
| 3 | H⁺-Al(111): Dynamics of Electronic Excitations | 45 |
| 3.1 | Computational Details | 46 |
| 3.2 | The H-Al(111) System: Ground-State Properties | 49 |
| 3.3 | Time-Dependent Adsorbate Level Positions | 51 |
| 3.3.1 | PDOS of the Kohn-Sham Groundstate | 51 |
| 3.3.2 | Frozen Density Kohn-Sham PDOS | 53 |
| 3.3.3 | Brako-Newns-Anderson Type Model Hamiltonian | 56 |
| 3.3.4 | Rate Equation | 58 |
| 3.3.5 | Summary | 60 |
| 3.4 | Kohn-Sham Electronic Excitation Spectra | 61 |
| 3.4.1 | Ground-State Kohn-Sham Electronic Excitation Spectrum: Atom Scat- tering | 61 |
| 3.4.2 | Frozen Density Kohn-Sham Electronic Excitation Spectrum: Ion Scat- tering | 65 |
| 3.4.3 | Kohn-Sham Electronic Excitation Spectra After Scattering | 67 |
| 3.5 | Summary | 71 |
| 4 | H⁺-Al(111): Charge Transfer - Impact Site and XC-Functional | 73 |
| 4.1 | Publication: Contributions to Plasma Physics 59 , e201800184 (2019) . . . | 75 |
| 5 | H⁺-Al(111): Energy Transfer During Neutralization | 89 |
| 5.1 | Publication: Physical Review B 102 , 235421 (2020) | 91 |
| 6 | H⁺-Au(111): Similarities and Differences to H⁺-Al(111) | 101 |
| 6.1 | Introduction | 101 |
| 6.2 | Computational Aspects | 103 |
| 6.3 | Non-Binding Pseudo-Hydrogen in Front of an Al ₁₈₈ -Cluster | 104 |
| 6.4 | Results | 109 |
| 6.5 | Summary | 110 |
| 7 | Summary and Outlook | 111 |
| A | Supplementary Details | 115 |
| A.1 | Kohn-Sham Eigenvalue of H Atom | 115 |
| A.2 | Additional Information on Adsorbate Level Width | 115 |
| B | Excitation Energy and Kohn-Sham Excitation Spectra | 119 |

| | | |
|----------|---|------------|
| C | On the Excitation of Plasmons | 125 |
| <hr/> | | |
| D | Failure of TDDFT-MD AGGA – Auger Processes | 131 |
| D.1 | Introduction | 131 |
| D.2 | Helium Ion and Argon Ion Impinging on Al(111) | 132 |
| <hr/> | | |
| E | Scripts and Implementations | 135 |
| E.1 | Script for Projecting Wavefunctions | 135 |
| <hr/> | | |
| E.2 | Velocity Phase Factor | 137 |
| <hr/> | | |
| | Bibliography | 139 |
| <hr/> | | |
| | Curriculum Vitae | 161 |
| <hr/> | | |
| | Danksagung | 163 |
| <hr/> | | |
| | Selbstständigkeitserklärung | 165 |
| <hr/> | | |

DEUTSCHSPRACHIGE ZUSAMMENFASSUNG

Die Untersuchung von Prozessen an der Grenzfläche zwischen einem Plasma und einer Festkörperoberfläche ist von hohem Interesse für viele verschiedene Forschungsbereiche mit einer großen Vielfalt an technischen Anwendungen. Diese reichen von der Elektronikbranche, über Oberflächenchemie und Fusionsforschung bis hin zu Medizin, Pharmazie und vielen weiteren. Allerdings fehlt häufig ein genaues Verständnis der grundlegenden Prozesse an der Plasma-Festkörper-Grenzfläche. Ein Ansatz für ein detaillierteres Verständnis ist es, die Wechselwirkung von Atomen, Ionen oder Molekülen mit der Oberfläche zu isolieren und Streuexperimente durchzuführen. Von besonderem Interesse sind dabei niederenergetische und hyperthermale Projektile. Diese besitzen kinetische Energien beginnend in der Größenordnung von chemischen Bindungsenergien (Größenordnung 1 eV). Diese sind zu langsam, um die Oberfläche zu zerstören oder zu sputtern, bringen aber selbst genug Energie ein, um nennenswerte Anregungen im elektronischen System zu verursachen.

In dieser Arbeit wurden time-dependent density-functional theory (TDDFT)-Berechnungen in Verbindung mit Ehrenfest molecular dynamics (MD)-Simulationen durchgeführt, um den Ladungs- und Energietransfer zwischen hyperthermischen Ionen und Metalloberflächen, auf welche diese einfallen, zu untersuchen. Die Rechnungen wurden mit dem Octopus-Code durchgeführt. Der Fokus dieser Arbeit liegt auf der resonanten Neutralisation von Protonen (H^+), welche mit einer Al(111)-Oberfläche wechselwirken. Die Oberfläche wird durch eine Clustergeometrie modelliert.

Von großer Bedeutung für TDDFT-MD-Simulationen ist die Qualität der auf das Austausch-Korrelations-Potential angewandten Approximation, welche im Detail untersucht und diskutiert wurde. Schwierigkeiten im Zusammenhang mit der Spinpolarisation innerhalb der Berechnungen wurde ebenfalls analysiert. Weiterhin wurde der Neutralisationsprozess untersucht, Neutralisationsabstände bestimmt und der Energietransfer in elektronische, kinetische und phononische Freiheitsgrade analysiert.

Es wurde festgestellt, dass der Unterschied in der kinetischen Anfangsenergie zwischen H^+ und H^0 der erforderlich ist, um identische Austrittsgeschwindigkeiten zu erreichen innerhalb des untersuchten Bereichs der kinetischen Energien (2 eV bis 50 eV) das Vorzeichen wechselt. Dies wird auf die Neutralisationsabstände zurückgeführt und die Differenz zwischen der Grundzustands-Potentialenergiefläche und dem H^+ -Al(111)-Wechselwirkungspotential bei diesen Abständen.

Zusätzlich wurden elektronische Kohn-Sham-Anregungsspektren nach dem Neutralisationsprozess untersucht und eine Methode vorgeschlagen, die einen Einblick in die technischen Details hinter den beobachteten Spektren ermöglicht. Insbesondere wurde fest-

gestellt, dass die elektronischen Kohn-Sham-Anregungsspektren Anregungen zeigen, die über fast alle elektronischen Zustände verteilt sind. Dies wird aus technischer Sicht erklärt durch den Übergang des ungebundenen und unbesetzten $1s$ -Niveaus des Protons weit oberhalb der Oberfläche in das entsprechende gebundene und besetzte Niveau des H-Atoms in chemischer Bindung nahe der Al-Oberfläche.

Ergänzt wird diese Arbeit durch Erweiterungen der Simulationen auf eine Au(111)-Oberfläche. Lösungsansätzen für die technischen Schwierigkeiten, um die Simulation des Au-Clusters möglich zu machen werden präsentiert und diskutiert. Die Rolle der d Valenzelektronen des Au-Substrats auf den Abstand des Ladungstransfers erweist sich als klein.

ABSTRACT

The investigation of processes at the interface between a plasma and a solid surface is of high interest to many different research areas with a vast variety of technical applications. These extend from electronics, surface chemistry and fusion research, to medicine, pharmacy and many more. However, an accurate understanding of the fundamental processes at the plasma-solid interface is often missing. One approach towards a more detailed understanding is to isolate the interaction of atoms, ions, or molecules with the surface and perform scattering experiments. Of special interest are low energy and hyperthermal projectiles with kinetic energies starting in the order of chemical binding energies (in the order of 1 eV) where projectiles are too slow to destroy or sputter the surface but contribute themselves enough energy to cause notable excitations within the electronic system.

In this work, time-dependent density-functional theory (TDDFT) simulations have been employed together with Ehrenfest molecular dynamics (MD) as implemented in the Octopus code to investigate the charge and energy transfer between hyperthermal ions and metal surfaces. The focus of this work lies on the resonant neutralization of protons (H^+) interacting with an Al(111) surface. The surface is modeled by a cluster geometry.

Of major importance to TDDFT-MD simulations is the the quality of the approximation applied to the exchange-correlation potential which is investigated and discussed in detail. Also, difficulties connected with the spin-polarization within the calculations are analyzed. Furthermore, the neutralization process is studied, neutralization distances are determined and the energy transfer into electronic, kinetic and phononic degrees of freedom is analyzed.

It has been found that the difference in initial kinetic energy between H^+ and H^0 projectiles required to yield identical exit velocities changes sign within the studied range of kinetic energies (2 eV to 50 eV). This is traced back to the neutralization distances and the difference between both, the ground-state potential energy surface and the H^+ -Al(111) interaction potential at those distances.

Additionally, Kohn-Sham electronic excitation spectra after the neutralization process are analyzed and a method that allows for an insight into the technical details behind the observed spectra is proposed and evaluated. Notably, it has been found that the Kohn-Sham electronic excitation spectra show excitations distributed over almost all electronic states. This is explained from a technical point of view by the transition of the unbound and unoccupied 1s level of the proton far above the surface to the corresponding bound and occupied level of the H atom in a chemical bond close to the Al-surface.

This work is complemented by simulations of an Au(111) surface. Solutions of the technical problems that make the simulation of the Au-cluster feasible are presented and

discussed. The role of the d valence electrons of the Au-substrate on the charge transfer distance is minor.

SYMBOLS, UNITS AND ACRONYMS

Symbols

| | |
|--|--|
| Ψ_0 | Ground-state wavefunction of interacting electrons |
| $\Psi(t)$ | Time-dependent wavefunction of interacting electrons at time t |
| \bar{p} | Antiproton |
| $\delta\Lambda$ | Electronic excitation spectrum |
| $\delta\Lambda^{\text{BO}}$ | Electronic excitation spectrum as defined in Equation 3.11 |
| $\delta\Lambda^{\text{frozen}}$ | Electronic excitation spectrum as defined in Equation 3.14 |
| Φ_j^{BO} | Ground-state electronic Kohn-Sham wavefunction with band index j |
| $\Psi_j^{\text{TD}}(t)$ | Time-dependent electronic Kohn-Sham wavefunctions at time t |
| E_{kin} | Kinetic Energy |
| z_{jellium} | Position of the jellium edge with respect to the uppermost layer of Al atoms |
| z_{H} | Distance between H atom and position of the uppermost layer of Al atoms |
| z_{image} | Image plane position with respect to the uppermost layer of Al atoms |
| $z_{\text{spin-trans}}$ | Spin transition distance with respect to the uppermost layer of Al atoms |
| Φ_0 | Ground-state wavefunction of non-interacting electrons |
| n_0 | Ground-state density |
| E_{exc} | Nonadiabatic energy as defined in Equation 3.13 |
| $\tilde{E}_{\text{exc}}^{\text{BO}}$ | Energy as defined in Equation 3.12 |
| $\tilde{E}_{\text{exc}}^{\text{frozen}}$ | Energy as defined in Equation 3.15 |
| $n(\mathbf{r}, t)$ | Time-dependent density |
| n_a^{BO} | projected density of states as defined in Equation 3.2 |
| n_a^{frozen} | projected density of states as defined in Equation 3.5 |

Units

| | |
|--------------|--|
| \AA | Ångström, length unit, $1 \text{\AA} = 10^{-10} \text{ m}$ |
| atu | Atomic time unit, $1 \text{ atu} \approx 0.0242 \text{ fs} = 2.42 \cdot 10^{-17} \text{ s}$, |

In a semi-classical picture, one atu is the time needed for an electron in the first Bohr orbit to travel one Bohr radius.

| | |
|------|--|
| avu | Atomic velocity unit, 1 avu $\approx 2.188 \cdot 10^6$ m/s, The speed of an electron in the first Bohr orbit. |
| bohr | Bohr unit or atomic unit, length unit, 1 bohr $\approx 0.529 \text{ \AA} = 5.29 \cdot 10^{-11}$ m, Radius of the Hydrogen atom in its electronic ground-state. Please note: in atomic units, bohr is also the unit of the electric dipole moment, i.e. 1 bohr $\approx 8.478 \cdot 10^{-30}$ Cm ≈ 2.54 D |
| eV | Electron Volts, energy unit, 1 eV $\approx 1.602 \cdot 10^{-19}$ J |
| H | Hartree, energy unit, 1 H ≈ 27.2114 eV $\approx 4.36 \cdot 10^{-18}$ J, One Hartree is two times the ionization energy of the Hydrogen atom. |

Acronyms

| | |
|-------|--|
| ADSIC | averaged density self interaction correction |
| AGGA | adiabatic generalized gradient approximation |
| ALDA | adiabatic local density approximation |
| BCA | binary collision approximation |
| BNA | Brako-Newns-Anderson |
| BO | Born-Oppenheimer |
| CBM | conduction band minimum |
| CI | configuration interaction |
| DFA | density-functional approximation |
| DFT | density-functional theory |
| DFTB | density-functional based tight binding |
| DOS | density of states |
| eh | electron-hole |
| GGA | generalized gradient approximation |
| HCI | highly charged ions |
| HOMO | highest occupied molecular orbital |
| LCAO | linear combination of atomic orbitals |
| LDA | local density approximation |
| LDFA | local density friction approximation |
| LDOS | local density of states |
| LR | linear response |
| LUMO | lowest unoccupied molecular orbital |

| | |
|----------|--|
| MD | molecular dynamics |
| MIM | metal-insulator-metal |
| NACTs | non-adiabatic coupling terms |
| NEGF | non-equilibrium Green functions |
| OEP | optimized effective potential |
| PDOS | projected density of states |
| PES | potential energy surface |
| pseudo-H | non-binding pseudo-Hydrogen |
| RPA | random phase approximation |
| SIC | self interaction correction |
| SIE | self interaction error |
| TDDFT | time-dependent density-functional theory |
| VBM | valence band maximum |
| XC | exchange and correlation |

1.1 The Study of Plasma-Surface Interactions and Related Physical Phenomena

An accurate understanding of processes at the interface between a plasma and a solid surface is of high interest to many different research areas with a vast variety of applications. These range from the field of surface chemistry,^[2,3] to electronics,^[4] fusion research,^[5,6] pharmacy,^[7] medicine,^[8] and many more.

Take as an example a Tokamak fusion reactor.^[6] Upon operation, the reactor wall is exposed to a constant bombardment of hyperthermal (1 eV–100 eV) and high-flux (around 10^{16} ions per cm^2 and s) hydrogen atoms and ions that originate in instabilities in the core plasma. Unfortunately, these projectiles contribute to an erosion of the wall and a deterioration of quality. Especially for this deleterious effect, a detailed knowledge of the plasma-surface interaction is critical for a safe operation with good performance.^[9,10]

Another example for which knowledge of plasma-solid interactions are relevant are electronic applications for which it was shown that the exposure of certain surfaces to a plasma yields electric conductivity improvements.^[11] This was traced back to an increase in the free-carrier concentration as a result of introducing additional hydrogen into the material. For other surfaces, an enhancement of visible light absorption resulting in higher photocurrent densities was observed.^[12] In this case, the plasma was cause to a modified surface structure.

Low-temperature plasmas are e.g. successfully employed in medical applications. Here, the surface the plasma interacts with is a biological material. The improvement of wound healing and cancer therapy being just two out of many applications.^[8] Sterilization and decontamination effects of plasmas are also widely appreciated. They are not only applied to sterilize medical equipment but also to clean and disinfect tissue in dental cavities.^[8]

Relevant to the chemical industry are experiments that show that the exposure of surface reactions to a plasma often improves the efficiency of the reaction, in some cases even with synergetic effects between plasma and catalyst.^[13] The reasons are multiple: catalyst properties are modified due to the presence of a plasma (e.g. work function or roughness changes) and plasma properties change due to the presence of a catalyst (e.g. electric field enhancement due to surface roughness).^[13] During a chemical surface reaction, some reactants may be in an (electronic or vibrational) excited state due to the presence of a plasma. This causes the corresponding reaction barrier to change and may even open the

possibility for completely different reaction paths ultimately yielding a synergetic efficiency improvement of the process. The applicability of a catalytic effect obtained through the presence of a plasma does extend to a significant number of cases, the Haber-Bosch process or CO₂ reduction through dry reforming being only two representatives of relevance to industry (see Refs. [14–16]). For a detailed overview see e.g. Bogaerts et al.^[2] or Mehta et al.^[3]

As drawn out, the study of the plasma-surface interface is a vibrant and active field of research. Whereas, as pointed out above, many industrial applications are used on a daily basis, some (e.g. plasma catalysis applications) are not yet ready for industrial use.^[2] The reasons for this are of course manifold, however, Mehta et al. pointed out that in case of plasma-enhanced catalysis

‘The key bottlenecks for progress [...] is limited understanding of the fundamental mechanisms at play.’^[3]

Similar points of view are to be found all over the literature about plasma-surface interaction, see e.g. Refs. [2, 17, 18].

These *fundamental mechanisms* are themselves multifarious and regard e.g. the influence of the plasma parameters on the type and efficiency of energy transfer between the particles in the plasma or the surface, the efficiency and effect of secondary electron emission, the distribution of charge after scattering, or the influence on the reaction rate and respective reaction mechanisms. Also the interplay between the different elementary processes is very complex and exact parameters are (if at all) known for very few cases and with limited accuracy.^[17,18]

Modeling the entire plasma-solid interface requires overcoming extended time and length scales for systems often far from equilibrium.^[18] Despite not being able to simulate the plasma-solid interface as a whole, current theoretical treatments are successfully able to study isolated phenomena. This can ultimately result in a combined treatment of the methods,^[18] connecting theoretical approaches that extend from phenomenological treatments or mesoscopic simulations like classical molecular dynamics (MD) simulations,^[19] to solving the quantum Boltzmann equation,^[20] to *ab initio* methods such as density-functional theory (DFT) and time-dependent density-functional theory (TDDFT), and finally to non-equilibrium Green functions (NEGF).^[21] Mesoscopic simulations often rely on empirical parameters e.g. for neutralization distances of ions or secondary electron emission coefficients. It is exactly here, where TDDFT based *ab initio* simulations are needed and are able to yield insights into the time-development and dynamics of charge and energy transfer between projectiles and surfaces. Questions regarding electron dynamics can be answered with TDDFT based simulations directly. In the present thesis TDDFT-MD simulations will be employed for the study of charge and energy transfer of hyperthermal ions impinging on solid surfaces. We focus on selected, representative materials and analyze the resonant neutralization of ions impinging on them.

1.1.1 Ion-Surface Scattering

One pathway to bring light into the underlying *fundamental mechanisms* of plasma-surface interactions, is to analyze the interaction of ions with solid surfaces through scattering experiments. In contrast to plasma experiments, beam experiments allow for an analysis of the isolated phenomena of projectiles incident on solid surfaces. I.e., it is possible to isolate the single scattering event from the plasma environment and to obtain detailed information about the ion-surface scattering. These scattering experiments are performed since long and have a much longer tradition than plasma enhanced surface catalysis experiments.

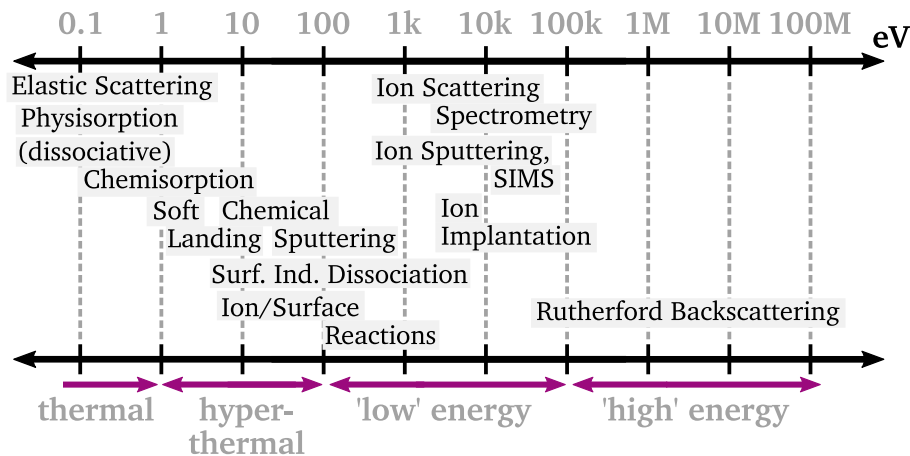


Figure 1.1: Selected fundamental processes in ion/molecule surface collisions. Labels are put in the energy range where these processes are typically studied. Visualization follows Ref. [22]. The present work focuses on hyperthermal projectiles.

Scattering Experiments Scattering experiments can be classified in different ways: by the ionic charge of the projectiles (single charged ions, multiple charged ions, highly charged ions), the type of projectile (single atomic ions, polyatomic ions, cluster ions, ionized biomolecules), the surface (metallic surfaces, isolating surfaces), the angle of incidence (e.g. grazing incidence experiments), or their energy range (thermal, hyperthermal, low energy, high energy). Categories are arbitrarily chosen depending on e.g. the research question, dominating physical effects or the experimental setup. Examples for different physical phenomena at a given kinetic energy are visualized in Figure 1.1. These range from high velocity projectiles which significantly influence the geometry of the surface and are able to sputter the surface, to comparatively low velocity projectiles that have a kinetic energy comparable to chemical binding energies on the surface. The latter are of special interest for this work.

When hyperthermal ions from inside a plasma approach a surface, they are accelerated by the plasma sheath potential and can be scattered, and neutralized, at the surface which is the cause for a charge and energy transfer. To perform ion-surface scattering experiments, a sophisticated experimental setup is required where, of course, each experiment differs from one another. For an overview see e.g. Refs. [22–26]. However, the common

denominator of the experimental setup are: 1) an ion source, 2) an accelerator, 3) a mass selector and a focusing unit, 4) a sample, and 5) an analysis unit. The mode of operation of an ion source can be based on very different effects, e.g. discharge ion sources that produce positive and negative ions from appropriate gas mixtures^[27] or ion sources that produce ions from electron impact.^[28] Charged particles are then accelerated and specific energy ranges are selected e.g. with the help of a Wien filter. After scattering, ions can be measured using e.g. a microchannel plate detector^[29] and secondary electrons can be measured e.g. with the help of an electron spectrometer. It is clear that, in order to avoid collisions between the ion beam with background gas, high vacuum conditions are required. The main factor setting the requirements for the quality of the vacuum are given by the target contamination. In case of single crystal metal targets, these are typically pressures lower than 10^{-9} Torr that allow to work with a clean surface during an experiment.^[22] In any case, almost every research question is associated to a unique experimental setup and has to be considered individually.

Regarding chemical reactivity (e.g. surface induced dissociation), ionic molecules like H_2^+ , O_2^+ , D_2^+ , D_3^+ , N_2^+ , CO^+ or CH_n^+ impinging on different (e.g. metallic) surfaces in their ground-state or an excited state are often investigated, see e.g. Refs. [30–34].

Hyperthermal Ions In this work, we will investigate hyperthermal ions scattering off surfaces, i.e. projectiles with kinetic energies that start at an energy range comparable to chemical binding energies in the system. Hyperthermal ions are not fast enough to cause a complete reorder of the substrate material as expected in a simulation of e.g. 'low energy' or 'high energy' projectiles. Hyperthermal ions are especially interesting because they probe the fundamental dynamics of energy and charge transfer. Due to the small de Broglie wavelengths of the projectiles, scattering trajectories can be expected to be classical.^[35] Investigations based on electronic structure calculations are therefore well suited because they are able to capture electronic effects during the interaction from a quantum mechanical foundation. Applications of the hyperthermal energy regime are e.g. the production or modification of thin films,^[36] the modification of self-assembled monolayers^[37] or fusion research.^[6] Experiments have also been performed e.g. for hyperthermal alkali ions scattering off coinage metal surfaces.^[38–40]

1.1.2 Energy and Charge Transfer Channels

For ions scattering off surfaces, one can identify different charge transfer channels which are i) *resonant neutralization*, ii) *Auger neutralization* (i.e. neutralization processes whose description requires more than one electron) and iii) *over the barrier neutralization*. These processes are described below and are visualized in Figure 1.2.

Resonant Neutralization A theoretical description of charge transfer was first given by Oliphant and Moon^[41] and dates back to as early as 1930, when they stated: *'The Neutralisation of a Positive Ion at a Metal Surface, [is] considered as a Transition of an Electron between States of Equal Energy.'*^[41] Figure 1.2a shows the original idea of Oliphant and

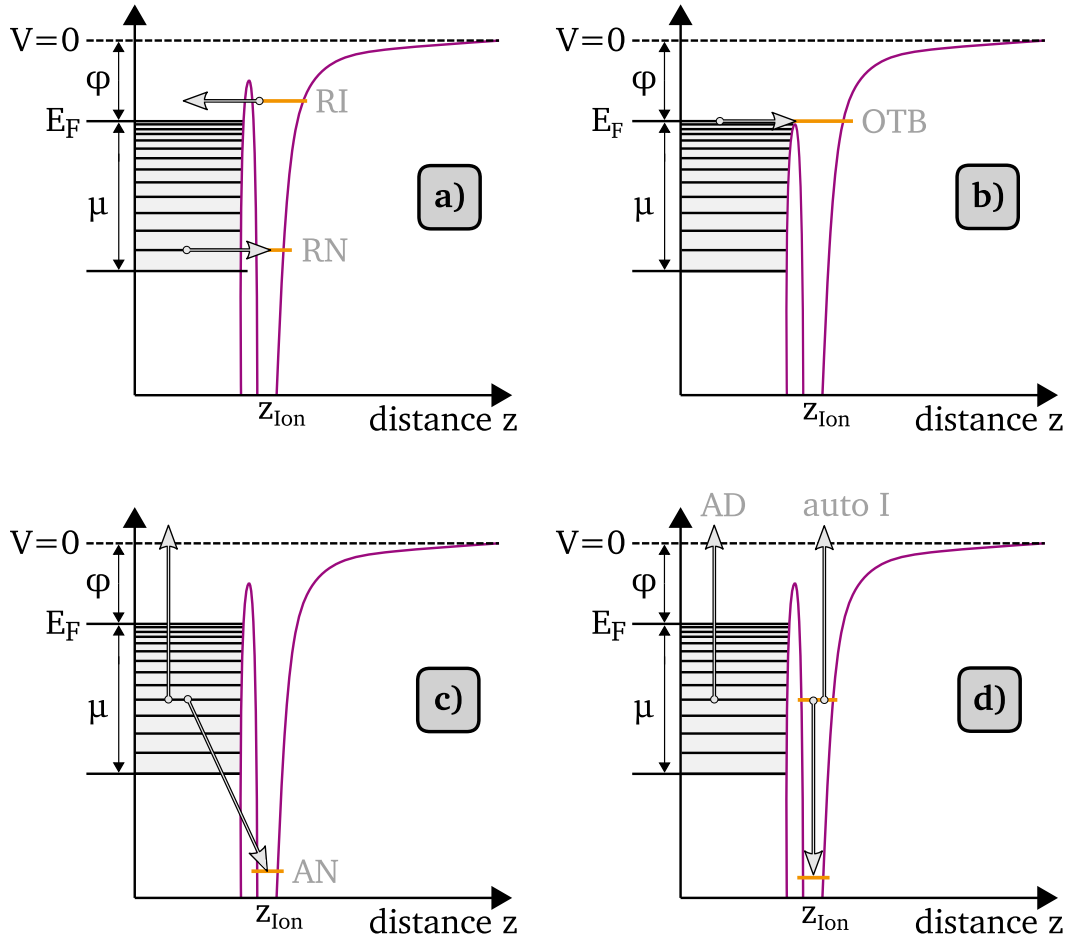


Figure 1.2: Visualization of charge transfer processes. ϕ is the surface workfunction, E_F the Fermi energy, $V = 0$ the vacuum level, μ the bandwidth of the metal and z_{Ion} the ion position. The grey region left to the barrier visualizes the density of states (DOS) of the metal surface. The energy levels of the projectile are coloured orange and serve to illustrate the different processes. The images show: **a)** resonant neutralization (RN) and resonant ionization (RI), **b)** over the barrier neutralization (OTB), **c)** Auger neutralization (AN), **d)** Auger deexcitation (AD) and autoionization (auto I). Visualization follows Refs. [41–43].

Moon. $V = 0$ is the vacuum energy, ϕ the metal workfunction, E_F the Fermi energy and μ the metal bandwidth. They pointed out that if an ion has an unoccupied energy level it can be occupied by an electron with the same energy by tunneling through the potential barrier between the metal and the ion. This neutralization process is called *resonant neutralization*. The inverse process of an occupied projectile energy level above the Fermi energy of the surface where the electron tunnels from the projectile to the surface is called *resonant ionization*.

As pointed out by Merino,^[44–46] an example for *resonant ionization* are H^+ scattering off

an Al-surface with kinetic energies < 5 keV. This system will also be investigated with the help of TDDFT-MD simulations in chapter 3, 4 and 5.

Auger Neutralization Shortly after Oliphant and Moon, Massey^[47] and Shekter^[48] extended the previous concepts and considered *Auger neutralization* as additional neutralization channel. Detailed work regarding the emission of electrons near a surface through Auger transitions was performed by Hagstrum.^[42] *Auger neutralization* describes a 'two-center' process where an electron from a different energy level inside the metal tunnels non-resonantly to the ion. Simultaneously, a second electron from inside the metal is excited carrying away the excess energy.^[42,47,48] An example may be the neutralization of He^+ in front of a Al(111) surface that was studied by different groups.^[49-52] In case of multi or highly charged ions (HCI) with several unoccupied energy levels on the projectile, further two-electron transitions may be active. *Auger deexcitation* and *autoionisation* describe an electron located at the projectile which is deexcited into a lower lying energy level on the projectile while simultaneously ejecting a second electron from the metal (*Auger deexcitation*) or the projectile (*autoionisation*).^[53] A visualization of these effects is shown in Figure 1.2c and d.

Please note that in present implementations of TDDFT in the adiabatic approximation, Auger effects are not captured. Details see Appendix D.

Over the Barrier Neutralization In case of unoccupied energy levels on the projectile very close to the Fermi energy of the metal, an *over the barrier* neutralization may be anticipated as well.^[43,54] *Over the barrier* refers to the situation that the energy barrier between surface and ion is sufficiently small and in consequence allows electrons—without the need to tunnel—to neutralize the ion. This neutralization channel is effective e.g. for highly charged ions (HCI) interacting with metal surfaces. For an example see e.g. Burgdörfer et al.^[43] who studied N^{6+} scattering off an Au surface.

Electron Promotion Please note that, in case of close collisions between projectile and substrate atoms, the overlap of the wave functions may result in an *electron promotion* effect. I.e., due to the small distance between two atoms, electronic states are shifted and occupied states may be promoted above the metal Fermi energy resulting in excited (i.e. *hot*) electrons, see also subsection 1.1.3. This effect was described in case of 50 keV Ar/Ar⁺ collision by Fano and Lichten^[55] and applied in simulations by e.g. Duvenbeck et al.^[56] in the description of a collision between an Ag projectile with kinetic energy of 5 keV and an Ag(111)-surface.

The above outlined description of neutralization effects with a clear separation between the different neutralization channels is in reality much more complex. Different neutralization and ionization channels may be considered simultaneously. Furthermore, the position of energy levels is not fixed but due to chemical bonds and (dynamical) image charge effects depends on distance, too. This issue will be discussed in section 1.2.

1.1.3 Electronic Excitations on Surfaces

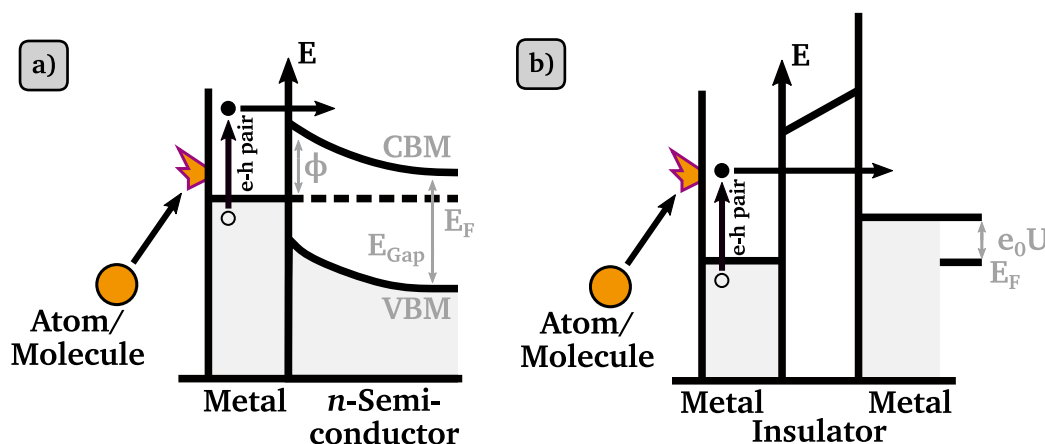


Figure 1.3: Experimental setup for measuring electron-hole (eh) pair excitations from chemical surface reactions using **a)** a Schottky diode, and **b)** a metal-insulator-metal (MIM) device. E_F is the Fermi energy, valence band maximum (VBM) and conduction band minimum (CBM). Visualization follows Ref. [57].

For the study of atomic or molecular systems, the Born-Oppenheimer (BO)^[58] theory has proven to be extraordinarily useful. Within the BO approximation, the motion of the electrons is decoupled from the motion of the nuclei. By this, one only considers the electronic (adiabatic) eigenstates and neglects the remaining non-adiabatic coupling terms (NACTs).^[59] The approximation is based on the fact that due to their significant mass difference of at least around 1 to 1836 (mass ratio between electron and proton), the time-scale of electronic and atomic dynamics is significantly different. The NACTs are proportional to the mass ratio and therefore expected to be small.^[59] With the help of the BO approximation, a vast number of physical phenomena can be explained, the field of surface science being only one of many representatives.^[60] For example, molecular dynamics (MD) simulations for molecule-surface interactions or the scattering of atoms on surfaces and energy transfer into e.g. phononic degrees of freedom can often be studied reliably within the BO approximation,^[61] see also section 1.2

However, the importance of non-adiabatic effects must not be underestimated as there exist many processes where non-adiabatic effects are relevant. An example controversially discussed in the literature are chemically induced electronic excitations at metal surfaces, see e.g. Refs. [62–70]. A very intensively studied case are diatomic molecules interacting with metal surfaces where the molecular vibration can be strongly coupled to the metal electrons resulting in an efficient energy transfer channel.^[69,71]

Please note that ion scattering is per-definition an electronically non-adiabatic process. Non-adiabatic refers here to the situation, that the combined system of ion and surface is not in the electronic (i.e. Born-Oppenheimer) ground-state. This must be considered especially in investigations that focus on the charge transfer or the energy transfer into the electronic degrees of freedom.

Electronic Excitation Experiments Electronically non-adiabatic atom-surface or molecule-surface coupling has been demonstrated in surface chemistry experiments, see Refs. [38–40, 71–76]. The experimental measurement of electronic excitations from adsorption has first been realized by Nienhaus et al.^[72] who investigated electron-hole (eh) pair creation in the adsorption of H at Ag and Cu surfaces with the help of a Schottky type diode experimental setup depicted in Figure 1.3a: The metal is in contact with a semiconductor resulting in a Schottky barrier. H adsorption on the metal substrate leads to an excitation of eh pairs, excited electrons are able to overcome the Schottky barrier and can be measured as a chemicurrent. A critical value for measuring the chemicurrent is the metal film thickness, which is usually below of approximately 100 Å. Such thin metal films on top of a semiconductor are mostly obtained by evaporation.

Gadzik^[57] investigated theoretically a metal-insulator-metal (MIM) detector for the study of laser-excited hot electrons. Diesing et al.^[77–81] used a MIM detector to investigate positive ions (Ar^{q+}) and atoms scattering off an Ag surface which is schematically shown in Figure 1.3b. These MIM devices have the advantage that the internal barriers can be tuned by a tunnel voltage. Thanks to the tunability of the MIM detector, it is possible to investigate both, the hole as well as the electron of the eh pair excitation. The work of Ray et al.^[38–40] extends the above investigations to include hyperthermal alkaline ions scattering off metal surfaces.

1.2 Additional Theoretical Concepts and Computational Approaches

After the short introduction into the basic concepts and the experimental background in section 1.1, the present section 1.2 will introduce additional theoretical concepts and computational approaches. We start from classical simulations and the computation of energy dissipation in subsection 1.2.1. The term 'classical' refers in this context to simulations where it is not compulsory to calculate electronic wavefunctions in order to work. This section continues with the introduction of the Newns-Anderson model and applications to ion-surface interaction in subsection 1.2.2. At the end, wave packet propagation, DFTB and TDDFT-MD will be discussed shortly in subsection 1.2.3. Please note that the here given list of computational methods does not claim to be complete but is rather intended to give the reader an overview about selected concepts. Further information can e.g. be found in Refs. [18, 23, 61, 82–86] or the references mentioned below.

1.2.1 Classical Simulations for Scattering, and Energy Dissipation

Understanding experimental results comes hand in hand with data obtained from simulations. There exists no single simulation technique that is able to capture all effects relevant to all kinds of scattering experiments. In consequence, the simulation method has to be chosen always in consideration of the problem. In simulations where one is interested e.g. in the energy transfer into phononic degrees of freedom or in investigating surface sputtering, there is no need to employ rather time-consuming quantum-mechanical simulations. Experiments can already be explained with the help of less time-consuming classical molecular dynamics (MD) simulations and simulations based on the binary collision approximation (BCA).

Classical Molecular Dynamics (MD) There exist very detailed theoretical works e.g. for a description of projectiles with kinetic energies that are suitable to cause a complete re-order of the surface atoms, see e.g. Refs. [26, 86]. For a theoretical understanding, these systems are typically treated by classical molecular dynamics (MD) simulations where atoms are described through potentials and obey the Newtonian equations of motion. Electrons are not treated explicitly but are contained within the potentials for the atom. Nevertheless, quantum effects like the van-der-Waals interaction can be included into these potentials. The simulations are numerically more efficient compared to DFT based MD simulations described below and allow for model systems with billions of atoms.^[87] Simulations are often performed with the program LAMMPS¹ by Plimpton.^[86] As an example, classical MD simulations have successfully been employed to explain unexpected spectra of low-energy Ar⁺ ions colliding with a Cu(111) surface by Vidal et al.^[88] or the calculation of the sputtering yield in Ag sputtering by Kucharczyk et al.^[89]

¹LAMMPS is an acronym for Large-scale Atomic/Molecular Massively Parallel Simulator.

An extension to classical MD simulations are DFT based MD simulations. Here, atoms are represented by (pseudo-)potentials and electrons as wavefunctions. Forces acting upon the ions are calculated from DFT and ions obey the Newtonian equations of motion. For details on DFT see section 2.1.

Binary Collision Approximation (BCA) A computationally even less demanding approach is a simulation technique called binary collision approximation (BCA), which is a Monte-Carlo method that follows all collision cascades of a projectile in a target in detail. At the end of a simulation, a three-dimensional distribution of the projectiles in the solid is obtained. From this information, experimentally accessible parameters like penetration depth, vacancy concentration or sputter yields are obtained. A very successful representative for a simulation software that employs the BCA is the SRIM² code^[85,90,91] which allows for a simulation of practically all atomic projectile and target materials and was (as of today) used in more than 700^[91] scientific publications.

Within the classical MD simulations and simulations based on the BCA, the ion charge is usually neglected. However, energy dissipation due to electronic friction can and is easily included into both, the MD simulations and the BCA simulations introduced above. This is done very successfully with the help of the Lindhard-Scharff model for electronic friction:

Lindhard-Scharff Model for Electronic Friction An atomic or ionic projectile approaching a surface will at some point be exposed to electronic friction effects that arise from the surrounding electronic density. This is especially important when the trajectory is partly within the substrate, e.g. when scattering from the second, third or lower lying substrate atomic layers occurs. A theoretical approach is to treat the metal as a free, degenerate electron gas. Following the work of Fermi and Teller,^[92] Lindhard and Scharff gave an approximate formula for the energy loss per traveled unit length dE/dx of a particle with velocity v :^[93]

$$\frac{dE}{dx} = -A \cdot v \quad (1.1)$$

The constant A can e.g. be derived from theory or approximated by experimental data, for a discussion see Refs. [94–96]. Examples for an application can be found in Refs. [63, 97]. For proton projectiles with kinetic energies in the order of 100 keV or above, this formula is no longer valid because the projectile velocity has to be small compared to the average velocity of valence electrons of the substrate atoms. The Lindhard-Scharff model has been further developed to account for higher order terms or molecules, see e.g. Refs. [94, 95, 98].

When employing ab-initio based MD simulations, friction can be included with the local density friction approximation (LDFA).^[63] For an example see the work of Juaristi,^[99] or Alducin et al.^[100] who simulated atom and ion scattering on metal surfaces with ab-initio dynamics with electronic friction.

²SRIM is an acronym for Stopping and Range of Ions in Matter.

Electronic Friction Effects From Dynamical Image Charge A further source for energy dissipation into electronic degrees of freedom arises from the presence of an ion with non-vanishing net charge q located above a metal surface and moves with a velocity \mathbf{v} . For small \mathbf{v} and large distances, the interaction energy necessary to bring a particle with charge q from infinity to a distance $z = \alpha$ converges to the statical limit $E_{\text{im}} = -q^2/(4\alpha)$, with α as the distance between particle and image plane position z_{image} , i.e. the classical image charge potential of a charge q at a distance $z - z_{\text{image}}$ in front of the image plane position is:^[101,102]

$$V_{\text{im}} = -\frac{q}{4 \cdot (z - z_{\text{image}})} \quad (1.2)$$

In some cases, the ion velocity is high and the induced image charge does not build up instantaneously. Then, the dynamical screening effect is one source for additional energy dissipation.^[103,104] Considering this additional energy dissipation is relevant for some experiments as it is often convenient to perform ion scattering e.g. on a surface under grazing incidence. In some experiments, the incident angle Φ_{in} goes down to $\Phi_{\text{in}} \approx 0.1^\circ$, such that the projectiles normal velocity v_z is orders of magnitude different from its parallel velocity $|v_{\parallel}|$, see e.g. Ref. [105].

A very detailed analysis for this effect can be found in the work of García de Abajo and Echenique,^[101] who investigated this wake potential with different approaches (i.e. a specular-reflection model and a Hamiltonian treatment) and different dielectric functions. Furthermore, they specified the general treatment to the case of normal incidence and to a projectile that moves parallel to the surface.

Winter^[105] employed their approach and concluded that for a proton in front of an Al surface with a kinetic energy in the parallel component $< 25 \text{ keV}$ the approximation through Equation 1.2 '[...] is a good description down to distances $z[-z_{\text{image}}] \approx 2 \text{ au}$; for faster projectiles this approach is poorer and holds only for larger distances [...]'.^[105]

The general case including the normal impact was treated with the same methodology in a publication preceding Ref. [101], by Gras-Marti and Echenique^[96] who studied a proton with kinetic energy of 1 keV . They calculated an energy dissipation ΔW during the approach from ∞ to 1 \AA above the Al jellium edge of $\Delta W \approx 0.07 \text{ eV}$. In case of Al(111), the image plane position is located at $z_{\text{image}} = 3.14 \text{ bohr}$ ^[106] above the uppermost layer of Al atoms, the jellium edge³ at $z_{\text{jellium}} = 2.21 \text{ bohr}$.

In chapter 5, we employed TDDFT-MD simulations to determine the energy dissipation from antiprotons of different velocities impinging on a half-spherical Al-cluster.

³The position of the jellium edge of a (111) surface z_{jellium} is connected to the lattice constant c through the interlayer spacing $d_{111} = c/\sqrt{3}$ by $z_{\text{jellium}} = d_{111}/2$.

1.2.2 Newns-Anderson Model

One aspect inherently connected to the ion-surface interaction regards the question of the distance where the electronic charge transfer takes place. For example, Winter^[105] suggested that a neutralization distance could be obtained from experimental results. This brings the question of neutralization distance also into the focus of theoretical work. From a theoretical side, the question of charge transfer dynamics in ion scattering has often been approached by using a Brako-Newns-Anderson (BNA) type Hamiltonian^[107–109] or an LCAO Hamiltonian.^[44] There also exist approaches based on a Newns-Anderson Hamiltonian that describe correlation with the help of Green's function techniques.^[110–112] These model Hamiltonians are introduced in the present section.

Originally, in 1961, Anderson developed a model Hamiltonian to describe nonmagnetic impurities in nonmagnetic metals.^[113] Later, several authors^[107,114] used the same type of Hamiltonian to describe chemisorption on metal surfaces—one of them being Newns, who discussed different properties of chemisorption on metal surfaces with great success. Therefore, in the surface physics community, these type of model Hamiltonians are usually referred to as Newns-Anderson Hamiltonians.^[115] The general Hamiltonian $H(t)$ for the combined system of a metal surface and an adatom adsorbing on it is formulated as:

$$H(t) = H_m + H_{\text{ad}}(t) + H_a(t) + H_C(t), \quad (1.3)$$

$$H_m = \sum_{\mathbf{k}\sigma} \varepsilon_{\mathbf{k}} c_{\mathbf{k}\sigma}^\dagger c_{\mathbf{k}\sigma}, \quad (1.4)$$

$$H_{\text{ad}} = \sum_{\mathbf{k}\sigma} [V_{\mathbf{k}}(t) c_{\mathbf{k}\sigma}^\dagger c_{a\sigma} + h.c.], \quad (1.5)$$

$$H_a = \varepsilon_a(t) \sum_{\sigma} n_{a\sigma} \quad (1.6)$$

$$H_C = U(t) n_{a\uparrow} n_{a\downarrow}, \quad (1.7)$$

with $n_{a\sigma} = c_{a\sigma}^\dagger c_{a\sigma}$. $c_{\mathbf{k}\sigma}$ is the annihilation operator of a metal state with parallel wavevector \mathbf{k} and spin $\sigma \in \{\uparrow, \downarrow\}$. $\varepsilon_{\mathbf{k}}$ is the electron band energy and ε_a the energy level of the state on the atom. a describes a quantum number corresponding to the wavevector component normal to the surface. $V_{\mathbf{k}}$ describes the coupling between the metal states and the adsorbate by its matrix elements and U is the intraatomic Coulomb interaction on the atom. Time-dependence is introduced by the motion of the scattering atom or ion which in most cases is taken as constant in velocity. Obtaining the time-dependent parameters of Equation 1.3 is not trivial and investigated in different publications. For an overview see e.g. Ref. [116].

The time-dependent problem of Equation 1.3 is solved by the Schrödinger equation, i.e.:

$$i \frac{\partial \Psi(t)}{\partial t} = H(t) \Psi(t), \quad (1.8)$$

where Ψ is the electronic wavefunction of the system with given initial conditions.

Adsorbate Level Position and Width For the case $U(t) \equiv 0$, Equation 1.3 is a single-particle Hamiltonian. Nonetheless, even in this case it remains very difficult to solve.^[117] However, it allows to derive an interesting aspect of the behavior of the adatom valence state $|\Phi_a\rangle$ upon adsorption. Namely, as pointed out by Grimley,^[114] the projected density of states (PDOS) $n_a(\varepsilon)$ of the wavefunction $|\Phi_a\rangle$ of the adsorbate atom^[118]

$$n_a(\varepsilon) = \sum_i |\langle \Psi_i | \Phi_a \rangle|^2 \delta(\varepsilon - \varepsilon_i) \quad (1.9)$$

where $|\Psi_i\rangle$ is the set of all wavefunctions and ε_i is the corresponding eigenvalue. n_a can be expressed in terms of the adsorbate level width Γ and a shift to the adsorbate level position denoted by ξ , i.e.:^[118]

$$n_a(\varepsilon) = \frac{1}{\pi} \frac{\Gamma}{[(\varepsilon - \varepsilon_a - \xi)^2 + \Gamma^2]} \quad (1.10)$$

In other terms: An atom or molecule in vacuum has a well defined and discrete set of eigenvalues. A metal surface on the other side, provides an infinite reservoir of electrons and a continuum of electronic states. Upon adsorption, the atomic/molecular eigenstates are coupled to the metal states leading to a shifting and broadening of the adsorbate level. Often, the shift ξ is not explicitly distinguished from ε_a , the term $(\varepsilon_a + \xi)$ is then referred to as 'adsorbate level position'. In the following chapters, we choose for the distance \mathbf{R} dependent adsorbate level position $\varepsilon_a(\mathbf{R}) := (\varepsilon_a + \xi)$.

Calculation of Charge and Energy Transfer Due to the complicated Hamiltonian of Equation 1.3, a direct solution is often not feasible. Therefore, several steps for the description are taken, for an overview see e.g. Ref. [116]. Often, the non-interacting electron case is discussed, where $U = 0$. Whereas in case of the originally studied problems of Anderson, the intra-atomic Coulomb interaction U was crucially important, it is not the case in scattering simulations. Aiming for a solution, Brako and Newns^[108,119,120] implemented a non-interacting Anderson model that describes the coupling between the valence level of the atom and the metal electron states, in which the energy and lifetime broadening of the valence level are explicitly time-dependent. Time-dependence is motivated by the motion of the projectile relative to the surface. They started from a model Hamiltonian of the form given in Equation 1.3 and solved the equation of motion for the $c_{k\sigma}(t)$ and $c_{a\sigma}(t)$, i.e.:

$$\frac{\partial c_{a\sigma}(t)}{\partial t} = i[H, c_{a\sigma}(t)] \quad (1.11)$$

$$\frac{\partial c_{k\sigma}(t)}{\partial t} = i[H, c_{k\sigma}(t)] \quad (1.12)$$

Then, the charge transfer (i.e. the charge q on the adatom orbital at time t) can be calculated as:^[108]

$$q := \langle n_{a\sigma}(t) \rangle = \langle c_{a\sigma}^\dagger(t) c_{a\sigma}(t) \rangle \quad (1.13)$$

Secondly, one wishes to calculate the probability $P(\varepsilon)$ that the system is in an excited state of energy ε after the atom scattering. Therefore, one assumes that the system starts at time t_0 when the electronic system is in its ground-state $|t_0\rangle$ with energy E_0 and evolves (in the Schrödinger picture) into an excited state $|\infty\rangle$. Then, the energy transfer can be calculated from $P(\varepsilon)$, where^[120]

$$P(\varepsilon) = \langle \infty | \delta(\varepsilon - [H(\infty) - E_0]) | \infty \rangle \quad (1.14)$$

Depending on the Hamiltonian, Equation 1.14 is then rewritten in order to allow for an efficient computation.

Examples The authors of Ref. [108] used the model Hamiltonian to describe one-level resonant neutralization, their calculations investigated Na scattering from a W(110) surface. Merino et al. used a similar Hamiltonian to study the interaction between H^+ and an Al surface, see Refs. [44–46]. This approach was further refined and applied by several groups for different physical systems. More recent examples are e.g. Li^+ scattering on Cu(111)^[121] or Na^+ scattering on Au(111), Pd(111), Cu(111), and Cu(110) surfaces.^[122] Iglesias-García, García and Goldberg formulated a more sophisticated Hamiltonian and studied Auger neutralization of He^+ scattering on Al.^[121] Bird et al.^[123,124] investigated the case of H scattering at an Al(111) surface and compared e.g. electronic excitation spectra obtained from the Hamiltonian approach to results from TDDFT-MD simulations. Pamperin, Bronold and Fehske extended the Hamiltonian further and studied e.g. the resonant neutralization of many-level systems,^[111] and included also Auger neutralization.^[125]

The Newns-Anderson Hamiltonian was also applied to study adsorption phenomena on surfaces, for an overview see e.g. Ref. [118].

1.2.3 Wave Packet Propagation, TDDFTB-MD and TDDFT-MD

Wave Packet Propagation A second approach to calculate the final charge of a projectile is with the help of a wave packet propagation approach. In the wave packet propagation method, the time-dependent Schrödinger equation is solved for a single electron in a problem specific potential. Borisov et al.^[126] applied this to the case of an initial wave packet of a bound state of the free H^- ion in a time varying potential corresponding to the movement of the ion in front of the surface. The method was used to study e.g. the dynamics of electron transfers between an H^- ion and a Cu(111) surface for different kinetic energies, see Ref. [126].

Gainullin^[127–129] applied this method to estimate the probability of an alkali projectile to be neutral or charged after scattering from a metallic surface. The neutralization probability is then estimated, as ‘the amount of electron lost by a neutral atom’^[129] during the motion along the outgoing trajectory starting at the point z_F . z_F denotes the distance where the adsorbate level crosses the Fermi energy. This concept was also employed by other authors.^[108]

TDDFT Based Tight Binding Molecular Dynamics (TDDFTB-MD) Density-functional based tight binding (DFTB) is an approximation to DFT method presented in section 2.1. It provides functionalities similar to DFT while being one or two orders of magnitude faster, see e.g. Refs. [130–132]. Time-dependency is implemented e.g. in the DFTB+ simulation software that allows for molecular dynamics (MD) simulations, too.^[133] Examples for charge transfer between similar systems like the ones studied in this thesis are the collision between C^+ and C_{60} by Niehaus et al.^[134] or the collision between C_{60}^{2+} and C_{60} by Jakowski et al.^[135] However, as DFTB is an approximation to DFT, it has at least the same if not more drawbacks.^[136] Work comparing the charge or energy transfer in an ion-surface collision between DFTB and TDDFT is not yet to be found in the literature.

TDDFT-MD Simulations An increase in computational power made it possible to employ time-dependent density-functional theory (TDDFT) based molecular dynamics (MD) simulations to study non-adiabatic effects in rather extended systems. Details on TDDFT-MD simulations are given in chapter 2. Here, we give an overview on theoretical studies of selected systems.

Recently, significant insights were gained with the help of TDDFT-MD simulations for ion/atom propagation within solids. Schleife et al.^[137] investigated the electronic stopping in proton propagation through gold with a focus on different orientations with respect to the periodic metal. Zeb et al.^[138] studied the propagation of H and He through gold and came to the conclusion, that as soon as the electronic excitation extends to the electronic d -band, additional friction from the d -electrons can be observed. Quashie and Correa^[139] discussed results for H and He propagation through Ni.

For the case of atoms scattering off surfaces, significantly less studies have been published. Lindenblatt et al.^[97,140,141] investigated H scattering on an Aluminum surface and investigated electronic excitations arising from electronic friction and the spin-transition. Ion scattering has been reported by Moss, Isborn and Li^[142] who studied the electronic charge transfer from the Al(100) face of an Al_{58} -cluster to an incident Li^+ . TDDFT-MD simulations of ions accounting for resonant charge transfer have also been carried out for a proton scattered at a Li_4 -cluster by Castro et al.,^[143] and collisions with carbon nanostructures by Krashennnikov et al.,^[144] or DNA fragments by Seraide et al.,^[145] or graphene fragments by Bubin et al.,^[146] or graphene and boron nitride by Zhao et al.,^[147] and for Cl^- incident on a $MoSe_2$ monolayer by Wang et al.^[148] or H^+ and He^+ interacting with a graphite surface by Ojanperä et al.^[149]

A very important question for plasma enhanced surface reactions is about the energy dynamics during a charge transfer process, i.e. about the distribution of excited or transferred holes and electrons and their influence on surface chemistry. First attempts to calculate chemical reaction barriers for excited systems are taken by e.g. Lee and Schleife^[150] who studied changes in diffusion barriers for oxygen diffusion in proton-irradiated magnesium oxide or by Jafarzadeh et al. who investigated binding energies of CO_2 on electronically charged, Ni_5 and Cu_5 -clusters.^[151]

1.3 Overview of This Thesis and the Investigated Problems

This thesis discusses results from time-dependent density-functional theory (TDDFT) simulations for the charge and the energy transfer during the collision of a hyperthermal ion (i.e., an ion with an initial kinetic energy in the sub-eV up to few 10-eV range) with a metal surface.

An interesting model system for which both theoretical^[44,46,66,83,99,107–109,152–159] and experimental^[105,160–167] investigations by various groups are available, is the case of a proton (H^+ ion) incident on an Al(111) surface. Comparison of data is carried through for adsorbate level widths in chapter 3. A great advantage of this system lies in the rather simple electronic structure of both, the projectile and the adsorbate. Merino et al.^[46] identified the charge transfer between the Al orbitals and the hydrogen 1s orbital process for a H^+ at low kinetic energies (less than 4 keV) scattering on an Al(111) surface as a resonant charge transfer process.

The main focus of this thesis will lie on the description of different aspects of H^+ -scattering on the (111) site of an Al-cluster. They are complemented by simulations of H^+ -scattering on the (111) site of an Au-cluster.

This thesis is organized as follows:

- In chapter 2 the theoretical concepts underlying the present work are introduced and discussed. Namely, the density-functional theory (DFT) and time-dependent density-functional theory (TDDFT) approach. Limiting aspects regarding the focus of research of this thesis are identified and discussed, and concepts behind the simulation software are introduced together with the employed software packages.
- In chapter 3, physical properties of the Al(111) surface and an H atom adsorbing on the surface are summarized. Information on the simulations and the computational details is given. The main part of this chapter is concerned with the presentation and discussion of a method to derive the adsorbate level position and width from a TDDFT-MD simulation. In the last part of chapter 3 this method is extended to the case of Kohn-Sham electronic excitation spectra. The time-development of the Kohn-Sham spectra is investigated and the energy distribution after scattering is discussed.
- In chapter 4, the charge transfer between H^+ and an Al(111) surface represented by a finite-size cluster is discussed. Among other results, the influence of the exchange and correlation (XC)-functional is analyzed and compared to differences arising from the impact site. Additionally, electronic excitations arising from an H^0 with impact at the fcc-hollow site and a subsequent sub-surface trajectory were compared to the electronic excitations induced by an H^+ with the same trajectory. This work was published in a peer-reviewed journal.
- In chapter 5, the electronic energy transfer during and after the impact of a hyperthermal H^+ on an Al(111) surface represented by a cluster is discussed in detail. The validity of the employed approach is analyzed in-depth. Differences in the energy

transfer for impact at the on-top and fcc-hollow site are investigated. The energy transfer connected to the charge transfer, energy dissipation into phononic degrees of freedom, energy dissipation from electronic friction of the projectile propagating within the target and from building up the image charge, and the excitation of plasmons are considered. Additionally, the difference in initial kinetic energy between H^+ and H^0 projectiles required to yield identical exit velocities is derived. This work was published in a peer-reviewed journal.

- In chapter 6, the numerically demanding H^+ -Au(111) system is investigated. Differences for the charge and energy transfer between Al(111) and Au(111) are analyzed and traced back to differences in the local density of states between both surfaces.
- In Appendix A, additional information on the adsorbate level widths calculated in subsection 3.3.2 are given. Appendix B discusses the connection between Kohn-Sham electronic excitation spectra and the excitation energy of the Kohn-Sham system. Appendix C discusses the excitation of plasmons after proton scattering from an Al_{188} -cluster. Appendix D discusses Auger processes for the example of an He^+ and an Ar^+ projectile scattering on the Al_{188} -cluster. Auger processes are as of today not contained in a TDDFT simulation

Please note that throughout this work, atomic units are used if not stated otherwise, i.e. distance is measured in bohr ($1 \text{ bohr} \approx 5.29 \cdot 10^{-11} \text{ m}$), time in atu ($1 \text{ atu} \approx 2.42 \cdot 10^{-17} \text{ s}$), energy in H ($1 \text{ H} \approx 4.36 \cdot 10^{-18} \text{ J}$), and velocity in avu ($1 \text{ avu} \approx 2.188 \cdot 10^6 \text{ m/s}$).

The present chapter gives a short introduction into the theoretical approach employed within this thesis for the simulation of the charge and energy transfer of an ionic projectile interacting with a metal surface. In section 2.1 the foundations underlying ab-initio simulations that use density-functional theory (DFT) are drawn out, and section 2.2 gives an introduction into time-dependent density-functional theory (TDDFT). Moreover, approximations that are necessary to make the simulations feasible are explained and discussed in section 2.3, followed by the numerical methods and computing programs used for the simulations presented in this thesis.

2.1 Density-Functional Theory

When in 1998 Walter Kohn was awarded the Nobel prize '[...] for his development of the density-functional theory'^[168] it was already clear that density-functional theory (DFT) had become tremendously useful when calculating physical and chemical properties of e.g. molecules or surfaces. The equation that describes the electronic ground-state of a system of n electrons and N nuclei is the time-independent Schrödinger equation. It reads in atomic units:^[169]

Time-Independent Schrödinger Equation

$$\hat{H}|\Psi(\mathbf{r}_1, \dots, \mathbf{r}_n, \mathbf{R}_1, \dots, \mathbf{R}_N)\rangle = E|\Psi(\mathbf{r}_1, \dots, \mathbf{r}_n, \mathbf{R}_1, \dots, \mathbf{R}_N)\rangle, \quad (2.1)$$

where \mathbf{r}_i and \mathbf{R}_j are the coordinates of the electrons and the nuclei, respectively. \hat{H} is the Hamiltonian operator, and $|\Psi\rangle$ the corresponding many-body wavefunction. The Hamiltonian consists of the kinetic energy of the electrons \hat{T}_{el} and the nuclei \hat{T}_{nuc} , the electrostatic interaction energy between the electrons themselves $\hat{V}_{\text{el-el}}$, between the nuclei $\hat{V}_{\text{nuc-nuc}}$, and between electrons and nuclei $\hat{V}_{\text{el-nuc}}$:

$$\hat{H} = \hat{T}_{\text{el}} + \hat{T}_{\text{nuc}} + \hat{V}_{\text{el-el}} + \hat{V}_{\text{el-nuc}} + \hat{V}_{\text{nuc-nuc}} \quad (2.2)$$

An exact solution of Equation 2.1 is accessible only for the most simple systems. As a step towards solving this equation for systems with more than only one or two particles, Born and Oppenheimer^[58] suggested to separate the electronic and nuclear degrees of freedom. This approximation is based on the observation that due to their significant mass

difference of at least 1 to 1836 (mass ratio between electron and proton), the time-scale of electronic and atomic dynamics is significantly different and can, in a first step, considered to be independent. Within this approximation, for a given set of nuclei positions \mathbf{R} , the equation that has to be solved reads:

$$\hat{H}_{\mathbf{R}}|\Psi_{\mathbf{R}}\rangle = E|\Psi_{\mathbf{R}}\rangle, \quad (2.3)$$

with $\hat{H}_{\mathbf{R}} = \hat{T}_{\text{el}} + \hat{V}_{\text{el-el}} + \hat{V}_{\text{el-nuc}} + V_{\text{nuc-nuc}}$ and $\Psi_{\mathbf{R}}$ being the corresponding electronic wavefunction.

A successful approach to solve this equation is called the Hartree-Fock method where the N -body wave function of the system is approximated by a single Slater determinant. In the Hartree-Fock approach, electrons of opposite spin are not correlated. As a consequence, within the Hartree-Fock approach, the term *correlation energy* refers to the energy difference to the exact solution. The Hartree-Fock method lays the foundation of further, more sophisticated approaches for solving this partial differential equation. Of those, an often used representative are the configuration interaction (CI) methods.^[170] The idea within the CI approach is to express the ground-state wave-function through a linear combination of Slater determinants that minimizes the energy. The numeric complexity of a full CI is factorial with the number of electrons and basis functions. As explained by Walter Kohn in his Nobel lecture,^[171] for any system containing several hundreds of atoms with each atom contributing several electrons to the system, these multi-particle wavefunctions encounter an *exponential wall*, i.e. they reach a point where the required computational power exceeds technological feasibility.

Thomas^[172] and Fermi^[173] chose a different path in order to solve Equation 2.3 which focuses on the electronic density $n(\mathbf{r})$ of a given system of identical fermions. The density is an observable of the many-body wavefunction Ψ . It is defined through the expectation value of the density operator $\hat{n}(\mathbf{r})$:

$$n(\mathbf{r}) = \langle \Psi | \hat{n}(\mathbf{r}) | \Psi \rangle \quad (2.4)$$

From the assumptions that (i) the electron-electron interaction is purely electrostatic and that (ii) the kinetic energy of a system with density n can be written as a local functional of n , an equation to calculate the ground-state energy of a system from the density (and not the wavefunctions) was derived.^[174] The Thomas-Fermi model (including the extensions made by Dirac^[175]) is today acknowledged as a *simple predecessor*^[117] of DFT because the chosen approximations for the kinetic energy, the description of the exchange energy and the neglect of correlation effects resulted in rather inaccurate results in most applications. However, these limitations were faced explicitly in the density-functional theory which is presented in the next section.

2.1.1 Hohenberg-Kohn Theorems

The main idea behind density-functional theory (DFT) is based on the proof that the electronic ground-state of a given many-particle system can be determined by finding the electron density of the ground-state. Thanks to this idea it is—compared to the approaches

mentioned in the previous section—computationally efficient and can in consequence be applied not only to simulations of few particles but to systems of hundreds and thousands of atoms. A starting point for any discussion about DFT are the Hohenberg-Kohn theorems and the Kohn-Sham equations (subsection 2.1.2).

Inspired by the Thomas-Fermi model, in 1964 Walter Kohn and Pierre Hohenberg formulated and proved the following two theorems:^[176]

Hohenberg-Kohn Theorem I

"The ground-state density $n_0(\mathbf{r})$ of a bound system of interacting electrons in some external potential $v(\mathbf{r})$ determines this potential uniquely [up to an uninteresting additive constant]." ^[171,176]

Since $n_0(\mathbf{r})$ determines the external potential and the total number of electrons, it contains the entire information about the Hamiltonian of the N electron system. Hence, it also determines implicitly all properties that are derivable from the Hamiltonian. While the theorem has been shown only for non-degenerate ground-states at the beginning, it can also be extended to degenerate ground-states.^[171]

Hohenberg-Kohn Theorem II

The ground-state density $n_0(\mathbf{r})$ minimizes the energy functional $E_{v(\mathbf{r})}[n]$.

$$E_0[n_0] = \min_n E_{v(\mathbf{r})}[n] = \min_n \left(F_{\text{HK}} + \int v(\mathbf{r})n(\mathbf{r})d^3\mathbf{r} \right) \quad (2.5)$$

The Hohenberg-Kohn functional F_{HK} is defined as the sum of the electron-electron interaction energy and the kinetic energy of the electron gas. In consequence, to obtain the ground-state energy for a given system, it is the energy functional that needs to be minimized.

2.1.2 Kohn-Sham Equations

Kohn and Sham developed an approach^[177] on how to solve the minimization problem given in Equation 2.5. The basic idea is to map the interacting many-body system on a non-interacting and fictitious fermionic system, whose ground-state electron density corresponds to the ground-state electron density of the real system. This is realized by expressing the energy as a sum of terms of which one involves an *in principio* 'unknown' functional. Furthermore, this term is expected to be accessible to local or semi-local approximations of the density. The electron density can then be refined in an iterative, self-consistent way.

The energy functional of the non-interacting system is expressed as follows:

$$E_{v(\mathbf{r})}[n] = T_s[n] + E_{\text{ext}}[n] + E_{\text{H}}[n] + E_{\text{XC}}[n], \quad (2.6)$$

where $T_s[n]$ is the kinetic energy of the non-interacting system,

$$E_H[n] = \frac{1}{2} \int \int \frac{n(\mathbf{r})n(\mathbf{r}')}{|\mathbf{r} - \mathbf{r}'|} d\mathbf{r} d\mathbf{r}' \quad (2.7)$$

the Hartree energy and $E_{\text{ext}}[n] = \int v(\mathbf{r})n(\mathbf{r})d\mathbf{r}$. The exchange-correlation energy $E_{\text{xc}}[n]$ contains those expressions that represent the differences in kinetic energy and electron-electron interaction between the fictitious system and the real system, and 'absorbs all the complicated many-body effects not contained in T_s , E_{ext} and E_H '.^[178]

$$E_{\text{xc}}[n] = F_{\text{HK}}[n] - T_s[n] - E_H[n] \quad (2.8)$$

The main aspect of the Kohn-Sham theory is now that the ground-state density n_0 of a system containing $2N$ interacting electrons can be determined by calculating a self-consistent solution of the Kohn-Sham equations:

Kohn-Sham Equations

$$\left(-\frac{1}{2} \nabla^2 + v_{\text{eff}}(\mathbf{r}) \right) \Phi_i(\mathbf{r}) = \varepsilon_i \Phi_i(\mathbf{r}) \quad (2.9)$$

The Φ_i are the one-particle-wave-functions in the effective one-particle potential $v_{\text{eff}}(\mathbf{r})$:

$$v_{\text{eff}}(\mathbf{r}) = v_{\text{ext}}(\mathbf{r}) + v_H(\mathbf{r}) + v_{\text{xc}}(\mathbf{r}), \quad (2.10)$$

a sum of the nuclei potential $v_{\text{ext}}(\mathbf{r})$, the Hartree potential $v_H(\mathbf{r}) = \int \frac{n(\mathbf{r}')}{|\mathbf{r} - \mathbf{r}'|} d\mathbf{r}'$ and the exchange-correlation potential $v_{\text{xc}}(\mathbf{r}) = \frac{\delta E_{\text{xc}}[n]}{\delta n(\mathbf{r})}$.

The electronic density can then be calculated using the one-particle wave-functions (also called Kohn-Sham orbitals) $\Phi_i(\mathbf{r})$ with the occupation numbers f_i by:

$$n(\mathbf{r}) = \sum_i f_i |\Phi_i(\mathbf{r})|^2, \quad (2.11)$$

with

$$f_i = \begin{cases} 2 & , \text{ for } \varepsilon_i < \varepsilon_F \\ 0 \leq f_i \leq 2 & , \text{ for } \varepsilon_i = \varepsilon_F \\ 0 & , \text{ for } \varepsilon_i > \varepsilon_F \end{cases} \quad (2.12)$$

valid for a spin-unpolarized system. ε_i denotes the eigenvalue of orbital i and ε_F refers to the Fermi energy of the system.

Unfortunately, the Kohn-Sham wave-functions lack a proper physical interpretation. The effective one-particle energies ε_i can e.g. be interpreted as the derivative of the total energy with respect to the occupation numbers as shown by Janak in his publication *Proof that $\frac{\partial E}{\partial n_i} = \varepsilon_i$ in density-functional theory.*^[179] However, Kohn-Sham orbitals are often successfully used to interpret simulation results, see e.g. Ref. [180].

2.1.3 Approximations to Exchange and Correlation

As seen in subsection 2.1.2, although DFT is in principle exact, there is at least one major approximation to be dealt with. It is the lack of knowledge about the exchange-correlation functional $E_{xc}[n]$. In the literature, density-functional theory (DFT) is sometimes distinguished from density-functional approximation (DFA)^[181] because DFT is an exact theory whereas *'the failures we report at meetings and in papers are not failures of DFT, but failures of DFAs'*^[181], as formulated by Becke. The exchange-correlation energy is defined by Equation 2.8. Although its exact value is unknown, there exist a huge number of approximations with different levels of complexity. For an overview see e.g. the library of exchange correlation functionals LIBXC described in Ref. [182] and references therein.

One way to classify all the existing functionals was introduced by Perdew and is known as the *Jacob's ladder* of the DFT-functionals.^[183] This ladder has several rungs that resemble the grade of complexity for the expression of the exchange-correlation functional. On the first rung, the *local density approximation* (LDA) is located. Perdew calls it the *'mother of all approximations'* because it has the most intuitive form including only the local spin density $n(\mathbf{r})$. On the second rung, the gradient of the local density is considered as well which leads to the gradient approximations with the *generalized gradient approximation* (GGA) being a very successful representative. The ladder continues with meta-GGA functionals and other rungs until the exactness finally reaches the *'heaven of chemical accuracy'* which from a today's point of view is unachievable. So to say, *it can only be dreamt of*—which is why this idea was baptized with the current name.

Furthermore, there exist functionals that take into account empirical corrections like the functional proposed by Becke^[184] or functionals that approximate the exchange-correlation potential with the help of machine learning techniques.^[185]

Local Density Approximation (LDA)

The main idea of the local density approximation (LDA) is to consider an electronic system (which is in general inhomogeneous) as being locally homogeneous. The exchange-correlation energy is then calculated as the integral over all space with the exchange-correlation energy density at each point assumed to be the same as in a homogeneous electron gas with that same density.^[186]

LDA - Exchange Correlation Functional

$$E_{xc}^{\text{LDA}}[n] = \int n(\mathbf{r}) \epsilon_{xc}^{\text{hom}}(n(\mathbf{r})) d\mathbf{r} \quad (2.13)$$

Still, the exchange-correlation energy $\epsilon_{xc}^{\text{hom}}$ of the homogeneous electron gas as a function of the density needs to be found. It consists of two parts: first, the exchange energy that can be calculated analytically (e.g. Ref. [186]) and second, the correlation energy that can be calculated using Monte-Carlo methods.^[187]

Compared to the Thomas-Fermi-Dirac model, this approximation gives good results, al-

though binding energies tend to be overestimated and lattice constants tend to be underestimated. Furthermore, non-local effects are neglected (which are needed in order to describe e.g. systems where the van-der-Waals interaction is relevant). The success of LDA stems from the fact that it has several formal properties in common with the exact E_{xc} that lead to error cancellations. For an overview on this subject see e.g. Ref [178].

Generalized Gradient Approximation (GGA)

The next generation of exchange-correlation functionals are formed by the generalized gradient approximations. Whereas the LDA only includes knowledge about the density at a given point \mathbf{r} , the gradient approximations also consider information about spatial variations of the electron density and, in consequence, include the density gradient. In 1986, Perdew and Wang presented the *generalized gradient approximation* (GGA)^[188]. The exchange-correlation functional is represented in the following way:

GGA - Exchange Correlation Functional

$$E_{\text{xc}}^{\text{GGA}}[n] = \int n(\mathbf{r}) \varepsilon_{\text{xc}}^{\text{GGA}}(n(\mathbf{r}), \nabla n(\mathbf{r})) d\mathbf{r} \quad (2.14)$$

Several GGA functionals were developed, for an overview see e.g. the article by Filippi, Gonye and Umrigar.^[189] Two often used representatives are the functionals developed by Perdew and Wang (PW91)^[190] and by Perdew, Burke and Ernzerhof (PBE).^[191] In calculations that use GGA functionals, improved energy differences and binding energies have been obtained compared to LDA calculations.^[190]

Bond lengths calculated using GGA functionals reduce significantly the over-binding obtained in calculations that use LDA functionals. However, they still show a slight over-binding tendency. This tendency can be traced back to the fact that in multi-center systems, e.g. the H_2 -molecule, the exact exchange hole is spread over both centers whereas the GGA exchange hole is inherently localized.^[192]

In the development of functionals, a natural next step was to include the second derivative of the density, leading to so-called meta GGA functionals. Generally, meta-GGA functionals also include a dependence on the kinetic energy density.

In order to better capture delocal effects, Kohn-Sham wavefunctions are included explicitly in the computation of the XC energy. This leads to hybrid functionals and exact exchange that are also a step towards solving the self interaction error.

Self-Interaction Error

As pointed out by Fermi and Amaldi^[193] and later emphasized by Perdew and Zunger^[194] many approximations to the exchange-correlation functional are not self-interaction free. *Self-interaction* is directly connected to the Hartree energy (Equation 2.7) which describes an electron interacting with all electrons in a given system. The term includes the interaction of the electron with its own meanfield, which the exact density-functional for

the ground-state energy corrects, i.e. it is strictly self-interaction free.^[194] Consequences of the self interaction error are numerous, e.g. the dissociation curve of an H_2^+ molecule is not well described because a delocalized solution of the electron is preferred due to the SIE.^[195,196] This deficiency was analyzed in detail for many systems.^[197] Furthermore, functionals with an SIE underestimate semiconductor band gaps^[198,199] and cause deviations from Koopmans theorem.^[198,200] In the context of TDDFT simulations, substantial errors for the excitation energies of charge-transfer excited states are traced back to the SIE.^[201] The asymptotic behavior of the exchange and correlation potential is not well described. In a finite system, the electronic density decays asymptotically exponential with r towards the vacuum as the electron density $n(\mathbf{r}) \propto e^{-\alpha|\mathbf{r}|}$ where α is related to the ionization potential of the system. Note that for LDA functionals, v_{XC} also decays exponentially because nonlocal interactions are not taken into account. However, in case of an exact XC-functional $v_{\text{XC}}(\mathbf{r}) \propto -1/|\mathbf{r}|$ is expected.^[202-204] There exist GGAs^[205] and meta-GGAs^[206,207] with the correct asymptotic behavior. However, it has been shown that, no GGA can give the exact functional derivative and the exact asymptotic exchange energy density.^[208] An interesting consequence is that Rydberg states, which are characteristic of the $-1/r$ behavior are not well described within local approximations.^[178,205] Consequences of the failure to reproduce the correct image potential of the electron regarding H in front of an Al surface are discussed in chapter 3.

There exist many approaches towards a solution of the SIE problem. A self interaction correction (SIC) was first formulated by Fermi and Amaldi,^[193] and later extended by Perdew and Zunger who proposed to subtract the SIE for each individual orbital.^[194] Legrand et al. developed a numerically less demanding averaged density self interaction correction (ADSIC)^[209] formalism. A different solution is to include the optimized effective potential (OEP) which is the exact Kohn-Sham potential for explicitly orbital-dependent energy functionals, either fully^[210] or in the Krieger-Li-Iafrate approximation.^[211] A further approach taken by different research groups is to include a self interaction correction directly into the atomic pseudopotential, i.e. to employ self-interaction corrected pseudopotentials.^[212,213] A comparison study for different XC functionals with a focus on the problem of self-interaction in TDDFT-MD simulations was presented by Quashie et al.^[214] who studied a proton interacting with a CH_4 molecule. A general overview on the self-interaction problem in DFT can be found e.g. in Ref. [215].

Spin-Polarization

Until now, it was assumed that a pair number of $2N$ electrons is equally distributed within the spin-up and spin-down channels of a given electron gas, i.e. $N_{\uparrow} = N_{\downarrow} = N$. However, as pointed out by e.g. Gunnarsson, Lundqvist and Wilkins,^[216] using the previously introduced local-density functional (Equation 2.13), the atomic energy of even very simple systems like the hydrogen atom, deviates around 10% from the exact value. The authors of Ref. [216] argued with the help of numerical results and *a priori* considerations that especially in applications with unpaired valence electrons, such as e.g. hydrogen or sodium atoms, a spin-density formalism must be used in order to improve the calculations. They argued that both, the exchange-correlation energy as well as the potential, are

to be calculated from the homogeneous (paramagnetic) electron liquid. When accounting for exchange and correlation, the spin-unpolarized theory thus views the electrons as a spin-compensated electron liquid,^[216] which is a very general approximation. In order to include spin-polarization into the calculations, the exchange-correlation functional is split into a part for n_{\uparrow} and another one for n_{\downarrow} . I.e. for the *local spin-density approximation* (LSDA):

$$E_{xc}^{\text{LSDA}}[n_{\uparrow}, n_{\downarrow}] = \int n(\mathbf{r}) \varepsilon_{xc}(n_{\uparrow}(\mathbf{r}), n_{\downarrow}(\mathbf{r})) d\mathbf{r} \quad (2.15)$$

In general, the exact result for the exchange energy of the spin-polarized density is calculated from:^[178]

$$E_x[n_{\uparrow}, n_{\downarrow}] = (E_x[2n_{\uparrow}] + E_x[2n_{\downarrow}])/2 \quad (2.16)$$

The correlation energy is usually represented in dependence of the total density $n(\mathbf{r})$ and the fractional polarization $\zeta = \frac{n_{\uparrow} - n_{\downarrow}}{n_{\uparrow} + n_{\downarrow}}$. As shown by von Barth and Hedin,^[217] the correlation energy of a spin-polarized homogeneous electron gas can be obtained with the help of random phase approximation (RPA) calculations.

Interestingly, the difference in atomization energy arising from the inclusion of spin-polarization amounts to the order of eV. In case of the hydrogen atom, Gunnarsson, Lundqvist and Wilkins^[216] obtained a difference between LDA and LSDA of 1.1 eV, with $E^{\text{LSDA}} = -13.38$ eV (exact result: $-0.5 H \approx -13.6$ eV).

Spin-polarization is highly relevant for the considerations underlying the present thesis. In a system that contains a hydrogen atom approaching a metal surface the local spin-polarization at the hydrogen atom is lost at the spin-transition distance z_s . This constitutes a nonadiabatic process which was investigated using TDDFT-MD by Lindenblatt and Pehlke^[140] or with the help of a time-dependent, mean-field Newns–Anderson model by Mizieliński et al.^[124] Consequences and problems for a proton approaching a metal surface are discussed in chapter 4.

2.2 Time-Dependent Density-Functional Theory

The density-functional theory (DFT) framework introduced in the previous section is usually referred to as ground-state theory. However, this is not correct because a given ground-state density $n_0(\mathbf{r})$ determines the potential $v(\mathbf{r})$ (up to an additive constant). From $v(\mathbf{r})$ one can obtain the full Hamiltonian and, solving the Schrödinger equation, a connection between $n_0(\mathbf{r})$ and any excited state is built. This means that excited states are also determined by the ground-state density and excitation energies are functionals of the ground-state density, too. Unfortunately, the functional connection remains unknown.^[178] Nevertheless, there exist several approaches to obtain information about the excited states from the so-called ground-state framework such as the Δ_{SCF} approach,^[218] constrained DFT^[219] or ensemble DFT.^[220,221] The present work takes another approach to simulate time-dependent phenomena. We use real-time time-dependent density-functional theory (TDDFT) which is often seen as an extension of DFT to the time-dependent regime. In the following, a short overview of the underlying physical concepts will be given. Detailed discussions can be found e.g. in Refs. [222–224].

2.2.1 Runge-Gross Theorem

Runge and Gross^[225] developed the proof for a theorem, which is analog to the Hohenberg-Kohn theorem (subsection 2.1.1) but valid for time-dependent problems. Today this theorem is generally referred to as the Runge-Gross theorem.

Runge-Gross Theorem

"Two densities $n(\mathbf{r}, t)$ and $n'(\mathbf{r}, t)$, that evolve from a common initial many-body state Ψ_0 under the influence of two different potentials $v(\mathbf{r}, t)$ and $v'(\mathbf{r}, t) \neq v(\mathbf{r}, t) + c(t)$ (both assumed to be Taylor-expandable around t_0), will start to become different infinitesimally later than t_0 . Therefore, there is a one-to-one correspondence between densities and potentials, for any fixed initial many-body state (given that the potentials differ by more than a time-dependent constant $c(t)$)."^[224,225]

The theorem is proofed in two steps. First, a one-to-one correspondence between current densities and external potentials is established. Second, the proof is extended to the case of densities. In the following, the mathematical proof from Runge and Gross^[223,225] will be sketched in its essential parts.

First Step: One starts from the equation of motion of the expectation value of the current density $\mathbf{j}(\mathbf{r}, t) = \langle \Psi(t) | \hat{\mathbf{j}}(\mathbf{r}) | \Psi(t) \rangle$

$$i \frac{\partial \mathbf{j}(\mathbf{r}, t)}{\partial t} = \langle \Psi(t) | [\hat{\mathbf{j}}(\mathbf{r}), \hat{H}(t)] | \Psi(t) \rangle \quad (2.17)$$

and takes two different time-dependent potentials, $v(\mathbf{r}, t)$ and $v'(\mathbf{r}, t)$, acting on a system with a given fixed initial state. The potentials must fulfill the condition that they are Taylor

expandable, i.e.:

$$v(\mathbf{r}, t) = \sum_{k=0}^{\infty} \frac{1}{k!} v_k(\mathbf{r})(t - t_0)^k \quad (2.18)$$

with the coefficients v_k and v'_k . Furthermore, the potentials must differ by more than just a time-dependent function $c(t)$: $v(\mathbf{r}, t) - v'(\mathbf{r}, t) \neq c(t)$, i.e. there exists a smallest integer $k \geq 0$ for which

$$v_k - v'_k \neq \text{const.} \quad (2.19)$$

The equation of motion for the difference of the two current densities at $t = t_0$ reads:

$$\begin{aligned} \left. \frac{\partial}{\partial t} \{ \mathbf{j}(\mathbf{r}, t) - \mathbf{j}'(\mathbf{r}, t) \} \right|_{t=t_0} &= -i \langle \Psi_0 | [\hat{\mathbf{j}}(\mathbf{r}), \{ \hat{H}(t_0) - \hat{H}'(t_0) \}] | \Psi_0 \rangle \\ &= -n(\mathbf{r}, t_0) \nabla (v(\mathbf{r}, t_0) - v'(\mathbf{r}, t_0)), \end{aligned} \quad (2.20)$$

with $\Psi_0 \stackrel{\text{def}}{=} \Psi(t_0)$.

If v and v' are different at times later than t_0 , then the two current densities \mathbf{j} and \mathbf{j}' will differ. To show this, two cases must be considered:

1. If condition 2.19 is satisfied for $k = 0$, then the right hand side of Equation 2.20 is different from zero infinitesimally later than t_0 . \mathbf{j} and \mathbf{j}' are then different, too.
2. If condition 2.19 is satisfied for $k > 0$, then the equation of motion is applied k times, where k is the smallest integer for which 2.19 holds, the following expression is obtained:

$$\left. \frac{\partial^{k+1}}{\partial t^{k+1}} \{ \mathbf{j}(\mathbf{r}, t) - \mathbf{j}'(\mathbf{r}, t) \} \right|_{t=t_0} = -n(\mathbf{r}, t_0) \nabla (v_k(\mathbf{r}, t_0) - v'_k(\mathbf{r}, t_0)) \quad (2.21)$$

This means that that $\mathbf{j} \neq \mathbf{j}'$ for $t > t_0$.

Both arguments allow for the conclusion that \mathbf{j} and \mathbf{j}' will differ infinitesimally later than t_0 .

Second step: The next step in the argumentation chain extends this result and shows that not only different current densities arise from different time dependent potentials v and v' but also the densities themselves are different. Taking the gradient of Equation 2.21 and using the continuity equation

$$\frac{\partial n(\mathbf{r}, t)}{\partial t} = -\nabla \cdot \mathbf{j}(\mathbf{r}, t) \quad (2.22)$$

the following equation is obtained:

$$\begin{aligned} \left. \frac{\partial^{k+2}}{\partial t^{k+2}} \{ n(\mathbf{r}, t) - n'(\mathbf{r}, t) \} \right|_{t=t_0} &= -\nabla \cdot \left. \frac{\partial^{k+1}}{\partial t^{k+1}} \{ \mathbf{j}(\mathbf{r}, t_0) - \mathbf{j}'(\mathbf{r}, t_0) \} \right|_{t=t_0} \\ &= \nabla \cdot (n(\mathbf{r}, t_0) \nabla (v_k(\mathbf{r}) - v'_k(\mathbf{r}))) \end{aligned} \quad (2.23)$$

The proof ends with showing that the right hand side of Equation 2.23 is nonzero if the condition set by Equation 2.19 is fulfilled. This is shown by *reductio ad absurdum*. Take $g_k(\mathbf{r}) = v_k(\mathbf{r}) - v'_k(\mathbf{r})$ and assume that the right hand side of Equation 2.23 vanishes. Now consider the integral $\int d^3r n(\mathbf{r}, t_0) |\nabla g_k(\mathbf{r})|^2$, which can be rewritten with the help of Green's theorem

$$\int d^3r n(\mathbf{r}, t_0) |\nabla g_k(\mathbf{r})|^2 = \oint d\mathbf{S} \cdot (n(\mathbf{r}, t_0) g_k(\mathbf{r}) \nabla g_k(\mathbf{r})) - \int d^3r g_k(\mathbf{r}) \nabla \cdot [n(\mathbf{r}, t_0) \nabla g_k(\mathbf{r})] \quad (2.24)$$

Gross and Kohn^[226] showed that the surface integral \oint vanishes for experimentally realizable potentials because they arise from finite normalizable external charge distributions which go to zero at least as $1/r$. The term with the minus sign in Equation 2.24 is zero by assumption. However, the term on the left hand side of Equation 2.24 is not zero because $g_k \neq 0$. With this, a contradiction is found and the Runge-Gross theorem is proofed.

Note that the argument of a vanishing surface integral does not limit TDDFT to the study of finite systems only.^[224,227,228] A simple example is the case of a periodic external potential with a wavelength of λ length units applied to a one-dimensional periodic system of κ length units periodicity. Then, the above mentioned surface can be chosen as two points with distance $(\kappa \cdot \lambda)$ length units, which makes the surface integral vanish. This reasoning is easily extended to 2D and 3D periodic systems. However, as has been shown by Maitra et al.^[227] there are external potentials and geometries for which this argument does not hold. In Ref. [227], the case of a ring-shaped system exposed to a uniform electric field was investigated as a model system to which the above adumbrated reasoning cannot be applied. For an in-depth discussions of the validity of time-dependent density-functional theory (TDDFT) for periodic systems see e.g. Refs. [224, 227, 228].

2.2.2 Van Leeuwen Theorem

The Runge-Gross theorem states that the time-dependent density $n(\mathbf{r}, t)$ of a many-body system with a given particle-particle interaction $w(\mathbf{r}, \mathbf{r}')$ and a given fixed initial state Ψ_0 is a unique functional of the time-dependent potential $v(\mathbf{r}, t)$. However, the great success of static DFT (see section 2.1) is based on a mapping between the system of interacting electrons and a system of non-interacting electrons with modified effective potential. A proof on the existence of such an alternative system in case of TDDFT was provided by van Leeuwen in 1999:^[229]

Van Leeuwen Theorem

"A time-dependent particle density $n(\mathbf{r}, t)$ obtained from a given many-particle system can, under mild restrictions on the initial state, always be reproduced by an external potential $v'(\mathbf{r}, t)$ in a many-particle system with different two-particle interactions $w'(\mathbf{r}, \mathbf{r}')$. Given the initial state of this other many-particle system, the potential $v'(\mathbf{r}, t)$ is unique up to a purely time-dependent function."^[229]

Two special cases of the van Leeuwen theorem are of particular interest. The first one is

the case of $w' = w$ which means that the two many-body systems share the same interaction between electrons. If the initial wavefunctions Ψ'_0 are chosen as $\Psi'_0 = \Psi_0$, there exists a unique potential $v'(\mathbf{r}, t)$ that yields $n(\mathbf{r}, t)$. This result corresponds to the Runge-Gross theorem.

If the case of non-interacting electrons is chosen, i.e. $w' = 0$, and assuming that there exists a non-interacting initial state Ψ'_0 that reproduces the same density and time derivative of the density as Ψ_0 , then the van Leeuwen theorem states that there exists a unique potential (up to a purely time-dependent function) $v'_{\text{eff}}(\mathbf{r}, t)$ in a non-interacting system which produces $n(\mathbf{r}, t)$ at all times $t > t_0$. With this result, a formal justification of the following time-dependent Kohn-Sham equation is provided.

2.2.3 Time-Dependent Kohn-Sham Equations

As discussed in subsection 2.2.2, it is guaranteed that the time-dependent density $n(\mathbf{r}, t)$ of an interacting system with initial state Ψ_0 exposed to a potential $v(\mathbf{r}, t)$ can be reproduced by a non-interacting system, too. The effective potential acting on the non-interacting system is given by

$$v_{\text{eff}}[n, \Psi_0, \Phi_0](\mathbf{r}, t) \quad (2.25)$$

In practice, a system at time t_0 is assumed to be in its ground-state. At a time $t > t_0$ a time-dependent perturbation $v_1(\mathbf{r}, t)$ is switched on and the system evolves under the influence of $v_1(\mathbf{r}, t)$. Then, it is justified to apply the Hohenberg-Kohn theorem to the initial state, i.e. to Φ_0 and Ψ_0 which are functionals of the ground-state density n_0 . As a consequence, the effective potential in Equation 2.25 can be expressed as a functional of the density only: $v_{\text{eff}}[n](\mathbf{r}, t)$

The following set of equations can then be defined for a fictitious system of non-interacting electrons, the equations are known as time-dependent Kohn-Sham equations:

Time-Dependent Kohn-Sham Equations

$$i \frac{\partial}{\partial t} \Phi_j(\mathbf{r}, t) = \left(-\frac{1}{2} \nabla^2 + v_{\text{eff}}[n](\mathbf{r}, t) \right) \Phi_j(\mathbf{r}, t) \quad (2.26)$$

$$n(\mathbf{r}, t) = \sum_j f_j^{t=0} |\Phi_j(\mathbf{r}, t)|^2 \quad (2.27)$$

With the occupation number $f_j^{t=0}$ at $t = 0$ as defined in Equation 2.11.

As explained above, the time-dependent Kohn-Sham equations (Equation 2.26 and 2.27) are usually computed under the initial condition of $\Phi_j(\mathbf{r}, t_0) = \Phi_j^0(\mathbf{r})$, i.e. initially occupied one-particle ground-state Kohn-Sham orbitals are propagated in time. Here, the effective potential differs from the one in Equation 2.6 with the initial-state dependence entering in the evaluation of v_{xc} , which is defined through:

$$v_{\text{eff}}[n](\mathbf{r}, t) = v_{\text{ext}}(\mathbf{r}, t) + v_{\text{H}}[n](\mathbf{r}, t) + v_{\text{xc}}[n](\mathbf{r}, t), \quad (2.28)$$

where the Hartree potential is $v_H[n](\mathbf{r}, t) = \int \frac{n(\mathbf{r}', t)}{|\mathbf{r} - \mathbf{r}'|} d\mathbf{r}'$ and depends only on the density at time t . As will be discussed in subsection 2.2.4, the time-dependence of the exchange correlation potential is usually treated within an adiabatic approximation.

2.2.4 Adiabatic Approximation to Exchange and Correlation

From the theoretical foundations of TDDFT it is quite clear that the true exchange-correlation functional is not only non-local in space, but also in time. This means that the exchange-correlation potential at a given time t depends not only on the density $n(t)$ but on all previous densities $n(t')$, with $t' < t$. Due to this temporal non-locality, the time-dependent exchange-correlation functional is called *memory dependent*. However, any practical application using TDDFT today employs the adiabatic approximation in order to describe exchange and correlation. One way to tackle this problem is to neglect all time dependence and – following the spirit of LDA, whose main idea is to approximate the spatially non-local exchange-correlation functional by a purely local functional – approximate the temporally non-local functional dependency by depending only on the density at one instant. This approach is called the *adiabatic approximation*:

Adiabatic Approximation

$$v_{xc}[n](\mathbf{r}, t) = v_{xc}[n(\cdot, t)](\mathbf{r}) \quad (2.29)$$

A combination of the adiabatic approximation together with the LDA (Equation 2.13) or the GGA (Equation 2.14), can be found in the literature under the name of adiabatic local density approximation (ALDA) or adiabatic generalized gradient approximation (AGGA). Consequences of this approximation are discussed in the literature by e.g. Maitra.^[222]

2.3 Computational Aspects and Employed Software Packages

2.3.1 Creation of Atomic Pseudopotentials: fhi98PP

With respect to the treatment of atomic nuclei, DFT based electronic structure calculations can be divided into three groups, each of which is suited to treat different physical phenomena with varying numerical requirements. The first group are all-electron calculations where each atomic type i with n_i protons in the system contributes $n_e = n_i$ electrons to the calculation and atoms are set explicitly. Examples are the electronic structure codes ELK,^[230] exciting^[231] or FLEUR.^[232]

Another path is taken within the jellium approach where the nuclei together with the core electrons are taken as equally distributed in a certain region of space. Despite its preferable computational performance and success^[233] in the early stage of DFT simulations, this approach is increasingly less used due to the restrictive initial approximation.

A very successful compromise between both, the numerical accuracy and the computational requirements of the two previously mentioned approaches to treat the nuclei within DFT simulations, constitutes the pseudopotential approach. In the present thesis, atomic nuclei are treated within this approach. Here, each atom type i adds $n_{i,e} \leq n_i$ electrons to the simulation, typically only valence electrons are treated explicitly within the Kohn-Sham equations. The remaining $n_i - n_{i,e}$ electrons (the core electrons) are included into the pseudopotential and are treated as frozen-in states.

The idea behind the pseudopotential approach is based on the assumption that only the valence electrons of the atoms are relevant for an accurate description of the properties of molecules (in this treatment described by atoms that formed chemical bonds). A mathematical more accurate justification for the so called frozen core approximation was given by von Barth and Gelatt^[234] who pointed out that, although there are quantities like the kinetic energy of the core electrons that vary significantly between bound and unbound atoms, it is still justified to treat the core electrons as frozen-in. The authors of Ref. [234] pointed out that this apparent contradiction can be explained by the fact that—in contrast to the kinetic energy—the total energy varies much less between the two situations and required corrections vanish to first order.

The use of pseudopotentials is motivated by the need to optimize DFT simulations in order to minimize the required computation time while limiting the introduced accuracy issues. The approach to not treat all atomic electrons explicitly reduces the number of Kohn-Sham states significantly. E.g. in case of the Al atom, out of the 13 electrons of a neutral atom, only 3 are treated explicitly whereas the remaining 10 electrons are taken into the core and treated as being part of the pseudopotential. They even are treated in a relativistic way. Furthermore, the pseudo valence electron wavefunctions $|\psi_{ps}\rangle$ are no longer required to be orthogonal to the core electron wavefunctions, which implies that in the region close to the atom core, the $|\psi_{ps}\rangle$ can have less nodes and thus require less Fourier components for their representation. This means that the use of pseudopotentials significantly reduces the needed wavefunction cutoff energy and the corresponding

computational effort.

Norm-Conserving Pseudopotentials Over the past decades, different flavours of pseudopotentials have been developed of which in this thesis the norm-conserving Troullier-Martins type pseudopotentials were employed.^[235,236] They ensure transferability, i.e. the ability to accurately describe the valence electrons in different chemical environments, by satisfying the following requirements:

1. all-electron and pseudo valence eigenvalues agree for a reference configuration (typically the neutral atom)
2. all-electron and pseudo wavefunctions agree beyond a cutoff radius r_{cutoff}
3. integrals of the charge density from 0 to r agree for $r > r_{\text{cutoff}}$ for each valence state, i.e. the norm is conserved
4. logarithmic derivatives $D_l(\epsilon, r) = r\psi'_l(\epsilon, r)/\psi_l(\epsilon, r)$ of all-electron and pseudo wavefunction and first energy derivatives $dD_l/d\epsilon$ agree at r_{cutoff}

The last point is already implied by the norm conservation. A detailed algorithm for producing a norm-conserving Troullier-Martins pseudopotential can be found in Ref. [236].

In general, from a solution of the radial equation for a spherical atom or ion

$$-\frac{1}{2}\varphi_l''(r) + \left[\frac{l(l+1)}{2r^2} + v_{\text{eff}}(r) - \epsilon_l \right] \varphi_l(r) = 0 \quad (2.30)$$

one can obtain the angular momentum l dependent screened potential for the valence electrons. The word *screened* refers to the fact that this potential still contains the Hartree and exchange-correlation potential of the pseudo wavefunctions which are in a following step subtracted to obtain the *unscreened* potential $V_l(r)$. As pointed out by Louie, Froyen and Cohen,^[237] an improvement of the unscreened potential can be obtained by taking into account a non-linear core-valence correction. In this case, an additional partial core density is distributed together with the pseudopotential.

V_l can be written as the sum of a purely local (i.e. only r -dependent) part $V_{\text{local}}(r)$ and non-local terms $\delta V_l(r)$:

$$V_l(r) = V_{\text{local}}(r) + \delta V_l(r), \quad (2.31)$$

The potential $V_l(r)$ approaches large distances like $\lim_{r \rightarrow \infty} V_l(r) = -Z_{\text{ion}}/r$ and eigenvalues and orbitals are by construction the same for the all-electron atom and the pseudo atom. Long-range effects are included in the local potential, and $\delta V_l = 0$ for $r > r_{\text{cutoff}}$. The semi-local operator describing this potential is then written as:

$$\hat{V}_{\text{SL}} = V_{\text{local}}(r) + \sum_{l,m} |Y_{lm}\rangle \delta V_l(r) \langle Y_{lm}|, \quad (2.32)$$

with the spherical harmonics Y_{lm} . V_l is semilocal because it is local in the radial part and non-local in the angular part.

Kleinman and Bylander^[238] pointed out that the semilocal operator can, within a reliable approximation, be replaced by a fully separated operator. The operator can be expressed as a sum of a purely local potential and a purely non-local potential:^[186]

$$\hat{V}_{\text{NL}} = V_{\text{local}}(r) + \sum_{lm} \frac{|\varphi_{lm}(\mathbf{r})\delta V_l(\mathbf{r})\rangle\langle\varphi_{lm}(\mathbf{r})\delta V_l(\mathbf{r})|}{\langle\varphi_{lm}(\mathbf{r})|\delta V_l(\mathbf{r})|\varphi_{lm}(\mathbf{r})\rangle} \quad (2.33)$$

Where the functions $\langle\varphi_{lm}(\mathbf{r})\delta V_l(\mathbf{r})|$ are projectors that are evaluated on the wavefunction $|\varphi\rangle$

$$\langle\varphi_{lm}\delta V_l|\varphi\rangle = \int \delta V_l(\mathbf{r})\varphi_{lm}^*(\mathbf{r})\varphi(\mathbf{r})d\mathbf{r} \quad (2.34)$$

The separable form carries a significant numerical advantage compared to the semi-local operator because calculating matrix elements $\langle\varphi_i|\delta\hat{V}_{\text{NL}}|\varphi_j\rangle$ is reduced to the calculation of products of projection operations.

For the applied TDDFT-molecular dynamics (MD) simulations, the introduced non-locality of the pseudopotential has to be taken into account for the regarding equations of motion (see subsection 2.3.3).

Generally speaking, the field of pseudopotentials is widespread with a huge number of science groups involved in development and improvement of reliable pseudopotentials. Further steps that aim to optimize pseudopotentials but exceed the scope of this thesis are e.g. ultrasoft pseudopotentials^[239] or the recently developed norm-conserving Vanderbilt (also called SG15) pseudopotentials.^[240,241]

A very convenient tool for creation and analysis of atomic pseudopotentials that was used throughout this work is the fhi98PP software by Fuchs and Scheffler.^[242] The package allows to generate norm-conserving pseudopotentials with the above depicted scheme with different approximations to exchange and correlation and *'facilitates a first assessment of the pseudopotentials' transferability, either in semilocal or fully separable form, by means of simple tests carried out for the free atom.*^[242]

2.3.2 Time Propagation of the Time-Dependent Kohn-Sham Equations

As a next step, the question on how to solve numerically the time-dependent Kohn-Sham equations (Equation 2.26 and 2.27) will be presented. The following explanations only serve as an overview on this complex subject, for further aspects like stability or numerical efficiency, see e.g. the publications by Castro, Marques and Rubio^[243] and Pueyo, Marques, Rubio and Castro.^[244] The time-dependent Kohn-Sham equations in the adiabatic approximation introduced in subsection 2.2.4 can be categorized as initial-value first-order ordinary differential equations. Formally, the initial value problem can be solved by applying the evolution operator $\hat{U}(t, 0)$ to the initial value ϕ_0 .^[245]

$$\phi(t) = \hat{U}(t, 0)\phi_0 \quad (2.35)$$

The time-ordered evolution operator is defined through:

$$\hat{U}(t, 0) = \sum_{n=0}^{\infty} \frac{(-i)^n}{n!} \int_0^t dt_1 \int_0^{t_1} dt_2 \cdots \int_0^{t_{n-1}} dt_n \mathcal{T}(\hat{H}(t_1)\hat{H}(t_2)\cdots\hat{H}(t_n)) \quad (2.36)$$

Where \mathcal{T} represents the time order product. Or, in a commonly used shorthand notation with the time-ordered exponential $\mathcal{T} \exp$:

$$\hat{U}(t, 0) = \mathcal{T} \exp \left\{ -i \int_0^t d\tau \hat{H}(\tau) \right\} \quad (2.37)$$

For the evaluation of Equation 2.35, three numerical choices have to be made:

1. An approximation for the evolution operator $\hat{U}(t + \delta t, t)$ is needed.
2. An interpolation scheme on how to approximate the 'future' Hamiltonian $\hat{H}(\tau)$ with $\tau > t$ is required.
3. As $\hat{U}(t + \delta t, t)$ is represented in terms of an exponential, an approximation for the exponential is required.

These choices are not for all schemes as easily separable from each other as presented here. However, for a clear overview on a time-propagation within TDDFT the following derivation pretends a clear separation:

Approximating the Evolution Operator For model systems, there exist global iteration schemes of the time-dependent Kohn-Sham equations,^[246] however, in case of small time steps δt – which are usually assumed in TDDFT simulations – the time development from a given time t_i to a time $t_i + \delta t_i$ described by the evolution operator of Equation 2.37 can be approximated as:^[247]

$$\hat{U}(t_i + \delta t_i, t_i) \approx e^{-i\delta t_i \hat{H}(t_i + \delta t_i/2)} \quad (2.38)$$

Then, the composition property $\hat{U}(t_3, t_1) = \hat{U}(t_3, t_2)\hat{U}(t_2, t_1)$ for times $t_1 < t_2 < t_3$ can be used:

$$\hat{U}(t_N, 0) = \prod_{i=0}^{N-1} \hat{U}(t_i + \delta t_i, t_i) \quad (2.39)$$

I.e. the propagation is carried out step-by-step. In case of the simulations of the present thesis, the time step δt_i was set constant, i.e. $\delta t_i = \delta t$.

An often chosen propagator uses the exponential midpoint (EM) rule to calculate the propagator $\hat{U}(t_i + \delta t, t_i)$, then:

$$\hat{U}_{\text{EM}}(t_i + \delta t, t_i) = e^{-i\delta t \hat{H}(t_i + \frac{\delta t}{2})} \quad (2.40)$$

But also other ways to express \hat{U} are taken, like the enforced time-reversal symmetry (ETRS) method, where:

$$\hat{U}_{\text{ETRS}}(t_i + \delta t, t_i) = e^{-i\frac{\delta t}{2} \hat{H}(t_i + \delta t)} \cdot e^{-i\frac{\delta t}{2} \hat{H}(t_i)} \quad (2.41)$$

Interpolating the Hamiltonian The propagators of Equation 2.40 and 2.41 contain a Hamiltonian $\hat{H}(\tau_i)$ that has to be evaluated at times $t_i \leq \tau_i \leq t_i + \delta t$. To obtain an estimation superior to a simple polynomial extrapolation, TDDFT codes use a *predictor-corrector* method where, as e.g. pointed out in Ref. [224], a five step iteration is used:

Predictor-Corrector Method (simple version)

The Hamiltonian $\hat{H}(\tau_i)$ at a time τ_i where $t_i \leq \tau_i \leq t_i + \delta t$ can be approximated using the following iteration scheme:^[224]

1. Obtain $\hat{H}(\tau_i)$ through extrapolation with a polynomial fit to k previous steps.
2. Propagate the time-dependent Kohn-Sham wavefunctions from time t_i to time $t_i + \delta t$.
3. From the new wavefunctions calculate $\hat{H}(t_i + \delta t)$.
4. Obtain $\hat{H}(\tau_i)$ by interpolating between $\hat{H}(t_i)$ and $\hat{H}(t_i + \delta t)$.
5. repeat steps (2)–(5) until self-consistency is achieved

Please note that implementations of this scheme differ between implementations of TDDFT in computational codes, e.g. the order of the interpolation polynomial are different (compare e.g. Refs. [243] and [248]).

The number of self-consistency steps in the predictor-corrector method depends critically on the chosen time step δt .

Approximating the Exponential Applying $\exp(\hat{A})$ where the matrix \hat{A} is typically of the form $-i\delta t\hat{H}(\tau)$ to a vector v , i.e. evaluating $\exp(\hat{A})v$ seems to be an easy task. However, the size of a Hamiltonian used in a DFT calculation is often in the order of $10^5 \times 10^5$ (in a plane wave calculation this depends on the number of plane waves and \mathbf{k} -points) which is orders of magnitude beyond numerical feasibility.^[243,249] As discussed in Ref. [243], three different approaches are usually taken to obtain a numerical approximation:

1. The exponential can be expanded into polynomials, e.g. in a Taylor expansion using:

$$\text{taylor}_k\{\exp(\hat{A})v\} = \sum_{n=0}^k \frac{1}{n!} \hat{A}^n v \quad (2.42)$$

or in any other complete and orthonormal base of polynomials. Often Chebychev polynomials have also been chosen for quantum chemistry codes.^[245]

2. A solution of the eigenvalue problem with the help of the Lanczos algorithm. The algorithm is based on a reduction to Krylov subspaces and shows a comparatively good performance for sparse matrices.^[250]

3. Splitting techniques like the split-operator method where the Hamiltonian \hat{H} is decomposed into two terms: the kinetic energy operator \hat{T} which is diagonal in Fourier space and the potential operator \hat{V} which is computed in real space. Using the (numerically efficient) Fast Fourier Transformation to transform between real space and Fourier space, the split-operator technique is a highly stable method.^[251] A higher order split-operator technique found often in TDDFT codes represents the Suzuki-Trotter expansion, first implemented by Sugino and Miyamoto.^[252]

In the present work, we used the exponential midpoint rule as implemented in the Octopus code combined with a fourth order Taylor expansion due to its favourable numerical performance and stability. However, in a very recent publication, Pueyo et al. have presented a detailed analysis with the conclusion: *'Among the new families of propagators studied in this paper, the fourth-order commutator-free Magnus expansion beats every other propagator in terms of cost/accuracy, making it the recommended method for TDDFT.'*^[244]

2.3.3 Dynamics of the Nuclei

Whereas the time-dependent Kohn-Sham equations describe the dynamics of the electrons, an approach on how to calculate the forces on the nuclei is outlined in the present section. Within the context of nonadiabatic DFT, two very successful approaches are the *surface-hopping* proposed by Tully^[253,254] and the *mean-field* methods. The difference between the two approaches lies in how the atomic system reacts to quantum transitions.

In the first one, particles move on the potential energy surface of one particular quantum state. Whereas in the latter one, the time evolution of the system is represented by one single trajectory. More explicitly, this single trajectory corresponds to an average over quantum states. Naturally, this description is expected to be inadequate in situations where two or more significantly distinct reaction paths could be taken, for these cases, a description within the *surface-hopping* approach might be favored. The *mean-field* approach is based on the Ehrenfest theorem which describes the time-development of a quantum mechanical operator \hat{A} and reads

$$\frac{d}{dt}\langle\hat{A}\rangle = -i\langle[\hat{A}, \hat{H}]\rangle + \left\langle\frac{\partial\hat{A}}{\partial t}\right\rangle, \quad (2.43)$$

where \hat{H} is the Hamiltonian of the system.

From Equation 2.43, the expectation value of the momentum of the ions follows directly and the equation of motion for a nucleus I at position \mathbf{R}_I reads:

$$M_I\ddot{\mathbf{R}}_I = -\langle\Psi(t)|\nabla_I\hat{H}_{\text{elec}}|\Psi(t)\rangle \quad (2.44)$$

where \hat{H}_{elec} denotes the sum of electron-ion and ion-ion interaction potentials, and $-\langle\nabla_I\hat{H}_{\text{elec}}\rangle$ is approximated by an electronic expectation value at the respective ionic coordinates.^[255]

The foundation of Ehrenfest molecular dynamics simulations is formed in conjunction with the time-dependent Kohn-Sham equations (Equation 2.26 and Equation 2.27). Equation 2.44 can then be transformed into the *electrostatic force theorem*, which reads:^[178]

$$M_I \ddot{\mathbf{R}}_I = - \int d^3r n(\mathbf{r}, t) \frac{Z_I(\mathbf{r} - \mathbf{R}_I)}{|\mathbf{r} - \mathbf{R}_I|^3} + \sum_{I \neq J} \frac{Z_I Z_J (\mathbf{R}_I - \mathbf{R}_J)}{|\mathbf{R}_I - \mathbf{R}_J|^3} \quad (2.45)$$

The *electrostatic force theorem* has the significant advantage that nuclear movement can be obtained from 'simple electrostatics as the sum of Coulomb forces exerted by the other nuclei and [...] the electron cloud'.^[256]

However, this is only true if local potentials are assumed for the nuclei. Usually in DFT codes, nuclei are represented by semi-local potentials (see subsection 2.3.1), which means that nonlocal terms have to be included in Equation 2.45. Details can be found in the work of Nagano et al.^[257] or in the work of Castro.^[258]

Please note that the time derivative of the total energy E_{tot} , i.e. the sum of kinetic energies of the nuclei and the electronic energy within the system, is constant in time for systems without energy sources. This changes when e.g. an external laser field is applied. The mathematical argumentation chain for a wavefunction $|\Psi(t)\rangle$ that obeys the time-dependent Schrödinger equation $i \frac{d}{dt} |\Psi(t)\rangle = \hat{H}_{\text{elec}} |\Psi(t)\rangle$ and the equation of motion (Equation 2.44) is the following:^[259]

$$\frac{d}{dt} E_{\text{tot}} = \frac{d}{dt} (E_{\text{kin, Ion}} + E_{\text{elec}}) \quad (2.46a)$$

$$= \frac{d}{dt} \left(\sum_{I=1}^{N_{\text{Ion}}} \frac{1}{2} M_I \dot{\mathbf{R}}_I^2 + \langle \Psi(t) | \hat{H}_{\text{elec}} | \Psi(t) \rangle \right) \quad (2.46b)$$

$$= \sum_{I=1}^{N_{\text{Ion}}} M_I \dot{\mathbf{R}}_I \ddot{\mathbf{R}}_I + \frac{d}{dt} (\langle \Psi(t) | \hat{H}_{\text{elec}} | \Psi(t) \rangle) \quad (2.46c)$$

$$= \sum_{I=1}^{N_{\text{Ion}}} M_I \dot{\mathbf{R}}_I \ddot{\mathbf{R}}_I + \underbrace{\sum_{I=1}^{N_{\text{Ion}}} \langle \Psi(t) | \nabla_I \hat{H}_{\text{elec}} | \Psi(t) \rangle \dot{\mathbf{R}}_I}_{=-M_I \ddot{\mathbf{R}}_I} \quad (2.46d)$$

$$+ \underbrace{\left(\frac{d}{dt} \langle \Psi(t) | \hat{H}_{\text{elec}} | \Psi(t) \rangle + \langle \Psi(t) | \hat{H}_{\text{elec}} \left(\frac{d}{dt} | \Psi(t) \rangle \right) \right)}_{=0} \quad (2.46e)$$

$$= 0 \quad (2.46f)$$

This calculation can be extended to the case of TDDFT-MD simulations that employ an adiabatic XC-functional, see e.g. Refs. [186, 259].

Within TDDFT-MD simulations, the energy conservation can be used as a test for the stability as well as for the numerical accuracy of the numerical integration of the time-dependent Kohn-Sham equations.

2.3.4 Model Systems with Non-Vanishing Net Charge

Electronic structure calculations can not only be realized for neutral systems, but are also able to treat charged systems. This feature is of special interest for the present thesis because ions are charged systems by definition. When performing a DFT-calculation, there are significant advantages of using periodic cells and plane waves, for example the translational symmetry of the potentials involved in the calculations is easily accounted for in reciprocal space^[260] and Fourier Transforms are calculated by very efficient algorithms such as the FFTW^[261] which makes e.g. the calculation of the ion-ion interaction using Ewald summations rapidly converging.^[262] However, in the case of a cell with a net charge, the total charge of the infinite system is itself infinite resulting in a divergent Coulomb energy. Further unwanted phenomena arise due to the periodicity, i.e. in the case of polarized slab geometries, the periodicity results in a chain of capacitors which has to be accounted for accordingly.^[263] Here we focus on the problem connected with the use of charged systems.

To deal with this problem a compensating background charge^[264] can be included. In this method, additionally to a charged defect, a homogeneous background charge is added to the system. This evades a diverging energy and reduces the calculation of the Coulomb energy to the problem of a periodically repeating array of charges in a neutralizing background. For example, the energy of formation of a defect with charge Q in an otherwise perfect infinite crystal with lattice parameter L can then be calculated by adding a correction factor ($\propto Q^2/L$) to the energy difference between the perfect system and the compensated system.^[264]

A common way to completely avoid the interaction of defects entirely in non-periodic systems, e.g. a charged molecule, is to apply a Coulomb cutoff technique.^[260] Please note that this technique is not unique to electronic structure calculations but is also applied in the simulation of stellar^[265] or biological systems.^[266] The strategy implemented in the Octopus code (see subsection 2.3.5) is described in Refs. [260, 267, 268] and explained in the following. In summary, the idea is to screen the unit cell from the undesired effect of some of its periodic images by relying entirely on the Fourier space.^[260] In principle, in a 3D-periodic system with lattice vector \mathbf{L} and reciprocal lattice vector $\mathbf{G} = 2\pi/\mathbf{L}$, the potential

$$V(\mathbf{r}) = \int n(\mathbf{r}')v(|\mathbf{r} - \mathbf{r}'|)d\mathbf{r}' \quad (2.47)$$

with $v(|\mathbf{r} - \mathbf{r}'|) = 1/(|\mathbf{r} - \mathbf{r}'|)$ can be expressed in reciprocal space as

$$V(\mathbf{G}) = n(\mathbf{G})v(\mathbf{G}). \quad (2.48)$$

To avoid all interactions between the undesired periodic replicas of the system Equation 2.48 is transformed into

$$\tilde{V}(\mathbf{G}) = \tilde{n}(\mathbf{G})\tilde{v}(\mathbf{G}). \quad (2.49)$$

In order to find \tilde{V} , we introduce a screening region \mathcal{D} . Outside of it the Coulomb interaction vanishes, i.e. in real space, the effective interaction of $\tilde{v}(r)$ has the form

$$\tilde{v}(r) = \begin{cases} 1/r & , \text{if } r \in \mathcal{D} \\ 0 & , \text{else} \end{cases} \quad (2.50)$$

In principle, this region can be chosen arbitrarily but is usually chosen as being cubic^[269] or spherical.^[268] In case of a spherical cutoff with radius $R = \sqrt{3}L$ (to span the cell),

$$\tilde{v}^{0D}(G) = \frac{4\pi}{G^2} [1 - \cos(GR)] \quad (2.51)$$

is obtained. 0D stands for the solution of a finite system i.e. not periodic or 'periodic in 0 dimensions', to be consistent with the nomenclature of Ref. [260]. For this method to work, the simulation cell with edge length L has to be embedded into a larger box with edge length $(1 + \sqrt{3})L$ where the density of the extra points is set to zero. This prohibits an interaction between the density of two neighboring cells. An extension to systems with reduced periodicity (i.e. nano-rods) is given by Rozzi et al. in Ref. [260].

2.3.5 (TD)DFT-MD Simulations: Octopus

The ground-state as well as the time-dependent density-functional theory simulations presented in this work have been performed with the code Octopus which is developed by Rubio et al., see Refs. [270–274]. The code is licensed under the GNU general public license v2.0. The Octopus code consists of more than 200 000 lines of code^[274] with an enormous number of implemented theoretical concepts that make it possible to tackle a huge amount of different problems. In this thesis, the description of the features of Octopus is limited to the ones relevant to understand the work carried through here.

Within Octopus, electrons are described quantum-mechanically. I.e. in case of electronic ground-state calculations they obey the Kohn-Sham equations (see Equation 2.9). When propagating the wavefunctions in time, the Octopus code uses the time-dependent Kohn-Sham equations (Equation 2.26) in order to describe the dynamics of the electrons. Ions are described by pseudopotentials as described in subsection 2.3.1 or by user-defined functions. In the present work, Troullier-Martins pseudopotentials were employed for ions, analytic functions for antiprotons. Forces on the ions were described by Ehrenfest molecular dynamics (see subsection 2.3.3). Quantities are expanded in a real space mesh and were propagated in real time.

Time Step, Mesh Spacing and Cutoff Energy As pointed out by Kosloff,^[245] the time step δt is linked to the simulation through the maximum frequency ω_{\max} of the Hamiltonian that has to be represented, $\delta t \lesssim 1/\omega_{\max}$. In case of a TDDFT simulation without an external time-dependent potential, ω_{\max} may be approximated from the spectrum of the ground-state Hamiltonian. In case of a time-dependent simulation, however, the critical quantity are the oscillations of the represented wavefunctions, determined by the kinetic energy term:

$$\mathbf{G}_{\max}^2/2 = 2\pi^2/\lambda_{\min}^2, \quad (2.52)$$

with λ_{\min} as the minimal wavelength that can be sampled. The cutoff energy E_{cut} corresponding to a given spacing Δx , can be estimated using $E_{\text{cut}} = \mathbf{G}_{\max}^2/2$, then

$$\lambda_{\min} = 2\pi/\sqrt{\mathbf{G}_{\max}^2} = 2\pi/\sqrt{2E_{\text{cut}}}. \quad (2.53)$$

With the help of the Nyquist–Shannon sampling theorem, it is clear that the spacing has to be at least $\Delta x \approx \lambda_{\min}/2 = \pi/\sqrt{2E_{\text{cut}}}$. The Octopus code represents the density n on the same mesh, i.e. $G_{\max}^n = 2G_{\max}$, yielding $\lambda_{\min}^n = \pi/\sqrt{2E_{\text{cut}}}$ and for a relation between employed spacing Δx^n and the cutoff energy E_{cut} used in plane wave codes

$$\Delta x^n \approx \frac{\lambda^n}{2} = \frac{\pi}{2\sqrt{2E_{\text{cut}}}} \quad (2.54)$$

However, is it advised to be cautious when comparing between the value of cutoff energies in plane-wave based calculations and the value of a spacing in a real-space calculation.

User Defined Region The Octopus software allows the use of user defined simulation regions in order to decrease the numerical effort for a simulation. The user defined regions are given by logic functions $f : \mathbb{R}^3 \rightarrow \{\top, \perp\}$ that map from the real space to the logical values \top and \perp . For all points in space (x, y, z) , the expression is evaluated. Only if the result is \top , then the point is contained in the simulation box. An example can be seen in Equation 3.1.

2.3.6 Attributing Electronic Charges to Atoms

One of the main aspects of the present work is to analyze the neutralization of an ion interacting with a surface. Therefore, it is necessary to quantify the electronic charge transfer. Attributing charges to atoms that are chemically bound within molecules is a challenging problem often discussed in the chemistry literature (e.g. Ref. [275]). Different methods to tackle this challenge have been proposed due to the multivalent nature of the problem, i.e. atomic charges that 'belong' to an atom, a molecule or a solid are not observables and, therefore, cannot be defined unambiguously within quantum mechanics.^[276] There are a huge number of different flavors to approach the problem of charge attribution in the present context that use different aspects of the system as a starting point. This section discusses selected methods:

Charge Attribution by Division of Space A very simple approach is to divide the space Ω into fragments Ω_i and attribute the charge within each fragment to the atom/molecule within this fragment. The division of space may be reasoned by

1. a self-defined volume (e.g. spherical) around an atom.
2. the ion geometry. An example is a charge distribution based on the Voronoi partition scheme.^[277] The electronic charge attributed to an atom in this scheme is identical to the charge within its corresponding Wigner-Seitz cell or – in case of finite structures – the corresponding Thiessen polygon. This partition of space is used since Descartes (see Ref. [277]) and was successfully applied to study phenomena in different fields of research. Modeling forest dynamics^[278] or the design of neural networks^[279] are

just two examples. However, the generality of this approach is also a great disadvantage because this partition scheme is not taking into account any information of the electronic structure of a given system.

3. the density itself, i.e. through a Bader charge distribution.^[280] In this partition scheme, the electronic density $n(\mathbf{r})$ is analyzed and critical points, where the density has a local minimum, are identified. The scheme proposed by Bader^[280] divides space into regions Ω each corresponding to usually one atom A . The dividing planes of these regions are such that they are surfaces of zero-flux, i.e. the gradient of the charge density is zero along the surface normal. Let $\hat{s}(\mathbf{r})$ be the surface normal, then for every point \mathbf{r}_s on the surface of Ω it holds:

$$\nabla n(\mathbf{r}_s) \cdot \hat{s}(\mathbf{r}_s) = 0 \quad (2.55)$$

The Bader charge q_A^{Bader} of an atom A is then obtained by

$$q_A^{\text{Bader}} = Z_A - \int_{\Omega_A} n(\mathbf{r}) d\mathbf{r} \quad (2.56)$$

The problem of finding the local minima in the charge density was approached by the Henkelman group whose effort resulted in a reliable and widely used¹ tool that grants easy calculation of the Bader charges for a given system and that scales linearly with the number of grid points.^[276,281]

Charge Attribution by Wavefunction Projection Another approach is based on the electronic wavefunctions, where a projection of the atomic Kohn-Sham wavefunction Φ onto the Kohn-Sham orbitals Ψ_k of the occupied states N_{occ} is performed

$$q^{\text{projection}} = \sum_{k=0}^{N_{\text{occ}}} |\langle \Psi_k | \Phi \rangle|^2 \quad (2.57)$$

This approach requires access to the (time-dependent) wavefunctions Ψ_k , where storing a wavefunction occupies at least the memory of the charge density. Although this approach may be preferred over the Bader approach because of its quantum-mechanical foundation, the latter carries a significant advantage regarding memory usage.

Charge Attribution from Dipole Variation In case of Born-Oppenheimer computations, Born effective charges can be computed from the variation of a dipole moment μ_z with respect to the atomic z coordinate

$$q^{\text{Born}} = \frac{\partial \mu_z}{\partial z} \quad (2.58)$$

¹Ref. [281] with around 2500 citations as of today.

Meister and Schwarz^[275] discussed 25 different definitions of charges based on a principal component analysis. They report that one single component has been found which covers 90% of the variances. Their result is an indication that despite the different absolute values obtained when applying different methods, there is only one underlying physical concept.

2.3.7 Additionally Employed Software Packages

In addition to the physics simulation software, this work used various tools and software packages in order to evaluate, analyze and visualize the data. Visualization of atomic geometries has mainly been performed with the *Atomic Simulation Environment* ASE^[282] and graphical production using the *Visual Molecular Dynamics* suite vmd.^[283] Paraview^[284] was used to visualize wavefunctions and densities, and in some cases ovito.^[285] Line and density plots have been produced using Matplotlib.^[286] Data extraction and processing was performed using bash-scripts^[287] and the Python programming language.^[288] The thesis itself was written using Latex.

The following chapter concerns itself with the calculation and interpretation of time-dependent Kohn-Sham adsorbate level positions and Kohn-Sham electronic excitation spectra obtained from TDDFT-MD simulations. The case of a hyper-thermal proton impinging on an Al(111) surface is studied here. A visualization of the electronic charge density difference induced by a proton (H⁺) in front of an Al-cluster (for an arbitrarily chosen iso-value) is depicted schematically in Figure 3.1.

First, the following section 3.1 gives an overview on the parameters of the H⁺-Al(111) simulation employed in the present chapter 3, in chapter 4 and in chapter 5. This introduction is followed by section 3.2, where relevant physical properties of the Al bulk, the here employed Al-clusters, the Al(111) surface and the H-Al(111) systems are discussed.

In section 3.3, the calculation of Kohn-Sham adsorbate levels (i.e. position ε_a and width Γ) based on DFT and TDDFT simulations is realized and evaluated with a Brako-Newns-Anderson (BNA) model Hamiltonian simulation and a rate equation approach. An alternative formulation for the calculation of ε_a and Γ for the case of systems far from an electronic equilibrium situation is introduced and evaluated. This alternative formulation is based on a non-self-consistent calculation of frozen-density Kohn-Sham orbitals. In section 3.4, the time-development of the artificial Kohn-Sham electronic excitation spectrum

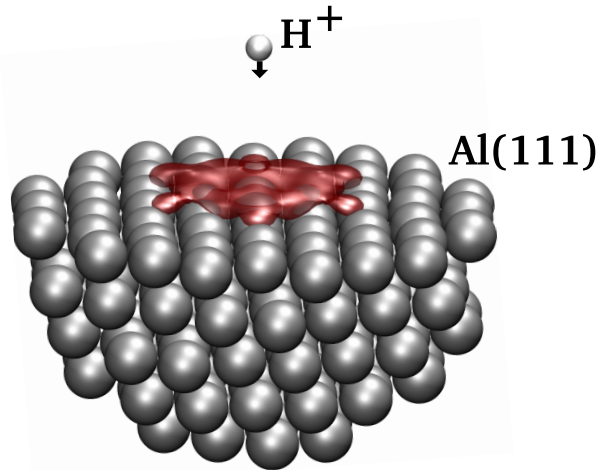


Figure 3.1: Visualization of the simulation. Proton (white sphere) in front of an Al₁₈₈-cluster. The red surface represents schematically the induced charge density difference arising from the presence of the proton with respect to the electronic ground-state of the cluster as obtained within a TDDFT-MD simulation. Starting distance for the simulations is 16 bohr. In this figure: $z_H = 14$ bohr.

and the corresponding alternative formulation are investigated against the background of ion-surface interaction. The case of the final excitation spectrum after scattering is also subject to section 3.4.

3.1 Computational Details

| Parameter | Unit | Value |
|----------------------------------|-------------------|--------------|
| Mesh Spacing | bohr | 0.5 |
| XC-Functional | | AGGA-PBE |
| Coulomb Cutoff | | spherical |
| Volume of Simulation Box | bohr ³ | 60 · 60 · 60 |
| Min Distance Atoms to Box Edge | bohr | 12.0 |
| Projectile Starting Distance z | bohr | 16.0 |
| Time Step | atu | 0.02 |

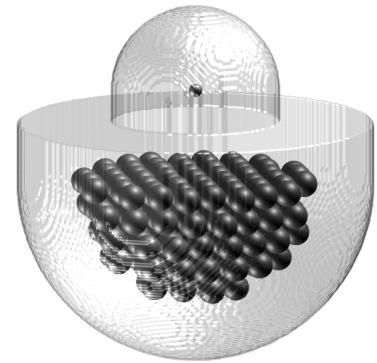


Table 3.1: **Left:** Overview of selected relevant parameters of the simulations with proton and Al_{188} and Al_{172} -clusters. Differences from these parameters are pointed out when required. **Right:** Visualization of the employed Al_{188} -cluster in the corresponding simulation cell.

For this work, density-functional theory simulations were employed with the simulation software Octopus (see subsection 2.3.5 and Refs. [270, 271, 273]). Most simulations have been performed with the generalized gradient approximation proposed by Perdew, Burke and Ernzerhof (PBE-GGA)^[191] exchange-correlation functional. To estimate the influence of the exchange-correlation functional, some simulations were performed employing a local density approximation (LDA).^[194] In the Octopus software, electronic wavefunctions and the electronic density are tabulated on a real-space mesh with equidistant mesh spacing, here $\Delta x = 0.5$ bohr. The same mesh spacing has been used for the x , y and z directions. The simulations have been performed inside a user-defined region that fits into a cube with edge size 60 bohr, and a minimum distance between atoms and the boundary of the user-defined region of 12 bohr. The user defined region (for details about the definition see subsection 2.3.5) can be described by a function $f(x, z, y)$ (values given in bohr, box center located at $x = y = z = 0$), where:

$$\begin{aligned}
 f(x, y, z) = & [(-30 \leq z \leq 0) \wedge (30 \geq \sqrt{x^2 + y^2 + z^2})] && \text{(lower half-sphere)} \\
 & \vee [(0 \leq z \leq 12) \wedge (30 \geq \sqrt{x^2 + y^2})] && \text{(large cylinder)} \\
 & \vee [(12 \leq z \leq 16) \wedge (14 \geq \sqrt{x^2 + y^2})] && \text{(small cylinder)} \\
 & \vee [(16 \leq z \leq 30) \wedge (14 \geq \sqrt{x^2 + y^2 + (z - 16)^2})] && \text{(upper half-sphere)} \quad (3.1)
 \end{aligned}$$

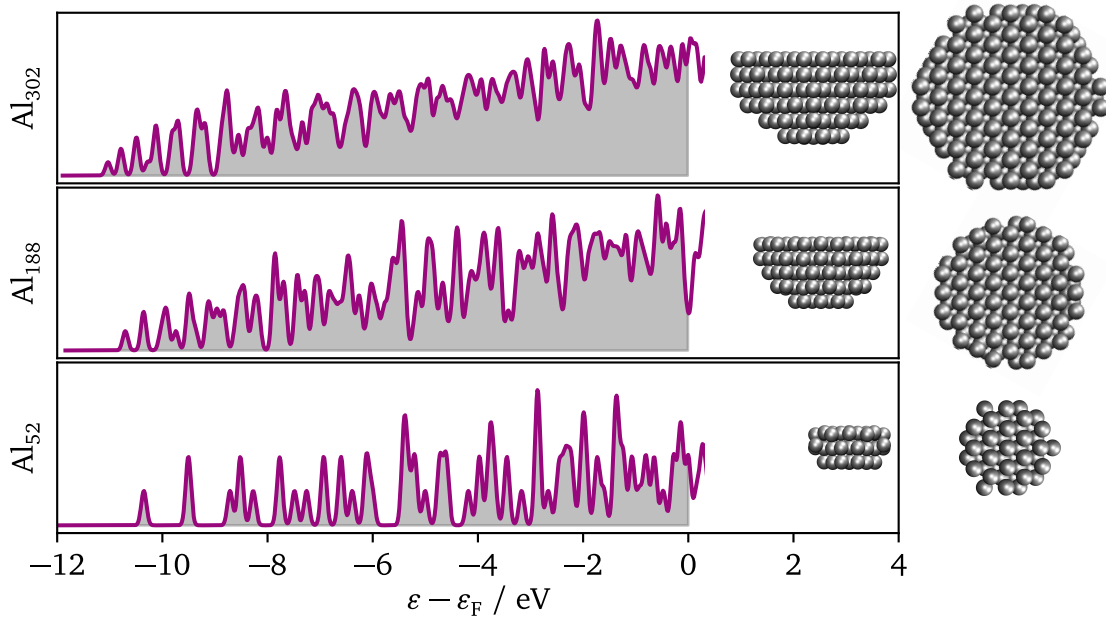


Figure 3.2: Density of (Kohn-Sham) states (DOS) of Al-clusters with 302, 188 or 52 atoms in arbitrary units. States are broadened with Gaussians of width $\sigma = 50$ meV. Unoccupied states (white background), are only shown up to 200 meV above ε_F . Side view and top view of the clusters are additionally shown.

This formula is visualized in Table 3.1. The first term describes the lower half sphere that contains the Al-cluster, the second one a cylinder on top of the half sphere with the same radius, the third term a smaller cylinder within which the projectile moves and the last term describes a sphere around the starting position of the projectile.

The H and Al ions are described by ionic semi-local norm-conserving Troullier-Martins pseudopotentials^[236] that were created with the fhi98PP software,^[242] see also subsection 2.3.1. Al has an atomic number of 13 with the electronic configuration of [Ne] 3s² 3p¹. In the creation of the pseudopotential, 10 electrons were treated as frozen-in core states and 3 as valence electrons. The cutoff radii $r_s^{\text{Al}} = 1.791$ bohr, $r_p^{\text{Al}} = 1.974$ bohr and $r_d^{\text{Al}} = 2.124$ bohr have been used. The p -potential has been chosen as the local potential. For the H pseudopotential cutoff radii $r_s^{\text{H}} = r_p^{\text{H}} = 1.276$ bohr, and the s -potential as local potential have been used. Pseudopotentials were filtered by the method of Tafipolsky and Schmid^[289] as implemented in Octopus to avoid Fourier components above the cutoff determined by the mesh spacing. In the ground-state calculations, a Methfessel-Paxton smearing with a very small smearing parameter of 20 meV was used.

The Al-clusters are obtained starting from a relaxed Al(111)-surface and cutting out a half sphere. Subsequently, the uppermost layer of Al-atoms has been kept fixed and the cluster has been relaxed ionically until the forces were below 10^{-3} H/bohr.

After the electronic ground-state relaxations, a bare H⁺ potential was added to the simulation cell at a distance of $z_{\text{init}} = 16$ bohr. The kinetic energies of the projectile at z_{init} are set

to $E_{\text{kin}}^{\text{init}} = 2 \text{ eV}$, 10 eV , or 50 eV . The dynamics of the projectile is described within Ehrenfest dynamics. The electron dynamics obey the time-dependent Kohn-Sham equations, with the corresponding adiabatic approximation applied to the XC-functional. A time-step of 0.02 au ($\approx 0.5 \text{ attoseconds}$) for the propagation of the Kohn-Sham wavefunctions is used; the time time-step for ion propagation is chosen to be the same. When propagating a proton from $z = 9 \text{ bohr}$ to $z = 3 \text{ bohr}$ in front of the Al_{188} -cluster with a mesh spacing of $\Delta x = 0.5 \text{ bohr}$ and a time step of $\Delta t = 0.02 \text{ au}$, the deviation of the total energy is below 20 meV . As shown in Equation 2.46, the total energy is conserved in an analytic calculation. The deviation of the total energy in a TDDFT simulation can be seen as a criterion for the quality of the employed numerical parameters. As implemented in Octopus, the exponent in the propagator is approximated using the exponential midpoint rule, and a fourth-order Taylor expansion of the exponential is used. An overview on selected parameters used in this chapter for the H^+ -Al systems is shown in Table 3.1.

Subsequent to the TDDFT-MD simulations, the time-dependent electronic density $n(\mathbf{r}, t)$ was used as input for a non-self consistent calculation of the Kohn-Sham states as implemented in Octopus. Details are given in subsection 3.3.2.

For convergence tests, Al-clusters with 52, 188, and 302 Al atoms were tested in the simulations. For the three clusters, the central atom of the uppermost Al-layer is located at $x = y = z = 0$. Figure 3.2 shows the geometry of the clusters and the density of states (DOS). For the Al_{188} -cluster, neighboring states at the lower valence band edge are at a distance of approximately 200 meV . Figure 3.3 shows the Bader charge as a function of distance for the Al_{188} -cluster and the Al_{302} -cluster for a proton projectile with initial kinetic energy $E_{\text{kin}}^{\text{init}} = 10 \text{ eV}$ at $z = 16 \text{ bohr}$. The electronic charge transfer sets in slightly earlier for the larger cluster. However, the difference regarding the charge transfer between the two employed cluster sizes is very small. From this we conclude that to describe charge transfer, the discretization of the electronic states of the employed cluster is not a problem. Further details on convergence can be found in the computational details in chapter 5.

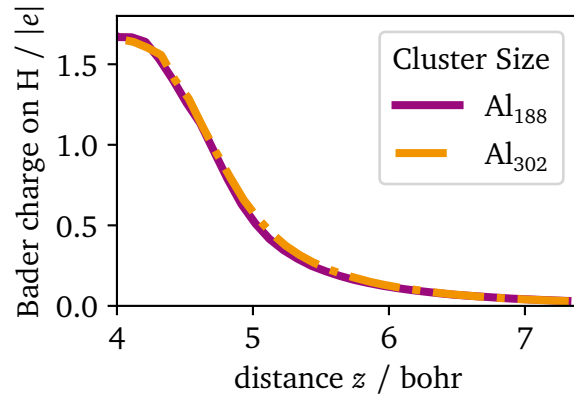


Figure 3.3: Bader charge obtained for a H^+ projectile with $E_{\text{kin}}^{\text{init}} = 10 \text{ eV}$ at an initial distance of $z_{\text{init}} = 16 \text{ bohr}$ impinging on the on-top site of an Al_n -cluster.

Please note that the effective potentials from semilocal approximations to the XC functional generally fail to reproduce the correct image potential for the electrons for large z . This problem could only be solved by taking into account non-local contributions, which

will make the time-dependent simulations presented in this and the following chapters numerically unfeasible. To estimate the deviation due to the semilocal approximation to the XC-potential the reader is referred to Fig. 1(b) in the publication by Nordlander and Tully.^[152] They have shown for a jellium surface, that deviations between the LDA effective potential and the true image potential arise for distances $z - z_{\text{jellium}} > 3.6$ bohr. In the simulations presented here, when the projectile has approached the surface and reached a separation from the surface equivalent to $z_{\text{H}^+} - z_{\text{jellium}} = 3.6$ bohr, the electron charge transfer to the proton is still less than approximately $0.1|e|$ (value for $E_{\text{kin}}^{\text{init}} = 2$ eV, see also chapter 5). In view of this small charge transfer at $z_{\text{H}^+} = 3.6$ bohr, and the small H–surface separation relevant in the present simulations, we assume that deviations of the effective potential from its correct image behavior can be neglected.

3.2 The H–Al(111) System: Ground-State Properties

The crystal structure of Al is face-centered cubic (fcc) with an experimental lattice constant of 7.653 bohr.^[299] In a periodic DFT calculation for the lattice constant of fcc Al, a value of 7.648 bohr is obtained with a mesh spacing of 0.5 bohr, $21 \times 21 \times 21$ k-points and a GGA-XC-functional. An all-electron calculation can be found in the literature,^[290] where a value of 7.634 bohr was obtained for the same XC-functional.

The DFT value for the work function of the Al(111) surface face is 4.09 eV.^[293] For the Al_{188} -cluster, the highest occupied molecular orbital (HOMO) is located at -4.15 eV below vacuum, the lowest unoccupied molecular orbital (LUMO) at -4.07 eV. For the larger Al_{302} -cluster, the HOMO level lies at -4.16 eV. The HOMO level of the Al-clusters can be seen as an approximation to the work function. It is important to keep in mind, that the clusters have a lower part which is no clean (111) face.

Relevant for the lowest energy at which a resonant charge transfer is allowed, is the lower valence band edge which in case of the here employed Al_{188} -cluster is 10.8 eV below the Fermi energy. Timmer and Kratzer^[70] reported 11 eV below the Fermi energy for a periodic surface. The image plane position for the Al(111) surface obtained by Lam and Needs in a self-consistent DFT simulation is located at $z_{\text{image}} \approx 3.14$ bohr^[106] in front of the uppermost layer of Al atoms. Chulkov et al.^[295] pointed out, that depending on the calculation method, this value shows a variation of ± 0.6 bohr.

The adsorption height and energy of the H above the fcc-hollow site are $z_{\text{ads}}^{\text{fcc-hollow}} = 1.89$ bohr and $E_{\text{ads}}^{\text{fcc-hollow}} = 1.93$ eV with respect to a spin-polarized H atom. At the energetically less favored on-top position, a minimum in the PES is found at $z_{\text{ads}}^{\text{on-top}} = 3.07$ bohr with an energy difference of 50 meV with respect to the fcc-hollow site.

Within the employed DFT approach, the electronic ground-state of the H^0 in a calculation in which spin-polarization is allowed, is spin-polarized. Upon adsorption, the spin-polarization is lost at a spin-transition distance $z_{\text{spin-trans}}$. Note, that for a ground-state calculation, this is an artifact of the employed XC-functional, see also Ref. [140]. For an impact on the Al(111) on-top site, the spin-transition distance $z_{\text{spin-trans}} = 4.86$ bohr, in agreement with Refs. [70, 140].

| | Unit | This Work | Ref. Data | Ref. |
|------------------------------------|------|-----------|--|----------------------------------|
| Lattice Constant | bohr | 7.648 | 7.634 ^{AE} 7.646 ^{PP} 7.653 ^{EXP} | [290] [290] [291] |
| Bulk Modulus | GPa | 80.0 | 78.077 ^{AE} 76.366 ^{PP} | [290] [290] |
| Al Bulk Plasmon Frequency | eV | | 15.0 ^{EXP} | [292] |
| HOMO of Al ₁₈₈ -cluster | eV | -4.15* | | |
| Work Function | eV | | 4.09 4.02 4.24 4.26 ^{EXP} | [293] [294] [295] [296] |
| Lowest State at $\bar{\Gamma}$ | eV | 10.8* | 11 | [70] |
| Jellium Edge | bohr | 2.21 | | |
| Image Plane Position | bohr | | 3.14 | [106] |
| H Spin Transition Height (top) | bohr | 4.86* | 4.88 4.91 | [140] [70] |
| H Adsorption Height (top) | bohr | 3.07* | 3.02 | [140] |
| H Adsorption Height (fcc-hollow) | bohr | 1.89* | | |
| Adsorption Energy (top) | eV | 1.88* | 1.83 | [70] |
| Adsorption Energy (fcc-hollow) | eV | 1.93* | 1.96 1.907 1.89 | [141] [297] [298] |

Table 3.2: Properties and geometrical data of fcc-Al, the Al₁₈₈-cluster, the Al(111) surface face and H interacting with a Al(111) surface face. Values with an asterisk (*) are obtained employing Al-cluster calculations. Position of the jellium edge calculated as given in section 1.2. Spin transition distance refers to the here employed DFT calculations. AE refers to an all-electron calculation with Wien2k, PP to a calculation with Abinit employing Troullier-Martins pseudopotential, both from Ref. [290]. EXP refers to the experimental values. Results for this work are obtained with the simulation parameters given in section 3.1 and Table 3.1. Jellium edge calculated from lattice constant.

Table 3.2 gives an overview on physical parameters relevant for the present work of the Al-bulk, the employed Al-cluster, the Al(111)-surface and the H–Al(111) interaction.

3.3 Time-Dependent Adsorbate Level Positions

To accurately describe the electronic charge transfer between a surface and an incoming ion, different theoretical approaches like the model Hamiltonians described in subsection 1.2.2 require information about the charge transfer rate, i.e. the height and width of the tunneling barrier. These can be connected with the adsorbate level position and width, which can be calculated from the projected density of states (PDOS), as discussed in subsection 1.2.2. In subsection 3.3.1 we will present and discuss the case of an H^0 in front of a metal surface. In subsection 3.3.2 and following, adsorbate level position and widths for the case of an H^+ are discussed. An ad-hoc method to obtain an alternative PDOS is presented and evaluated.

3.3.1 PDOS of the Kohn-Sham Groundstate

In subsection 1.2.2, a general definition of the PDOS of an adatom in front of a solid surface was given. As discussed e.g. by Norskov in Ref. [118], an investigation of the electronic structure in terms of adsorbate level position and width of an adatom on a surface can yield a comprehensive insight into the investigated system.

For the here employed simulations of a proton impinging on a surface, Equation 1.9 can be formulated in terms of the hydrogen 1s orbital $\langle H^{1s} |$ for a given projectile–surface distance projected onto the ground-state Kohn-Sham orbitals $|\Phi_k^{BO}\rangle$ of a given set of atomic coordinates \mathbf{R} . For the projection, the ground-state Kohn-Sham wavefunction at the corresponding position of the hydrogen atom is taken. The ε_k^{BO} are the Kohn-Sham eigenenergies of the Kohn-Sham ground-state orbitals where k denotes the band index and the resulting PDOS n_a^{BO} can be written (for one single \mathbf{k} -point) as:^[118,300,301]

Definition: H 1s ground-state Kohn-Sham PDOS

H 1s PDOS from projection onto ground-state Kohn-Sham orbitals:

$$n_a^{BO}(\varepsilon, \mathbf{R}) = \sum_k |\langle H^{1s} | \Phi_k^{BO}(\mathbf{R}) \rangle|^2 \cdot \delta(\varepsilon - \varepsilon_k^{BO}(\mathbf{R})) \quad (3.2)$$

In conjunction with Equation 1.10 the adsorbate level position ε_a and the width Γ is obtained through a fit function. I.e. the integral over Equation 3.2

$$\int_{-\infty}^{\varepsilon} n_a^{BO}(\varepsilon, \mathbf{R}) d\varepsilon = \sum_k |\langle H^{1s} | \Phi_k^{BO}(\mathbf{R}) \rangle|^2 \cdot \Theta(\varepsilon - \varepsilon_k^{BO}(\mathbf{R})) \quad (3.3)$$

is fitted onto the integral of Equation 1.10 i.e.:

$$\int_{-\infty}^{\varepsilon} n_a(\varepsilon, \mathbf{R}) d\varepsilon = \frac{1}{2} - \frac{1}{\pi} \arctan\left(\frac{1}{\Gamma}(\varepsilon_a(\mathbf{R}) - \varepsilon)\right) \quad (3.4)$$

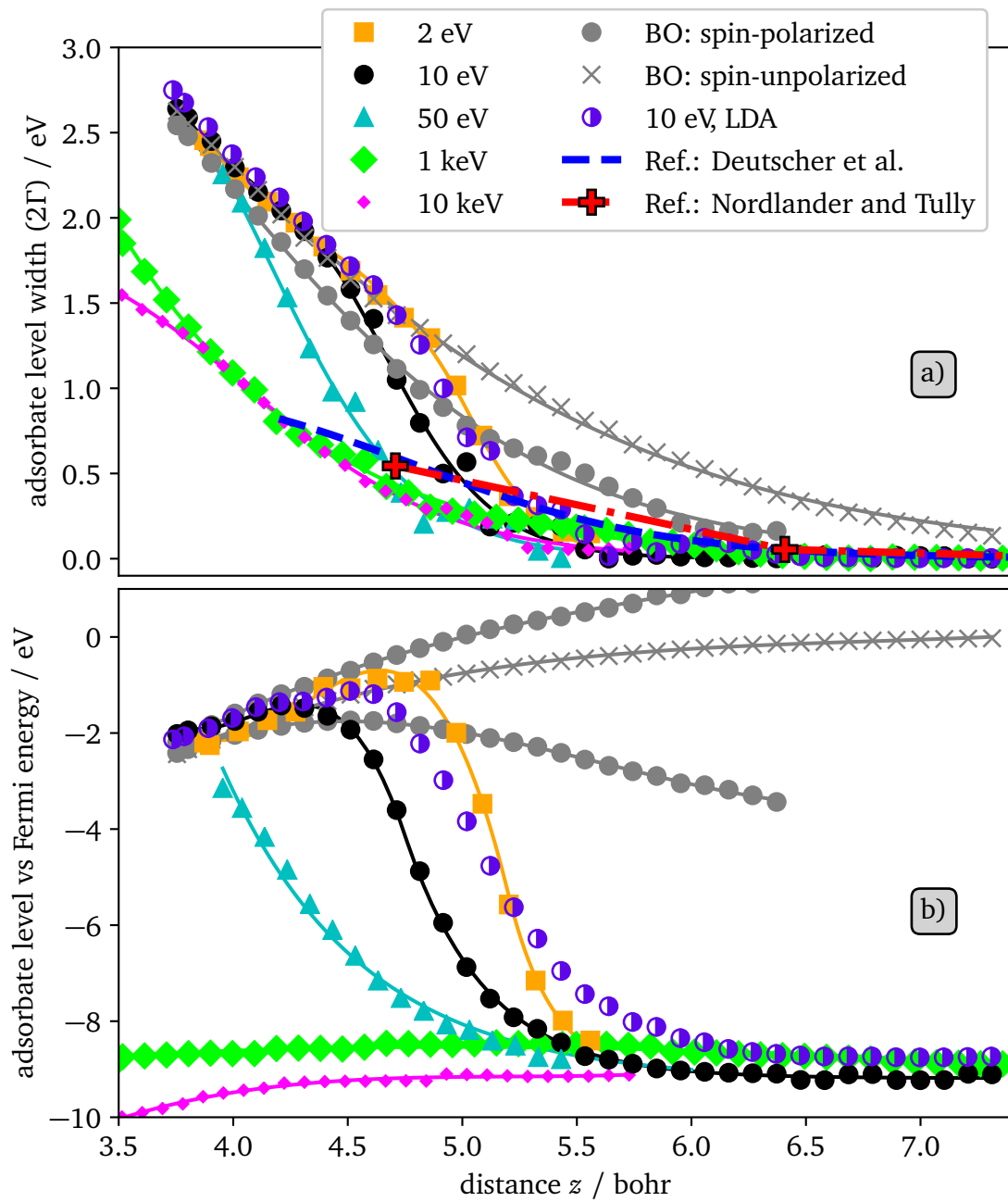


Figure 3.4: **a)** Adsorbate level width 2Γ and **b)** adsorbate level position of H^+ and H^0 impinging on (111) surface face of Al_{188} -cluster. Kinetic energies in the legend refer to kinetic energy at $z_{\text{init}} = 16$ bohr. BO refers to ground-state calculations. Reference data are from Deutscher et al.^[153] and from Nordlander and Tully^[66,152,302] (linear interpolation meant as guide to the eye). A logarithmic scale for the adsorbate level width as well as fit curves for the here presented data can be found in Appendix A on page 117. Data obtained following Equation 3.2 and 3.5. Please note: the HOMO level of the Al_{188} -cluster is -4.15 eV against vacuum, see Table 3.2.

In Figure 3.4, we present the data obtained for a spin-polarized and a spin-unpolarized H^0 in front of the Al_{188} -cluster (grey curves). Before reaching the spin-transition distance of $z_{\text{spin-trans}} = 4.86$ bohr (see Table 3.2), the adsorbate level width from a spin-unpolarized calculation is significantly above the width from a spin-polarized calculation. This is a well known result of the wrong description of exchange and correlation for atoms with an unpaired number of valence electrons (see section 2.1.3). Regarding the adsorbate level position in a spin-unpolarized calculation, the level is fixed artificially to the Fermi energy for $z \rightarrow \infty$ with a total charge $\neq 0$ (more electrons at the atom than expected from a neutral particle) due to the same reason. The adsorbate level position in the spin-polarized calculations approaches the Kohn-Sham eigenvalue for the H-atom for large distances z . For the here employed PBE-GGA these are $\varepsilon_{\uparrow} = -7.59$ eV and $\varepsilon_{\downarrow} = -0.65$ eV measured against the vacuum.

However, these ground-state DFT calculations neglect entirely that the H^+ projectile investigated here is not neutral but has a non-vanishing net charge and induces an image charge in the metal surface which influences the adsorbate level. In the following we will present and discuss an approach which is based on TDDFT-MD simulations.

3.3.2 Frozen Density Kohn-Sham PDOS

In the previous section, the general method on how to obtain a Kohn-Sham PDOS was given. In this section, we are aiming to describe the neutralization process with a similar methodology. In any case, it is important to keep in mind, that the ion-surface system considered throughout this thesis is not in an electronic equilibrium. Therefore, an adjustment of the above method is required.

Instead of a projection onto ground-state Kohn-Sham orbitals, a different set of orbitals and eigenvalues needs to be found. We consider the tunneling process between a metal surface and an ion. The tunneling does not occur in the ground-state effective potential, but in the time-dependent effective potential of the excited system. As pointed out in chapter 2, there exists a one to one mapping between electronic densities and effective potentials. Therefore, we will not take as a reference the electronic ground-state density but the time-dependent density. The electron dynamics occur in the time-dependent Kohn-Sham states. An approach to these time-dependent Kohn-Sham states can be generated from the time-dependent density with a frozen-density calculation.

During the time-dependent simulations the time-dependent electronic density $n(\mathbf{r}, t)$ is stored for different projectile-surface distances. For each $n(\mathbf{r}, t)$, a non self-consistent calculation of the Kohn-Sham states with frozen-in (i.e. fixed for a time t) electronic density was performed subsequently. Based on these frozen density orbitals $|\Phi_k^{\text{frozen}}(n(t), \mathbf{R}(t))\rangle$ with corresponding eigenvalues $\varepsilon_k^{\text{frozen}}$ an alternative PDOS is calculated. This PDOS will be termed n_a^{frozen} :

Definition: H 1s frozen-density Kohn-Sham PDOS

H 1s PDOS from projection onto orbitals obtained from a non self-consistent calculation with frozen-in electronic density:

$$n_a^{\text{frozen}}(\varepsilon, n(t), \mathbf{R}(t)) = \sum_k |\langle H^{1s} | \Phi_k^{\text{frozen}}(n(t), \mathbf{R}(t)) \rangle|^2 \cdot \delta(\varepsilon - \varepsilon_k^{\text{frozen}}(n(t), \mathbf{R}(t))) \quad (3.5)$$

The adsorbate level position $\varepsilon_a^{\text{frozen}}$ and width Γ^{frozen} is again obtained through a fit function to the integrated versions of Equation 1.10 and Equation 3.5. The above definition in Equation 3.5 is an ad-hoc definition and it is per se not clear, whether $\varepsilon_a^{\text{frozen}}$ and Γ^{frozen} have any physical meaning. Therefore, in this section and the following section, we will compare and evaluate the above definition. A conclusion can be found in subsection 3.3.5.

Adsorbate Level Width Comparison In Figure 3.4, we present the data obtained for simulations in which different XC-functionals were employed or with projectiles with different initial kinetic energies at a distance $z_{\text{init}} = 16 \text{ bohr}$ in front of the Al-cluster. For comparison, data from the literature obtained by Deutscher et al.^[153] and by Nordlander and Tully^[66,152,302] is shown, additionally. These authors obtained the adsorbate level width with the help of accurate density-functional potentials combined with a complex scaling theory. In their case, the Al was modeled by a jellium surface. As a consequence, their results are only given for projectile–surface distances $z > 4.3 \text{ bohr}$. On the other side, the results presented here from the TDDFT simulation are limited to distances where Γ is above the distance of two subsequent states in the Al-cluster (see Figure 3.2).

In order to compare to the literature data, we performed simulations of fast projectiles (i.e. 1 keV and 10 keV) where a minor charge transfer towards the projectiles is observed. As pointed out in chapter 5, for $z > 4.5 \text{ bohr}$, the electronic charge around the 1-keV projectile is below $0.05 |e|$ and a 1-keV antiproton showed an energy dissipation of 80 meV at $z = 5 \text{ bohr}$ which is a strong indication that the frozen-density adsorbate level position of a 1-keV H^+ may be close to those obtained in a self-consistent procedure of an H^+ in front of a metal surface (which is not accessible as pointed out above). Comparing the 1-keV adsorbate level width $2\Gamma^{\text{frozen}}$ with the data by Nordlander and Tully^[66,152,302] it has to be emphasized that the range in z where their values can be utilized is limited to one single point at $z \approx 4.7 \text{ bohr}$ of approximately 0.54 eV, our 1-keV value lies here at 0.39 eV. Deutscher et al. gave in their publication^[153] the following expression:

$$\Gamma(z) = \Gamma_0 / (1 + e^{\chi \cdot (z - z_{\text{jellium}} - z_{\text{crit}})}) \quad (3.6)$$

with $\Gamma_0 = 0.54 \text{ eV}$, $\chi = 1.85$, and $z_{\text{crit}} = 2.6 \text{ bohr}$ (Fig. 10 and Equation 43 in Ref. [153]). Their data points lie slightly higher than our data points with a maximum difference of approximately 200 meV at $z = 4.9 \text{ bohr}$.

Adsorbate Level Position For large projectile–surface distances z , the adsorbate level position $\varepsilon_a^{\text{frozen}}$ is approximately -13.6 eV against vacuum, i.e. the eigenvalue of H^+ . The Kohn-Sham eigenvalues of a charged H with electronic charge x in the range $0 \leq x < 1$ are shown in Figure A.1.

Note that for a distance z of 6.6 bohr, the difference between $\varepsilon_a(10 \text{ eV})$ and $\varepsilon_a(1 \text{ keV})$ is approximately 480 meV. In Table 3.3 the adsorbate level position at $z_{\text{H}} = 6.6$ bohr for projectiles with different initial kinetic energies at $z_{\text{H}}^{\text{init}} = 16$ bohr is shown together with the (very small) Bader charge at the projectile for that distance. The difference for the position of the adsorbate level of 480 meV is a result of the drastic change of the eigenvalue of the H atom with the electronic charge for small charges around it. In Figure A.1 the Kohn-Sham eigenvalue versus the electronic charge of an H atom is visualized. As can be read from Table 3.3, for the 10 eV trajectory, there is already a very small charge transfer towards the projectile that results in a lowering of the projectile’s eigenvalue.

As a first approximation, we cut out the electronic density around the projectile using a box with edge length 3 bohr. The center of the box is the projectile. We then calculate the projectile’s Kohn-Sham eigenvalue with a frozen-density calculation for the electronic density within this box. For the 10 eV projectile, this value is -11.39 eV versus E_F . Taking into account the image charge shift of the eigenvalue of $1 \text{ H}/(4 \cdot (z - z_{\text{image}})) \approx 1 \text{ H}/(4 \cdot (6.6 \text{ bohr} - 3.14 \text{ bohr})) \approx 1.97 \text{ eV}$ results in an adsorbate level position of $-11.39 \text{ eV} + 1.97 \text{ eV} = -9.42 \text{ eV}$ which (considering the rough approximation) compares well to -9.23 eV as given in Table 3.3.

Note that in Table 3.3, the value of $\varepsilon_a^{\text{frozen}}$ for the projectile with initial kinetic energy of 10 keV is not in line with the other points because for the projectile with initial kinetic energy of 10 keV, the image charge does not build up almost instantaneously. Therefore, the level shift from the image charge is smaller than the $1 \text{ H}/(4 \cdot (z - z_{\text{image}}))$ behavior.

The different position of the eigenvalue at that distance is also reflected in different electronic charge transfer rates (i.e. adsorbate level widths), see Figure A.2.

| $E_{\text{kin}}^{\text{init}}$ | $\varepsilon_a^{\text{frozen}} - \varepsilon_F / \text{eV}$ | $q_{\text{Bader}} / e $ |
|--------------------------------|---|--------------------------|
| 10 eV | −9.23 | 0.064 |
| 50 eV | −9.04 | 0.054 |
| 1 keV | −8.75 | 0.048 |
| 10 keV | −9.03 | 0.014 |

Table 3.3: Adsorbate level position $\varepsilon_a^{\text{frozen}}$ at $z_{\text{H}} = 6.6$ bohr for projectiles with different initial kinetic energies. q_{Bader} denotes the Bader charge of the projectile.

For times after the charge transfer, the adsorbate levels of the projectiles with $E_{\text{kin}}^{\text{init}} = 2 \text{ eV}$, $E_{\text{kin}}^{\text{init}} = 10 \text{ eV}$, and $E_{\text{kin}}^{\text{init}} = 50 \text{ eV}$ at $z_{\text{init}} = 16$ bohr are very close to the level obtained from a ground-state calculation. Details on charge transfer distances are given in chapter 4 and chapter 5.

In the charge transfer region, however, the adsorbate level width transitions between these two regimes. This is not expected from other theoretical studies and a result of

the employed TDDFT-MD method and therewith connected the time-development of the system on an average trajectory, where the tunneling process is not described by an instantaneous event but by its statistic average. However, these adsorbate levels allow for an accurate reproduction of the charge transfer within a simplified model, as discussed in the following subsection 3.3.3. Furthermore, in section 3.4 the adsorbate level position $\varepsilon_a^{\text{frozen}}$ serves for an interpretation of the artificial Kohn-Sham electronic excitation spectra.

3.3.3 Brako-Newns-Anderson Type Model Hamiltonian

In order to justify the ad-hoc definition for the time-dependent adsorbate level position and width given in Equation 3.5, C. Makait^[303] implemented a one dimensional Brako-Newns-Anderson (BNA)-type model Hamiltonian^[108] and studied the charge transfer as obtained from the TDDFT parameters shown in Figure 3.4. This work was performed as part of his Bachelor's thesis within our group. Here, a short overview will be given:

The tight-binding model Hamiltonian is visualized in Figure 3.5 and follows the ideas of Brako and Newns, see Ref. [108] and subsection 1.2.2. It is based on the idea of a linear chain of Al atoms. Each Al atom is represented by its s -orbital and interacts only with its nearest neighbor through a coupling parameter τ . Only the uppermost Al atom interacts with the projectile through a coupling parameter τ' . The Hamiltonian $\hat{H}(t)$ can then be written as:

$$\hat{H}(t) = \begin{pmatrix} \hat{A} & \\ & \hat{B} \end{pmatrix}, \quad (3.7)$$

where

$$\hat{A} = \begin{pmatrix} \varepsilon_a(t) & \tau'(t) \\ \tau'(t) & \varepsilon_m \end{pmatrix}, \quad (3.8)$$

$$\hat{B} = \begin{pmatrix} \varepsilon_m & \tau & & & \\ \tau & \varepsilon_m & \ddots & & \\ & \ddots & \ddots & \ddots & \\ & & & \tau & \varepsilon_m \end{pmatrix}. \quad (3.9)$$

Here, $\varepsilon_a(t)$ is the adsorbate level position and ε_m a descriptor for the energetic position of the metal states. Then, a propagation in time (see Equation 1.11 and Equation 1.12) is applied and combined with the distance-dependent (and therefore time-dependent) adsorbate level position and width obtained from the TDDFT simulation.

Figure 3.5 shows a comparison between the data obtained from the TDDFT simulation and the BNA-type simulation with a chain of 19 999¹ Al atoms. Generally speaking, both results are remarkably close, given that the BNA-type model Hamiltonian is significantly less complex and takes as input only two simple functions $\varepsilon_a(z)$, and $\Gamma(z)$ for a given kinetic

¹Simulation results do not show relevant differences for simulations with 311 Al atoms. However, 19 999 Al atoms could easily be simulated thanks to the numerical efficiency of the employed model.

energy. The increasing difference between the curves for higher kinetic energies arises due to the above mentioned difficulties to obtain correct values for Γ for distances where Γ is small.

The solution of the BNA-type model Hamiltonian has two major implications:

1. The BNA-type simulations may serve as an a-posteriori argument for the adsorbate level position and width as obtained from Equation 3.5, because they reliably reproduce the charge transfer from the TDDFT-MD simulation.
2. Vice versa, given the adsorbate level position and width, the computationally very demanding TDDFT-MD simulations can (at least in this case) be substituted by the computationally significantly less demanding BNA-type simulations.

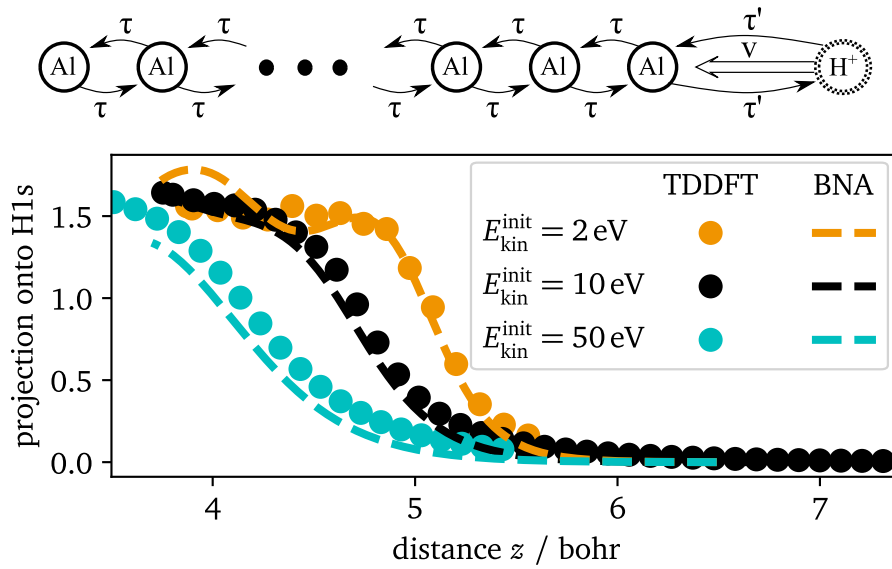


Figure 3.5: **Top:** Visualization of the Brako-Newns-Anderson (BNA)-type model Hamiltonian. **Bottom:** Electronic charge q for an incoming proton on an atom in top position of the (111) face of the Al_{188} -cluster with respect to the uppermost Al atomic layer as obtained from projection onto the H-1s orbital (Equation 2.57). TDDFT simulation compared to BNA-type model Hamiltonian simulations.

3.3.4 Rate Equation

The very good agreement between the TDDFT-MD simulation and the BNA-type model Hamiltonian simulation can be understood further with the help of a rate equation. Assume an initial state i (the H^+) and a final state f (the H^0). The here calculated adsorbate level width Γ is directly connected to the transition rate $\Gamma_{i \rightarrow f}(t)$, i.e. $\Gamma_{i \rightarrow f}(t) = 2\Gamma$.^[158] This allows to calculate the electronic charge q on the projectile by a simple integral:

$$q(z) = \int_{-\infty}^t \Gamma_{i \rightarrow f}(t) dt \stackrel{\Gamma_{i \rightarrow f}(t)=2\Gamma}{=} \int_{-\infty}^t 2\Gamma(t) dt \stackrel{v=-\frac{dz}{dt}}{=} \int_z^{-\infty} \frac{2\Gamma(z')}{v} dz' \quad (3.10)$$

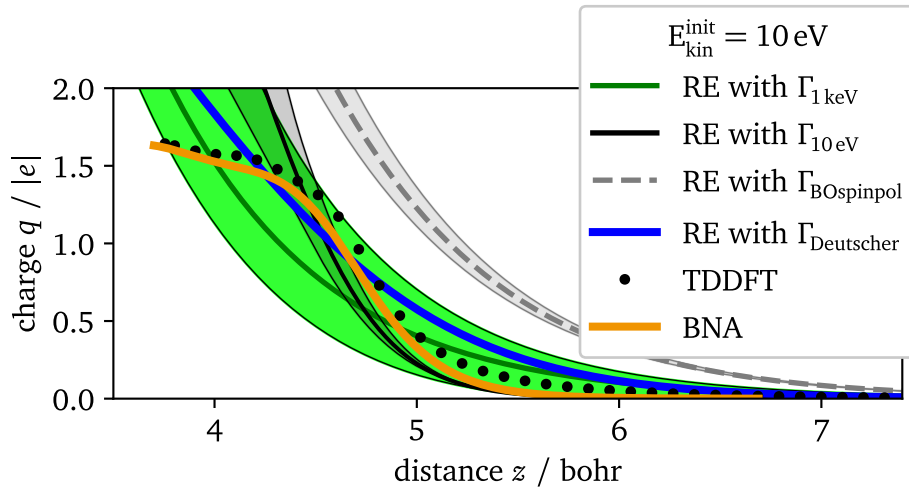


Figure 3.6: Charge on the H^+ projectile as obtained within a BNA-type model Hamiltonian simulation (BNA) and the TDDFT-MD simulations (TDDFT); data identical to Figure 3.5. Values for the transition rate employed in the Rate Equation (RE) approach (Equation 3.10) are taken from Figure 3.4 and Table A.1; coloring of the curves according to the way Γ was chosen. For the RE: $E_{\text{kin}} = \text{const}$. The confidence interval is chosen according to the quality of the fit parameters to Γ , see Table A.1. The integration of Equation 3.10 starts at $z = 15$ bohr. For $\Gamma_{\text{Deutscher}}$ see Equation 3.6.

In Figure 3.6 we compare the charge as obtained within this rate equation approach to the data obtained from the TDDFT-MD simulation and the BNA-type model Hamiltonian simulation. For simplicity, the velocity v of the projectile is assumed constant in the rate equation approach. We employed three different transition rates as obtained from the TDDFT simulations given in Figure 3.4 and Appendix A. These are $\Gamma_{10\text{eV}}$, $\Gamma_{\text{BOspinpol}}$ and $\Gamma_{1\text{keV}}$, see subsection 3.3.2 and Figure A.2. The colored region marks the confidence interval of the fitting curve to $\Gamma(z)$. Note that these are very broad because of the limited accuracy of

approximately ± 100 meV for Γ as obtained in the here employed TDDFT-MD simulations. Furthermore, for a fit curve on $\Gamma_{10\text{eV}}$, the number of data points before the charge transfer with a value of Γ above the accuracy is very small, see Figure A.2.

First, we employ the adsorbate level width $\Gamma_{10\text{eV}}$ as obtained from the TDDFT-MD simulation with the H^+ projectile with $E_{\text{kin}}^{\text{init}} = 10\text{eV}$ (black solid curve). The electronic charge on the projectile is in very agreement with the TDDFT data and the BNA data. This also explains why the charge transfer as described in the BNA type model Hamiltonian simulation agrees with the charge transfer from the TDDFT simulation: the transition rate is reliable. The charge transfer is shifted slightly towards the surface because the transition rate for large distances cannot be calculated with the required accuracy in the TDDFT simulations for distances where the adsorbate level width is small, see also subsection 3.3.2. For distances $z < 4.5$ bohr, the electronic charge on the projectile increases further and exceeds the value from the TDDFT and the BNA simulations because the rate is always increasing, too. This is of course not to be expected from the real system but just an artifact of this very simple approach. For this region, the BNA-type model Hamiltonian gives results closer to the TDDFT-MD simulations because it also considers the adsorbate level position.

Secondly, we employ the adsorbate level width $\Gamma_{\text{Bospinpol}}$ as obtained from the DFT ground-state calculation with a spin-polarized H^0 in front of the Al_{188} -cluster (grey dashed curve). As expected, this results in a large difference as compared to the TDDFT simulation, i.e. an outwards shift of the charge transfer of approximately 0.7 bohr. Here, the transition rate is overestimated due to the neglect of e.g. the induced image charge. A difference of 0.7 bohr is reflected e.g. in the kinetic energy difference between incoming and outgoing projectile. This kinetic energy difference is large for comparable distance differences, see Fig. 4 and Fig. 6 in chapter 5.

Thirdly, we employ the adsorbate level width $\Gamma_{1\text{keV}}$ as obtained from the TDDFT-MD simulation with the H^+ projectile with $E_{\text{kin}}^{\text{init}} = 1\text{keV}$ (green solid curve). Note that the values for $\Gamma_{1\text{keV}}$ are very close to the literature data by Deutscher et al.^[153] and by Nordlander and Tully.^[66,152,302] Interestingly, the differences in $q(z)$ between the rate equation approach with $\Gamma_{1\text{keV}}$ and the TDDFT data are very small. This is a consequence of the exponential-like decrease of Γ with respect to the distance z . As long as the electronic charge on the projectile is small, it is expected that $\Gamma_{1\text{keV}}(z) \approx \Gamma_{10\text{eV}}(z)$. Note that $\Gamma_{1\text{keV}}(z)$ and $\Gamma_{10\text{eV}}(z)$ do not coincide for $z \approx 7$ bohr as shown in Figure A.2 because in case of the hyperthermal projectile, a small electronic charge transfer towards the projectile yields a shift of the electronic eigenvalue of the projectile, see also Figure A.1. Once the charge transfer sets in, they start to differ significantly from each other. Γ exceeds a certain value (here around 80 meV) and the charge transfer occurs in a comparatively small range of z . However, this no longer has a notable effect on $q(z)$, because the charge transfer is completed on a rather small range of z .

For e.g. the projectile with $E_{\text{kin}}^{\text{init}} = 10\text{eV}$, the adsorbate level width $\Gamma_{10\text{eV}}$ presented in Figure 3.4 differs significantly from the data by Deutscher et al.^[153] and by Nordlander and

Tully^[66,152,302] for distances z after the charge transfer had set in. However, when calculating the distances where the charge transfer occurs with e.g. a rate equation, only minor differences are observed between the adsorbate level widths obtained from the TDDFT simulation and the data by Deutscher et al. and by Nordlander and Tully. For large distances, the value for Γ as obtained by Deutscher et al.^[153] and by Nordlander and Tully^[66,152,302] may even be more reliable than the value for Γ obtained in our TDDFT simulation. In the TDDFT simulation, the accuracy of Γ is determined by the energetic distance between two subsequent electronic states of the employed Al-cluster. However, the here presented TDDFT-MD simulations provide an additional path to calculate the adsorbate level widths and therewith the transition rate.

3.3.5 Summary

In this section, we showed that the electronic charge transfer as obtained from a TDDFT-MD simulation can be reproduced with the help of a simple tight-binding BNA-type model Hamiltonian. For each kinetic energy, the input required for the Hamiltonian reduces to two distance-dependent functions: $\varepsilon_a^{\text{frozen}}(z)$ and $\Gamma^{\text{frozen}}(z)$. It is demonstrated how these can be calculated from the time-dependent electronic density with the help of a frozen-density calculation.

Further supporting arguments for the reasonability of the approach are the agreement of Γ^{frozen} before charge transfer with literature data from Deutscher et al.^[153] and Nordlander and Tully^[66,152,302]

The well agreement between the TDDFT-MD results and the BNA-type model Hamiltonian for the distance of charge transfer was further investigated with the help of a rate equation. It was shown that $\Gamma^{\text{frozen}}(z)$ serves as a description for the charge transfer rate explaining also the well agreement between the TDDFT-MD results and the BNA-type model Hamiltonian.

After the charge transfer had set in, $\Gamma^{\text{frozen}}(z)$ as obtained from the TDDFT simulation for projectiles with e.g. $E_{\text{kin}}^{\text{init}} = 10 \text{ eV}$ and the literature data for Γ deviate strongly from another. However, before the charge transfer had set in, they are of comparable magnitude. For the calculation of the charge transfer distance as obtained e.g. in a rate equation approach, only the latter charge transfer rate is of importance as the charge transfer occurs in a rather small range of distance z and the tunneling rate decreases exponentially with z .

Furthermore, as will be seen in the following section, the time-dependent frozen-density adsorbate level position $\varepsilon_a^{\text{frozen}}$ is helpful in the interpretation of Kohn-Sham electronic excitation spectra.

3.4 Kohn-Sham Electronic Excitation Spectra: The Special Case of Ions in Front of Surfaces

In the previous section 3.3 an alternative PDOS for the special case of the here discussed time-dependent simulations was introduced and arguments for the reasonability of this approach were given. In the present section, Kohn-Sham electronic excitation spectra are examined. These spectra are not all-electron spectra but artificial Kohn-Sham spectra. In subsection 3.4.1, the definition employed in the literature will be recalled and discussed in light of the here investigated systems. In subsection 3.4.2, the concept of a frozen-density PDOS of section 3.3 will be extended to frozen-density Kohn-Sham electronic excitation spectra. In subsection 3.4.3 the final distribution of excitation energy in the Kohn-Sham spectra will be discussed.

3.4.1 Ground-State Kohn-Sham Electronic Excitation Spectrum: Atom Scattering

The calculation of electronic excitation spectra has been realized by different authors. Van Heys, Lindenblatt and Pehlke,^[248] and Lindenblatt and Pehlke^[140] studied the electronic excitations invoked by an H-atom impinging on an Al(111) surface. Grotemeyer and Pehlke^[69] analyzed the influence of a vibrating HCl molecule in front of an Al(111) surface. Zeb et al.^[138] analyzed the influence of the *d*-electrons in an Au bulk on the stopping power for H and He projectiles with the help of the electronic excitation spectrum. Gruner and Pentcheva^[304] calculated the time-dependent Kohn-Sham electronic excitation spectrum to investigate the dynamics of optical excitations in Fe/MgO(001) heterostructures.

For the case of a simulation in which the electronic excitations are not localized, the following definition holds:

Definition: Kohn-Sham Electronic Excitation Spectrum $\delta\Lambda^{\text{BO}}$

Artificial Kohn-Sham electronic excitation spectrum $\delta\Lambda^{\text{BO}}$ at a time t with respect to the electronic ground-state of a given atomic geometry $\mathbf{R}(t)$ with ground-state Kohn-Sham wavefunctions Φ_k^{BO} (here: one \mathbf{k} -point) and eigenenergies ϵ_k^{BO} . Ψ_j^{TD} are the time-propagated Kohn-Sham wavefunctions.

$$\begin{aligned} \delta\Lambda^{\text{BO}}(\epsilon, t, \mathbf{R}) = & \sum_j^{\text{occ}(t=0)} \sum_k |\langle \Psi_j^{\text{TD}}(t) | \Phi_k^{\text{BO}}(\mathbf{R}(t)) \rangle|^2 \cdot \delta(\epsilon - \epsilon_k^{\text{BO}}(\mathbf{R}(t))) \\ & - \sum_k^{\text{occ}} \delta(\epsilon - \epsilon_k^{\text{BO}}(\mathbf{R}(t))) \end{aligned} \quad (3.11)$$

Equation 3.11 follows the definition of Refs. [69, 140, 248].

The energy within the spectrum $\tilde{E}_{\text{exc}}^{\text{BO}}$ can be calculated from:

$$\tilde{E}_{\text{exc}}^{\text{BO}} = \int_{-\infty}^{\infty} \varepsilon \cdot \delta\Lambda^{\text{BO}} d\varepsilon \quad (3.12)$$

$\delta\Lambda^{\text{BO}}$ from an H^0 -projectile impinging on an Al(111) surface was discussed by Lindenthal and Pehlke.^[97] An electron-hole pair excitation at the Fermi energy is induced by the electronic friction throughout the process. It was observed that the electronic excitation spectrum shows in the case of H^0 a maximum at the Fermi energy and decays approximately exponentially towards both sides, see also Figure 3.10 or Ref. [140].

We can compare the energy within the spectrum $\tilde{E}_{\text{exc}}^{\text{BO}}$ to the excitation energy E_{exc} . E_{exc} is obtained from a comparison of electronic energies between the ground-state ($E_{\text{electronic}}^{\text{BO}}$) and the time-dependent simulations ($E_{\text{electronic}}^{\text{TD}}$).

$$E_{\text{exc}}(t, z(t), E_{\text{kin}}^{\text{init}}) = E_{\text{electronic}}^{\text{TD}}(t, z(t), E_{\text{kin}}^{\text{init}}) - E_{\text{electronic}}^{\text{BO}}(z(t)), \quad (3.13)$$

In Appendix B, it is shown that for small perturbations of the density, i.e. variations of the density to first order, $E_{\text{exc}}^{\text{BO}} \approx \tilde{E}_{\text{exc}}^{\text{BO}}$ which is a necessary condition for the physical relevance of $\delta\Lambda^{\text{BO}}$. In the above mentioned references [69, 138, 140, 248, 304] it was possible to gain further insight into the underlying physical processes with the help of the electronic excitation spectrum.

As is also shown in Appendix B, for the case of localized holes, $\tilde{E}_{\text{exc}}^{\text{BO}}$ is no longer a valid approximation for E_{exc} . This can be seen from Figure 3.7 where a comparison of $\tilde{E}_{\text{exc}}^{\text{BO}}$ and E_{exc} is shown for the case of an H^+ projectile with initial kinetic energy of $E_{\text{kin}}^{\text{init}} = 10 \text{ eV}$ impinging on the on-top site of an Al_{188} -cluster. In the simulations presented here, the initial configuration is an H^+ in front of a surface. Therefore, the initial configuration is far from equilibrium and the hole is (spatially and energetically) localized. Variations in the density are not small.

The electronic charge transfer rate shows a maximum at a distance of $z = 4.76 \text{ bohr}$ (see

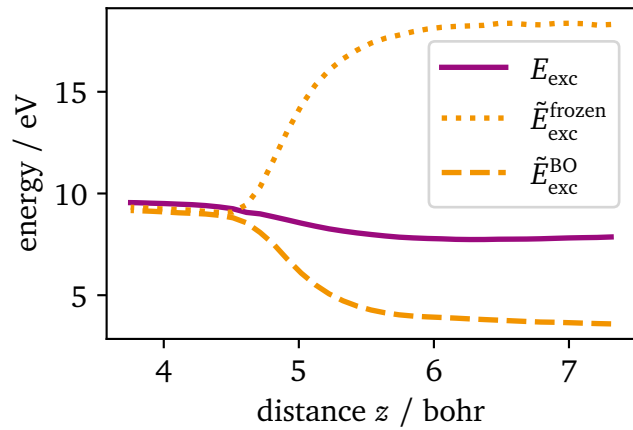


Figure 3.7: Comparison of energy terms for an H^+ projectile with $E_{\text{kin}}^{\text{init}} = 10 \text{ eV}$ impinging on the on-top site of an Al_{188} -cluster. Definition of energies are given in Equation 3.13, Equation 3.12 and Equation 3.15.

chapter 5). After the charge transfer, the hole is no longer localized and from Figure 3.7 one can see that $\tilde{E}_{\text{exc}}^{\text{BO}} \approx E_{\text{exc}}^{\text{BO}}$.

Figure 3.8a) shows the excitation spectrum $\delta\Lambda^{\text{BO}}$ as defined in Equation 3.11 for the case of a proton with $E_{\text{kin}}^{\text{init}} = 10$ eV at $z_{\text{init}} = 16$ bohr impinging on the on-top site of the (111) face of the Al_{188} -cluster. The location of the hole at the (artificial) Kohn-Sham eigenvalue of the spin-unpolarized H^0 -atom of -6.49 eV (GGA-PBE XC-functional) against vacuum is clearly visible. The excitation for large z at the Fermi energy arises from the induced image charge and the missing electron at the Al-surface which in a ground-state calculation is transferred to the H-atom. At a distance $z \lesssim 8$ bohr, an excitation distributed over the entire cluster appears. From Figure 3.8a) it is not clear, how this excitation arises. A technical explanation will be given in the following section.

As pointed out in this section, the electronic excitation spectrum $\delta\Lambda^{\text{BO}}$ has often successfully been used to interpret the distribution of the excitation energy into the electronic system for delocalized excitations. However, in case of the spatially and energetically localized hole as in case of an ion in front of a surface, the interpretation of $\delta\Lambda^{\text{BO}}$ is unclear. The interpretation of the Kohn-Sham electronic excitation spectrum $\delta\Lambda^{\text{BO}}$ with the help of Equation 3.11 is connected to the two following difficulties:

1. For the ion far above the surface, the hole at the projectile is spatially localized at the projectile and energetically localized at the position of the ground-state Kohn-Sham orbital.
2. For the ion far above the surface, $\tilde{E}_{\text{exc}}^{\text{BO}} \neq E_{\text{exc}}$ (Figure 3.7)

Please note that the second difficulty is a direct consequence of the first one.

In the next section, an alternative spectrum will be discussed. This spectrum is also not able to reproduce the excitation energy E_{exc} . However, it allows for an interpretation of the energy distribution after charge transfer. Once an insight into the the energy distribution after charge transfer is gained, the electronic excitation spectrum $\delta\Lambda^{\text{BO}}$ after scattering is discussed in subsection 3.4.3.

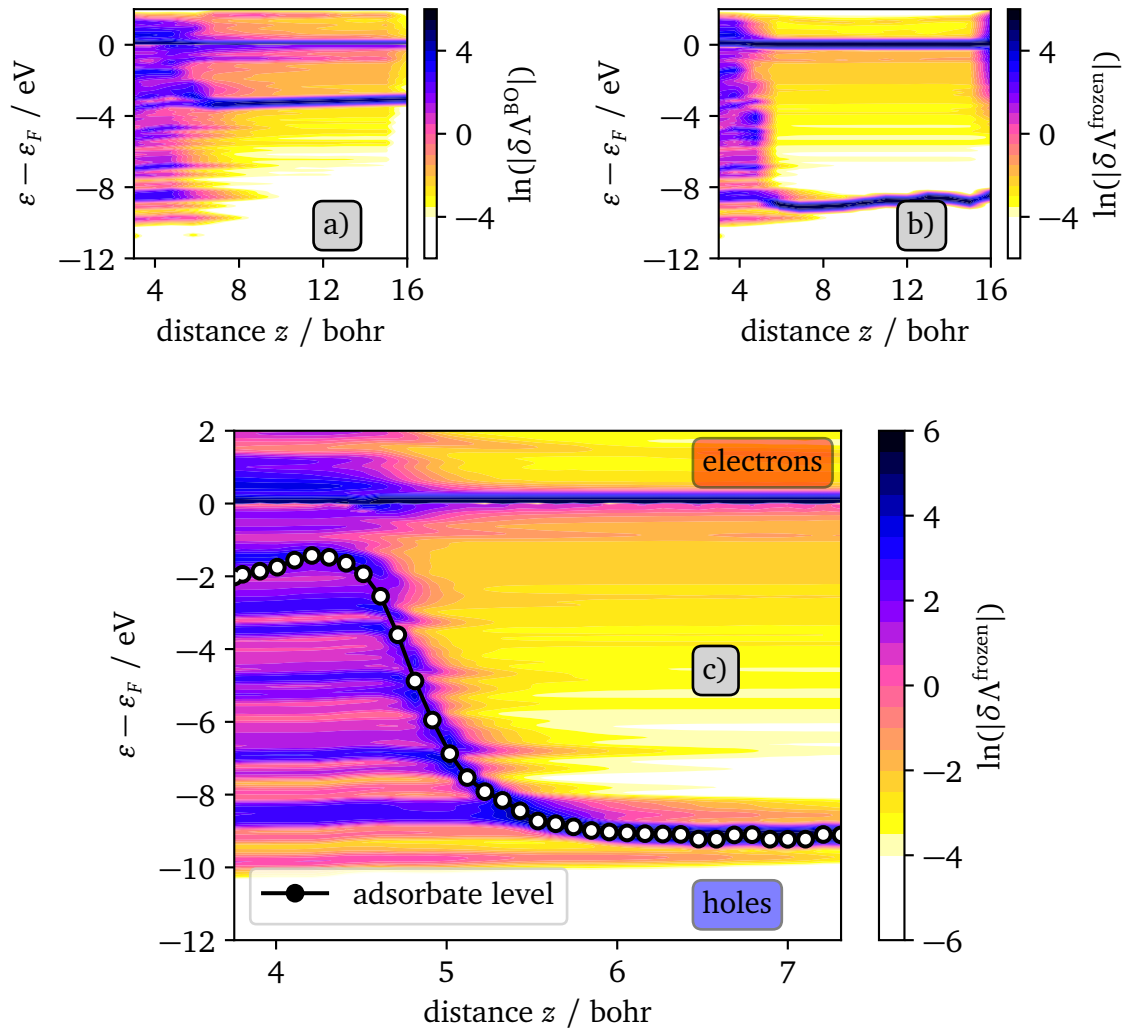


Figure 3.8: Distance dependent electronic excitation spectrum during impact of proton ($E_{\text{kin}}^{\text{init}} = 10 \text{ eV}$) on (111) facet of an Al_{188} -cluster. **a)** Projection onto ground-state following Equation 3.11. **b)** Projection onto orbitals calculated within frozen-density calculation following Equation 3.14 **c)** Zoom into b). Additionally, the frozen in adsorbate level position $\epsilon_a^{\text{frozen}}$ as presented in Figure 3.4 is shown in c). States are broadened using Gaussians with width 100 meV.

3.4.2 Frozen Density Kohn-Sham Electronic Excitation Spectrum: Ion Scattering

In the previous section, the electronic excitation spectrum $\delta\Lambda^{\text{BO}}$ was discussed. After the electronic charge transfer, the hole transferred to the cluster extends over a huge range of Kohn-Sham states. From $\delta\Lambda^{\text{BO}}$ it was not possible to explain the mechanism behind this behaviour. In the present section, the idea to project on an alternate set of Kohn-Sham orbitals employed in section 3.3 and resulting in Equation 3.5 is adapted. We take as a reference not the electronic density n_0 of the Born-Oppenheimer ground-state and therewith connected the ground-state Kohn-Sham orbitals. We rather base our evaluation on the time-dependent electronic density $n(\mathbf{r}, t)$ obtained within our TDDFT-MD simulations. This approach is motivated by the fact that the electronic tunneling occurs in the time-dependent effective potential and not in the ground-state effective potential. Therefore, the following definition of an alternative electronic excitation spectrum $\delta\Lambda^{\text{frozen}}$ is introduced here:

Definition: Frozen Density Kohn-Sham Electronic Excitation Spectrum $\delta\Lambda^{\text{frozen}}$

Artificial Kohn-Sham electronic excitation spectrum $\delta\Lambda^{\text{frozen}}$ with respect to a non self-consistent calculation, i.e. frozen-in electronic density for a given atomic geometry $\mathbf{R}(t)$ obtained within the TDDFT-MD simulation. Kohn-Sham orbitals are denoted as Φ_k^{frozen} with corresponding energies $\epsilon_k^{\text{frozen}}$.

$$\begin{aligned} \delta\Lambda^{\text{frozen}}(\epsilon, t, n(t), \mathbf{R}) = & \\ & \sum_j^{\text{occ}(t=0)} \sum_k |\langle \Psi_j^{\text{TD}}(t) | \Phi_k^{\text{frozen}}(n(t), \mathbf{R}(t)) \rangle|^2 \cdot \delta(\epsilon - \epsilon_k^{\text{frozen}}(n(t), \mathbf{R}(t))) \\ & - \sum_k \delta(\epsilon - \epsilon_k^{\text{frozen}}(n(t), \mathbf{R}(t))) \end{aligned} \quad (3.14)$$

Results for a simulation with an H^+ impinging on the on-top site of the (111) face of the Al_{188} -cluster with $E_{\text{kin}}^{\text{init}} = 10 \text{ eV}$ at $z_{\text{init}} = 16 \text{ bohr}$ are presented in Figure 3.8b) and c). There exists an evident difference between Figure 3.8a) and b) which is the position of the hole at the H^+ -projectile for large distances. For $\delta\Lambda^{\text{frozen}}$, the hole at the H^+ -projectile is located at the expected position of approximately -13.6 eV (hydrogen ionization energy) measured against the vacuum. The electronic charge around the projectile is zero and the eigenvalue of the hypothetical electron at the projectile within a frozen-density calculation is not influenced by e.g. a self-interaction error or a shift due to a missing account for spin-polarization. The projectile approaches the surface and in the region where the charge transfer occurs, electronic excitations extend over almost all electronic energy levels of the Al-cluster.

Figure 3.8c) shows in more detail the excitation spectrum $\delta\Lambda^{\text{frozen}}$ in the region where the charge transfer takes place. The stripe shape in the left part of the graph arises from the finite distance of electronic states and the broadening with Gaussians of width 100 meV

The adsorbate level position $\varepsilon_a^{\text{frozen}}$ as presented in Figure 3.4 is added to the graph. The origin of the above mentioned excitation of a wide range of bands can be explained with the help of $\varepsilon_a^{\text{frozen}}$: For large z and negligible electronic charge, the eigenvalue equals the exact value of $-0.5H$. After the charge transfer, the adsorbate level position coincides with the (ground-state) Born-Oppenheimer (BO) result. This is to be expected as it is generally assumed that for the present situation, the dynamics of an ionic projectile after the charge transfer is just like an initially neutral one, see e.g. Refs. [105, 116, 144]. In the region where the charge transfer takes place, the adsorbate level position transitions from the ionic level to the BO result. During this transition, electrons at intermediate energy levels can (and apparently do) tunnel onto the projectile resulting in an extended range of electronic excitations within the Al-cluster.

Note that the time-scale for propagation of the electronic excitation into the Al-bulk is connected to the plasmon frequency.

Supporting arguments for the above interpretation can be taken from Figure 3.9 where Kohn-Sham electronic excitation spectra $\delta\Lambda^{\text{frozen}}$ for projectiles with different initial kinetic energies are presented. Here, $E_{\text{kin}}^{\text{init}} = 2 \text{ eV}$, 10 eV and 1 keV with the on-top position as the impact site of the Al_{188} -cluster. For each spectrum, the adsorbate level position $\varepsilon_a^{\text{frozen}}(z)$ is shown in the same graph. Comparing Figure 3.9a), b) and c), it can clearly be seen that once the adsorbate level position increases, electronic excitations arise on the same energy within $\delta\Lambda^{\text{frozen}}$, i.e. energy of the hole is transferred into the Al states at the position of the adsorbate level.

Energy Within The Spectrum In analogy to Equation 3.12, the energy within the spectrum can be calculated from:

$$\tilde{E}_{\text{exc}}^{\text{frozen}} = \int_{-\infty}^{\infty} \varepsilon \cdot \delta\Lambda^{\text{frozen}} d\varepsilon, \quad (3.15)$$

Please note that after charge transfer, the $\delta\Lambda^{\text{BO}}$ and $\delta\Lambda^{\text{frozen}}$ are virtually identical, and in consequence, $\tilde{E}_{\text{exc}}^{\text{BO}} \approx \tilde{E}_{\text{exc}}^{\text{frozen}}$. Furthermore, the energy $\tilde{E}_{\text{exc}}^{\text{BO}}$ (Equation 3.12) and $\tilde{E}_{\text{exc}}^{\text{frozen}}$ (Equation 3.15) equal E_{exc} (Equation 3.13). This can be seen in Figure 3.7. After the charge transfer, $\delta\Lambda^{\text{BO}}$ shows the distribution of the electronic energy within the electrons and holes of the Kohn-Sham system. However, before the charge transfer, $\tilde{E}_{\text{exc}}^{\text{frozen}} \neq E_{\text{exc}}$ due to double counting of the hole at the projectile, and $\tilde{E}_{\text{exc}}^{\text{BO}} \neq E_{\text{exc}}$, as mentioned above.

In summary, with the help of the electronic excitation spectrum $\delta\Lambda^{\text{frozen}}$ as defined in Equation 3.14 it is possible to explain the mechanism behind the unexpected excitation spectrum after neutralization. This was not possible with the electronic excitation spectrum $\delta\Lambda^{\text{BO}}$ as defined in Equation 3.11. However, for both spectra, the excitation energy before the charge transfer is different from the value obtained from Equation 3.13.

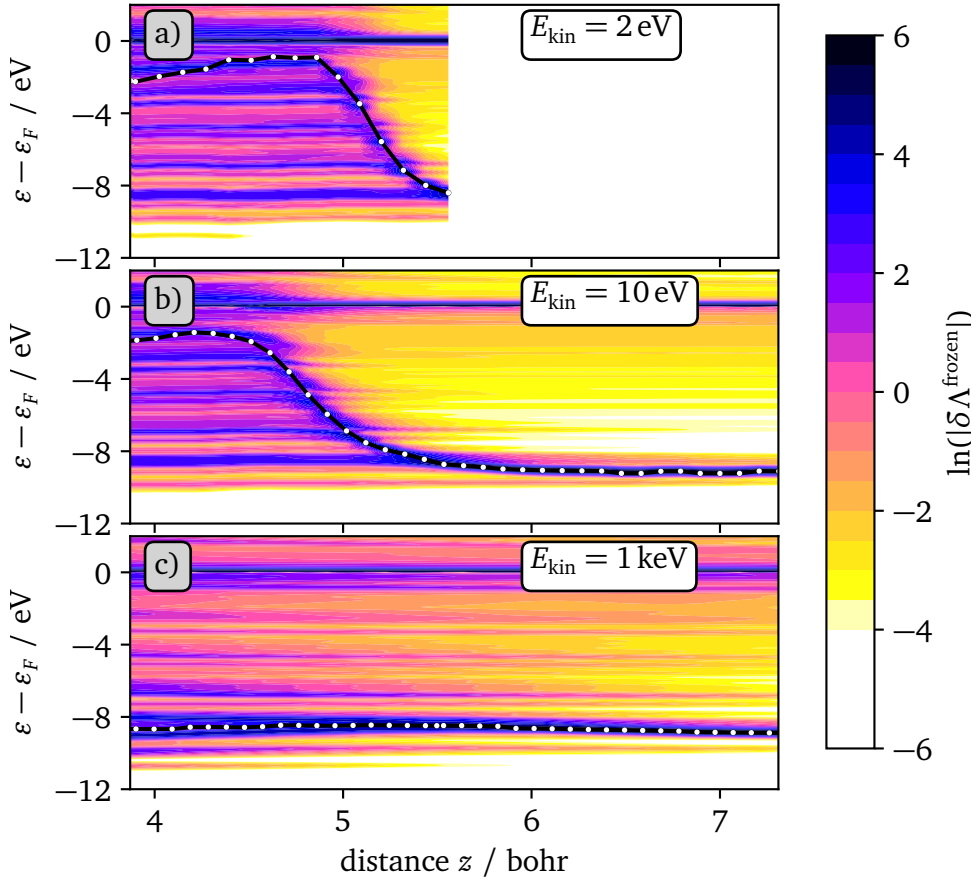


Figure 3.9: Kohn-Sham electronic excitation spectra $\delta\Lambda^{\text{frozen}}$ as defined in Equation 3.14. Electronic states are broadened with Gaussians of width $\sigma = 100$ meV. Additionally, adsorbate level positions $\varepsilon_a^{\text{frozen}}$ as defined in Equation 3.5 are drawn as small white dots. Kinetic energies of H^+ projectiles at $z^{\text{init}} = 16$ bohr are given in the inset. Please note: **b)** shows the same data as Figure 3.8c).

3.4.3 Kohn-Sham Electronic Excitation Spectra After Scattering

Following the discussion in the previous section about the interpretation of the Kohn-Sham electronic excitation spectra $\delta\Lambda^{\text{BO}}$ and $\delta\Lambda^{\text{frozen}}$, in this section we will investigate the electronic excitation spectrum in the outgoing trajectory. In principle, the electronic excitation spectrum can be accessed by experiments, see subsection 1.1.3. However, the regarding data is not to be found in the literature.

Figure 3.10 shows a comparison between $\delta\Lambda^{\text{BO}}$ arising upon impact of an H^+ and an H^0 projectile with $E_{\text{kin}}^{\text{init}} = 10$ eV at the exit distance $z_{\text{exit}} = 4.52$ bohr. The case of H^0 was discussed by Lindenblatt and Pehlke in Ref. [140], the excitation shows a maximum at

the Fermi energy and from there decays exponentially towards both sides. It arises due to electronic friction. Unsurprisingly, the spectrum after H^+ scattering looks entirely different as the potential energy of the initially ionic projectile is distributed over the electronic states of the Al-cluster. The Kohn-Sham excitation spectrum $\delta\Lambda^{\text{BO}}$ is further investigated in Figure 3.11.

In Figure 3.11, data after scattering of an H^+ impinging on an Al_{188} -cluster is presented for the exit distance $z_{\text{exit}} = 8$ bohr. In Figure 3.11a) the electronic excitation spectrum $\delta\Lambda^{\text{BO}}$ is shown. Apparently, excitations are distributed over the entire spectrum of the surface. Technically, this can be understood on base of the transition from the hydrogen adsorption level from an unbound and unoccupied one to an occupied one in a chemical bond, as described above. Please note that this is a result obtained within the limitations of the AGGA-TDDFT approach that is not able to capture Auger effects.

More details about the final distribution of the electrons and holes is given in Figure 3.11b) which shows the number of electrons and holes associated with the spectrum of Figure 3.11a). The excitations at the Fermi energy arise from electronic friction effects, i.e. electron-hole pair excitations. The remaining holes below the Fermi energy can be traced back to the initial hole at the H^+ projectile. Figure 3.11b) shows that the hole that was initially at the projectile is distributed into a wide range of electronic states. It can also be seen that practically no electrons are above the vacuum energy, i.e. secondary electron emission is not expected in this case. In these calculations, the integral over $\delta\Lambda^{\text{BO}}$ is approximately zero.

Figure 3.11c) shows the energy within the spectrum of Figure 3.11a). Only results to $\varepsilon - \varepsilon_F \leq 2$ eV are shown due to the limited number of unoccupied states in a ground-state-calculation. Assuming an exponentially decaying excitation spectrum $\delta\Lambda^{\text{BO}}$ in the region $\varepsilon - \varepsilon_F \geq 2$ eV in Figure 3.11a), the excitation energy within the spectrum $\tilde{E}_{\text{exc}}^{\text{BO}}$ can be obtained from Equation 3.12, resulting in a final value of $\tilde{E}_{\text{exc}}^{\text{BO}} = 8.3$ eV, 9.1 eV, 11.3 eV for $E_{\text{kin}}^{\text{init}} = 2$ eV, 10 eV, and 50 eV, respectively. This is in agreement with the excitation energies obtained from Equation 3.13: $E_{\text{exc}} = 8.6$ eV, 9.4 eV, 11.5 eV (see Table 3.4) and, as pointed out above, a necessary condition for the interpretation of $\delta\Lambda^{\text{BO}}$ as a Kohn-Sham

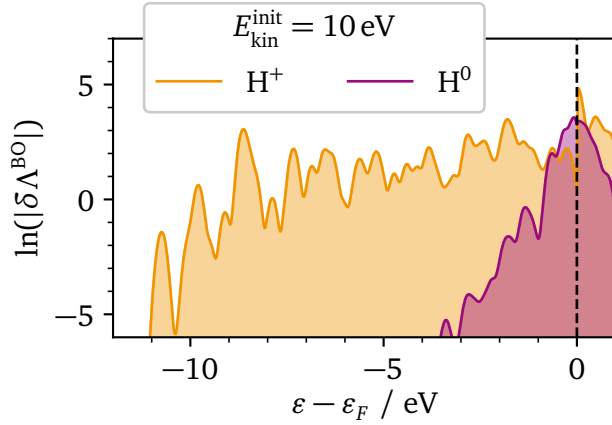


Figure 3.10: Kohn-Sham electronic excitation spectrum as obtained from Equation 3.11 at an exit distance $z_{\text{exit}} = 4.52$ bohr for H^+ and H^0 scattering off the on-top position of the Al_{188} -cluster with initial kinetic energy of $E_{\text{kin}}^{\text{init}} = 10$ eV at $z_{\text{init}} = 16$ bohr.

excitation spectrum.

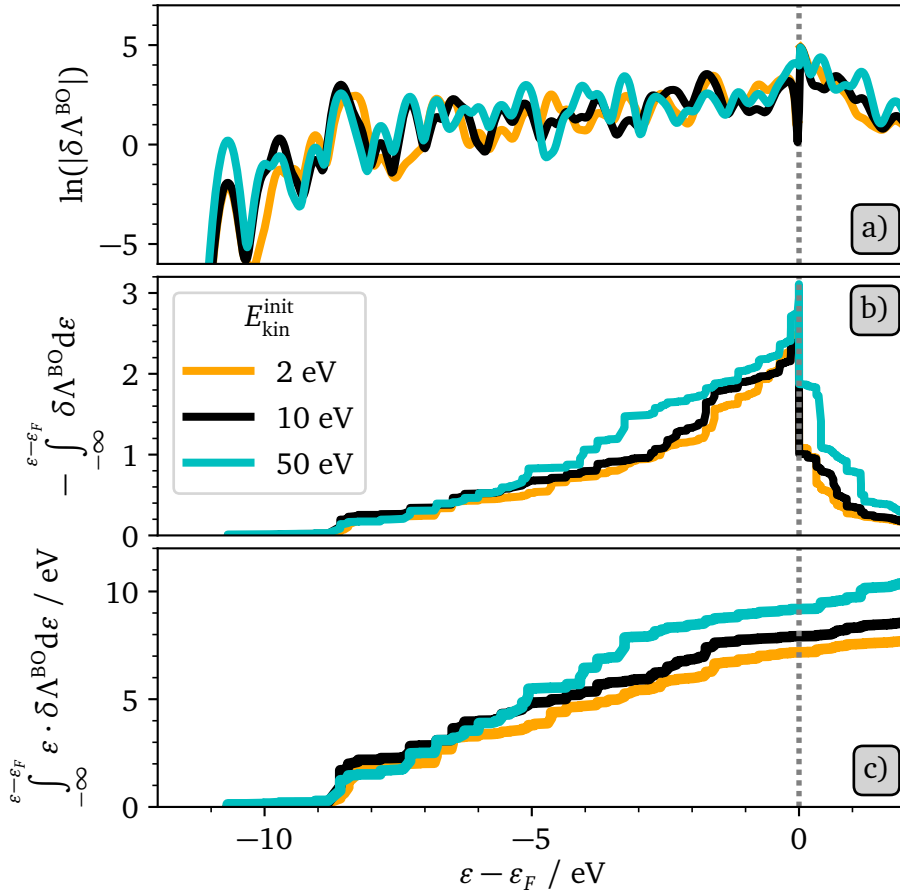


Figure 3.11: Evaluation of electronic excitation spectra $\delta\Lambda^{\text{BO}}$ for H^+ projectiles with different initial kinetic energies. Spectra are shown at $z_{\text{exit}} = 8$ bohr after reflection on the outgoing trajectory. **a)** Electronic excitation spectrum as defined in Equation 3.11, broadened with Gaussians of width $\sigma = 100$ meV, **b)** Cumulated number of holes/electrons, **c)** Integrated energy contained in the electrons and holes in the electronic excitation spectrum from $-\infty$ to $\varepsilon - \varepsilon_F$.

Plasmon Excitations For comparison we calculated the energy transfer into plasmonic degrees of freedom upon approach and charge transfer of the projectile. We apply a Fourier transformation to the oscillating electric dipole moment in z direction after scattering. Then, we analyze the strength and frequency and compare it to the according quantities from a laser excited cluster. We vary the amplitude of the laser until the strength of both electric dipole moments is in the same order of magnitude. Details are given in Appendix C on page 125. We find that after neutralization the excitation energy connected to the plasmon is in the order of 200 meV. This relatively small value is consistent with the work

| $E_{\text{kin}}^{\text{init}} / \text{eV}$ | $\tilde{E}_{\text{exc}}^{\text{BO}} / \text{eV}$ | $E_{\text{exc}} / \text{eV}$ |
|--|--|------------------------------|
| 2 | 8.3 | 8.6 |
| 10 | 9.1 | 9.4 |
| 50 | 11.3 | 11.5 |

Table 3.4: Comparison of electronic excitation energy in Figure 3.11 obtained from Equation 3.13 and Equation 3.12 for H^+ impinging on Al(111) surface face of Al_{188} -cluster. Initial kinetic energies are given for $z^{\text{init}} = 16 \text{ bohr}$.

of Gras-Marti and Echenique^[96] who obtained a value of approximately 70 meV for a 1 keV projectile, see also subsection 1.2.1.

Discussion Regarding the electronic excitation spectrum, one may have anticipated that only the electrons at the same energy as the ionic level tunnel from the surface to the projectile in order to neutralize it. This would in consequence yield a rather well peaked excitation spectrum at that level. The results obtained here, however, draw an entirely different picture and instead of such well peaked structure, the excitations are distributed over a wide range of states. Technically, this could be traced back to the change in the adsorbate level position.

Unfortunately, it remains unclear whether this behavior is a result of the chosen approximations to the TDDFT formalism or whether these results can also be observed in an appropriate experiment. Electronic excitation spectra are accessible e.g. with the sophisticated experimental setup by Diesing as described in subsection 1.1.3. However, in the experiment it may even be very challenging to separate between the neutralization spectrum from tunneling and the following electron-electron relaxations. The here employed approximations to the TDDFT method are not able to capture these electron-electron relaxation effects. From the theoretical side, the relaxation dynamics in excited metals has been studied by the method of Mueller and Rethfeld,^[305] who investigated the transient electron distribution due to (laser) excitation, thermalization, and relaxation.

3.5 Summary

First, the present chapter introduced the Al(111) surface and summarized data on the H–Al(111) interaction relevant to the present thesis. Furthermore, the employed atomic geometries which are finite-size Al_n -clusters were presented and discussed.

Secondly, the electronic charge transfer upon neutralization of a H^+ projectile was investigated. The charge transfer as obtained in a TDDFT-MD simulation was reproduced with a tight-binding Brako-Newns-Anderson (BNA) model Hamiltonian. The numerically very efficient tight-binding Hamiltonian takes for each kinetic energy two simple, distance-dependent functions as input and yields very good agreement with the TDDFT-MD simulation. The distance-dependent functions were termed $\varepsilon_a^{\text{frozen}}(z)$ and $\Gamma^{\text{frozen}}(z)$. They are obtained from the TDDFT-MD simulation by calculating a PDOS onto the Kohn-Sham states from a frozen-density calculation. Employing a rate equation, it was shown that the charge transfer rate as obtained from the TDDFT-MD simulation and the charge transfer rate calculated by Deutscher et al.^[153] and by Nordlander and Tully^[66,152,302] result in quantitatively similar charge transfer distances despite a very different overall behavior. It was shown that for the calculation of the charge transfer distance only the charge transfer rate prior to the charge transfer is important, where the TDDFT result and the literature data are of comparable magnitude.

Thirdly, Kohn-Sham electronic excitation spectra were investigated in this section with a major focus on the final distribution of the excitation energy within the Kohn-Sham electronic excitation spectra. The Kohn-Sham electronic excitation spectrum $\delta\Lambda^{\text{BO}}$ is often used in the literature and is based on a projection of the time-dependent Kohn-Sham orbitals onto the Kohn-Sham orbitals of the ground-state electronic density. Here, we proposed, calculated and discussed the Kohn-Sham electronic excitation spectrum $\delta\Lambda^{\text{frozen}}$ which is based on a projection of the time-dependent Kohn-Sham orbitals onto the Kohn-Sham orbitals obtained from a frozen-density calculation with frozen-in time-dependent density $n(t)$. The quality of $\delta\Lambda^{\text{BO}}$ and $\delta\Lambda^{\text{frozen}}$ was evaluated comparing the energy within the spectra to the excitation energy from a difference of time-dependent and ground-state electronic energies. It was found that, before the charge transfer when the excitation is localized at the projectile, the energy in both spectra was significantly different from the excitation energy.

After the charge transfer, the Kohn-Sham electronic excitation spectra from the here employed proton projectiles with $E_{\text{kin}}^{\text{init}} = 2 \text{ eV}$, 10 eV , and 50 eV at $z_{\text{init}} = 16 \text{ bohr}$ impinging on the on-top position of a Al_{188} -cluster show excitations distributed over a wide range of electronic states. From an analysis of $\delta\Lambda^{\text{frozen}}$ and $\varepsilon_a^{\text{frozen}}(z)$, this could be traced back to the change in the frozen-density adsorbate level position from the level of a free ion to the neutral and chemically bound atom. During this transition, there is an electronic charge transfer from the surface to the projectile at the same energy level resulting in the above described Kohn-Sham electronic excitation spectrum. In principle, electronic excitation spectra are accessible experimentally, e.g. with the experiments by Diesing as described in subsection 1.1.3. Please note that our TDDFT simulations do not describe e.g. electron-electron relaxation effects which would be expected in the experiment.

Based on the data presented in this chapter, different questions were pursued in the

following chapter 4 and chapter 5. Among others, these are:

- (i) What is the effect of the XC-functional? How sensitive are the results on the impact site?

Investigated in chapter 4.

- (ii) How to link the charge transfer and the energy dynamics? What are the differences regarding energy transfer between an H^+ and an H^0 projectile impinging on the Al(111) surface? How are the kinetic energies on the outgoing trajectory connected to the distance of charge transfer?

Investigated in chapter 5.

Publication

*"Time-dependent simulation of ion stopping:
Charge transfer and electronic excitations"*

N. Schlünzen, K. Balzer, M. Bonitz, L. Deuchler, E. Pehlke

Contributions to Plasma Physics **59**, e201800184 (2019)

Introduction In this chapter results from a common research activity between N. Schlünzen, K. Balzer, M. Bonitz, L. Deuchler, and E. Pehlke are presented. Schlünzen, Balzer and Bonitz applied non-equilibrium Green functions (NEGF)–Ehrenfest simulations to investigate the change of stopping power in correlated nano-scale materials. They especially concentrated on electronic correlation effects in the stopping of an ion projectile impinging on a honeycomb structure. L. Deuchler and E. Pehlke studied the charge transfer between a metallic substrate and an incoming proton with Ehrenfest-MD simulations based on TDDFT. In the publication, time-resolved non-adiabatic simulations of ion stopping that are capable of resolving the electronic processes in the projectile and in the target with these two complementing techniques (NEGF and TDDFT) are presented and discussed.

Main Findings Regarding the TDDFT-MD simulations, the present work discusses the charge transfer between an Al(111)-surface represented by a finite size cluster and a hyperthermal H⁺ projectile with normal incidence on the on-top site. The starting distance is $z_{\text{init}} = 16$ bohr, the initial kinetic energies are 2 eV, 10 eV, and 50 eV. A GGA-PBE XC-functional was employed.

For the different kinetic energies, the charge transfer rate shows a maximum at a distance between the projectile and the center of the uppermost Al-atom of 5.13, 4.76, and 4.18 bohr, respectively (see Fig. 1 of publication I on page 77). To estimate the influence of the impact site upon charge transfer, we calculated two impact points where the most differences would be expected. These are the on-top and the fcc-hollow position. The distance of charge transfer for a projectile with initial kinetic energy 10 eV between impact sites top and fcc-hollow is very small (< 0.05 bohr).

The influence of the XC-functional is analyzed by employing two different numerically feasible flavours of XC-functionals. Here the ALDA and AGGA XC-functionals. For the

ALDA, an outwards shift of the charge transfer is observed. The maximum of the charge transfer rate is shifted by approximately 0.25 bohr. This comes from, the differences in the description of the electronic ground-state of the H-atom. Currently, the influence of the adiabatic approximation to the XC-functional cannot be qualified as there do not exist feasible non-adiabatic XC-functionals. Furthermore, the initial state of the simulations of H^+ is spin-unpolarized and does not allow for a spin break during the simulation, for a discussion see also section 3.2.

Additionally, electronic excitations arising from an H^0 impinging on the fcc-hollow site with $E_{\text{kin}}^{\text{init}} = 10$ eV and a subsequent sub-surface trajectory were compared to the electronic excitations induced by an H^+ with the same trajectory. The variation of the electronic excitation energy comes out very similar when the projectile propagates within the metal cluster. This is in line with the observation that final projectile charges do not depend on the charge state of the incident particle for the given H^+ /Al system and velocity range by, for example, Zimny et al.,^[306] Jouin et al.,^[159] and Torralba et al.^[155] The stopping power obtained in the TDDFT-MD simulations are in agreement with the values derived from a linear-friction ansatz^[97] as well as an extrapolation of data from Schleife et al.^[307] and PSTAR.^[308] Differences in electronic excitations for different initial kinetic energies are discussed in more detail in chapter 5.

Outlook TDDFT based MD simulations allow for a material-specific ab initio description of time-dependent charge and energy transfer and screening. In particular, the resonant charge transfer from an Al(111)-surface to an impinging H^+ serves as a model in which also slow (i.e. hyperthermal) projectiles are accessible to a TDDFT-MD based analysis.

Synergy benefits are expected from a combined treatment of the NEGF and the TDDFT method. As discussed in Appendix D, Auger effects are not included in the TDDFT-MD simulations. Future developed XC-functionals that may even include Auger effects can most likely be benchmarked by NEGF simulations. On the other hand, the NEGF simulations did not include a realistic treatment of the impacting ion. Here, a combination with TDDFT provided model parameters could be the basis for major progress.

From the presented analysis, different paths open up for further investigation and the following questions need to be answered:

- (i) How to extrapolate the cluster results to the extended surface and what are implications to experiments?

Investigated in chapter 5.

- (ii) How to reach a deeper understanding of the electronic excitation energy that arises during the charge transfer process? What differences are to be expected from different initial kinetic energies? Does the insensitivity of the charge transfer regarding impact position imply that the electronic excitation is similar, too?

Investigated in chapter 5.

- (iii) How do results change when simulations are extended to further substrate systems?

Investigated in chapter 6.



Received: 17 December 2018 | Revised: 15 February 2019 | Accepted: 20 February 2019 | Published on: 22 March 2019

DOI: 10.1002/ctpp.201800184

ORIGINAL ARTICLE

Contributions to
Plasma Physics

Time-dependent simulation of ion stopping: Charge transfer and electronic excitations

N. Schlünzen¹ | K. Balzer² | M. Bonitz¹ | L. Deuchler¹ | E. Pehlke¹¹Institut für Theoretische Physik und Astrophysik,
Christian-Albrechts-Universität zu Kiel, Kiel,
Germany²Rechenzentrum, Christian-Albrechts-Universität
zu Kiel, Kiel, Germany***Correspondence**N. Schlünzen, Institut für Theoretische Physik und
Astrophysik, Christian-Albrechts-Universität zu
Kiel, Leibnizstraße 15, 24098 Kiel, Germany.
Email: schlunzen@theo-physik.uni-kiel.de

The energy loss of charged particles in matter has been studied for many decades, both, analytically and via computer simulations. While the regime of high projectile energies is well understood, low energy stopping in solids is more challenging due to the importance of non-adiabatic effects and electronic correlations. Here we consider two problems: the charge transfer between substrate and projectile and the role of electronic correlations, specifically formation of doubly occupied lattice sites in the material during the stopping process. The former problem is treated by time-dependent density functional theory simulations and the latter by non-equilibrium Green functions.

KEYWORDS

charge transfer, doublon formation, nonequilibrium Green functions, stopping power, TDDFT simulations

1 | INTRODUCTION

The impact of ions on a solid surface is of prime importance for plasma physics and surface science and has been studied for decades, both, experimentally and theoretically. The theoretical approaches include scattering theory^[1] or uniform electron gas models.^[2] Here the primary input is the dynamic inverse dielectric function (or dynamic structure factor, DSF) for which electron gas models or recently developed quantum Monte Carlo methods^[3] can be applied. Recently, also ab initio simulations of ion stopping based on time-dependent density functional theory (TDDFT) were reported for metals,^[4] semimetals,^[5] or boron nitride and graphene sheets^[6] and other materials. These simulations account primarily for valence–electron excitation. Good results for the stopping power of high energy ions in matter are also provided by the SRIM code^[7] that uses the binary collision approximation in combination with an averaging over a large range of experimental situations. Stopping power simulations have also been extensively applied for plasmas using kinetic equations. Here, again, the energy loss is usually computed by integrating of the DSF of the plasma which can be understood as a linear-response approach. At the same time, time-resolved simulations have been performed based on quantum kinetic theory^[8,9] which allow one to go beyond the linear response approximation. This is of particular importance in case of strong excitation or for the treatment of fast non-adiabatic processes in the target.

Aside from high-density plasmas (warm dense matter), for example, Zylstra et al.^[10] and Kremp et al.,^[11] ion stopping is also of central relevance for low-temperature plasmas in contact with a solid surface. This latter system is in the focus of the present paper. In these plasmas most of the ions are usually in equilibrium with the neutral gas and are at room temperature. In addition, close to the surface (in the plasma sheath) ions may be accelerated by the sheath electric field up to keV energies, for a recent overview on plasma–surface simulations see Bonitz et al.^[12] Even though the overall behavior of the stopping power as a function of ion impact energy is understood, for low-temperature plasmas special questions remain open. This includes: how does charge transfer between substrate and ion occur (neutralization of projectile)? How does it depend on the impact energy

and on the substrate material? In what distance from the target does it occur? Furthermore, how does the stopping behavior change in the case of nontrivial targets that either have a complicated surface morphology, nanostructuring or exhibit strong electronic correlations? Answers to these questions are not only of fundamental interest but are also important for applications as they may give rise to new plasma–surface combinations with non-traditional properties.

The goal of the present paper is to address some of these questions that are of relevance for low-temperature plasmas. We present time-resolved non-adiabatic simulations of ion stopping that are capable of resolving the electronic processes in the projectile and in the target. In particular, we concentrate on two questions. The first is the charge transfer between a metallic substrate and an incoming proton which we treat via TDDFT (c.f., Section 2). The second question is the change of stopping power in correlated nano-scale materials. Here we apply non-equilibrium Green functions (NEGF)–Ehrenfest simulations, extending the recent work of Balzer et al.^[13,14] The NEGF approach is introduced in Section 3 and applied to finite honeycomb Hubbard clusters. Finally, in Section 4 we discuss how the two complementary approaches might be combined in the future in order to achieve a comprehensive description of ion and electron dynamics at the plasma–solid interface.

2 | TDDFT SIMULATIONS OF CHARGE TRANSFER AND ION STOPPING

In this section we present ab initio molecular dynamics (MD) simulations for the neutralization of an ion, H^+ , incident on a simple metal surface, Al(111), which we have carried through using the Octopus code.^[15–17] The metal substrate is represented by a cluster. The coupled system of the ions and the electrons is described in an approximate way by using Ehrenfest dynamics.^[15,18] The Al atomic coordinates will be kept fixed during the time-dependent simulation, but this restriction could easily be lifted without any significant additional computational effort. The electrons are described within TDDFT.^[15,19,20] The time-dependent Kohn–Sham equations, which in case of a local potential v read (in atomic units)

$$i \frac{\partial \psi_j(\mathbf{r}, t)}{\partial t} = -\frac{1}{2} \nabla^2 \psi_j(\mathbf{r}, t) + \left(v(\mathbf{r}, t) + \int d^3 \mathbf{r}' \frac{n(\mathbf{r}', t)}{|\mathbf{r} - \mathbf{r}'|} + v_{XC}(\mathbf{r}, t) \right) \psi_j(\mathbf{r}, t), \quad (1)$$

are integrated together with the Ehrenfest equation of motion. The electron density is calculated from the sum over the probability densities of the time-dependent Kohn–Sham states that are occupied in the initial state, which itself is constructed by combining the separately calculated electronic Kohn–Sham ground-states of the metal atom cluster and the incident particle. The adiabatic approximation is applied to the exchange–correlation (XC) potential v_{XC} , and, in addition, an approximate XC functional from ground-state DFT is used:

$$v_{XC}(\mathbf{r}, t) \approx v_{XC}^{\text{approx}}([n(\cdot, t)], \mathbf{r}). \quad (2)$$

In case of a proton incident on a metal surface, the electronic system is initially strongly locally excited. This is different from the case of an atom, for example H^0 , scattered at the surface.^[21] The adiabatic approximation of the XC potential will be a more serious approximation in case of the strongly locally electronically excited system. In particular, Auger transitions are not expected to be accounted for.^[22,23] However, this is not a major restriction in case of the present simulations, because Merino et al.^[24] have concluded from their study using a model Hamiltonian that at the low H^+ kinetic energies considered here (below keV) the charge transfer is dominated by resonant processes. Finally, we note that the TDDFT–MD simulations we present below refer to the valence electrons only. The core electronic states of the metal atoms have been incorporated into an ionic pseudopotential. Moreover, also the s -wavefunction of the H-atom is pseudoized.

Important insight into proton neutralization at Al surfaces has been achieved by various authors using rate equations^[25,26] or (Newns–Anderson-type) model Hamiltonians.^[24,27–30] While strong correlation effects can be incorporated into model Hamiltonians, the advantage of the direct simulation of the charge transfer process using a TDDFT code like Octopus lies in the ab initio determination of the time-dependent electron density (i.e., screening and charge transfer), the effective potential, and hence the time-dependent electron tunnelling probabilities.

TDDFT–MD simulations of ions accounting for resonant charge transfer have been carried out by other authors before, for example, for the interaction of Li^+ with an Al_{58} -cluster by Moss et al.,^[31] for a proton scattered at a Li_4 -cluster by Castro et al.,^[32] and collisions with carbon nanostructures by Krashennnikov et al.,^[33] or DNA fragments by Seraide et al.,^[34] or graphene fragments by Bubin et al.,^[35] or graphene and boron nitride by Zhao et al.,^[6] and for Cl^- incident on a $MoSe_2$ monolayer by Wang et al.^[36] This has lead to many significant scientific advances. However, there are open questions concerning, for example, the resonant charge transfer in particular at low kinetic energies and the effect of the approximation to the XC-potential.^[37,38] Moreover, technological advances allow for the treatment of more extended systems. Here we present a TDDFT–MD simulation of the charge transfer and energy dissipation for an H^+ ion with initial kinetic energy 2 eV ... 50 eV incident on an Al(111) metal surface (modelled by a cluster), and compare to the energy dissipation in case of an incident H-atom.

Technical details of the TDDFT–MD simulations are summarized below.

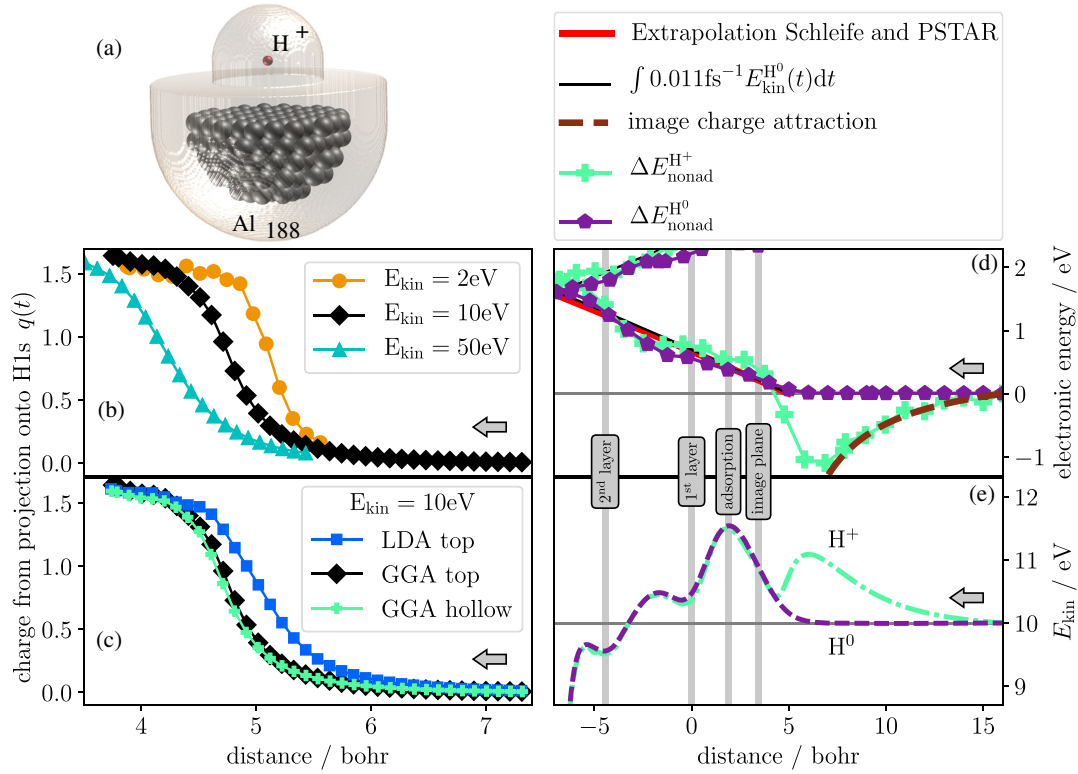


FIGURE 1 (a) Visualization of Al-cluster and simulation box in case of H–Al on-top collision; graphic produced using the vmd software.^[40] (b) Charge transfer from the Al(111) target to the H⁺ projectile incident on an Al on-top site as obtained from the TDDFT-MD simulations (Equation (3)). The uppermost Al-layer is located at $z = 0$ bohr. (c) Comparison of charge transfer for H⁺-projectile incident on an Al-hollow or on-top site and comparison between GGA and LDA results. (d) Comparison of the variation of the electronic excitation energy (Equations (4) and (5)) and (e) the kinetic energy of the H⁺ or H⁰ projectile incident on the Al(111) fcc hollow-site. The H penetrates the surface and propagates through the first two layers inside the Al-cluster until it is reflected at the third Al-layer

2.1 | Computational details

The Octopus code (version 6) by Rubio et al.^[15–17] has been employed for all TDDFT-MD simulations presented in this paper. The adiabatic approximation is applied to v_{xc} , together with the Perdew–Burke–Ernzerhof (PBE) generalized gradient approximation (GGA) for exchange and correlation from ground-state DFT (PBE-GGA)^[39]. The Al(111) surface is modelled by a cluster containing either 172 Al-atoms (for H⁺ incident at the Al(111) hollow site) or 188 Al-atoms (for H⁺ incident at the on-top site). The Al-clusters have been created by cutting out half-spheres from a (111)-oriented substrate with lattice constant of 4.047 Å as determined from ground-state DFT calculations with the convergence parameters and pseudopotential as described below. The uppermost Al-layer has been fixed and an ionic relaxation of the remaining Al-atoms has been performed. The simulation has been performed inside a user-defined region (see Figure 1a) that fits into a cube with edge size 60 bohr, and a minimum distance between atoms and the boundary of the user-defined region of 12 bohr. The FFT for solving the Poisson equation requires a box with twice the edge length of the cube described above. Ions are represented by norm-conserving Troullier–Martins pseudopotentials^[41] created with FHIPP.^[42] In case of the Al atom, 10 electrons are treated as frozen-in core states. The non-local pseudopotential is p -local in case of Al and s -local in case of H. The following cut-off radii have been used for the creation of the pseudopotentials: $r_{1s}^{\text{Al}} = 1.791$ bohr, $r_{2p}^{\text{Al}} = 1.974$ bohr, $r_{3d}^{\text{Al}} = 2.124$ bohr, $r_{1s}^{\text{H}} = 1.276$ bohr, $r_{2p}^{\text{H}} = 1.276$ bohr. Fourier components of the pseudopotentials beyond the cut-off determined by the real-space mesh size are filtered using the method of Tafipolsky and Schmid^[43] as supplied within Octopus. The Kohn–Sham wavefunctions are sampled on a real-space grid. We have used a spacing $\Delta x = 0.5$ bohr. As a test, we have carried through simulations with either smaller spacings ≥ 0.4 bohr or larger cluster (302 atoms for H⁺ towards the on-top position). The electronic ground state of the Al-cluster has been determined using a Methfessel–Paxton smearing^[44] with a small smearing parameter of 20 meV.

In case of the H⁺ projectile, the bare H-pseudopotential has been added to the simulation box. In case of the H⁰ projectile, in addition the spin-polarized ground-state Kohn–Sham wavefunction of the H-atom has been calculated and added to the set of wavefunctions. The initial distance between target and projectile is set to 16 bohr. An initial velocity has been assigned to the

projectile, corresponding to a kinetic energy of 2, 10, or 50 eV. The initial-state Kohn–Sham wavefunction of the H-atom has been multiplied with a boost phase factor.^[22,45] The Al atomic positions were kept fixed during the simulations. A time step of 0.02 atomic time units (0.5 attoseconds) has been used for the propagation of the Kohn–Sham wavefunctions. The exponent in the propagator is approximated using the exponential midpoint rule, and a fourth-order Taylor expansion of the exponential is used as implemented in Octopus^[46].

2.2 | Charge transfer H^+ /Al(111)

The charge transfer from the Al-substrate to the H^+ projectile as derived from the TDDFT-MD simulations is shown in Figure 1b for the initial condition that the projectile is incident on the on top-site of the Al(111) surface. Only the incoming part of the trajectory—before the H–Al head-on collision—is analysed. As the eigenvalue of the hydrogen 1 s level is located inside the valence band of bulk Al, resonant neutralization via elastic tunnelling of the electron from the metal to the proton is possible.^[24] In order to quantify the charge transfer $q(t)$ to the incident H^+ ion we project the time-dependent Kohn–Sham wavefunctions $|\psi_j(t)\rangle$ onto the H1s-orbital $|1s\rangle$. Including the occupation f_j this yields the local charge of the H-ion

$$q(t) = \sum_j f_j |\langle 1s | \psi_j(t) \rangle|^2. \quad (3)$$

In Figure 1b the transferred charge is plotted as a function of the distance of the projectile from the Al-surface. The neutralization of the proton occurs at a distance between 4 and 6 bohr in front of the surface, depending on proton velocity. This is consistent with the respective distance obtained by Jouin and Gutierrez.^[26] The H^+ neutralization has been reported in the literature^[29] to be very efficient. As the slower projectile spends a longer time at a certain separation in front of the metal surface, the neutralization of the slower particle occurs at larger separation from the surface. The charge on the H finally exceeds a value of 1.0. Negatively charged hydrogen is well known, for example, in case of metal hydrides.^[47] The quantitative value (as compared to other definitions of local ionic charges) may be partially affected by the overlap of the H1s wavefunction with the electronic states of the Al-cluster. The data may be useful for the parametrization of the H–Al interaction in many-particle model Hamiltonians.

As can be read from the results for the charge transfer to a proton with initial kinetic energy of 10 eV shown in Figure 1c, the charge-transfer dynamics is rather insensitive to the point of incidence on the Al-surface. This was to be expected in view of the small corrugation of the effective potential and electron density far above the metal surface layer. However, we note a significant sensitivity of the charge-transfer dynamics on the choice of the approximation—here local-density approximation (LDA) versus PBE-GGA—applied to the electronic ground-state XC-energy functional. We suggest that this may be due to differences in the description of the electronic ground state of the H-atom.

There is a well-known difficulty to describe long-range correlations with semilocal approximations for the XC energy functional in ground-state calculations^[48]. For example, when describing the dissociation of H_2 with a semilocal XC-functional, an artificial transition to a spin-polarized system is in general used to describe total energies at large atom separation.^[48,49] In time-dependent simulations of H^0 incident on a metal surface, the H^0 atom has been assumed to be electronically spin-polarized at large separations from the surface and loses spin polarization when interacting with the surface.^[50,51] We also use an initially spin-polarized H^0 -atom in the present simulations in Section 2.3. In case of H^+ incident on the Al-cluster in the present calculation the initial configuration is spin-unpolarized and there is no term in the Hamiltonian that could break this symmetry during time evolution. We therefore suspect that the exchange-correlation effects are not well accounted for by the present spin-unpolarized semilocal approximation to v_{XC} , and more advanced approximations would be desirable.^[48] For the model-Hamiltonian calculations, the problem of correlation has been approached using, for example, as approximation for the correlation in multiple-level systems $U \rightarrow \infty$.^[30]

It is argued that no electron–electron relaxation (Auger effect) occurs when the present adiabatic XC-functionals are employed.^[22,23] Theoretical work on the He^+ /Al system shows that in case of the projectile velocity range applied here, the Auger channel is the relevant one in order to be able to describe the experiment.^[52–55] First test calculations within the framework described above for a He^+ ion ($E_{\text{kin}} = 2$ H) incident on an Al(111) surface, confirm that Auger processes do not show in the calculations performed using an adiabatic GGA XC-functional. Hence, other methods beyond the TDDFT-MD with adiabatic GGA have to be used if Auger transitions are to be considered.

2.3 | Energy dissipation for H^+ , H^0 projectiles penetrating the Al-surface

TDDFT-MD simulations of an H^+ or an H^0 projectile starting 16 bohr above the hollow site of the Al(111) surface facet of the Al-cluster with an initial kinetic energy of 10 eV show—in agreement with similar previous TDDFT-MD simulations for H^0 by Lindenblatt et al.^[21,56]—that the projectile (in case of H^+ after neutralization) penetrates the Al-surface. It propagates

through the top two metal layers before it is reflected at the third atomic layer in a head-on collision. In Figure 1d the variation of the electronic excitation energy with respect to its initial value is plotted versus the distance of the projectile from the surface (defined by the position of the top layer Al atoms). In case of the uncharged H^0 this equals the electronically nonadiabatic energy, which is defined by the difference between the electronic energy in the time-dependent simulation and the energy of the electronic ground state at frozen-in atomic coordinates $R(t) = (\mathbf{R}_1(t), \dots, \mathbf{R}_N(t))$:

$$\Delta E_{\text{nonad}}^{H^0} := E_{\text{td}}(t) - E_{\text{gs}}(R(t)). \quad (4)$$

In case of a proton incident on the surface, in addition the energy needed to ionize an H-atom, i.e. to transfer one electron from the H^0 -atom to the Al-cluster, has been subtracted for the sake of easier comparison to the case of H^0 :

$$\Delta E_{\text{nonad}}^{H^+} := E_{\text{td}}(t) - E_{\text{gs}}(R(t)) - (E_{\text{ion}}(H) - W_{\text{A}}(\text{Al-cluster})). \quad (5)$$

All energies refer to DFT calculations with PBE-GGA applied to v_{XC} . In Figure 1e the kinetic energies of the H^+ and H^0 projectiles are visualized. The neutral H^0 projectile approaches the surface, accelerates inside the chemisorption well and transverse the adsorption position (at 1.89 bohr) where it gains the adsorption energy of 1.93 eV. This results in an increase of the kinetic energy of the projectile, however, part of the kinetic energy of the projectile is dissipated into electron-hole pair excitations.^[21] The charged projectile H^+ is accelerated towards the surface due to the image-charge attraction.^[57] The image plane of Al(111) is located at $z_{\text{image}} = 3.49$ bohr in front of the surface, according to Chulkov and Silkin.^[58] The image-charge potential $1/(4[z - z_{\text{image}}])$ that would be induced in case of an infinitely large surface slab is included in Figure 1d by the brown dashed curve. In case of the finite cluster utilized here, the attractive potential will deviate from the simple image-potential form. The kinetic energy gain of about 0.54 eV due to attraction by the image charge of a proton starting infinitely far away from a plane surface and reaching a surface separation of 16 bohr is not accounted for in our calculation. As can be seen by comparing Figure 1d and e, while the kinetic energy increases due to image-charge attraction, the electronic excitation energy decreases by about the same amount (brown dashed curve in Figure 1d). This is in line with the conservation of total energy. Note that E_{gs} in Equation (5) refers to the electronic ground state, that is, an uncharged H^0 . Thus the change of electrostatic energy due to polarization of the Al-cluster by the proton is included in $\Delta E_{\text{nonad}}^{H^+}$. At a surface separation between 4.5 and 6.0 bohr, the partially charged H^+ loses kinetic energy. This region coincides with the region where the charge transfer occurs (see Figure 1c). The deceleration of the projectile is ascribed to Coulomb repulsion between the projectile and the Al-cluster. In case of an infinitely large substrate and in the adiabatic limit the charge transferred to the projectile will, in the electrostatic case, come from infinity. Hence we have to be aware that the above Coulomb repulsion effect will be limited to the finite-size clusters. The cluster-size convergence is expected to be slow. Thus we cannot easily generalize the result of the rather similar variation of the kinetic energy of the H^+ and H^0 projectile at distances smaller than 4.5 bohr from our cluster calculation to the case of a metallic half space. However, as far as the interaction with the Al-cluster used in the simulations is concerned, the H^+ loses its charge in front of the surface and the variation of the electronic excitation energy comes out very similar when the projectile propagates within the metal cluster. This is in line with the observation that final projectile charges do not depend on the charge state of the incident particle for the given H^+ /Al system and velocity range by, for example, Zimny et al.^[25], Jouin et al.,^[26] and Torralba et al.^[29] The similar behavior between H^+ and H^0 incident on, for example, a graphene sheet has been noted before in TDDFT-MD calculations by Krashennnikov et al.^[33]

For clarity we point out that, while not immediately deducable from Figure 1d and e, the neutralization of the H^+ in front of the surface is associated with a strong energy transfer into hole excitations of the metal substrate as the hole tunnels from the proton into the metal.

Stopping power for protons in bulk Al has been discussed and analysed in detail by several authors using TDDFT-dynamics^[4,59,60] or linear-response theory.^[61,62] A neutral hydrogen atom impinging on the Al(111) surface and penetrating into the crystal has been studied before in Lindenblatt et al.^[21,56] Theory for bulk electronic stopping agrees with experimental data, especially in the low-energy range subject to the present investigation. For comparison, in Figure 1d we include the stopping power derived from a linear-friction ansatz^[21] (black curve) as well as an extrapolation of data from Schleife et al.^[60] and PSTAR^[63] (red curve). The starting point of both curves is chosen to coincide with the commencing electron-hole pair creation. Thus we agree with previous work^[4,21,59–62] that electronic stopping of hydrogen (after neutralization) within the Al-metal can reliably be simulated by TDDFT. At the same time, many questions remain to be solved, for a discussion see Section 4.

3 | NEGF-EHRENFEST APPROACH TO ION STOPPING IN CORRELATED MATERIALS

3.1 | Theory overview

A method that allows for a systematic treatment of electronic correlations in a solid-state material and, at the same time, of inhomogeneity effects induced by an external excitation are (real-time) NEGF.^[64–67] The central quantity is the one-particle

NEGF

$$G_{ij\sigma}(t, t') = -i\hbar \langle T_C c_{i\sigma}(t) c_{j\sigma}^\dagger(t') \rangle \quad (6)$$

which appears as a two-time generalization of the one-particle density matrix $\rho_{ij\sigma}(t) = -\frac{i}{\hbar} G_{ji\sigma}(t, t^+)$, where the notation t^+ means $t = t + \epsilon$ with $\epsilon \rightarrow 0$, and G determines all time-dependent one-particle observables. In the definition of the NEGF, $c_{i\sigma}^\dagger$ ($c_{i\sigma}$) are creation (annihilation) operators in the Heisenberg picture for electrons in a single-particle orbital $|i\rangle$ with spin projection σ , and the expectation value is computed with the equilibrium density operator of the system. Furthermore, times are running along the Keldysh contour C , with T_C denoting ordering of operators on C .^[65,68,69] The equations of motion for the NEGF are the two-time Keldysh–Kadanoff–Baym equations (KBE)^[65]

$$\sum_k [i\hbar \partial_t \delta_{ik} - \bar{h}_{ik\sigma}(t)] G_{kj\sigma}(t, t') = \delta_C(t - t') \delta_{ij} + \sum_k \int_C ds \Sigma_{ik\sigma}(t, s) G_{kj\sigma}(s, t') \quad (7)$$

$$\sum_k G_{ik\sigma}(t, t') [-i\hbar \bar{\partial}_{t'} \delta_{kj} - \bar{h}_{kj\sigma}(t')] = \delta_C(t - t') \delta_{ij} + \sum_k \int_C ds G_{kj\sigma}(t, s) \Sigma_{ik\sigma}(s, t') \quad (8)$$

a set of two integro-differential equations, where the Hamiltonian $\bar{h}(t)$ contains the one-particle kinetic, potential and mean-field energy, whereas correlation effects are contained in the two-time selfenergy $\Sigma(t, t')$ that can be approximated as a functional of the NEGF according to a diagrammatic many-body perturbation expansion. Note, that in the given form of the KBE we do not consider spin changes and assume a paramagnetic system.

As an approximation for the selfenergy beyond the Hartree–Fock (HF) level (for which $\Sigma = 0$ and mean-field contributions are incorporated in $\bar{h}(t)$), we consider in the present work the second-order Born (2B) approximation,^[64,65] which conserves total energy, particle number and momentum and is specified in Equation (12) below for the case of a local Hubbard-type interaction. For more advanced expressions for the selfenergy, such as GW , T matrix or third order, for example, Schlünzen et al.^[70,71] In addition to the use of the 2B approximation, we simplify the solution of the KBE in one of two ways:

- i we apply the generalized Kadanoff–Baym ansatz (GKBA) with HF propagators, as proposed in Ref. [72], to reduce the computational effort of solving the KBE (7) and (8) from a scaling $\sim T_{\text{tot}}^3$ with the total simulation duration to $\sim T_{\text{tot}}^2$, see Lipavský et al.^[73] for details,
- ii we consider the selfenergy to be local in space, $\Sigma_{ij\sigma}(t, t') = \delta_{ij} \Sigma_{i\sigma}(t, t')$, for which the KBE can be solved very efficiently using the auxiliary-Hamiltonian representation introduced in Hermanns et al.^[74]

Both strategies allow us to reach sufficiently long propagation times that are needed to treat electronic excitations during charged-particle stopping scenarios with sub-keV impact energies. To include an external moving charge (projectile) into the KBE simulations, we choose an NEGF–Ehrenfest approach which was first presented in Balzer et al.^[13] and applied in Balzer et al.^[14] and Bonitz et al.^[75] In the course of this, the trajectory $r(t)$ of the projectile is calculated on the fly by Ehrenfest dynamics using a classical potential that is derived from the Coulomb interaction between the projectile’s charge Ze and the time-dependent total charge density $\rho(R, t)$ of all constituents of the material.

As a prototype model for a correlated material, we consider single-band Hubbard nano clusters with a 2D honeycomb structure, the interparticle distance $a_0 = 1.42 \text{ \AA}$ and L sites that have spatial coordinates R_i . With a nearest-neighbour hopping J and an on-site Coulomb interaction U , the cluster Hamiltonian reads

$$H = -J \sum_{\langle i,j \rangle \sigma} c_{i\sigma}^\dagger c_{j\sigma} + U \sum_i \left(n_{i\uparrow} - \frac{1}{2} \right) \left(n_{i\downarrow} - \frac{1}{2} \right) + \sum_{i\sigma} W_i(t) c_{i\sigma}^\dagger c_{i\sigma} \quad (9)$$

where $n_{i\sigma} = c_{i\sigma}^\dagger c_{i\sigma}$ is the electron density, and $\langle i, j \rangle$ indicates summation over nearest neighbours. In our calculations, we chose the hopping parameter as $J = 2.8 \text{ eV}$, which results from a mapping of ab initio calculations to graphene-type systems in the tight-binding approximation.^[76,77] This choice provides a typical setting with a realistic synchronization of the projectile–lattice time scales. Furthermore, the last term of Equation (9) describes the Coulomb interaction of the lattice electrons with the projectile in terms of a time-dependent on-site energy

$$W_i(t) = -\frac{1}{4\pi\epsilon_0} \frac{Ze^2}{|r(t) - R_i|}. \quad (10)$$

Throughout, we consider the case of half filling and measure times in units of $t_0 = \hbar/J$. Inside the KBE, the many-body Hamiltonian (9) translates into a one-particle Hamiltonian

$$\bar{h}_{ij\sigma}(t) = -J\delta_{ij} + \left[U \left(\langle n_{i\sigma}(t) \rangle - \frac{1}{2} \right) + W_i(t) \right] \delta_{ij}. \quad (11)$$

Note that, for Hubbard systems, the Fock terms of the mean field are absent. In addition, we employ the second Born (2B) selfenergy of the form

$$\Sigma_{ij\sigma}^{2B}(t, t') = \hbar^2 U^2 [G_{ij\sigma}(t, t')]^2 G_{lj\sigma}(t', t) \quad (12)$$

where, in the special case of a “local” selfenergy (local 2B), the site-off-diagonal components are neglected, as mentioned above. The trajectory along which the projectile passes through the cluster is calculated from the potential

$$V(t) = \frac{Ze^2}{4\pi\epsilon_0} \sum_i \frac{\rho(R_i, t)}{|r(t) - R_i|} \quad (13)$$

where $\rho(R_i, t) = -\sum_\sigma \left(\langle n_{i\sigma}(t) \rangle - \frac{1}{2} \right)$ is the total charge density on the cluster, assuming a positive background that results from the atomic cores in a real material. As initial conditions we use $r(t_{-\infty}) = (x_0, y_0, -z_0)$, where z_0 is chosen such that the projectile penetrates the cluster at half the simulation time, and $dr/dt(t_{-\infty}) = (0, 0, v_0)$, performing calculations for a perpendicular incidence, with the honeycomb cluster located in the xy -plane.

A central observable which characterizes the stopping process is the energy loss of the projectile (P),

$$S = E_{\text{kin}}^P(t_{+\infty}) - E_{\text{kin}}^P(t_{-\infty}) \quad (14)$$

where $E_{\text{kin}}^P(t_{-\infty}) \equiv E_{\text{kin},0}^P = \frac{1}{2}mv_0^2$ and $E_{\text{kin}}^P(t_{+\infty})$ denote the initial and final kinetic energies, before and after passing through the cluster, respectively. Further important observables are the different energy contributions on the cluster, that is, the kinetic, potential, and interaction energy:

$$E_{\text{kin}}(t) = \Re \left[-J \sum_{ij} \delta_{(ij)} \rho_{ji}(t) \right], \quad E_{\text{pot}}(t) = \Re \left[\sum_i W_i(t) \rho_{ii}(t) \right] \quad \text{and} \quad (15)$$

$$E_{\text{int}}(t) = \frac{i\hbar}{2} \Im \left[\sum_{ij} \int_C ds \Sigma_{ij}(t, s) G_{ji}(s, t^+) \right] \quad (16)$$

where the latter is decomposed into mean field (Hartree–Fock) and correlation energy according to $E_{\text{HF}}(t) = \Re[\sum_i U \rho_{ii}(t)]$ and $E_{\text{corr}}(t) = E_{\text{int}}(t) - E_{\text{HF}}(t)$. Furthermore, we analysed the evolution of the local and cluster-averaged double occupation,

$$d_i(t) = \langle n_{i\uparrow}(t) n_{i\downarrow}(t) \rangle = -\frac{i\hbar}{U} \sum_k \int_C ds \Sigma_{ik}(t, s) G_{ki}(s, t^+), \quad d_{\text{avg}}(t) = \frac{1}{L} \sum_{i=1}^L d_i(t) \quad (17)$$

where spin indices are omitted.

3.2 | Time-resolved energy exchange between projectile and cluster

Below we present numerical results of the KBE coupled to the semiclassical projectile dynamics, as introduced in Balzer et al.^[13] We consider two honeycomb clusters that are described by the Hubbard model (9) containing $L = 24$ and $L = 54$ sites, respectively, see Figure 4 for a sketch of the former. We start by giving an overview of the general dynamical behavior of correlated 2D systems during the impact of a charged particle. For the 54-site cluster, the results are shown in Figure 2 for the case of a proton, penetrating the lattice at the centroid point C with $\mathbf{R}_C = \left(-\frac{1}{6}a_0, -\frac{\sqrt{3}}{3}a_0, 0 \right)$. We apply the NEGF approach including the GKBA, as introduced in Section 3.1, to study the coupled projectile–lattice dynamics. Thereto, we first generate the correlated ground state of the electrons on the lattice via an adiabatic-switching procedure, where the interaction U of the system is slowly ramped to its final value during the initial time-propagation interval (see Schlünzen and Bonitz^[67] for details). We consider the case of $U = 4J$ —a configuration that allows for the build-up of correlations. Once the interacting ground state is reached, the projectile dynamics starts by solving the coupled Equations (9) to (13). For a broad range of projectile energies, $10^{-1} \text{ keV/u} < E_{\text{kin},0}^P < 10^3 \text{ keV/u}$, we compute the dynamical evolution of relevant energies of both, the lattice electrons and the proton. The results are shown in Figure 2. For better comparability, all quantities are plotted as a function of the time-dependent projectile position $z^P(t)$. To further illustrate the dependence of the relevant observables on the ion impact energy we show slices for three different ion–surface distances, $z^P/a_0 = 0, 2.5, 5$, corresponding to the impact time ($z^P = 0$) and two slightly later times, in Figure 3.

Consider first the *kinetic energy of the projectile* that is shown in part (e) of Figures 2 and 3. The energy loss of the projectile to the cluster can be seen from a vertical cut through Figure 2e at large z^P . One clearly recognizes the familiar bell-shaped dependence on the impact energy with a single peak around 10 keV/u. On the other hand, looking at horizontal cuts provides the time dependence of the proton energy: before the impact (negative z^P) the proton gains energy because it is attracted by the electrons of the cluster, whereas after the impact the proton loses energy to the electrons (more than it had gained before), see

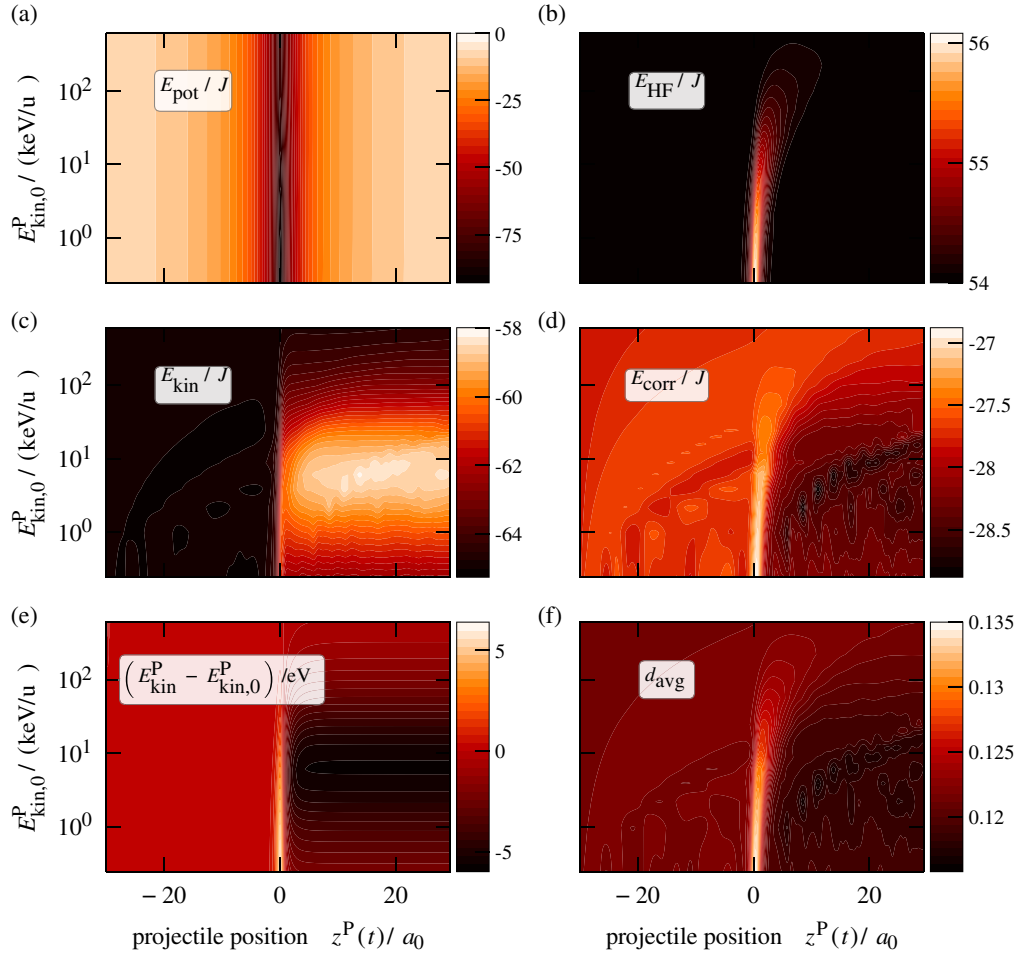


FIGURE 2 Evolution of relevant energies during the impact of a proton at point C (c.f., Figure 4) on a 54-site honeycomb cluster at correlation strength $U = 4 \text{ J}$ for different initial kinetic energies in the range $10^{-1} \text{ keV/u} < E^P_{\text{kin},0} < 10^3 \text{ keV/u}$, indicated on the y-axis. The x-axis contains the current height of the proton, $z^P(t)$, (impacting from the left) above the cluster plane. Since the projectile velocity is almost constant, the height is a measure of time. (a): potential energy, (b): Hartree-Fock energy, (c): kinetic energy, (d): correlation energy, and (f): average double occupation of the lattice electrons; (e): kinetic energy loss of the projectile. The colour scale is shown to the right of each figure. To ease the analysis of the data, three vertical cuts at $z^P = 0; 2.5; 5$ through each graph are shown in Figure 3

also Figure 3e. A general discussion of this behavior has been given in Balzer et al.^[13] Here we provide more details of the physics including a breakup of the energy gain of the electrons into different contributions: potential energy in the field of the projectile, kinetic energy, mean-field energy, and correlation energy.

The *potential energy of the cluster electrons* in the Coulomb field of the projectile, Equation (15), is shown in Figure 2a. While, in the absence of the projectile this energy is zero, during the impact the attraction of the electrons towards the projectile impact point gives rise to a large (negative) energy—electrons are confined in a potential well centred at the impact point. For each projectile energy, $E^P_{\text{kin},0}$, the potential energy is perfectly symmetric with respect to the impact point $z^P = 0$. This demonstrates that there is no drift of the ion in x - and y -direction during the penetration process. Next consider the *kinetic energy* of the electrons, Figure 2c, and compare it to the kinetic energy of the projectile, Figure 2e. For any vertical cut through the figures (constant $z^P > 0$) the two energies are essentially mirror images of each other. The maximum energy reduction of the projectile (maximal stopping) is observed slightly below $E^P_{\text{kin},0} = 10 \text{ keV/u}$, exactly where the electrons experience the highest kinetic-energy gain. This is even more clearly visible in blue and green curves in Figure 3c and e. Figure 2b shows the *Hartree-Fock part of the interaction energy* of the electrons. It is directly proportional to the electron density, compare Equation (16) and, thus, illustrates the density response to the projectile. Note the striking difference in the two limiting cases of low and high ion energy, respectively: for low $E^P_{\text{kin},0}$, the electron density adiabatically follows the external excitation, leading to a symmetric bell-shaped curve, similar to E_{pot} . In contrast, for high-energy ions, the interaction time is too short for the electronic system to respond, therefore the

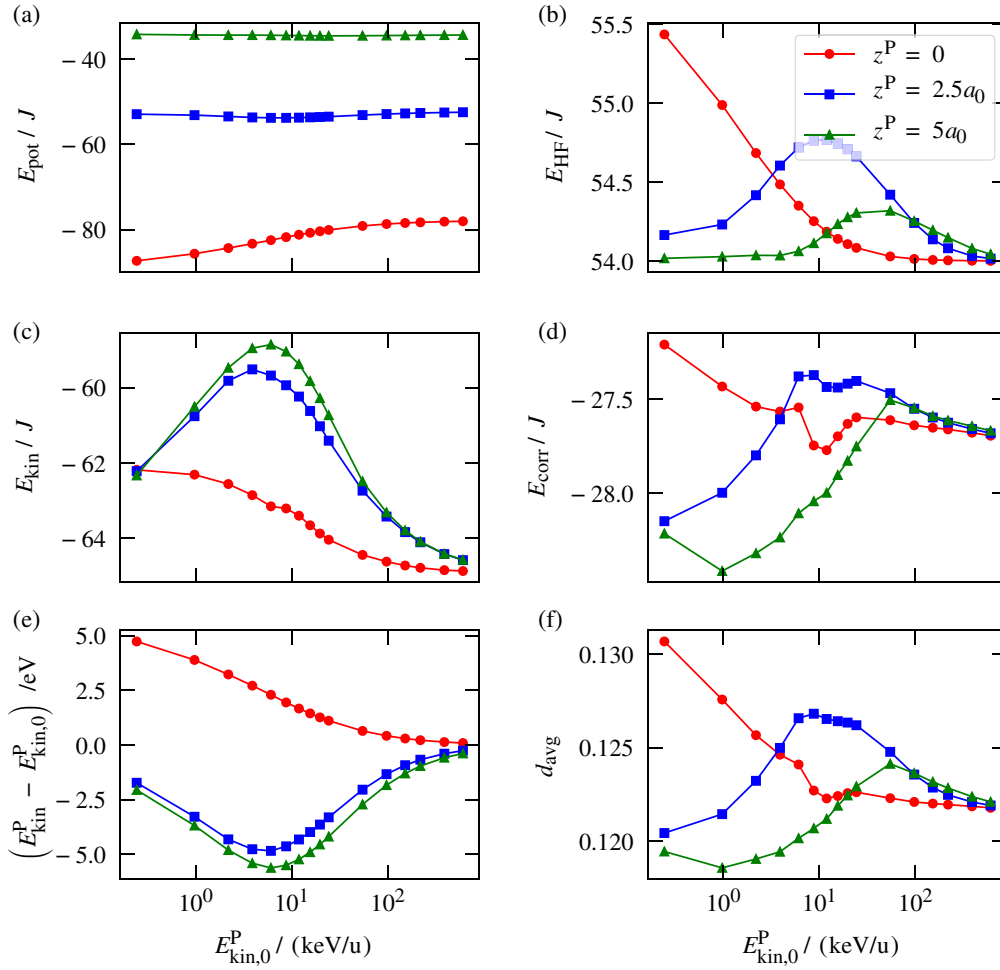


FIGURE 3 Same as Figure 2, but for three cuts at fixed values z^P of the proton coordinate (height above the plane): in the cluster plane ($z^P = 0$, red line) and two distances after the impact (blue and green), see inset of top right figure

density and, thus, E_{HF} do not change significantly—even during the particle impact. The physics inbetween these two limits is dominated by an increasingly delayed and broadened response of the electron density, due to the build up of electron–electron correlations. The same trends are seen also in Figure 3c: for example, the red curve demonstrates the reduction of the electronic density response with increasing projectile speed. Consider now the *correlation energy* of the electrons, E_{corr} , Equation (16), and the closely related average doublon number, d_{avg} , Equation (17), that are displayed in Figures 2(d) and (f), respectively. Both quantities show a very similar behavior that resembles that of the Hartree–Fock energy, E_{HF} , compare figure part (b). Thus, both quantities mainly following the evolution of the density, as well, which is also seen in Figure 3, compare parts (d, f) to part (b).

The time-dependent re-distribution of the energy gained by the electrons between kinetic, mean-field and correlation energy can be clearly seen in Figure 3(b-d), compare the red and green curves. When the projectile departs towards positive z^P , the kinetic energy always increases because the potential well that has trapped the electrons is removed. At the same time, Hartree–Fock and correlation energy decrease, for impact energies below 10 keV/u, compare Figure 3b and d. In contrast, for impact energies exceeding approximately 10 keV/u (25 keV/u) the Hartree–Fock (correlation) energy increase.

3.3 | Correlated-energy dissipation for impact energies below 1 keV

In this section, we perform additional simulations for an $L=24$ -site honeycomb cluster (c.f., visualization in Figure 4), where we focus, in particular, on correlation effects at small proton energies. To reach sufficiently long simulation times, in this case, we do not perform an adiabatic switching on of the interaction U but start from the Hartree ground state, for the inclusion of a correlated initial state, see Semkat et al.^[78,79]. In this case the proton impact should occur only after the initial transient

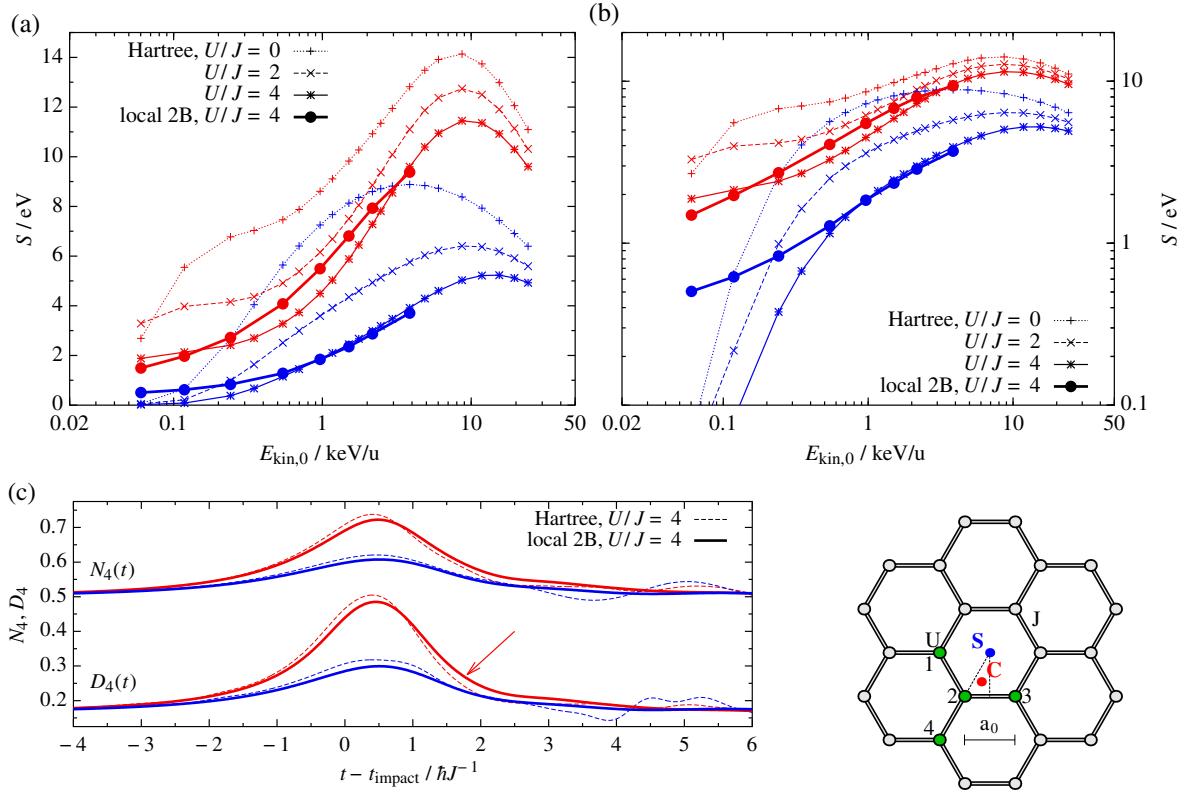


FIGURE 4 (a) and (b): Energy loss $S(E_{\text{kin},0}^{\text{P}})$ of a proton passing through a 24-site honeycomb cluster ($J = 2.8$ eV, $a_0 = 1.42$ Å.) at three correlation strengths $U/J = 0, 2, 4$, for two different impact points marked in the bottom right figure: C ($-a_0/6, -a_0/\sqrt{3}, 0$), red lines) and S (cluster center, blue lines). (b) The same data as (a) on a logarithmic scale to better resolve the low-energy behaviour. For $U/J = 4$, we include, in addition to the Hartree calculations, results obtained in the local second-order Born approximation (local 2B). Note that, at impact energies below 2 keV, electron–electron correlations tend to increase the energy loss compared to the mean-field result. (c): Time evolution of the density $N_4(t)$ and double occupation $D_4(t)$, as defined in the text (averages over the four green sites in the bottom right figure), for the impact energy $E_{\text{kin},0}^{\text{P}} = 1$ keV. The red arrow marks the ion-induced doublon excitation that is observed in the correlated simulations

dynamics which are caused by the sudden (nonadiabatic) switch on of the 2B selfenergy. These transient dynamics also change the initial Hartree double occupation $d_{\text{avg}}(t_{-\infty}) = \frac{1}{2L} \sum_{i\sigma} \langle n_{i\sigma}(t_{-\infty}) \rangle = 0.25$ to some smaller value (for details see Balzer et al.^[13]). Extending the work of Balzer et al.,^[13] we consider in the following two different initial positions of the proton: the points S (cluster center, blue) and C (centroid point, red) as sketched in Figure 4.

Figure 4a and b shows the energy loss in a broad range of proton energies between 0.05 and 25 keV/u for three different values of the interaction strength $U/J \leq 4$. For the point C (red curves), the peak position of the energy loss is located roughly around 10 keV/u, while, for the point S (blue curves), the maximum of the stopping power varies between 4 keV/u ($U=0$) and 15 keV/u ($U/J=4$). Generally, we observe that, in the investigated regime, an increase of the interaction strength U leads to a smaller energy loss for fixed impact parameters. Moreover, when the energy is decreased below 0.1 keV/u, the energy loss rapidly vanishes, in a mean-field description, due to a rather instantaneous change of the charge density on the cluster, which we attribute to the onset of the adiabatic-response regime.

In the next step, we examine the influence of electron–electron correlations on the energy loss. In the 2B approximation for a moderate interaction strength of $U/J = 4$, we find clear deviations from the Hartree results. Around $E_{\text{kin},0}^{\text{P}} = 1$ keV/u, the correlated result for the stopping power significantly exceeds the Hartree result, for the starting point C, while for the point S the correlated results remain close to the mean-field result. When the impact energy is further reduced the situation changes. For the impact point C correlated and uncorrelated simulations do not differ systematically. In contrast, for impact point S the correlated calculation leads to a significantly increased energy loss compared to the mean-field simulation. Moreover, at and below 0.2 keV/u, the energy loss seems to be dominated by correlation effects, as the mean-field results rapidly vanish, for point S. This low-energy behavior needs further investigation since here also effects beyond the second-Born approximation might become important.

Let us now return to the impact energy $E_{\text{kin},0}^{\text{P}} = 1 \text{ keV/u}$. We expect that the increased energy loss obtained in the local 2B calculations for the starting point C, is a consequence of enhanced doublon formation on the cluster, triggered by the interaction with the proton along the excitation protocol discussed in Balzer et al.^[14] This protocol connects single-electron and doublon states in a strongly correlated Hubbard model via nonadiabatic Landau–Zener transitions. As an indication that such excitations play a crucial role, we mention that, for the case C, the maximum value of the interaction energy with the proton at the nearest lattice site, $|W_{i=2}(t)|$, is about twice as large as the electron–electron interaction strength U , which was found to be the optimum condition for ion-induced doublon excitation in Balzer et al.^[14] In contrast, this energy is of the order of U , for the impact point S. For cases where the maximum value of the interaction with the proton is smaller, $|W| \lesssim U$, doublon production should be not as efficient as for on-site energies $W \gtrsim 2U$, compare Balzer et al.^[14] and Bonitz et al.^[75]

Additional support for these arguments is obtained from an analysis of the time evolution of the electron density and double occupation on the cluster. In Figure 4c, we show two quantities: $N_4(t) = \frac{1}{4} \sum_{\alpha=1}^4 \langle n_{\alpha\sigma}(t) \rangle$ and $D_4(t) = \frac{1}{4} \sum_{\alpha=1}^4 d_{\alpha}(t)$, that is, the density and doublon number averaged over the four sites that are nearest to the impact point C, compare the green sites labelled 1 to 4 in the cluster sketch of Figure 4. We observe that, after the impact, the relaxation of the density towards the equilibrium value $N_4 = \langle n_{i\sigma} \rangle = 0.5$ is slightly different for the cases C and S. In the former case, the density in 2B approximation remains larger than the Hartree result whereas, in the latter case the second-Born result is slightly lower, at least up to the time $t - t_{\text{impact}} \approx 2.5\hbar J^{-1}$. From the quantity D_4 we find that this difference in the evolution of the densities is associated with a larger doublon number after the impact, in a correlated simulation, for the case C, see the red arrow. Also, note, that we have computed D_4 in Hartree approximation with the full mean-field NEGF $G(t, t')$ according to Equation (17) instead of evaluating just the uncorrelated part $D_4^{\text{uncorr}} = \frac{1}{4} \sum_{\alpha=1}^4 \langle n_{\alpha\sigma}(t) \rangle^2$, that has the equilibrium limit $D_4(t \rightarrow \infty) = 0.25$.

Even though the effect of doublon excitation is not strong, in the present case, recent simulations have confirmed the importance of this effect, as will be discussed in Section 4.

4 | CONCLUSIONS AND OUTLOOK

In this article we presented new results of time-dependent quantum simulations for the dynamics of ions near a solid surface. Such processes are of prime importance for the interaction of plasmas with solids where many questions remain poorly understood. We focused on two important aspects of ion stopping in nanoscale solid systems exposed to low-energy projectiles: (a) the charge transfer from the surface to the projectile and (b) the modification of the projectile energy loss in case of a target material with strong electronic correlations. While the former problem was studied using time-dependent DFT simulations, the latter one was studied using NEGF simulations for small honeycomb Hubbard clusters. The results for the two problems are summarized below before we discuss future developments.

In our TDDFT simulations we have used an adiabatic GGA for the exchange–correlation potential and, thus, restricted ourselves to a resonant charge-transfer process. A proton incident on an Al(111) surface serves as a well-established model system, which has been studied intensely for a long time using model Hamiltonians.^[24,27–30] The strength of TDDFT-MD lies in the ab initio material-specific description of the time-dependent charge and energy transfer and the screening. Tunnelling rates differ from estimates from electronic ground-state theory. Limitations of the approach are due to the adiabatic approximation for exchange and correlation plus the semilocal approximation applied to the exchange–correlation energy functional of ground-state DFT, and improvements pose an open problem.

In our NEGF simulations we have concentrated on electronic correlation effects in the stopping of ions. We have confirmed that, at impact energies below 1 keV correlations tend to increase the energy transfer to the target, compared to an uncorrelated (Hartree) simulation. Among the possible mechanisms is the excitation of doublons in the target. In Bonitz et al.^[75] it was shown that, for a proper choice of impact energy, and for a more strongly coupled hexagon cluster ($U/J \geq 10$) of size $L = 12$ an ion impacting in the cluster center may excite a large doublon number that does not decay after the projectile has left. Moreover, it was shown in Balzer et al.^[14] and Bonitz et al.^[75] that, in the case of multiple ion impacts, the doublon number can be increased further.

Let us now discuss the combined treatment of the two effects. Even though charge transfer is most likely not relevant for the kinetic energy loss of the projectile, it may well affect the electronic processes in the target, including doublon excitations. Answering these questions, though, requires a combination of the two simulation methods. However, presently none of the two methods is capable of incorporating the missing effect. Present approximations to the exchange–correlation potential in TDDFT simulations do not describe strongly correlated systems and, thus, cannot treat doublon formation in the target. On the other hand, NEGF simulations of charge transfer have recently been attempted for simple model systems (1D Hubbard chains) in Bonitz et al.^[12,75]. However, these simulations did not include a realistic treatment of the impacting ion. Here, a combination with TDDFT could be the basis for major progress. A possible combination could be via a Newns–Anderson model for the projectile where TDDFT provides selfconsistent model parameters. A second promising combination of the two

methods consists in the derivation of improved exchange–correlation functionals for TDDFT that include finite-temperature effects^[80,81] and their benchmarking by NEGF simulations. This will be particularly important for the treatment of Auger-type processes in the interaction of an ion or atom with the surface which are straightforwardly described within NEGF already with second-order Born selfenergies, for example, Bonitz et al.^[12] and Covito et al.^[82] These combinations of TDDFT and NEGF are expected to be of high importance for the development of accurate simulations of low-temperature plasma–surface interaction. Moreover, such combinations should also be of high interest for other fields including surface physics and chemistry.

ACKNOWLEDGMENTS

Helpful discussions with A. Dávila are gratefully acknowledged. We further acknowledge computing time at the Rechenzentrum of Kiel University where the calculations have been carried out.

REFERENCES

- [1] I. Nagy, B. Apagyi, *Phys. Rev. A* **1998**, 58, R1653.
- [2] J. M. Pitarke, R. H. Ritchie, P. M. Echenique, *Phys. Rev. B* **1995**, 52, 13883.
- [3] T. Dornheim, S. Groth, J. Vorberger, M. Bonitz, *Phys. Rev. Lett.* **2018**, 121, 255001.
- [4] M. Quijada, A. G. Borisov, I. Nagy, R. Díez Muño, P. M. Echenique, *Phys. Rev. A* **2007**, 75, 042902.
- [5] A. Ojanperä, A. V. Krashennnikov, M. Puska, *Phys. Rev. B* **2014**, 89, 035120.
- [6] S. Zhao, W. Kang, J. Xue, X. Zhang, P. Zhang, *J. Phys. Condens. Matter* **2015**, 27, 025401.
- [7] F. James, M. D. Ziegler, J. P. B. Ziegler, *Nucl. Instrum. Methods Phys. Res. B* **2010**, 268(11), 1818 19th International Conference on Ion Beam Analysis.
- [8] M. Bonitz, D. Kremp, S. Kosse, D. C. Scott, W. D. Kraeft, presented at *Proceedings of the XXII. Int. Conf. on Phenomena in Ionized Gases*, Hoboken, NJ, **1995**.
- [9] M. Bonitz, D. Kremp, S. Kosse, D. C. Scott, W. D. Kraeft, *Physics of Strongly Coupled Plasmas*, World Scientific, Singapore, **1996**, p. 117.
- [10] A. B. Zylstra, J. A. Frenje, P. E. Grabowski, C. K. Li, G. W. Collins, P. Fitzsimmons, S. Glenzer, F. Graziani, S. B. Hansen, S. X. Hu, M. Gatu Johnson, P. Keiter, H. Reynolds, J. R. Rygg, F. H. Séguin, R. D. Petrasso, *Phys. Rev. Lett.* **2015**, 114, 215002.
- [11] D. Kremp, M. Schlanges, W. D. Kraeft, *Quantum Statistics of Nonideal Plasmas*, Springer, Berlin, Heidelberg, **2005**.
- [12] M. Bonitz, A. V. Filinov, J. W. Abraham, K. Balzer, H. Kaehlert, E. Pehlke, F. X. Bronold, M. Pamperin, M. Becker, D. Loffhagen, H. Fehske, *Front. Chem. Sci. Eng.* **2018** in press, arXiv:1809.02473.
- [13] K. Balzer, N. Schlünzen, M. Bonitz, *Phys. Rev. B* **2016**, 94, 245118.
- [14] K. Balzer, M. Rasmussen, N. Schlünzen, J. P. Joost, M. Bonitz, *Phys. Rev. Lett.* **2018** 121, 267602. DOI:10.1103/PhysRevLett.121.267602.
- [15] M. A. L. Marques, A. Castro, G. F. Bertsch, A. Rubio, *Comput. Phys. Commun.* **2003**, 151(1), 60.
- [16] A. Castro, H. Appel, M. Oliveira, C. A. Rozzi, X. Andrade, F. Lorenzen, M. A. L. Marques, E. K. U. Gross, A. Rubio, *Phys. Status Solidi B Basic Solid State Phys.* **2006**, 243(11), 2465.
- [17] X. Andrade, D. Strubbe, U. De Giovannini, A. H. Larsen, M. J. T. Oliveira, J. Alberdi-Rodriguez, A. Varas, I. Theophilou, N. Helbig, M. J. Verstraete, L. Stella, F. Nogueira, A./a. Aspuru-Guzik, A. Castro, M. A. Marques, A. Rubio, *Phys. Chem. Chem. Phys.* **2015**, 17, 31371.
- [18] D. Marx, J. Hutter, *Ab Initio Molecular Dynamics: Basic Theory and Advanced Methods*, Cambridge University Press, Cambridge, **2009**.
- [19] M. A. L. Marques, C. A. Ullrich, F. Nogueira, A. Rubio, K. Burke, E. K. U. Gross Eds., *Time-Dependent Density Functional Theory. Lecture Notes in Physics*, Vol. 706, Springer, Berlin, Heidelberg, **2006**.
- [20] M. A. L. Marques, N. T. Maitra, F. M. S. Nogueira, E. K. U. Gross, A. Rubio Eds., *Fundamentals of Time-Dependent Density Functional Theory. Lecture Notes in Physics*, Vol. 837, Springer, Berlin, Heidelberg, **2012**.
- [21] M. Lindenblatt, E. Pehlke, A. Duvenbeck, B. Rethfeld, A. Wucher, *Nucl. Instrum. Methods Phys. Res., Sect. B* **2006**, 246(2), 333.
- [22] R. Nagano, K. Yabana, T. Tazawa, Y. Abe, *Phys. Rev. A* **2000**, 62, 062721.
- [23] V. Kapoor, *Phys. Rev. A* **2016**, 93, 063408.
- [24] J. Merino, N. Lorente, M. Y. Gusev, F. Flores, M. Maazouz, L. Guillemot, V. A. Esaulov, *Phys. Rev. B* **1998**, 57, 1947.
- [25] R. Zimny, Z. L. Mišković, N. N. Nedeljković, L. D. Nedeljković, *Surf. Sci.* **1991**, 255(1), 135.
- [26] H. Jouin, F. A. Gutierrez, *Phys. Rev. A* **2011**, 84, 014901.
- [27] J. Merino, N. Lorente, P. Pou, F. Flores, *Phys. Rev. B* **1996**, 54, 10959.
- [28] J. Merino, N. Lorente, F. Flores, M. Y. Gusev, *Nucl. Instrum. Methods Phys. Res., Sect. B* **1997**, 125(1), 288.
- [29] M. C. Torralba, P. G. Bolcatto, E. C. Goldberg, *Phys. Rev. B* **2003**, 68, 075406.
- [30] C. David, P. N. Langreth, *Phys. Rev. B* **1991**, 43, 2541.
- [31] C. L. Moss, C. M. Isborn, X. Li, *Phys. Rev. A* **2009**, 80, 024503.
- [32] A. Castro, M. Isla, J. I. Martínez, J. A. Alonso, *Chem. Phys.* **2012**, 399, 130.
- [33] A. V. Krashennnikov, Y. Miyamoto, D. Tománek, *Phys. Rev. Lett.* **2007**, 99, 016104.
- [34] R. Seraide, M. A. Bernal, G. Brunetto, U. de Giovannini, A. Rubio, *J. Phys. Chem. B* **2017**, 121(30), 7276.
- [35] S. Bubin, B. Wang, S. Pantelides, K. Varga, *Phys. Rev. B* **2012**, 85, 235435.
- [36] Z. Wang, S.-S. Li, L.-W. Wang, *Phys. Rev. Lett.* **2015**, 114, 063004.
- [37] N. T. Maitra, *J. Phys. Condens. Matter* **2017**, 29(42), 423001.
- [38] S. Zhao, W. Kang, J. Xue, X. Zhang, P. Zhang, *Phys. Lett. A* **2015**, 379, 319.
- [39] J. P. Perdew, K. Burke, M. Ernzerhof, *Phys. Rev. Lett.* **1996**, 77, 3865.
- [40] W. Humphrey, A. Dalke, K. Schulten, *J. Mol. Graph.* **1996**, 14, 33.
- [41] N. Trouiller, J. L. Martins, *Phys. Rev. B* **1991**, 43, 1993.
- [42] M. Fuchs, M. Scheffler, *Comput. Phys. Commun.* **1999**, 119(1), 67.
- [43] M. Tafipolsky, R. Schmid, *J. Chem. Phys.* **2006**, 124(17), 174102.
- [44] M. Methfessel, A. T. Paxton, *Phys. Rev. B* **1989**, 40, 3616.
- [45] G. A. Franco, *Ph.D. Thesis*, Université Catholique de Louvain (Ottignies-Louvain-la-Neuve), **2013**.
- [46] A. Castro, M. A. L. Marques, A. Rubio, *J. Chem. Phys.* **2004**, 121(8), 3425.
- [47] T. Noritake, M. Aoki, S. Towata, Y. Seno, Y. Hirose, E. Nishibori, M. Takata, M. Sakata, *Appl. Phys. Lett.* **2002**, 81(11), 2008.
- [48] M. Fuchs, Y.-M. Niquet, X. Gonze, K. Burke, *J. Chem. Phys.* **2005**, 122(9), 094116.

- [49] O. Gunnarsson, B. I. Lundqvist, *Phys. Rev. B* **1976**, 13, 4274.
- [50] M. Lindenblatt, E. Pehlke, *Phys. Rev. Lett.* **2006**, 97, 216101.
- [51] M. S. Miziański, D. M. Bird, M. Persson, S. Holloway, *J. Chem. Phys.* **2005**, 122, 084710.
- [52] M. A. Cazalilla, N. Lorente, R. Díez Muiño, J.-P. Gauyacq, D. Teillet-Billy, P. M. Echenique, *Phys. Rev. B* **1998**, 58, 13991.
- [53] E. C. Diego Valdés, J. M. Goldberg, R. C. M. Blanco, *Phys. Rev. B* **2005**, 71, 245417.
- [54] N. P. Wang, E. A. García, R. Monreal, F. Flores, E. C. Goldberg, H. H. Brongersma, P. Bauer, *Phys. Rev. A* **2001**, 64, 012901.
- [55] M. Pamperin, F. X. Bronold, H. Fehske, *Plasma Sources Sci. Technol.* **2018**, 27(8), 084003.
- [56] M. Lindenblatt, J. van Heys, E. Pehlke, *Surf. Sci.* **2006**, 600(18), 3624.
- [57] H. Winter, *J. Phys. Condens. Matter* **1996**, 8(49), 10149.
- [58] E. V. Chulkov, V. M. Silkin, P. M. Echenique, *Surf. Sci.* **1999**, 437(3), 330.
- [59] A. A. Correa, J. Kohanoff, E. Artacho, D. Sánchez-Portal, A. Caro, *Phys. Rev. Lett.* **2012**, 108, 213201.
- [60] A. Schleife, Y. Kanai, A. A. Correa, *Phys. Rev. B* **2015**, 91, 014306.
- [61] I. Campillo, J. M. Pitarke, A. G. Eguiluz, *Phys. Rev. B* **1998**, 58, 10307.
- [62] A. Atef Shukri, F. Bruneval, L. Reining, *Phys. Rev. B* **2016**, 93, 035128.
- [63] M. J. Berger, J. S. Coursey, M. A. Zucker, J. Chang, *Stopping-Power and Range Tables for Electrons, Protons, and Helium Ions*, Physical Measurement Laboratory, Gaithersburg, **1999**. <https://dx.doi.org/10.18434/T4NC7P>.
- [64] G. Stefanucci, R. van Leeuwen, *Nonequilibrium Many-Body Theory of Quantum Systems*, Cambridge University Press, Cambridge, UK **2013**.
- [65] L. P. Kadanoff, G. Baym, *Quantum Statistical Mechanics*, Benjamin, New York, NY **1962**.
- [66] K. Balzer, M. Bonitz, *Nonequilibrium Green's Functions Approach to Inhomogeneous Systems*, Springer, Berlin, Germany **2013**.
- [67] N. Schlünzen, M. Bonitz, *Contrib. Plasma Phys.* **2016**, 56(1), 5.
- [68] L. V. Keldysh, *J. Exp. Theor. Phys.* **1965**, 20, 1018 (*Zh. Eksp. Teor. Fiz.* **1964**, 47, 1515).
- [69] M. Bonitz, A. P. Jauho, M. Sadovskii, S. Tikhodeev, *Phys. Status Solidi B Basic Solid State Phys.* **2018** in press, arXiv:1901.01065.
- [70] N. Schlünzen, S. Hermanns, M. Bonitz, C. Verdozzi, *Phys. Rev. B* **2016**, 93, 035107.
- [71] N. Schlünzen, J.-P. Joost, F. Heidrich-Meisner, M. Bonitz, *Phys. Rev. B* **2017**, 95, 165139.
- [72] P. Lipavský, V. Špička, B. Velický, *Phys. Rev. B* **1986**, 34, 6933.
- [73] S. Hermanns, K. Balzer, M. Bonitz, *Phys. Scr.* **2012**, 2012(T151), 014036.
- [74] K. Balzer, M. Eckstein, *Phys. Rev. B* **2014**, 89, 035148.
- [75] M. Bonitz, K. Balzer, N. Schlünzen, M. Rasmussen, J.-P. Joost, *Phys. Status Solidi B Basic Solid State Phys.* **2018**, 1800490. <https://doi.org/10.1002/pssb.201800490>.
- [76] S. Reich, J. Maultzsch, C. Thomsen, P. Ordejón, *Phys. Rev. B* **2002**, 66, 035412.
- [77] J.-P. Joost, N. Schlünzen, M. Bonitz, *Phys. Status Solidi B Basic Solid State Phys.* **2019**, 1800498, <https://doi.org/10.1002/pssb.201800498>.
- [78] D. Semkat, D. Kremp, M. Bonitz, *Phys. Rev. E* **1999**, 59, 1557.
- [79] D. Semkat, D. Kremp, M. Bonitz, *J. Math. Phys.* **2000**, 41(11), 7458.
- [80] T. Dornheim, S. Groth, T. Sjostrom, F. D. Malone, W. M. C. Foulkes, M. Bonitz, *Phys. Rev. Lett.* **2016**, 117, 156403.
- [81] T. Dornheim, S. Groth, M. Bonitz, *Phys. Rep.* **2018**, 744, 1.
- [82] F. Covito, E. Peretto, A. Rubio, G. Stefanucci, *Phys. Rev. A* **2018**, 97, 061401.

How to cite this article: Schlünzen N, Balzer K, Bonitz M, Deuchler L, Pehlke E. Time-dependent simulation of ion stopping: Charge transfer and electronic excitations. *Contributions to Plasma Physics* 2019;59:e201800184. <https://doi.org/10.1002/ctpp.201800184>

CHAPTER 5

H⁺-AL(111): ENERGY TRANSFER DURING NEUTRALIZATION

Publication

"Energy transfer during resonant neutralization of hyperthermal protons at an aluminum surface studied with time-dependent density functional theory"

L. Deuchler, E. Pehlke

Physical Review B **102**, 235421 (2020)

Introduction In his review, comparing the scattering of neutral projectiles and ionic projectiles which are or are not neutralized, Winter^[105] traces back energy and angle shifts observed in the spectra of the projectile after scattering at the metal surface to an image charge effect. As he points out, this effect should provide a means to experimentally estimate the neutralization distance of the H⁺ projectile by observation of the kinetic energy transfer. The acceleration and deceleration of the projectile by the attractive force from its image charge – as long as it is not neutralized – affects the kinetic energy and angle distribution of the scattered (neutralized) particle.

Here we adapted the ideas by Winter and simulated hyperthermal H⁺ and H⁰ scattering with perpendicular incidence on an Al(111)-surface represented by a cluster from *ab initio*. Following the investigation of charge transfer from the previous chapter 4, we here focus on the energy dynamics throughout the process.

Main Findings We investigated the energy dynamics of for protons at an initial distance of 16 bohr in front of the Al-clusters with kinetic energies of $E_{\text{kin}}^{\text{init}} = 2 \text{ eV}$, 10 eV, and 50 eV.

Upon impact, the image charge within the cluster does not build up instantaneously. To estimate the energy dissipation of this process for the studied range of kinetic energies, simulations were employed where the proton was substituted by an antiproton. Even up to $E_{\text{kin}}^{\text{init}} = 1 \text{ keV}$ the energy dissipation stays small, i.e. 80 meV at $z = 5 \text{ bohr}$ and 150 meV at $z = 4 \text{ bohr}$.

The energy transfer between the projectile and the Al upon charge transfer was investigated by comparing the electronic energy of the time-dependent simulation from the value obtained in a ground-state calculation. For impact upon the on-top site, this excitation energy amounts to $E_{\text{exc}} = 8.6 \text{ eV}/9.4 \text{ eV}/11.3 \text{ eV}$ for $E_{\text{kin}}^{\text{init}} = 2 \text{ eV}/10 \text{ eV}/50 \text{ eV}$ respectively, at

$z = 5$ bohr on the outgoing trajectory. In case of the impact on the fcc-hollow site, the electronic friction effects from propagation within the bulk were subtracted by comparing to a time-dependent simulation with an H^0 projectile. The difference $\Delta\tilde{E}_{\text{exc}}$ at $z_{\text{exit}} = 5$ bohr between the on-top and the fcc-hollow impact sites for $E_{\text{kin}}^{\text{init}} = 2$ eV, 10 eV, and 50 eV amounts to $\Delta\tilde{E}_{\text{exc}} = 0.55$ eV, 0.61 eV, and 0.45 eV (higher value for impact on-top).

In order to exclude artifacts in the simulation due to the charging of the Al cluster during H^+ neutralization a simulation with a proton incident on an initially negatively charged Al_{188}^- -cluster was performed. It was found that for distances between projectile and surface below 8 bohr, differences in ΔE_{kin} are below 0.1 eV. It was therefore deduced that results obtained from a cluster simulation could also be used to describe the interaction between H^+ and the infinitely extended Al(111) surface.

As a next step, the obtained data was used to extrapolate to the extended Al(111) surface. It was found that, in order to obtain identical exit velocities in case of projectiles with $E_{\text{kin}} \approx 50$ eV, H^+ needs to be initially faster than H^0 by about 1.2 eV (on-top trajectory) to 0.4 eV (fcc-hollow trajectory). In contrast, for projectiles with $E_{\text{kin}} \approx 2$ eV the sign changes and H^+ needs to be initially slower than H^0 by about 0.8 eV (on-top trajectory) to 1.0 eV (fcc-hollow trajectory). This is explained by the difference between the ground-state potential energy surface and the H^+ -Al(111) interaction potential which is repulsive in the region of neutralization. This kinetic energy difference should be measurable in an experiment.

Furthermore, the energy transfer into phononic degrees of freedom was estimated by comparing simulations where the Al-atoms were kept at fixed positions to simulations where the Al-atoms were allowed to move. The difference in kinetic energy ΔE_{kin} after scattering for a head-on collision between an H^+ projectile and an Al atom at the on-top site are $\Delta E_{\text{kin}} = -0.28/-1.21/-6.51$ eV for $E_{\text{kin}}^{\text{init}} = 2/10/50$ eV, respectively. The kinetic energy transfer into the phononic degrees of freedom during the central collision is small compared to the initial kinetic energy due to the significant mass difference between H and Al.

Outlook Based on the results presented in the previous chapter 3 and chapter 4, this publication gives a comprehensive insight into the energy transfer during resonant neutralization of hyperthermal protons at an Aluminum surface. The H^+ -Al system is very attractive for an analysis due to its model-like character: the metal has a rather simple electronic structure and the projectile is one of the simplest one can think of (limitations are discussed by e.g. Merino et al. in Ref. [46]). This makes it an ideal starting point for any analysis. However, in the broader context discussed in chapter 1 questions about transferability of the results to further systems arise directly. Therefore, in chapter 6, the effect of the metallic band-structure to the neutralization is investigated.

In chapter 7, a broader view on the physical results and the simulation is given.

Energy transfer during resonant neutralization of hyperthermal protons at an aluminum surface studied with time-dependent density functional theory

Lukas Deuchler^{*} and Eckhard Pehlke[†]*Institut für Theoretische Physik und Astrophysik, Christian-Albrechts-Universität zu Kiel, D-24098 Kiel, Germany*

(Received 20 August 2020; accepted 1 December 2020; published 17 December 2020)

We present time-dependent density functional molecular dynamics (TDDFT-MD) simulations with an adiabatic approximation to the exchange-correlation potential for hyperthermal protons (H^+) with initial kinetic energies in the range of 2–50 eV impinging on the fcc-hollow site and the on-top site of an Al(111) surface. The surface is modeled by a finite-size cluster and the results are generalized to H^+ -Al surface scattering. From the simulation, neutralization distances are determined and the time development of the kinetic energy and the electronic excitation energy are derived. The results can be rationalized on the basis of the ground-state potential energy surface and the H^+ -Al(111) interaction potential. Furthermore, the difference in initial kinetic energy between H^+ and H^0 projectiles required to yield identical exit velocities is derived. Notably, this difference changes sign within the studied range of kinetic energies. This is traced back to the neutralization distances and the difference between both the ground-state potential energy surface and the H^+ -Al(111) interaction potential at those distances.

DOI: [10.1103/PhysRevB.102.235421](https://doi.org/10.1103/PhysRevB.102.235421)

I. INTRODUCTION

Modeling the interaction of plasmas with solid surfaces is a challenging problem within low-temperature plasma science and technology [1,2]. Ions are accelerated by the plasma sheath potential and can be scattered, and neutralized, at the surface. The question of charge transfer dynamics in ion scattering has often been approached from the theoretical side by using a Brako-Newns-Anderson type Hamiltonian [3–5] or an LCAO Hamiltonian [6]. There also exist approaches based on a Newns-Anderson Hamiltonian that describe correlation with the help of Green's function techniques [7–9]. In this paper we will discuss results from time-dependent density functional theory (TDDFT) simulations [10–12] for the charge and the energy transfer during the collision of a hyperthermal ion (i.e., an ion with an initial kinetic energy in the sub-eV up to few 10-eV range) with a metal surface. In these simulations, the entire information about the electronic structure of the projectile and the substrate is taken into account. As an example already intensely investigated experimentally [13–21] and theoretically [6,22–34] by various groups, we consider a proton (H^+ ion) incident on an Al(111) surface. The main focus of our study will be on the energy transfer from the incident ion into the electronic degrees of freedom of the substrate.

In his review, comparing the scattering of neutral projectiles and ionic projectiles which are or are not neutralized, Winter [15] traces back energy and angle shifts observed in the spectra of the projectile after scattering at the metal surface

to an image charge effect. As he points out, this effect should provide a means to experimentally estimate the neutralization distance of the H^+ projectile by observation of the kinetic energy transfer: The acceleration and deceleration of the projectile by the attractive force from its image charge—as long as it is not neutralized—affects the kinetic energy and angle distribution of the scattered (neutralized) particle. However, Winter also explicates that for H^+ scattered at an Al(111) target the experimental data suggest a peak of the distribution function of charge transfer at around 6 bohr in front of the image plane, while the value expected from theory was around 3 bohr [15,35]. It has been argued that Auger neutralization should dominate over the resonant charge transfer process in order to understand the experiment [16]. Merino *et al.* [25], however, have come to the conclusion that at low proton kinetic energies (less than 4 keV) the charge transfer between the Al orbitals and the hydrogen 1s orbital is a resonant one. Moreover, in Ref. [6] Merino *et al.* construct a “diabatic” state and present an interaction energy of the proton (H^+) in front of an Al(100) surface, which deviates from the $1/[4(z - z_{\text{image}})]$ image behavior when the proton gets close to the surface. In this paper we present TDDFT molecular dynamics (MD) simulations for the resonant charge transfer of hyperthermal protons incident on an Al(111) surface. As we deal with small kinetic energy of the projectile we do not consider further effects like core electron promotion [36]. We demonstrate a method to derive an approximation to the H^+ -Al(111) interaction potential directly from the simulation by means of an extra TDDFT-MD run for a fast (1 keV) proton. This yields the “generalization” of the image potential to small (<7 bohr) projectile–surface separations, where the interaction indeed becomes repulsive. This affects the energy transfer between the projectile and the metal.

^{*}deuchler@theo-physik.uni-kiel.de[†]pehlke@theo-physik.uni-kiel.de

II. COMPUTATIONAL METHODS

The simulations (i.e., both the TDDFT-MD simulations and the DFT-based relaxations) have been carried through with the program OCTOPUS (version 6) [12,37,38]. The generalized gradient approximation PBE-GGA [39] has been used for the exchange-correlation energy functional (from ground-state DFT). The H^+ ion is incident normally to an Al(111) surface at a fcc-hollow or a top site. The surface is modeled using Al clusters with 172 or 188 atoms for H^+ incident at the fcc-hollow or top site, respectively. The clusters have been created starting from a relaxed Al(111) surface (with a theoretical Al lattice constant 7.648 bohr) and cutting out a half sphere. Subsequently, the uppermost layer of Al atoms has been kept fixed and the cluster has been relaxed ionically until the forces are below 10^{-3} Hartree/bohr. H and Al are described by ionic semilocal norm-conserving Troullier-Martins pseudopotentials [40] created and analyzed using the FHI98PP software [41]. The Al pseudopotential has been created with 10 electrons as frozen-in core states and cutoff radii $r_s^{\text{Al}} = 1.791$ bohr, $r_p^{\text{Al}} = 1.974$ bohr, $r_d^{\text{Al}} = 2.124$ bohr. The p potential has been chosen as the local potential. For the H pseudopotential we have used cutoff radii $r_s^{\text{H}} = r_p^{\text{H}} = 1.276$ bohr, and the s potential has been chosen as the local potential.

In the time-dependent simulations, the adiabatic approximation is applied to the exchange-correlation (XC) potential v_{XC} , together with the above mentioned PBE-GGA [39] for the XC functional from ground-state DFT. The wave functions are confined to a user-defined box with distance between the box edge and atoms of at least 12 bohr, which fits into a cube with 60-bohr edge length. The FFT for solving the Poisson equation requires a box with twice the edge length of this cube. A Coulomb kernel with a spherical cutoff as provided within OCTOPUS has been used [42]. The Kohn-Sham wave functions are sampled on a real-space mesh with mesh spacing $\Delta x = 0.5$ bohr. The filtering method of Tafipolsky and Schmid [43] is applied to the pseudopotentials in order to avoid Fourier components above the cutoff determined by the mesh spacing. Prior to the time-dependent simulation, the electronic ground state of the Al cluster was determined. Formally, a Methfessel-Paxton smearing [44] has been applied, with the smearing parameter finally reduced to the very small value of 20 meV.

The time-dependent Kohn-Sham wave functions are propagated using a time step of 0.02 atu (0.5 attoseconds). For simplicity, the ionic time step has been chosen identical to the electronic time step. After the ground state of the Al cluster has been determined, a bare H pseudopotential has been added to the simulation box at a distance of 16 bohr above the first layer of Al-surface atoms. The total charge of the system is +1 (i.e., equals the proton charge). In order to minimize the number of ground-state calculations for the subsequent determination of electronic excitation energies, all Al atomic coordinates are kept frozen during the time-dependent simulations. The only exceptions are three simulations entering Table II, which, beside electronically nonadiabatic effects, include the kinetic energy transfer into the substrate ionic degrees of freedom (13 Al atoms were allowed to move). In those simulations, the position of the ions follows from

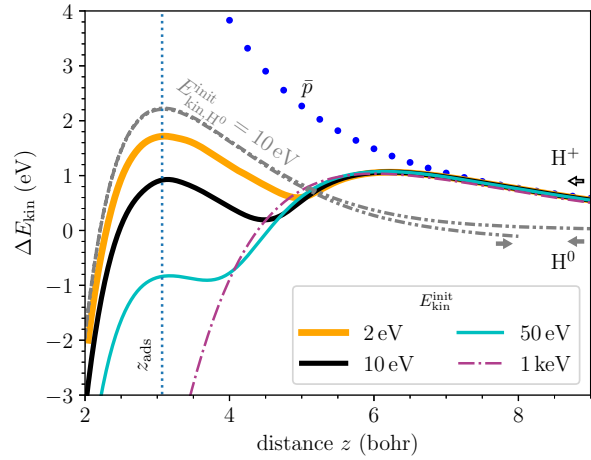


FIG. 1. Variation of kinetic energy for protons (H^+ , solid and dash-dotted curves) and a spin-unpolarized hydrogen atom (H^0 , dash-dot-dotted curve) impinging on the Al(111) on-top site of an Al_{188} cluster. For comparison, the change of ground-state potential energy for an antiproton is shown (\bar{p} , dots). The initial kinetic energy of the projectile at $z_{\text{init}} = 16$ bohr is noted in the legend.

Ehrenfest dynamics [12,45], i.e., the ions move along a unique trajectory.

For convergence analysis, time-dependent calculations for the $E_{\text{kin}}^{\text{init}} = 10$ eV on-top trajectory have been performed with a larger Al-cluster size of 302 atoms. As a result, the values for charges $q(z)$ as defined in Eq. (4) vary less than $0.03e$. Decreasing either the mesh spacing Δx from 0.5 to 0.4 bohr, or the time step Δt from 0.02 to 0.01 atu resulted in a variation of q that is one order of magnitude less. Regarding the kinetic energy convergence with Δx and Δt , maximum differences of 10 meV were obtained during scattering, in both cases.

Regarding the accuracy of the dissipated energy, we compared the kinetic energy loss of an H^0 atom impinging on the Al(111) fcc-hollow site of an Al_{52} and an Al_{172} cluster with $E_{\text{kin}}^{\text{init}} = 10$ eV. The difference due to the two cluster sizes amounts to 200 meV with respect to the propagation inside the bulk from $z^{\text{in}} = 8$ bohr to $z^{\text{out}} = 8$ bohr with reflection at the third layer. For comparison, in this case a total energy of 3.0 eV is dissipated due to electronic friction effects.

III. RESULTS

A. Proton impinging on Al(111) on-top site

We have carried through TDDFT-MD simulations for H^+ ions starting at $z_{\text{init}} = 16$ bohr in front of the Al cluster with initial kinetic energy $E_{\text{kin}}^{\text{init}}$ of 2, 10, and 50 eV. The proton is incident normally to the Al(111) surface at the on-top position. The change of kinetic energy of the projectile,

$$\Delta E_{\text{kin}} = E_{\text{kin}}(z(t)) - E_{\text{kin}}^{\text{init}}, \quad (1)$$

is shown in Fig. 1 as a function of distance z of the H^+ from the topmost Al layer. We find that—as long as the electron transfer from the cluster to the H^+ has not yet occurred—all curves almost lie on top of each other, independent of the initial kinetic energy. This is interpreted in terms of conservation

of total energy $E_{\text{kin}}(z) + E_{\text{tot}}^{(+)}(z)$. Here $E_{\text{tot}}^{(+)}(z)$ denotes the (non-ground-state) potential energy of a positive elementary charge in front of the electrically polarized cluster, provided that there is no charge transfer (i.e., describing the interaction of the positive charge with its induced image dipole). In order to obtain an estimate for this H^+ -Al(111) interaction potential $E_{\text{tot}}^{(+)}(z)$ in Fig. 1 we present the change of kinetic energy ΔE_{kin} of a fast H^+ projectile with initial kinetic energy equal to 1 keV. From the projection of the time-dependent Kohn-Sham orbitals onto the H1s orbital (details will be given below) we conclude that the charge transfer to the 1-keV projectile is negligible (less than $0.05 |e|$) as long as $z > 4.5$ bohr.

B. H^+ -Al(111) interaction potential

Our simple interpretation of the motion of the H^+ in terms of a potential energy surface $E_{\text{tot}}^{(+)}(z)$ neglects energy dissipation due to dynamical screening [46,47] of the Coulomb potential of the positively charged projectile incident on the metal surface. In order to obtain a rough estimate for the electronically nonadiabatic effects due to the electron-hole pair excitations in the Al cluster induced by coupling to the time-dependent Coulomb potential of the projectile we have carried through TDDFT-MD simulations for antiprotons with initial kinetic energy 50 eV, 1 keV, and 10 keV. The initial configuration has been prepared by adding the antiproton to a simulation box containing an uncharged, electronically relaxed Al cluster. We note that therewith the polarization of the Al cluster by the antiproton has been neglected in the initial state deliberately (in order to stay in line with the H^+ simulations). The contribution of the antiproton at $\mathbf{r}_{\bar{p}}$ to the electron potential energy is described by a soft Coulomb potential,

$$v_{\bar{p}}(\mathbf{r}) = \frac{1}{\sqrt{(0.2 \text{ bohr})^2 + |\mathbf{r} - \mathbf{r}_{\bar{p}}|^2}}. \quad (2)$$

Results are summarized in Fig. 2 and compared to the variation ΔE_{kin} obtained from energy conservation and the Born-Oppenheimer surface of the antiproton in front of the metal cluster. Even up to $E_{\text{kin}}^{\text{init}} = 1$ keV the energy dissipation stays small on the energy scale shown, i.e., 80 meV at $z = 5$ bohr and 150 meV at $z = 4$ bohr. For a comparison of results for H^+ approaching a jellium surface we refer the reader to Ref. [48]. In case of the faster antiproton with initial kinetic energy of 10 keV, the electronically nonadiabatic effects become distinctly larger, as can be read from Fig. 2. Hence such a simulation would not be useful any more for our purpose of approximating a quasiadiabatic potential energy surface—while the 1-keV result appears to be useful in the sense that electronically nonadiabatic effects stay sufficiently small. For this reason we still use 1-keV trajectories for comparison in case of H^+ incident on the Al surface.

In Fig. 1 ΔE_{kin} derived from the Born-Oppenheimer surface of the antiproton is compared to ΔE_{kin} for H^+ incident on the (111) surface of an Al cluster with initial kinetic energy of 1 keV. At large distance, $z > 7$ bohr, the two curves for ΔE_{kin} nearly coincide. At smaller H^+ -cluster separation the (approximate) potential energy of the positively charged H^+ and the negatively charged \bar{p} projectiles start to deviate strongly from each other. This cannot be ascribed to an elec-

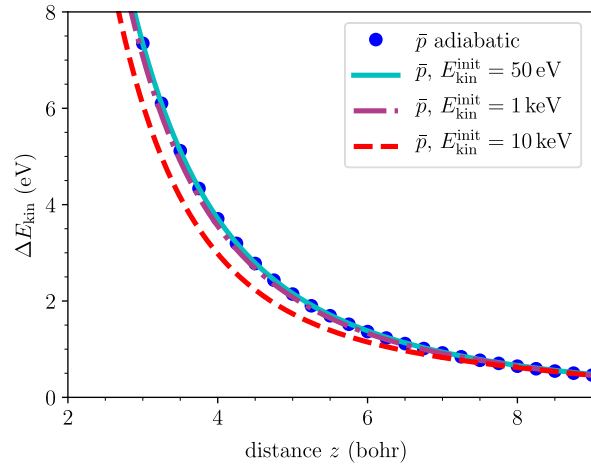


FIG. 2. Variation of the kinetic energy of an antiproton (\bar{p}) incident normally on the Al(111) surface of the Al_{188} cluster at the Al on-top site for initial kinetic energy at $z_{\text{init}} = 16$ bohr of 50 eV, 1 keV, and 10 keV. Initially, the antiproton has been positioned in front of the not electrically polarized Al cluster. Data are compared to $\Delta E_{\text{kin}}(z)$ derived from energy conservation and the Born-Oppenheimer surface of an antiproton in front of the Al cluster.

tronically nonadiabatic effect, as the energy dissipation for the antiproton has been shown to be small and the respective difference persists also for small kinetic energy of the H^+ . Obviously, the electric polarization of the Al cluster can no longer be described within linear response. The H^+ projectile is decelerated which we attribute to the Coulomb repulsion between the H^+ and the Al ion cores. This means that even before neutralization the dynamics of the H^+ does not follow the simple $1/[4(z - z_{\text{image}})]$ image potential, but that $E_{\text{tot}}^{(+)}(z)$ becomes repulsive at short distance to the Al metal surface. We emphasize that there is an analogous result already known in the literature: Merino *et al.* [25] have constructed a “diabatic” state and obtained an interaction energy of H^+ in front of an Al(100) surface that deviates from the image potential in a similar way.

C. Comparison of trajectories between initially neutral and charged cluster

In order to exclude artifacts in the simulation due to the charging of the Al cluster during H^+ neutralization we have performed a simulation with a proton incident on an initially negatively charged Al_{188}^- cluster. The comparison to a simulation for H^+ incident on the initially neutral Al_{188}^0 cluster is shown in Fig. 3. Due to the stronger Coulomb attraction between H^+ and Al_{188}^- , the projectile is accelerated more strongly while approaching the surface. We have accounted for this extra acceleration by choosing a smaller initial kinetic energy of 9.7 eV of the proton in case of H^+ incident on Al_{188}^- . This is consistent with the difference in potential energy of an antiproton in front of an Al_{188}^0 cluster or an Al_{188}^- cluster at distances $z = 8$ bohr and $z = 16$ bohr. As can be read from Fig. 3, the kinetic energy as a function of the z coordinate in case of both trajectories of the H^+ - Al_{188} cluster basically

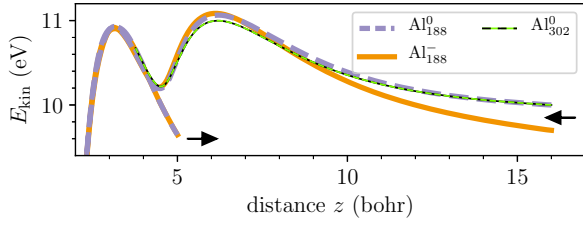


FIG. 3. Kinetic energy of a proton with $E_{\text{kin}}^{\text{init}} = 10$ eV at $z_{\text{init}} = 16$ bohr (dashed lines) and $E_{\text{kin}}^{\text{init}} = 9.7$ eV (solid line) impinging at the top site of a neutral Al_{188}^0 (thick dashed line), a neutral Al_{302}^0 (thin dashed line), or a negatively charged Al_{188}^- cluster (thick solid line).

coincides for separations less than about 8 bohr. The similarity of the variation of E_{kin} vs z for $z < 8$ bohr in case of the Al_{188} simulations shown in Fig. 3 suggests that at a separation of the H^+ projectile from the infinitely extended Al(111) surface less than about 8 bohr the projectile-surface interaction can be approximated by the TDDFT-MD cluster simulation. We argue that the difference between the screening charges for the charged and uncharged cluster will be more extreme than the difference between the screening charges induced in the uncharged cluster and the infinitely extended surface. To investigate this in more detail, a simulation with a neutral cluster containing 302 Al atoms is also shown in Fig. 3. For H-Al distances < 8 bohr,

$$\begin{aligned} & |(E_{\text{kin}}^{\text{Al}_{302}}(z) - E_{\text{kin}}^{\text{Al}_{302}}(z = 8 \text{ bohr})) \\ & - (E_{\text{kin}}^{\text{Al}_{188}}(z) - E_{\text{kin}}^{\text{Al}_{188}}(z = 8 \text{ bohr}))| < 0.1 \text{ eV}. \end{aligned} \quad (3)$$

In the following we shall use the results of the Al-cluster simulations for H-Al distances < 8 bohr to describe interaction between H^+ and the infinitely extended Al(111) surface.

D. Electronic energy transfer in the neutralization region for impact at on-top and fcc-hollow site

When the H^+ projectile approaches the surface, charge is transferred from the Al cluster to the projectile at some separation which depends on $E_{\text{kin}}^{\text{init}}$. The electronic charge q at the projectile has been derived by a projection of the time-dependent Kohn-Sham wave functions $\psi_j(t)$ onto the hydrogen 1s orbital $\phi^{\text{H}1s}$, i.e.:

$$q(t) = \sum_j^{\text{occ}} |\langle \psi_j(t) | \phi^{\text{H}1s}(z(t)) \rangle|^2. \quad (4)$$

Spin degeneracy is accounted for by twofold occurrence of wave functions in the summation. The charge calculated in this way is quantitatively consistent with a Bader charge analysis [49] of the electron density. Figure 4 shows the charge transfer rate dq/dz from the surface towards the projectile impinging on the Al(111)-top site. dq/dz shows an extremum at 5.13, 4.76, and 4.18 bohr in case of $E_{\text{kin}}^{\text{init}} = 2, 10$, and 50 eV, respectively. Within the TDDFT-MD approach, the charge transfer region is broad. The charge $q(z)$ is not normalized; it approaches values distinctly larger than one in case of the H atom getting close to (and hence chemically interacting with) the Al surface. Hence we refrain from an interpretation of dq/dz in terms of a transition probability.

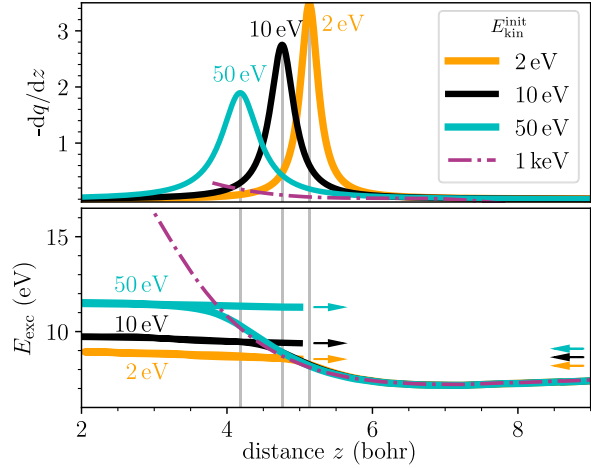


FIG. 4. H^+ impinging on the (111) facet of the Al cluster at the on-top position. (Top) $-dq/dz$, with q denoting the electronic charge on the projectile and z the projectile-surface distance for H^+ projectiles with $E_{\text{kin}}^{\text{init}} = 50, 10$, and 2 eV. Units are $|e|/\text{bohr}$. Charges have been calculated using Eq. (4). (Bottom) Excitation energy as defined in Eq. (5).

The electronic excitation energy E_{exc} of the complete system (including the hydrogen projectile and the Al cluster) is defined by the difference between the electronic energy E_{elec} from the time-dependent (TD) simulation and the electronic energy of the system in its electronic ground state (BO):

$$E_{\text{exc}}(z(t), E_{\text{kin}}^{\text{init}}) := E_{\text{elec}}^{\text{TD}}(z(t), E_{\text{kin}}^{\text{init}}) - E_{\text{elec}}^{\text{BO}}(z(t)). \quad (5)$$

Results are shown in the bottom panel of Fig. 4. For illustration we note that in case of an extended (periodic) metal surface and initially infinite proton-surface separation the excitation energy E_{exc} would correspond to the ionization energy of the projectile (13.6 eV) minus the surface work function [4.09 eV in case of Al(111)][50].

Next we address the dependence of excitation energy on the impact site. As our focus is on electronic excitations, we still keep the atom coordinates of the Al substrate frozen. The H^+ has been chosen to impinge on the fcc-hollow site of the Al(111) surface, as distinct differences to impact onto the Al top site are to be expected in this case. Simulation results are summarized in Fig. 5. The charge transfer $-dq/dz$ is virtually identical for impact on fcc-hollow and top sites. As to be expected, the energy dissipation is distinctly larger for the H^+ incident on the Al-hollow site as (after neutralization) the projectile penetrates into the Al substrate and experiences energy losses by electronic friction [51,52].

As motivated above, as a reference for the excited system we choose E_{exc} from the 1-keV trajectory (this system has almost negligible charge transfer within the range of z in Fig. 4; see Sec. III A). In fact, the E_{exc} curves for $E_{\text{kin}}^{\text{init}} = 2, 10$, and 50 eV—where $E_{\text{kin}}^{\text{init}}$ is the kinetic energy of the proton at $z = 16$ bohr—closely overlap with this reference as long as the charge transfer is negligible. When the charge transfer is almost completed, the excitation energy stops following $E_{\text{exc}}^{\text{1keV}}$ and—in case of the impact at the on-top site—does not vary more than 100 meV over the remaining trajectory. We obtain

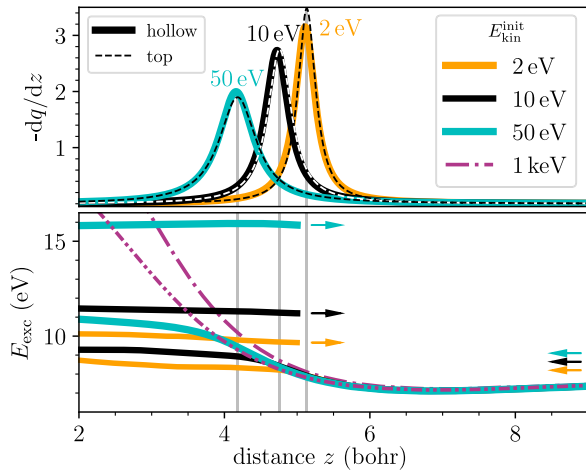


FIG. 5. H^+ impinging on the (111) facet of the Al cluster at the fcc-hollow position. (Top) Same quantity as in Fig. 4 but for the fcc-hollow impact point. For comparison, data for impact at the on-top site are shown by dashed lines. (Bottom) Excitation energy as defined in Eq. (5). Dash-dotted line represents the $E_{\text{kin}} = 1$ keV trajectory with impact point at the on-top site.

$E_{\text{exc}} = 8.6 \text{ eV}/9.4 \text{ eV}/11.3 \text{ eV}$ for $E_{\text{kin}}^{\text{init}} = 2 \text{ eV}, 10 \text{ eV},$ and 50 eV , respectively, at $z = 5$ bohr on the outgoing trajectory.

In case of impact at the fcc-hollow site (see Fig. 5), a direct analysis of the data is complicated by the additional strong electronic friction that arises during propagation of the H through the bulk material. We will target this issue in the following section.

The charge of the outgoing particle (while not well described within spin-unpolarized DFT—the ionicity comes out too negative) is close to the charge calculated for the respective ground state. Hence the simulated ionicity of the scattered projectile is not an indication for a true excitation of the outgoing particle, and we suggest that the excitation energy is finally mostly deposited in the electronic degrees of freedom of the target. In case of the on-top trajectory it can be read from Fig. 4.

E. Energy dissipation after neutralization and comparison to neutral hydrogen

The total energy E_{BO} (i.e., the potential energy) for a hydrogen atom H^0 in front of the on-top and fcc-hollow sites of an Al cluster is visualized in the bottom panel of Fig. 6. In case of the H atom kept fixed atop the Al on-top position, the energy minimum of the one-dimensional cut through the potential energy surface is at $z = 3.1$ bohr. It is a well-known property of currently feasible approximations to the ground-state XC functional, that the electronic ground state of an H^0 atom far away from the surface has to be taken from a spin-polarized calculation. At distances smaller than about 5 bohr, the electronic ground states from a spin-unpolarized and a spin-polarized calculation coincide, in agreement with Ref. [53]. Thus, in case of a proton incident on the Al surface, for the incoming part of the trajectory spin polarization is not expected to be relevant because neutralization mostly

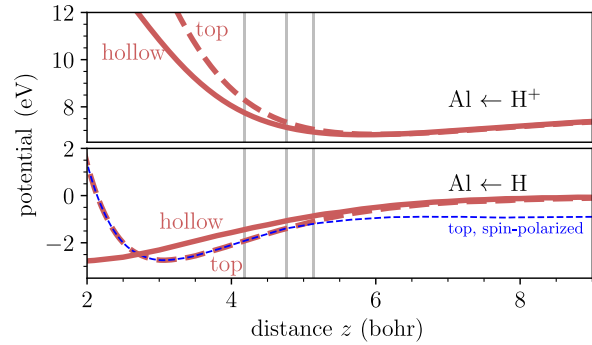


FIG. 6. Born-Oppenheimer surface of the spin-unpolarized H-Al cluster system with total charge +1 (lower graph) and interaction potential curve of an H^+ projectile with $E_{\text{kin}}^{\text{init}} = 1$ keV (proton in front of the cluster, upper graph). Thick full lines denote results for impact at the fcc-hollow site, and thick dashed lines denote results for impact at the on-top site. For comparison, the Born-Oppenheimer surface of an H^0 in front of the Al_{188} cluster from a calculation that allows for spin polarization is also shown (thin blue dashed curve). Vertical lines mark the extrema of dq/dz from Fig. 4.

takes place at a H-Al separation where the energy difference between spin-polarized and spin-unpolarized ground state is small. However, for a neutral particle moving away from the surface, the energy difference between a spin-polarized and a spin-unpolarized simulation would affect the kinetic energy of the outgoing projectile. Due to this inherent property of the chosen approximate XC functional we show results only for distances up to 5 bohr in the exit trajectory. The upper curves of Fig. 6 represent a H^+ -Al(111) interaction potential, i.e., H^+ in front of the Al cluster. The curve is calculated from the electronic and ionic energy of the simulation with the $E_{\text{kin}} = 1$ keV H^+ projectile.

In order to separate the electronic friction effects after neutralization from effects due to H^+ propagation and neutralization one has to subtract the excitation energy of an H^0 projectile from the E_{exc} of H^+ :

$$\Delta E_{\text{exc}}(z) := E_{\text{exc}}(z, E_{\text{kin}}^{\text{init}}) - E_{\text{exc}}^{\text{H}^0}(z, E_{\text{kin}}^{\text{init}, \text{H}^0}). \quad (6)$$

$E_{\text{kin}}^{\text{init}, \text{H}^0}$ should be chosen in such a way that kinetic energies between H^+ and H^0 coincide after the charge transfer. For simplicity, we have chosen $E_{\text{kin}}^{\text{init}, \text{H}^0} = E_{\text{kin}}^{\text{H}^+}(z = 16 \text{ bohr})$. This leads to a difference in E_{kin} after charge transfer between the H^0 and H^+ trajectories of about 0.4, 0.7, and 1.6 eV (for $E_{\text{kin}}^{\text{init}, \text{H}^0} = 2, 10,$ and 50 eV).

For the results shown in Fig. 7 we have treated the scattering of the H^0 at the Al cluster also spin unpolarized. The resulting ΔE_{exc} for $E_{\text{kin}}^{\text{init}} = 2, 10,$ and 50 eV are shown as full lines in the panels of Fig. 7. They are compared to respective results for impact on the Al(111) top site (dashed lines). Note that the difference in ΔE_{exc} arises not only because the ground-state potential energy of H adsorbing atop the Al on-top or fcc-hollow site for the same distance is different, but also because the H^+ -Al(111) interaction potential for both situations is differently corrugated, too, as can be seen in Fig. 6. ΔE_{exc} is determined by that part of the trajectory before

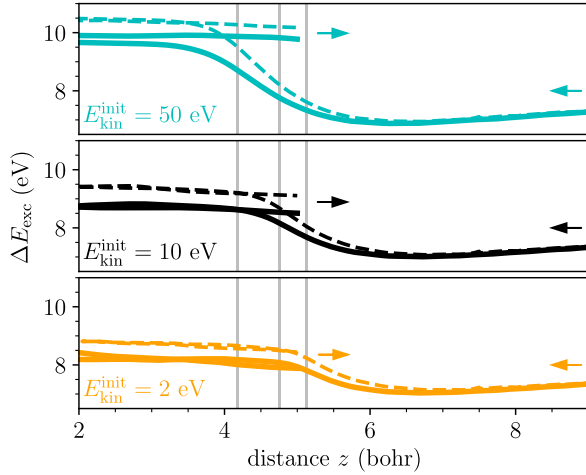


FIG. 7. Difference of the electronic excitation energy between an H^+ impinging on an Al cluster and an H^0 impinging on an Al cluster. ΔE_{exc} is defined in Eq. (6); here the kinetic energies of H^+ and H^0 are chosen to coincide at $z = 16$ bohr and are denoted in the inset of the graphs. The simulation for the H^+ as well as for the H^0 was treated spin unpolarized. For comparison, two different impact sites are shown: on-top (dashed lines) and fcc-hollow (straight lines) sites. Arrows denote the direction of motion.

neutralization where the projectile moves in the generalized image potential. The difference in ΔE_{exc} at $z_{\text{exit}} = 5$ bohr between the on-top and the fcc-hollow impact sites for $E_{\text{kin}}^{\text{init}} = 2, 10$, and 50 eV amounts to $0.55, 0.61$, and 0.45 eV, respectively (see Fig. 7).

It has been discussed in the literature, by, e.g., Winter [15] or Krashennnikov *et al.* [54] that after the charge transfer, an ionic projectile behaves just like an initially neutral one. In our TDDFT-MD simulations we observe small differences in the time development of the kinetic energy. Largest deviations occur in case of a proton impinging on the hollow site, which, however, are only of a similar size as the cluster size convergence effect presented in Sec. II. When the hydrogen is propagating inside the bulk material, differences in the time development of the kinetic energy of ≈ 250 meV are observed. The reason for this is not yet clear; it might be due to both the additional electron in case of the H^0 -Al-cluster simulation as well as the H^+ -ionization energy deposited in the Al cluster in case of the simulation with H^+ incident on the cluster.

F. Extrapolation from the cluster to the extended surface

We extrapolate our results from the Al cluster used in the simulation to the infinite Al(111) surface. Differences arise for two reasons: (i) In the simulation, the projectile starts at a finite separation $z_{\text{init}} = 16$ bohr in front of the Al(111) facet of the cluster instead of an initially arbitrary large separation. (ii) In case of large H^+ -Al_n separation, the image force acting on the H^+ is different for the finite-size cluster (where an image dipole is generated) and the metallic half space (where an image charge builds up).

In Sec. III C, we have argued that for H^+ -Al_n distances $z < 8$ bohr the results of the Al-cluster simulations can be used to

describe the interaction between H^+ and the extended Al(111) surface. Furthermore, at a separation of H^+ from the Al(111) surface of $z = 8$ bohr, the \bar{p} -Al_n and the H^+ -Al_n interaction potentials shown in Fig. 1 deviate by only 54 meV from each other, which corroborates the assumption that at separations $z > 8$ bohr the interaction between the proton and the metal surface is sufficiently well described by the image potential [55],

$$E_{\text{image}}(z) = -\frac{1}{4(z - z_{\text{image}})}, \quad (7)$$

as nonlinearities appear to be small (as derived from the cluster calculation, which, however, has a different asymptotic behavior). For the position z_{image} of the image plane in front of the Al(111) layer we use the value $z_{\text{image}} = 3.14$ bohr obtained by Lam and Needs [56] within self-consistent pseudopotential-based density-functional calculations. Values for z_{image} have been discussed in the literature by Chulkov *et al.* in Ref. [57] where they have pointed out a variation of ± 0.6 bohr depending on the calculation method. If z_{image} is allowed to vary by ± 0.6 bohr, this would induce an uncertainty of $E_{\text{image}}(z = 8 \text{ bohr})$ of ± 0.2 eV. The kinetic energy of the projectile very far away from the surface, $E_{\text{kin}}(z = \infty)$, is connected with the kinetic energy of the projectile at $z = 8$ bohr by energy conservation, i.e.:

$$E_{\text{kin}}(z = \infty) = E_{\text{kin}}(z = 8 \text{ bohr}) + E_{\text{image}}(z = 8 \text{ bohr}). \quad (8)$$

We propagate the H^+ projectile from $z = 16$ bohr towards the surface and use the value of kinetic energy at $z = 8$ bohr in order to extrapolate to the kinetic energy of the proton at $z = \infty$ impinging on an infinite surface. We then let it propagate to the adsorption position of the H atom on the Born-Oppenheimer surface z_{ads} (which is significantly closer to the bulk than the neutralization position). As a last step we perform TDDFT-MD simulations with a neutral, spin-polarized H^0 atom and try to find the initial kinetic energy that leads to the same kinetic energy at the adsorption position as in the simulations with an H^+ projectile. The corresponding values for the kinetic energy are presented in Table I.

Specifically, for an H^+ impinging on the hollow site with a kinetic energy of the proton at $z = 16$ bohr of $E_{\text{kin}}^{\text{init}} = 2$ eV (first two rows of Table I, which actually refer to the same TDDFT-MD simulation) the extrapolation to the infinite surface yields $E_{\text{kin}}(z = \infty) = 1.36$ eV. The kinetic energy of this projectile at the adsorption position (last column of Table I) is 4.03 eV and can also be obtained from a neutral H^0 projectile with an initial kinetic energy of 2.31 eV. The difference Δ between kinetic energy of H^+ and H^0 at $z = \infty$ amounts in this case to $\Delta \approx 1.0$ eV, denoted as Δ in Table I. In agreement with Ref. [51] we observe that in case of the H^0 projectile electronic friction effects start being relevant for $z < 8$ bohr. For this reason we assume here that $E_{\text{kin}}^{\text{H}^0}(z = \infty) \approx E_{\text{kin}}^{\text{H}^0}(z = 8 \text{ bohr})$.

Under the assumption of Sec. III E that after neutralization both projectiles behave the same, Table I draws an interesting picture about the initial kinetic energies resulting in the same kinetic energy of the projectile within the Al. For the lower kinetic energies of this study the initial kinetic energy far above the surface is for the H^+ projectile smaller than for

TABLE I. Kinetic energy of the H^+ or H^0 projectile (units of eV) approaching the Al cluster or Al(111) surface as a function of distance z from the plane of Al atoms. Simulations with H^0 are started from a ground-state simulation allowing for spin polarization. Impact points are fcc-hollow site or on-top site. Adsorption positions of H on Al(111) in ground-state calculation are $z_{\text{ads}}^{\text{hollow}} = 1.9$ bohr or $z_{\text{ads}}^{\text{top}} = 3.1$ bohr. Δ is the difference between the initial kinetic energies of H^+ and H^0 required to obtain identical velocities of the H^0 after scattering. ^aExtrapolation using Eq. (8); ^bvalue obtained from $E_{\text{kin}}(z = \infty) - E_{\text{image}}(z)$; ^cvalue taken from $z = 16$ bohr; ^dvalue taken from cluster simulation.

| | | $z = \infty$ | $z = 16$ bohr | $z = 8$ bohr | $z = z_{\text{ads}}$ |
|--------|------------------------------|--------------------|--------------------|--------------------|----------------------|
| hollow | $H^+ \rightarrow$ Al cluster | | 2.00 | 2.76 | 4.03 |
| | $H^+ \rightarrow$ Al surface | 1.36 ^a | 1.89 ^b | 2.76 ^d | 4.03 ^d |
| | $H^0 \rightarrow$ Al cluster | 2.31 ^c | 2.31 | 2.31 | 4.03 |
| | | $\Delta = +1.0$ | | | |
| hollow | $H^+ \rightarrow$ Al cluster | | 10.00 | 10.76 | 11.49 |
| | $H^+ \rightarrow$ Al surface | 9.36 ^a | 9.89 ^b | 10.76 ^d | 11.49 ^d |
| | $H^0 \rightarrow$ Al cluster | 9.95 ^c | 9.95 | 9.95 | 11.48 |
| | | $\Delta = +0.6$ | | | |
| hollow | $H^+ \rightarrow$ Al cluster | | 50.00 | 50.76 | 49.86 |
| | $H^+ \rightarrow$ Al surface | 49.36 ^a | 49.89 ^b | 50.76 ^d | 49.86 ^d |
| | $H^0 \rightarrow$ Al cluster | 48.92 ^c | 48.92 | 48.92 | 49.88 |
| | | $\Delta = -0.4$ | | | |
| top | $H^+ \rightarrow$ Al cluster | | 2.00 | 2.76 | 3.72 |
| | $H^+ \rightarrow$ Al surface | 1.36 ^a | 1.89 ^b | 2.76 ^d | 3.72 ^d |
| | $H^0 \rightarrow$ Al cluster | 2.16 ^c | 2.16 | 2.16 | 3.76 |
| | | $\Delta = +0.8$ | | | |
| top | $H^+ \rightarrow$ Al cluster | | 10.00 | 10.76 | 10.92 |
| | $H^+ \rightarrow$ Al surface | 9.36 ^a | 9.89 ^b | 10.76 ^d | 10.92 ^d |
| | $H^0 \rightarrow$ Al cluster | 9.47 ^c | 9.47 | 9.47 | 10.91 |
| | | $\Delta = +0.1$ | | | |
| top | $H^+ \rightarrow$ Al cluster | | 50.00 | 50.76 | 49.16 |
| | $H^+ \rightarrow$ Al surface | 49.36 ^a | 49.89 ^b | 50.76 ^d | 49.16 ^d |
| | $H^0 \rightarrow$ Al cluster | 48.15 ^c | 48.15 | 48.15 | 49.11 |
| | | $\Delta = -1.2$ | | | |

the H^0 projectile, i.e., $E_{\text{kin}}^H(z = \infty) < E_{\text{kin}}^{H^0}(z = \infty)$ whereas for the higher kinetic energies this relation inverts to $E_{\text{kin}}^H(z = \infty) > E_{\text{kin}}^{H^0}(z = \infty)$. Results are consistent with Fig. 6, i.e., a change of sign is also expected from the energy difference between the H^+ -Al(111) interaction potential and the ground-state potential energy surface of H^0 in front of the Al(111) surface in the neutralization region.

G. Energy transfer from central collision

In order to draw a complete picture of the energy transfer, the energy dissipation into phononic degrees of freedom has to be calculated. Therefore, we perform TDDFT-MD simulations for the previously discussed Al_{188} cluster with H^+ initially located $z = 16$ bohr above the Al atoms. Thirteen Al atoms closest to the impact point (impact at on-top site) were allowed to move in order to include the kinetic energy transfer into the substrate ionic degrees of freedom; the kinetic

TABLE II. Comparison of kinetic energies of H^+ projectiles incident on the Al(111) on-top site in case of frozen-in Al coordinates ($E_{\text{kin}}^{\text{fix}}$) and non-frozen-in Al coordinates ($E_{\text{kin}}^{\text{free}}$) when the projectile has reached $z_{\text{exit}} = 8$ bohr. For comparison, ΔE_{CC} denotes the kinetic energy transfer into the substrate in a head-on collision between an H atom and an Al atom [see Eq. (9)].

| $E_{\text{kin}}^{\text{init}}/\text{eV}$ | $(E_{\text{kin}}^{\text{free}} - E_{\text{kin}}^{\text{fix}}) _{z_{\text{exit}}}/\text{eV}$ | $\Delta E_{\text{CC}}/\text{eV}$ |
|--|---|----------------------------------|
| 2 | -0.28 | -0.14 |
| 10 | -1.21 | -1.39 |
| 50 | -6.51 | -6.95 |

energy of the projectile is denoted as $E_{\text{kin}}^{\text{free}}$. Table II shows the difference in kinetic energy $(E_{\text{kin}}^{\text{free}} - E_{\text{kin}}^{\text{fix}})|_{z_{\text{exit}}}$ at the exit position $z_{\text{exit}} = 8$ bohr. $E_{\text{kin}}^{\text{fix}}$ refers to the kinetic energy of the projectile impinging on the Al cluster with frozen-in Al atomic coordinates.

The kinetic energy difference ranges from -0.28 eV for $E_{\text{kin}}^{\text{init}} = 2$ eV to -6.51 eV for $E_{\text{kin}}^{\text{init}} = 50$ eV. A semiquantitative understanding can be obtained from studying a simple central collision between a proton of mass m_H and an aluminum atom of mass m_{Al} . The kinetic energy transfer in a central collision is given by

$$\Delta E_{\text{CC}} = -\frac{4m_H m_{\text{Al}}}{(m_H + m_{\text{Al}})^2} E_{\text{kin}}^{z=\infty} \approx -0.139 E_{\text{kin}}^{z=\infty}, \quad (9)$$

This results in an expected energy transfer of -0.14 eV for $E_{\text{kin}}^{\text{init}} = 2$ eV to -6.95 eV for $E_{\text{kin}}^{\text{init}} = 50$ eV.

The kinetic energy transfer into the phononic degrees of freedom during the central collision is small compared to the initial kinetic energy due to the significant mass difference between H and Al. For $E_{\text{kin}} \leq 10$ eV this brings the energy transfer caused by the image potential effects—which we discussed in the previous chapters—into the same order of magnitude.

IV. SUMMARY

We have performed TDDFT-MD simulations for the neutralization of hyperthermal H^+ projectiles impinging on an Al(111) surface, which is modeled by a finite-size cluster. It has been remarked by Winter *et al.* [15] that the neutralization distance may be derived from a comparison of scattered ionic and neutral projectiles. Following these ideas, we have

simulated the process from *ab initio* and calculated the scattering of H^+ and H^0 projectiles for two different impact sites. By this means we have been able to link the charge transfer with the electronic energy transfer due to neutralization.

In case of the projectiles studied here with a kinetic energy ranging between 2 and 50 eV, the maximum of the neutralization rate occurs in a region between $z = 4.2$ bohr and $z = 5.1$ bohr in front of the uppermost Al atom layer, independent of impact site. Additionally, we find that, in order to obtain identical exit velocities in case of projectiles with $E_{\text{kin}} \approx 50$ eV, H^+ needs to be initially faster than H^0 by about 1.2 eV (on-top trajectory) to 0.4 eV (fcc-hollow trajectory).

In contrast, for projectiles with $E_{\text{kin}} \approx 2$ eV the sign changes and H^+ needs to be initially slower than H^0 by about 0.8 eV (on-top trajectory) to 1.0 eV (fcc-hollow trajectory). This is explained by the difference between the ground-state potential energy surface and the H^+ -Al(111) interaction potential which is repulsive in the region of neutralization.

ACKNOWLEDGMENTS

We thank A. C. Dávila López for helpful discussions. Calculations were carried out at the Rechenzentrum der Universität Kiel.

- [1] I. Adamovich, S. D. Baalrud, A. Bogaerts, P. J. Bruggeman, M. Cappelli, V. Colombo, U. Czarnetzki, U. Ebert, J. G. Eden, P. Favia, D. B. Graves, S. Hamaguchi, G. Hieftje, M. Hori, I. D. Kaganovich, U. Kortshagen, M. J. Kushner, N. J. Mason, S. Mazouffre, S. M. Thagard *et al.*, *J. Phys. D* **50**, 323001 (2017).
- [2] M. Bonitz, A. Filinov, J.-W. Abraham, K. Balzer, H. Kählert, E. Pehlke, F. X. Bronold, M. Pamperin, M. Becker, D. Löffhagen, and H. Fehske, *Frontiers Chem. Sci. Eng.* **13**, 201 (2019).
- [3] D. M. Newns, *Phys. Rev.* **178**, 1123 (1969).
- [4] R. Brako and D. Newns, *Surf. Sci.* **108**, 253 (1981).
- [5] J. Geerlings, J. Los, J. Gauyacq, and N. Temme, *Surf. Sci.* **172**, 257 (1986).
- [6] J. Merino, N. Lorente, P. Pou, and F. Flores, *Phys. Rev. B* **54**, 10959 (1996).
- [7] D. C. Langreth and P. Nordlander, *Phys. Rev. B* **43**, 2541 (1991).
- [8] M. Pamperin, F. X. Bronold, and H. Fehske, *Phys. Rev. B* **91**, 035440 (2015).
- [9] M. Bonitz, K. Balzer, N. Schlünzen, M. R. Rasmussen, and J. Joost, *Phys. Status Solidi (b)* **256**, 1970028 (2019).
- [10] M. A. L. Marques, C. A. Ullrich, F. Nogueira, A. Rubio, K. Burke, and E. K. U. Gross, editors, *Time-Dependent Density Functional Theory*, Lecture Notes in Physics Vol. 706 (Springer, Berlin/Heidelberg, 2006).
- [11] M. A. L. Marques, N. T. Maitra, F. M. S. Nogueira, E. K. U. Gross, and A. Rubio, editors, *Fundamentals of Time-Dependent Density Functional Theory*, Lecture Notes in Physics Vol. 837 (Springer, Berlin/Heidelberg, 2012).
- [12] M. A. Marques, A. Castro, G. F. Bertsch, and A. Rubio, *Comput. Phys. Commun.* **151**, 60 (2003).
- [13] R. Baragiola, E. Alonso, J. Ferron, and A. Oliva-Florio, *Surf. Sci.* **90**, 240 (1979).
- [14] D. Hasselkamp, S. Hippler, and A. Scharmann, *Nucl. Instrum. Methods Phys. Res. B* **18**, 561 (1986).
- [15] H. Winter, *J. Phys.: Condens. Matter* **8**, 10149 (1996).
- [16] H. Winter and A. Borisov, *Nucl. Instrum. Methods Phys. Res. B* **115**, 211 (1996).
- [17] H. Nienhaus, R. Zimny, and H. Winter, *Radiat. Eff. Defects Solids* **109**, 1 (1989).
- [18] A. Borisov and H. Winter, *Nucl. Instrum. Methods Phys. Res. B* **115**, 142 (1996).
- [19] M. Okada and Y. Murata, *J. Phys.: Condens. Matter* **9**, 1919 (1997).
- [20] W. Heiland, *Surf. Sci.* **251-252**, 942 (1991).
- [21] H. Eder, F. Aumayr, P. Berlinger, H. Störi, and H. Winter, *Surf. Sci.* **472**, 195 (2001).
- [22] P. Nordlander and J. C. Tully, *Phys. Rev. B* **42**, 5564 (1990).
- [23] P. Nordlander and J. C. Tully, *Phys. Rev. Lett.* **61**, 990 (1988).
- [24] S. A. Deutscher, X. Yang, and J. Burgdörfer, *Phys. Rev. A* **55**, 466 (1997).
- [25] J. Merino, N. Lorente, M. Y. Gusev, F. Flores, M. Maazouz, L. Guillemot, and V. A. Esaulov, *Phys. Rev. B* **57**, 1947 (1998).
- [26] A. Borisov, D. Teillet-Billy, and J. Gauyacq, *Nucl. Instrum. Methods Phys. Res. B* **78**, 49 (1993).
- [27] M. C. Torralba, P. G. Bolcatto, and E. C. Goldberg, *Phys. Rev. B* **68**, 075406 (2003).
- [28] R. Monreal and F. Flores, in *Theory of the Interaction of Swift Ions with Matter. Part I*, Advances in Quantum Chemistry Vol. 45 (Academic Press, Cambridge, 2004), pp. 175–199.
- [29] K. Snowdon, R. Hentschke, A. Närmann, W. Heiland, E. Mühling, and W. Eckstein, *Nucl. Instrum. Methods Phys. Res. B* **23**, 309 (1987).
- [30] B. Obreshkov and U. Thumm, *Phys. Rev. A* **87**, 022903 (2013).
- [31] H. Jouin and F. A. Gutierrez, *Phys. Rev. A* **80**, 042901 (2009).
- [32] H. Jouin and F. A. Gutierrez, *Phys. Rev. A* **84**, 014901 (2011).
- [33] J. Juaristi, *Nucl. Instrum. Methods Phys. Res. B* **230**, 148 (2005), Atomic Collisions in Solids.
- [34] N. Schlünzen, K. Balzer, M. Bonitz, L. Deuchler, and E. Pehlke, *Contrib. Plasma Phys.* **59**, e201800184 (2019).
- [35] Please note that the image plane position of an Al(111) surface is located approximately 3.14 bohr in front of the uppermost Al atom; see Ref. [56].
- [36] K. A. H. German, C. B. Weare, and J. A. Yarmoff, *Phys. Rev. B* **50**, 14452 (1994).
- [37] A. Castro, H. Appel, M. Oliveira, C. A. Rozzi, X. Andrade, F. Lorenzen, M. A. L. Marques, E. K. U. Gross, and A. Rubio, *physica status solidi (b)* **243**, 2465 (2006).
- [38] X. Andrade, D. Strubbe, U. De Giovannini, A. H. Larsen, M. J. T. Oliveira, J. Alberdi-Rodriguez, A. Varas, I. Theophilou, N. Helbig, M. J. Verstraete, L. Stella, F. Nogueira, A. Aspuru-Guzik, A. Castro, M. A. L. Marques, and A. Rubio, *Phys. Chem. Chem. Phys.* **17**, 31371 (2015).
- [39] J. P. Perdew, K. Burke, and M. Ernzerhof, *Phys. Rev. Lett.* **77**, 3865 (1996).

- [40] N. Troullier and J. L. Martins, *Phys. Rev. B* **43**, 1993 (1991).
- [41] M. Fuchs and M. Scheffler, *Comput. Phys. Commun.* **119**, 67 (1999).
- [42] C. A. Rozzi, D. Varsano, A. Marini, E. K. U. Gross, and A. Rubio, *Phys. Rev. B* **73**, 205119 (2006).
- [43] M. Tafipolsky and R. Schmid, *J. Chem. Phys.* **124**, 174102 (2006).
- [44] M. Methfessel and A. T. Paxton, *Phys. Rev. B* **40**, 3616 (1989).
- [45] D. Marx and J. Hutter, *Ab Initio Molecular Dynamics: Basic Theory and Advanced Methods* (Cambridge University Press, Cambridge, 2009).
- [46] A. Liebsch, *Phys. Rev. B* **36**, 7378 (1987).
- [47] S. Andersson and B. N. J. Persson, *Phys. Rev. Lett.* **50**, 2028 (1983).
- [48] A. Gras-Marti, P. Echenique, and R. Ritchie, *Surf. Sci.* **173**, 310 (1986).
- [49] W. Tang, E. Sanville, and G. Henkelman, *J. Phys.: Condens. Matter* **21**, 084204 (2009).
- [50] A. Kiejna and B. I. Lundqvist, *Phys. Rev. B* **63**, 085405 (2001).
- [51] M. Lindenblatt, E. Pehlke, A. Duvenbeck, B. Rethfeld, and A. Wucher, *Nucl. Instrum. Methods Phys. Res. B* **246**, 333 (2006).
- [52] M. Alducin, R. D. Muiño, and J. I. Juaristi, *Prog. Surf. Sci.* **92**, 317 (2017).
- [53] M. Lindenblatt and E. Pehlke, *Phys. Rev. Lett.* **97**, 216101 (2006).
- [54] A. V. Krashennnikov, Y. Miyamoto, and D. Tománek, *Phys. Rev. Lett.* **99**, 016104 (2007).
- [55] N. D. Lang and W. Kohn, *Phys. Rev. B* **7**, 3541 (1973).
- [56] S. C. Lam and R. J. Needs, *J. Phys.: Condens. Matter* **5**, 2101 (1993).
- [57] E. Chulkov, V. Silkin, and P. Echenique, *Surf. Sci.* **437**, 330 (1999).

6.1 Introduction

Experimental studies are naturally not limited to the above discussed Al substrate but are extended over almost all kinds of materials. As a first step away from the Al, we here choose an Au surface which has been analyzed theoretically^[138] and experimentally by different groups.^[25,40,309,310] The comparison of charge and energy transfer between an Al and an Au surface is especially interesting because in chapter 3 it was observed that during the electronic charge transfer between surface and projectile, the artificial Kohn-Sham frozen-density adsorbate level position $\epsilon_a^{\text{frozen}}$ transitioned continuously from -0.5 H (against vacuum) to a value close to the Fermi energy, i.e. through almost the entire DOS of the cluster. As the Au DOS is significantly shaped by the contributions of the *d*-electrons, one may speculate a much higher tunneling rate. However, as will be discussed in this chapter, tunneling rates are very similar.

Theoretical work from Zeb et al.^[138] investigated the propagation of a proton through an Au bulk. They came to the conclusion, that as soon as the electronic excitation from electronic friction effects extends to the electronic *d*-band, additional friction from the *d*-electrons can be observed.

An experimental example for ion scattering on an Au-surface are the measurements by He and Yarmoff^[309] who studied Sr⁺ scattering off Au surfaces. Their experimental results indicate that a mixed-valence resonance affects the final charge state of the projectile. The experiments are motivated by the theoretical work of Shao et al.^[311] and supported by simulations by Pamperin et al.^[111] who employed a parametrized Anderson-Newns model and investigated the charge transfer between the projectile and the surface. Their employed model requires external parameters, of which some could also be obtained from a TDDFT-MD simulation. The here employed TDDFT-MD simulations with an AGGA XC-functional, on the other hand side, are not able to capture the above described many body effects.

Comparing Au with the previously investigated Al, they share several physical properties which may also be relevant in a simulation of the electronic charge transfer. Both metals have a similar experimental value for the lattice constant (Al: 4.05 \AA ,^[299] Au: 4.08 \AA ^[299]). The experimental work function (Al(111): 4.26 eV ,^[296] Au(111): 5.3 eV ^[296]) and the lowest state at $\bar{\Gamma}$ (Al₁₈₈-cluster: -14.9 eV vs. vacuum, Au₁₈₈-cluster: -13.53 eV vs. vacuum) differ by approximately 1 eV and 1.4 eV . The image plane position z_{image} is for gold closer

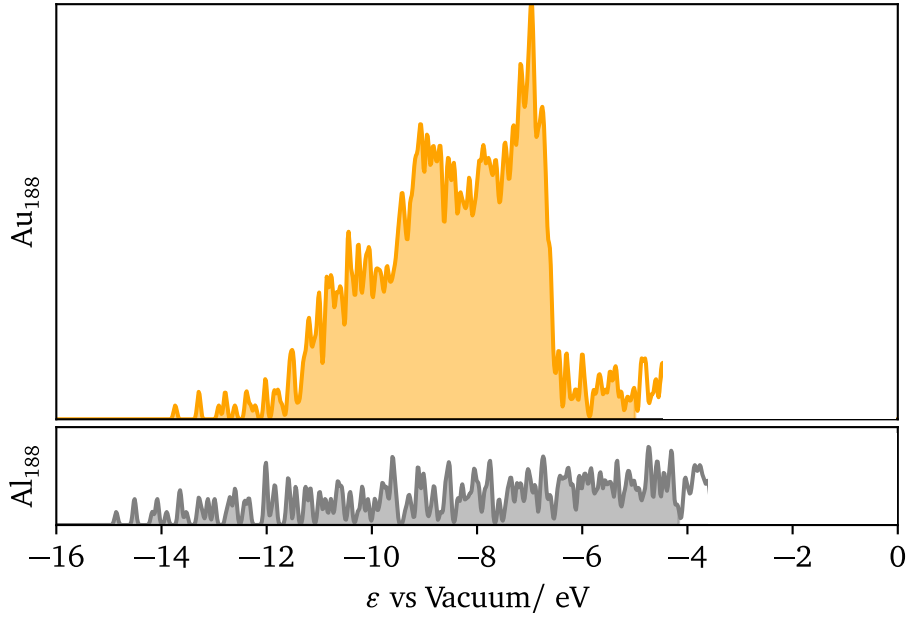


Figure 6.1: Density of (Kohn-Sham) states (DOS) for the Au_{188} -cluster and the Al_{188} -cluster in arbitrary units (but same for both graphs). States are broadened with Gaussians of width $\sigma = 30$ meV. Please note that the Au pseudopotentials contribute 11 valence electrons per atom, whereas the Al pseudopotentials contribute 3 valence electrons per atom. 28 unoccupied states have been included in the calculations of which 20 are drawn with a white background in the graph. Higher energetic states are not shown here. The work functions ϕ for the clusters with the here employed computational parameters can be approximated by the HOMO of the clusters, i.e.: $\phi(Al_{188}) = 4.15$ eV and $\phi(Au_{188}) = 4.98$ eV.

to the surface: $z_{\text{image}}^{\text{Au}} \approx 2.14$ bohr^[295] and $z_{\text{image}}^{\text{Al}} \approx 3.14$ bohr.^[106] The most apparent difference between Au and Al is the electronic band structure as shown in Figure 6.1 for the corresponding Al_{188} and Au_{188} clusters. As generally known, the band structure of Au has a high DOS in the d -band.

The extension of the previously presented simulations to the case of an Au-cluster is inherently connected to an increase of numerical requirements:

- Due to the electronic structure of the Au atom, significantly more electrons have to be included in a simulation with the same number of atoms compared to a calculation with an Al-cluster. In case of Au, at least 11 electrons are usually taken as valence electrons whereas in case of Al, only 3 are required.
- The Au pseudopotentials require a higher wavefunction cutoff, i.e. a lower mesh spacing because the d -orbitals are located comparatively close to the atomic nucleus.

- As the time step is connected to the mesh spacing (see subsection 2.3.5), a smaller value for the time step is required, too.

In the present chapter, we tackle the problem of H^+ scattering off the (111) surface face of an Au_{188} -cluster. The main focus of this chapter lies on developing and justifying a path that allows for an efficient calculation of the problem. The computational difficulties will be tackled with the help of an antiproton (\bar{p}) and a non-binding pseudo-Hydrogen (pseudo-H). At the end, simulation results are discussed and compared to H^+ scattering off an Al_{188} -cluster and difficulties as well as similarities in the electronic charge transfer will be discussed.

6.2 Computational Aspects

| Parameter | Unit | Value |
|----------------------------------|-------------------|------------------------|
| Mesh Spacing | bohr | 0.25 |
| XC-Functional | | AGGA-PBE |
| Coulomb Cutoff | | spherical |
| Volume of Simulation Box | bohr ³ | $60 \cdot 60 \cdot 44$ |
| Min Distance Atoms to Box Edge | bohr | 12.0 |
| Projectile Starting Distance z | bohr | 9.0 |
| Time Step | atu | 0.01 |

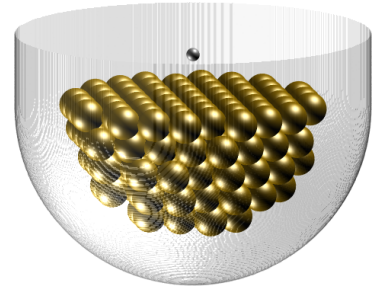


Table 6.1: **Left:** Overview of most relevant parameters of the simulations with proton and Au_{188} . **Right:** Visualization of the employed cluster in its corresponding simulation cell.

As discussed in the previous section, a smaller spacing is required for a simulation with the Au-cluster and therewith connected the necessity to decrease the time step. From a convergence analysis, it was obtained that $\Delta x = 0.25$ bohr and a time step of $\Delta t = 0.01$ atu are required to maintain the deviation of the total energy below 60 meV when propagating the proton towards the Au_{188} -cluster from $z = 9$ bohr to $z = 3$ bohr. For comparison, when propagating a proton in front of an Al_{188} -cluster (see chapter 3, 4 and 5) from $z = 9$ bohr to $z = 3$ bohr with a mesh spacing of $\Delta x = 0.5$ bohr and a time step of $\Delta t = 0.02$ atu, the deviation of the total energy is below 20 meV. The number of electrons included in the Al-simulation is 3 per atom, in case of Au-simulations 11 per atom.

Apart from the parameters given in Table 6.1, parameters used for the simulation are identical to the ones presented in section 3.1 on page 46. The Au pseudopotential was created using the fhi98PP software (see subsection 2.3.1) with $r_s^{Au} = 2.523$ bohr, $r_p^{Au} = 2.649$ bohr, and $r_d^{Au} = 2.523$ bohr, and taken as p -local. For the employed parameters, a lattice constant of 4.15 Å (Ref. [294]: 4.06 Å with the same XC-functional) and a HOMO level for the Au_{188} -cluster of 4.98 eV is obtained. The HOMO level can be seen as an ap-

proximation to the workfunction, as discussed in section 3.2. In Ref. [294] a workfunction of 5.15 eV was obtained.

Based on the experience from chapter 3, 4 and 5, different techniques have been employed to decrease the computation time by minimizing the computation cell, the initial distance, and through this the total propagation time. The techniques employed are:

1. The simulation does not start from the electronic ground-state of the cluster. For the simulation presented here, the TD-simulation starts from a ground-state calculation of an artificially non-binding pseudo-Hydrogen (pseudo-H). Please note that a similar technique has been used before in Ref. [149] by Ojanperä et al.
2. The simulation starts closer to the Au-cluster (initial distance of 9 bohr), this allows for both, a smaller cell size as well as less time propagation steps.

Both arguments require a careful analysis regarding validity and applicability. It is especially important that these two steps do not change the physical results of the presented simulations.

6.3 Non-Binding Pseudo-Hydrogen in Front of an Al_{188} -Cluster

We introduce the concept of a non-binding pseudo-Hydrogen (pseudo-H) which is defined to be identical to the potential of the H pseudopotential in the distance r from the nucleus with $2.6 \text{ bohr} < r < \infty$. In case of $r < 2.6 \text{ bohr}$, the potential is set to be practically infinite (here: 10H). Figure 6.2 shows the highest occupied molecular orbital (HOMO) level of the non-binding pseudo-Hydrogen with respect to the total electronic charge included in a spin-unpolarized DFT ground-state calculation of the pseudo-atom. This kind of simulation is highly artificial and serves the mere purpose to show that in a ground-state calculation of the non-binding pseudo-Hydrogen in front of the Al-cluster or the Au-cluster, no pure 'orbital' of the pseudo-H is below the Fermi energy of neither Al(111) nor Au(111). However, due to chemical interactions, the level may vary and it has to be made sure, that no charge is accumulated around the pseudo-H.

To identify an optimal starting distance of the H^+ , we analyze the case of an antiproton (\bar{p}) and of the non-binding pseudo-Hydrogen in front of the Al_{188} -cluster in a ground-state

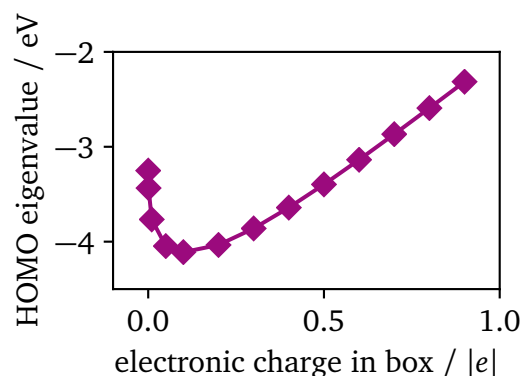


Figure 6.2: Calculation of HOMO eigenvalue of non-binding pseudo-Hydrogen in a spherical simulation box with radius $r = 20 \text{ bohr}$ and mesh spacing $\Delta x = 0.2 \text{ bohr}$.

calculation and discuss both of the arguments from above with the help of Figure 6.3 and Figure 6.4.

The antiproton is represented by a soft Coulomb potential $v_{\bar{p}}(\mathbf{r})$ with:

$$v_{\bar{p}}(\mathbf{r}) = \frac{1}{\sqrt{(0.2 \text{ bohr})^2 + |\mathbf{r} - \mathbf{r}_{\bar{p}}|^2}} \quad (6.1)$$

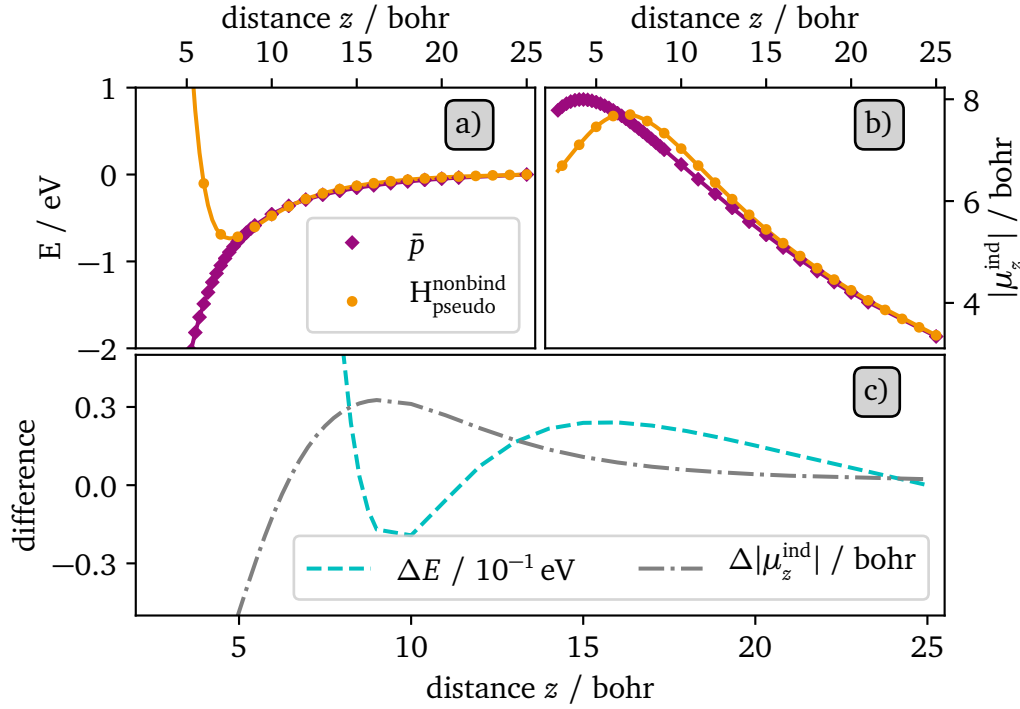


Figure 6.3: **Ground-state calculation:** Comparison between an Antiproton (\bar{p}) and an artificially non-binding pseudo-Hydrogen ($H_{\text{pseudo}}^{\text{nonbind}}$) in a ground-state calculation in front of an Al₁₈₈-cluster. **a)** Total energy E with respect to $z = 25$ bohr, **b)** dipole moment change induced within cluster, see Equation 6.2, **c)** differences of the curves in a) and b), i.e. between \bar{p} and $H_{\text{pseudo}}^{\text{nonbind}}$.

Non-Binding Pseudo-Hydrogen in Ground-State Calculation Figure 6.3 shows the differences between a ground-state calculation of an antiproton in front of an Al₁₈₈-cluster and the non-binding pseudo-Hydrogen in front of the Al₁₈₈-cluster. In a), total energy differences with respect to a particle at $z = 25$ bohr are presented. b) shows the absolute value of the induced dipole moment in the z direction μ_z^{ind} within the Al₁₈₈-cluster. I.e.:

$$\mu_z^{\text{ind}}(z) = \mu(z) - \mu_{\text{Al}_{188}} - \mu_X(z) \quad (6.2)$$

where X stands for the antiproton or the pseudo-H. Figure 6.3c shows the difference between the antiproton and the non-binding pseudo-Hydrogen (pseudo-H). At a distance of

$z \approx 9$ bohr, the variation of the energy—which in case of an atom would be the DFT-GGA adsorption curve—is very similar when comparing the \bar{p} and the non-binding pseudo-Hydrogen. The most negative value for the difference between the two curves is reached at $z = 10$ bohr and amounts to 20 meV (i.e. 4.2% of the value for the absolute energy difference). For smaller distances, the energy difference increases dramatically because the non-binding pseudo-Hydrogen becomes repulsive for small distances. The variation of the absolute value of the induced dipole moment exhibits a maximum at $z = 9$ bohr of approximately $\Delta|\mu_z^{\text{ind}}| \approx 0.3$ bohr (i.e. 4.6% of the value for the absolute dipole moment difference).

Given that no additional charge is accumulated around the pseudo-H, a ground-state calculation of a non-binding pseudo-Hydrogen at a distance of $z = 9$ bohr in front of an Al surface is a reasonable starting configuration for a time-dependent simulation with a proton in front of the surface. The extension of the ground-state results to time-dependent simulations will be investigated next.

Non-Binding Pseudo-Hydrogen as a Starting Point in a Time-Dependent Calculation

A proton in front of a surface induces an image charge. This image charge does not form instantaneously but builds up with a time scale corresponding to the plasmon frequency. Figure 6.4 shows the induced dipole moment change in the z direction μ_z^{ind} within the Al_{188} -cluster as defined in Equation 6.2 by a proton in a time-dependent simulation. The time-dependent simulations start from different distances and ground-state (GS) calculations. The initial configuration is either the electronically relaxed Al_{188} -cluster or the electronically relaxed Al_{188} -cluster with a non-binding pseudo-Hydrogen at a distance $z = 16$ bohr or $z = 10$ bohr. Initial kinetic energies are 10 eV, 1 keV, or 10 keV.

From all three graphs it is directly clear that starting from GS causes an initial perturbation resulting in an oscillation in $|\Delta\mu_z^{\text{ind}}|$. The height of the oscillation is determined by the value of the induced dipole moment at the same distance. The lowest value for the oscillation is 0 as expected from the ground-state, the highest value is twice the value obtained in the calculation with a \bar{p} or an pseudo-H. These oscillations die off relatively fast, however, they become relevant already for a 1-keV projectile with a starting distance of $z = 16$ bohr. Figure 6.4 also shows that the introduced error when starting from a GS can easily be avoided when starting from a non-binding pseudo-Hydrogen based calculation.

Please note that, even though the starting configuration with a non-binding pseudo-Hydrogen represents an improvement over a ground-state starting configuration and the induced density is for small velocities exact, the exact starting wavefunctions also carry a phase which this method does not attribute to.

Simulation Parameters For the H^+ -Au-cluster simulations we employ the computational parameters presented in section 3.1. Considering the results of the above considerations, we apply the following changes:

- Denser mesh spacing $\Delta x = 0.25$ bohr.
- Smaller time step of $\Delta t = 0.01$ au.

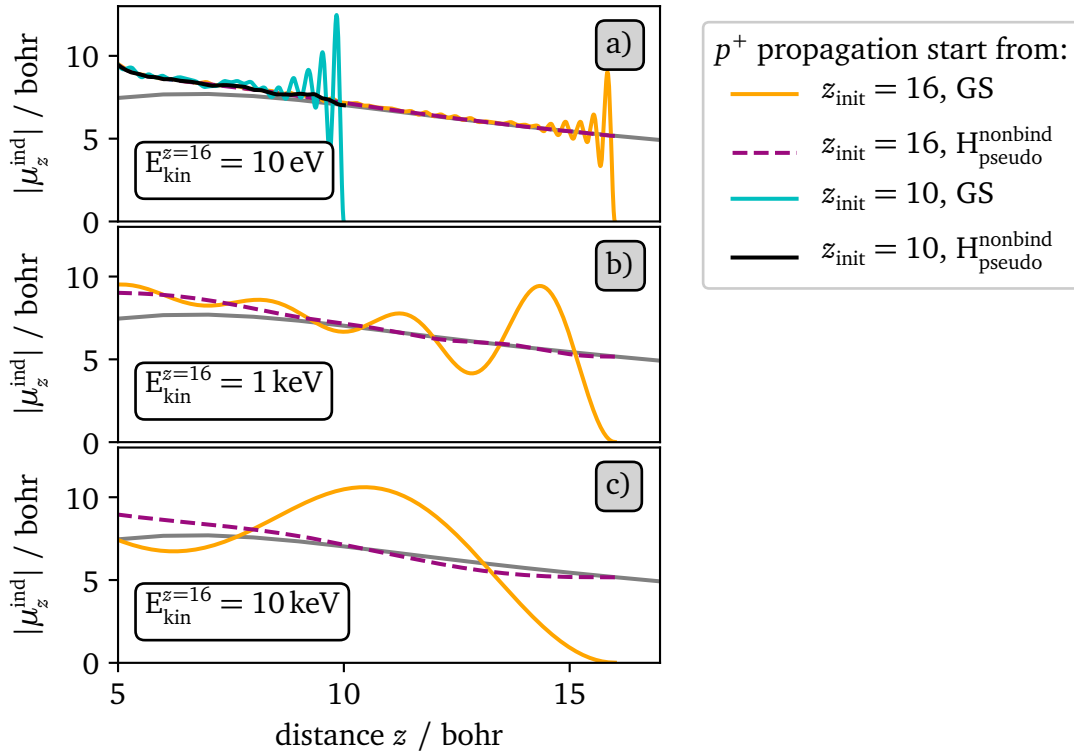


Figure 6.4: Comparison of induced time-dependent dipole moment (Equation 6.2) from proton (p^+) projectiles starting at $z_{\text{init}} = 16$ bohr or $z_{\text{init}} = 10$ bohr with initial kinetic energy of **a)** 10 eV, **b)** 1 keV, or **c)** 10 keV in front of an initially neutral Al_{188} -cluster (GS) or from a ground-state calculation of a non-binding pseudo-Hydrogen in front of a Al_{188} -cluster ($H_{\text{pseudo}}^{\text{nonbind}}$). The impact point is the on-top position. For comparison, the induced dipole moment change in a ground-state calculation of a non-binding pseudo-Hydrogen in front of an Al_{188} -cluster as presented in Figure 6.3 is drawn by a dashed grey line here.

- Smaller computation cell of $60 \cdot 60 \cdot 44 \text{ bohr}^3$, i.e. the wavefunctions are tabulated on a grid within a region defined by the following function:

$$f(x, y, z) = [(-22 \leq z \leq 0) \wedge (30 \geq \sqrt{x^2 + y^2 + z^2})](\text{half-sphere}) \vee [(0 \leq z \leq 22) \wedge (30 \geq \sqrt{x^2 + y^2})] \quad (\text{cylinder}) \quad (6.3)$$

The simulation cell is shown in Table 6.1.

- The initial configuration is the electronic ground-state of the Al_{188} -cluster with a non-binding pseudo-Hydrogen at a distance of $z = 9$ bohr.

In Figure 6.5a and b, we compare the kinetic energy difference and the electronic charge transfer as obtained within a Bader charge analysis from two simulations. One of them

(grey curve) is the simulation of an H^+ scattering off the Al_{188} -cluster for the simulations of chapter 3, 4, and 5 with a kinetic energy of $E_{kin}^{init} = 10$ eV at an initial distance of 16 bohr. The second one (black dashed curve) shows an H^+ scattering off the Al_{188} -cluster with the above presented parameters, i.e. the computation cell is defined in Equation 6.3, the starting configuration a pseudo-H in front of the Al_{188} -cluster and the initial velocity chosen to coincide with the previous simulation. Both simulations are in perfect agreement. This serves as a strong indication, that a reliable simulation for a gold cluster with these parameters can be realized.

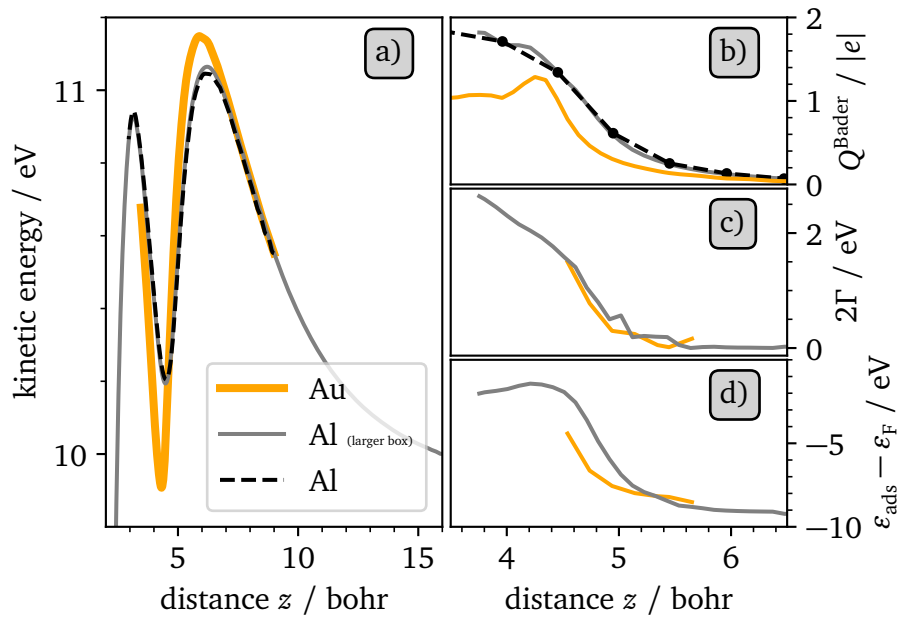


Figure 6.5: **a)** Comparison between H^+ scattering off an Al_{188} -cluster and an Au_{188} -cluster. Kinetic energy of proton impinging on Au chosen to coincide with kinetic energy of proton impinging on Al at $z = 9$ bohr from chapter 5. Dashed black curve represents simulation of H^+ impinging on Al inside a box with the same parameters as in the H^+ -Au simulation (see Table 6.1). **b)** Electron charge around the projectile obtained within a Bader charge analysis for the three systems. Bader volumes for the Au and Al simulation in the same box differ by less than 1%. **c)** Adsorbate level width as defined in Equation 3.5. **d)** Adsorbate level position with respect to the Fermi energy as defined in Equation 3.5.

6.4 Results

In Figure 6.5 we present results for the simulation of an H^+ scattering off the above described Au_{188} -cluster. The initial kinetic energy is chosen to coincide with the kinetic energy of the $H^+ - Al_{188}$ system at $z = 9$ bohr, i.e. $E_{kin}^{init} \approx 10.55$ eV.

As long as the projectile is charged and sufficiently far away from the surface, an image charge builds up in the metal. For different metals, this results in very similar attractive potentials and very similar differences in the kinetic energy of the projectile, as long as the position of the image plane z_{image} is comparable. Here: $z_{image}^{Au} \approx 2.14$ bohr^[295] and $z_{image}^{Al} \approx 3.14$ bohr.^[106] Figure 6.5a shows the kinetic energy of the projectile with respect to the distance z from the uppermost atomic layer for the simulation employing an Al_{188} -cluster and an Au_{188} -cluster. Differences between the $H^+ - Au$ and $H^+ - Al$ systems are very small, the slightly higher kinetic energy of the $H^+ - Au$ (ca. 100 meV faster) at $z \approx 6$ bohr can be explained with the help of Figure 6.5b, the charge transfer sets in closer to the surface allowing for the projectile to travel a longer distance within the attractive image potential and thus gaining more kinetic energy.

The valence s orbitals of Au are more extended as compared to Al, which may yield a broader adsorbate level width for H in front of the Au surface and therewith a higher tunneling rate. However, this is not observed in the simulation. As can be seen from Equation 1.9, the adsorbate level width is determined by the coupling between the H 1s level and the Kohn-Sham states of the metal, i.e. the local density of states (LDOS) of the metal. The smaller adsorbate level width for the H–Au-system is a consequence of the higher LDOS for the Al as compared to Au in the energy range where the H 1s orbital is located, i.e. at the lower band edge E_{VB} .¹ At the lower band edge, the LDOS for both metals can be approximated by a three-dimensional free electron gas, i.e.:^[312]

$$LDOS(E) \propto \kappa \cdot \sqrt{E - E_{VB}} \quad (6.4)$$

For Au, this only holds in the energy range where the d -electrons can be neglected. It is $E_{VB}^{Au} = -13.53$ eV vs. vacuum and $E_{VB}^{Al} = -14.9$ eV vs. vacuum, furthermore from the work of Papaconstantopoulos^[312] it can be obtained that at the lower valence band edge $\kappa_{Au} \approx \kappa_{Al}$. Therefore, in case of the here employed Au-cluster simulations the coupling between the H 1s level and the Kohn-Sham states of the Au-cluster is smaller than with the Kohn-Sham states of the Al-cluster. In consequence, the adsorbate level width is smaller and therefore, the tunneling rate is minor.

Compared to the s -electrons, the d -electrons of Au are located closer to the nuclei. In our study, we did not find indications that they play a relevant role in the electronic charge transfer investigated here. Up to the distance where the charge transfer sets in, the adsorbate level position is located at an energy where the PDOS of the Au can be described by Equation 6.4, i.e. below the electronic d -band of Au. Therefore the coupling between the adsorbate level with the d -band is small and the influence of the d -band on the tunneling rate is small, too. Once the charge transfer sets in, it occurs in a comparatively small range of z with an exponentially increasing charge transfer rate, see also subsection 3.3.4.

¹In case of the here employed clusters E_{VB} is approximated by the position of the lowest energy state at \bar{r} .

A notable influence of the coupling between the adsorbate level and the Au d -band on the charge transfer is not observed here.

6.5 Summary

In this chapter, the charge transfer between a hyperthermal proton (H^+) projectile impinging normally on an Au(111) surface modeled by an Au_{188} -cluster was investigated. Computational parameters were tested and analyzed in-detail, employing a non-binding pseudo-Hydrogen and an antiproton \bar{p} . We study the proton impact on an Au_{188} -cluster with kinetic energy of approximately 10 eV. This allows for a comparison to the previous chapter 3, 4 and 5 where the interaction between a hyperthermal H^+ and an Al(111) surface modeled by a cluster was investigated.

Notably, regarding charge transfer distances, differences for the H^+ /Au and the H^+ /Al are very small. In case of Au the maximum charge transfer occurs at a distance z between projectile and surface of $z = 4.63$ bohr (Al: 4.76 bohr, see chapter 5), setting in slightly closer to the surface in case of the Au-cluster. This was traced back to a lower LDOS for the Au_{188} -cluster and thus a narrower adsorbate level width and a smaller tunneling rate. Note, the difference is less than the difference for the maximum charge transfer distance observed in chapter 4 for H^+ /Al(111) between a simulation employing a LDA XC-functional and a simulation employing a GGA XC-functional.

Zeb et al.^[138] investigated the propagation of a proton through an Au bulk. They came to the conclusion, that as soon as the electronic excitation from electronic friction effects extends to the electronic d -band, additional friction from the d -electrons can be observed. The influence of the substrate d -electrons for the here investigated charge transfer is minor. This is a consequence of the position of the adsorbate level at the distance where the charge transfer sets in. At that distance, the coupling of the projectile's $1s$ level to the d -electrons is small and the influence of the d -electrons on the adsorbate level width and therewith connected the influence on the tunneling rate is small, too. Once the charge transfer sets in, it occurs in a comparatively small range of z with an exponentially increasing charge transfer rate.

The present work shows detailed *ab-initio* investigations of hyperthermal ions impinging on metal surfaces which are modeled by finite clusters. Time-dependent density-functional theory-molecular dynamics simulations were employed to describe the energy transfer and the electronic charge transfer between surface and projectile.

In his review, comparing the scattering of neutral projectiles and ionic projectiles which are or are not neutralized in grazing incidence experiments, Winter^[105] traces back energy and angle shifts observed in the spectra of the projectile after scattering at the metal surface to an image charge effect. As he points out, this effect should provide a means to experimentally estimate the neutralization distance of the H^+ projectile by observation of the kinetic energy transfer. The acceleration and deceleration of the projectile by the attractive force from its image charge – as long as it is not neutralized – affects the kinetic energy and angle distribution of the scattered (neutralized) particle.

Here we adapted the ideas by Winter and simulated hyperthermal H^+ and H^0 scattering with perpendicular incidence on an Al(111) and an Au(111)-surface represented by a cluster from *ab initio*.

Charge Transfer In this work, the charge transfer between a metal surface and an incoming projectile was investigated. The influence for different initial kinetic energies, impact sites, XC-functionals, and substrate materials was analyzed.

For H^+ impact on the on-top Al(111) surface site of the cluster kinetic energies of $E_{\text{kin}}^{\text{init}} = 2 \text{ eV}$, 10 eV and 50 eV were considered. The maximum in the charge transfer rate occurs at a distance above the surface of 5.13 bohr, 4.76 bohr, and 4.18 bohr, respectively. In these simulations, an AGGA XC-functional was employed.

The major source challenging the accuracy of DFT calculations originates in the unknown expression of the exchange and correlation (XC)-functional and the approximations to it. For the TDDFT simulations we employed the adiabatic approximation to the time-dependent XC-functional. As of today, numerically feasible non-adiabatic XC-functionals do not exist. The influence of the approximation to the ground-state XC-functional was analyzed by employing two different numerically feasible flavours of XC-functionals. Here the adiabatic local density approximation (ALDA) and adiabatic generalized gradient approximation (AGGA) XC-functionals. For the ALDA, an outwards shift of the charge transfer is observed. The maximum of the charge transfer rate is shifted by approximately 0.25 bohr ($E_{\text{kin}}^{\text{init}} = 10 \text{ eV}$). This comes from the differences in the description of the electronic ground-state of the H-atom.

To estimate the influence of the impact site upon charge transfer, we calculated two impact points where the most differences would be expected. These are the on-top and the fcc-hollow position. The distance of charge transfer for a projectile with initial kinetic energy 10 eV between impact sites top and fcc-hollow is very small (< 0.05 bohr). However, the kinetic energy transfer is distinguishably different due to differences in both, the adsorption curves and the H^+ -Al(111) interaction potential as discussed below.

The charge transfer as obtained in the TDDFT-MD simulation could be reproduced with a tight-binding Brako-Newns-Anderson (BNA)-like model Hamiltonian. The numerically very efficient tight-binding Hamiltonian takes for each kinetic energy two simple, distance-dependent functions as input and yields very good agreement with the TDDFT-MD simulation. The distance-dependent functions were obtained from the TDDFT-MD simulation by calculating a PDOS onto the Kohn-Sham states obtained from a frozen-density calculation. Employing a rate equation, it was shown that the charge transfer rate as obtained from the TDDFT-MD simulation and the charge transfer rate calculated by Deutscher et al.^[153] and by Nordlander and Tully^[66,152,302] result in quantitatively similar charge transfer distances despite a very different overall behavior. It was shown that for the calculation of the charge transfer distance only the charge transfer rate prior to the charge transfer is important, where the TDDFT result and the literature data are of comparable magnitude.

To investigate the influence of the density of states (DOS) of the target material we employed simulations for H^+ impact on Au. Notably, comparing the charge transfer distances of H^+ impinging on the (111) surface site of an Al cluster and on an Au cluster, differences are very small. In case of Au the maximum charge transfer occurs at a distance between projectile and surface of $z_{Au} = 4.63$ bohr and $z_{Al} = 4.76$ bohr, i.e. setting in slightly closer to the surface in case of the Au-cluster. This was traced back to the local density of states (LDOS) for the Au and Al-clusters. For the Au-cluster, at the lower valence band edge the LDOS at the same energy distance from vacuum is lower resulting in a narrower adsorbate level width and a smaller tunneling rate.

Energy Transfer As a next step, the energy dynamics upon impact of H^+ on Al(111) were investigated in detail. An H^+ carries an additional excitation energy of around 13.6 eV as compared to an H^0 projectile which upon neutralization are to be transferred to the cluster. The following mechanisms for an energy transfer have been considered (please note that these are in some cases not clearly separable from each other): the energy transfer connected to the charge transfer, energy dissipation into phononic degrees of freedom, energy dissipation from electronic friction of the projectile propagating within the target and from building up the image charge, and the excitation of plasmons.

The energy transfer between the projectile and the Al upon charge transfer was investigated by comparing the electronic energy of the time-dependent simulation from the value obtained in a ground-state calculation. For impact upon the on-top site, this excitation energy amounts to $E_{exc} = 8.6 \text{ eV}/9.4 \text{ eV}/11.3 \text{ eV}$ for $E_{kin}^{init} = 2 \text{ eV}/10 \text{ eV}/50 \text{ eV}$ respectively, at $z = 5$ bohr on the outgoing trajectory. In case of the impact on the fcc-hollow site, the electronic friction effects from propagation within the bulk were subtracted by comparing to a time-dependent simulation with an H^0 projectile. The difference $\Delta \tilde{E}_{exc}$ at $z_{exit} = 5$ bohr be-

tween the on-top and the fcc-hollow impact sites for $E_{\text{kin}}^{\text{init}} = 2 \text{ eV}$, 10 eV , and 50 eV amounts to $\Delta\tilde{E}_{\text{exc}} = 0.55 \text{ eV}$, 0.61 eV , and 0.45 eV (higher value of E_{exc} for impact on-top).

The excitation energy E_{exc} after charge transfer can be read from the the artificial Kohn-Sham electronic excitation spectrum. One may have anticipated that the charge transfer from the surface into the projectile's adsorbate level would exhibit a single peak in the Kohn-Sham electronic excitation spectrum. However, the Kohn-Sham electronic excitation spectra show excitations distributed over a wide range of electronic states, which cannot come from Auger effects because they are not contained in the current simulation. To investigate this further, we calculated a frozen-density adsorbate level position $\epsilon_a^{\text{frozen}}$. Technically, the excitation within the spectrum was traced back to the transition of $\epsilon_a^{\text{frozen}}$ from an unbound and unoccupied Hydrogen $1s$ level to an occupied one in a chemical bond with the surface. During this transition, a resonant neutralization between electronic states of the surface towards the projectile occurs resulting in the above described Kohn-Sham electronic excitation spectrum. In principle, electronic excitation spectra are measurable in experiments, e.g. with the sophisticated experimental setup by Diesing et al.^[80,81]

The energy transfer into phononic degrees of freedom was estimated by simulating a central collision between the H^+ projectile and the Al cluster (impact on-top) with two simulations. For the first one, the Al atoms were kept fixed, while for the second one, the Al atom coordinates at the impact site were allowed to move. The difference in kinetic energy ΔE_{kin} after scattering for a head-on collision between an H^+ projectile and an Al atom at the on-top site are $\Delta E_{\text{kin}} = -0.28/-1.21/-6.51 \text{ eV}$ for $E_{\text{kin}}^{\text{init}} = 2/10/50 \text{ eV}$, respectively. These results are in agreement with an estimated energy transfer in a central elastic collision.

A first step towards making our results more accessible to experiments was to extrapolate the obtained data for the finite clusters to the extended Al(111) surface. It was found that, in order to obtain identical exit velocities in case of projectiles with $E_{\text{kin}} \approx 50 \text{ eV}$, H^+ needs to be initially faster than H^0 by about 1.2 eV (on-top trajectory) to 0.4 eV (fcc-hollow trajectory). In contrast, for projectiles with $E_{\text{kin}} \approx 2 \text{ eV}$ the sign changes and H^+ needs to be initially slower than H^0 by about 0.8 eV (on-top trajectory) to 1.0 eV (fcc-hollow trajectory). This was explained by the difference between the ground-state potential energy surface and the $\text{H}^+ - \text{Al}(111)$ interaction potential which is repulsive in the region of neutralization.

Outlook The here presented *ab initio* simulations are based on TDDFT Ehrenfest MD simulations that employ the adiabatic approximation to the exchange correlation functional. With the current approach, Auger effects are not included which puts strict limitations to the range of materials that can reliably be investigated. In the literature it is argued that this may be due to the adiabatic approximation. Future developments of approximations that do include time-dependency into the evaluation of the XC-functional are likely to help answering this question.

Furthermore, there is a well-known difficulty to describe long-range correlations with semilocal approximations for the XC energy functional in ground-state calculations. For example, when describing the dissociation of H_2 with a semilocal XC-functional, an arti-

ficial transition to a spin-polarized system is in general used to describe total energies at large atom separation.^[313,314] The simulations of H^+ employed here do not contain this artificial spin-transition because the initial state is spin-unpolarized and does not allow for a spin break during the simulation. In the simulations employed here, this artificial spin-transition is expected to play a minor role. However, when studying further combinations of projectile and target materials, this issue is likely to become more important. Therefore, simulations employing XC-functionals that contain non-local contributions to the evaluation of the XC-potential would be desirable.

In chapter 5 it was argued that the employed cluster results can be used to describe the interaction between H^+ and a surface for normal incidence. Experiments like the ones by Winter^[105] for H^+ scattering are often performed under grazing incidence where TDDFT-MD simulations that employ a cluster may not yield reliable results. There, TDDFT-MD simulations that employ a periodic surface may be better suited. For the simulation of higher kinetic energies, core electron promotion may become important, too.^[315] In such case, the here employed pseudopotential approach is not appropriate. One solution may be to treat less electrons as frozen-in core states or to employ an all-electron simulation.

A natural way to extend the here investigated simulations is to analyze further projectile and/or substrate materials. For example including impurities or contamination of the substrate material by e.g. considering additional oxygen adsorbates may be relevant. An investigation of hyperthermal ionic alkaline metal projectiles or ionic earth-alkaline metal projectiles scattering on different coinage metal surfaces like e.g. in Refs. [39, 40] may also be of interest.

A.1 Kohn-Sham Eigenvalue of H Atom

In Figure A.1 we present the eigenvalues of a charged H pseudopotential. The electronic charge is varied between 10^{-6} electrons and 1 electron. Calculations were performed with fhi98PP.

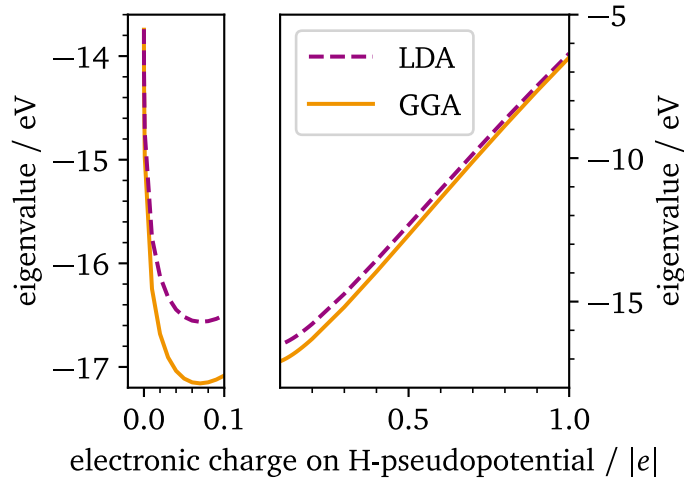


Figure A.1: Electronic charge around an H atom and the corresponding 1s Kohn-Sham eigenvalue calculated for the LDA and the GGA-PBE XC-functional. Calculation performed with fhi98PP.

A.2 Additional Information on Adsorbate Level Width

This section contains additional information to section 3.3. In Figure A.2 we present the distance dependent adsorbate level width in a logarithmic scale.

To facilitate usage of the data given in Figure 3.4 we applied the following fit functions for the adsorbate level position $\varepsilon_a^{\text{frozen}}$ and width $2\Gamma^{\text{frozen}}$:

| E_{kin} | $\Gamma_{2\text{eV}}$ 2 eV | $\Gamma_{10\text{eV}}$ 10 eV | $\Gamma_{50\text{eV}}$ 50 eV | $\Gamma_{1\text{keV}}$ 1 keV |
|-----------------------|-------------------------------|---------------------------------|---------------------------------|---------------------------------|
| Γ_0 | $1.76 \pm 22\%$ | $2.38 \pm 10\%$ | $3.43 \pm 15\%$ | $10.59 \pm 31\%$ |
| χ | $5.76 \pm 17\%$ | $4.25 \pm 10\%$ | $3.22 \pm 11\%$ | $1.37 \pm 3\%$ |
| d_{crit} | $5.01 \pm 2\%$ | $4.66 \pm 1\%$ | $4.16 \pm 2\%$ | $2.40 \pm 13\%$ |
| $z_{T,\Gamma}$ | 5.0 | 4.5 | - | - |
| $a_{0,\Gamma}$ | 109.65 | 170.80 | - | - |
| $a_{1,\Gamma}$ | -73.55 | -121.18 | - | - |
| $a_{2,\Gamma}$ | $16.80 \pm 26\%$ | $29.29 \pm 54\%$ | - | - |
| $a_{3,\Gamma}$ | $-1.29 \pm 25\%$ | $-2.38 \pm 53\%$ | - | - |
| I_0 | -9.187 | -9.187 | -9.187 | - |
| α | $1.06 \cdot 10^{12}$ | $3.58 \cdot 10^6$ | $4.18 \cdot 10^3$ | - |
| κ | 2.251 | 1.684 | 1.279 | - |
| z_{T,ε_a} | 5.2 | 4.75 | - | - |
| a_{0,ε_a} | 730.12 | 768.64 | - | -32.86 |
| a_{1,ε_a} | -516.68 | -571.31 | - | 13.59 |
| a_{2,ε_a} | 120.88 | 140.82 | - | -2.60 |
| a_{3,ε_a} | -9.37 | -11.55 | - | 0.17 |

Table A.1: Parameters for fit curves shown in Figure 3.4. Energies are in eV, distances are in bohr. Note that $a_{0,\Gamma}$, $a_{1,\Gamma}$, and a_{0,ε_a} , a_{1,ε_a} are obtained from the continuity constraints in Equation A.2 and Equation A.1. Given accuracy are the standard derivations of fit parameters.

$$\Gamma(z) = \begin{cases} \Gamma_0 / (1 + e^{\chi \cdot (z - d_{\text{crit}})}) & \text{for } z > z_{T,\Gamma} \\ a_{0,\Gamma} + a_{1,\Gamma}z + a_{2,\Gamma}z^2 + a_{3,\Gamma}z^3 & \text{for } z < z_{T,\Gamma} \end{cases} \quad (\text{A.1})$$

$$\varepsilon_a^{\text{frozen}}(z) = \begin{cases} I_0 + \alpha e^{-\kappa^2 z} & \text{for } z > z_{T,\varepsilon_a} \\ a_{0,\varepsilon_a} + a_{1,\varepsilon_a}z + a_{2,\varepsilon_a}z^2 + a_{3,\varepsilon_a}z^3 & \text{for } z < z_{T,\varepsilon_a} \end{cases} \quad (\text{A.2})$$

with the additional constraint that $\Gamma(z)$ and $\frac{d}{dz}\Gamma(z)$ are continuous at $z_{T,\Gamma}$. $\varepsilon_a^{\text{frozen}}(z)$ and $\frac{d}{dz}\varepsilon_a^{\text{frozen}}(z)$ are continuous at z_{T,ε_a} .

The choice of the fit curves originates in the work of Deutscher et al., see Ref. [153]. Fit parameters are given in Table A.1.

The adsorbate level widths $\Gamma_{1\text{keV}}$ and $\Gamma_{10\text{eV}}$ are expected to coincide for large z . This is not the case for $z \approx 7$ bohr. For the 10 eV projectile, a small electronic charge transfer towards the projectile yields a decrease in the eigenvalue of the projectile (see Figure A.1) and lowers the transition rate.

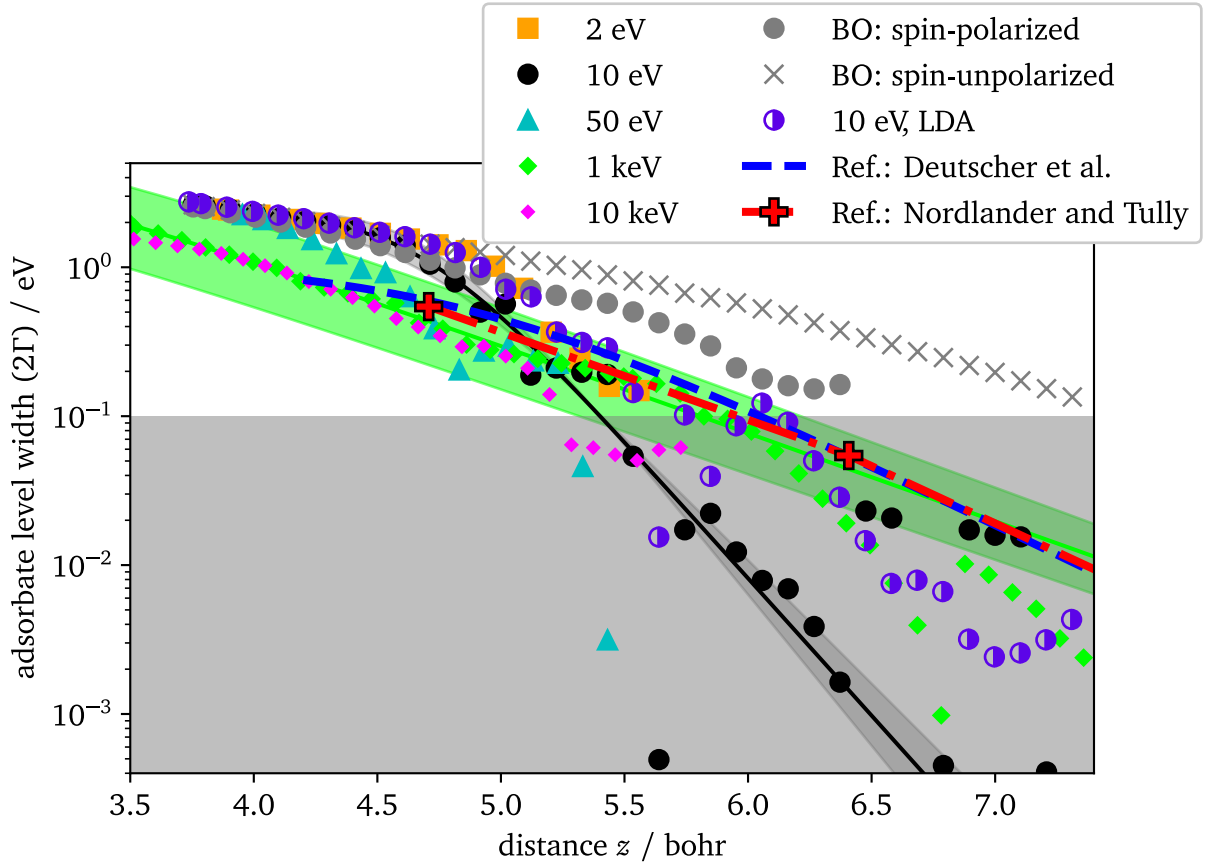


Figure A.2: Adsorbate level width as shown in Figure 3.4 on page 52 in a logarithmic scale. The grey drawn area marks widths below 100 meV, i.e. adsorbate level widths below the accuracy of the present calculation. Confidence interval drawn as obtained from the fitting procedure, values are given in Table A.1. Please note that this is not a sharp border but serves as a mere reminder. Reference data are from Deutscher et al.^[153] and from Nordlander and Tully^[66,152,302] (linear interpolation meant as guide to the eye).

In a ground-state DFT calculation, the total energy of the system is—for the exact XC-functional—equal to the ground-state energy of the interacting many body system. In subsection 2.3.3 it was discussed that upon time propagation in an Ehrenfest-MD simulation, the many-body system as well as a TDDFT system that employs an adiabatic XC-functional conserve the total energy (see Equation 2.46). Therefore, provided that both simulations start from ground-state, under a time-dependent perturbation, the electronic excitation energy of a many body system may be calculated with the help of a TDDFT simulation.

This chapter discusses the connection between the electronic excitation energy E_{exc} as defined in Equation 3.13 and the Kohn-Sham electronic excitation spectrum $\delta\Lambda^{\text{BO}}$ as defined in Equation 3.11.

It will be shown that in case of small differences between the time-dependent electronic density and the ground-state electronic density, the excitation energy E_{exc} can also be approximated by the Kohn-Sham electronic excitation spectrum $\delta\Lambda^{\text{BO}}$. This is a necessary condition for the interpretation of $\delta\Lambda^{\text{BO}}$ as an approximation to the excitation spectrum. Please note that the here presented derivation is very closely related to the derivation of the linear response formulation of TDDFT, see e.g. Refs. [316, 317] or chapter 4.5 of Ref. [222]. For the benefit of the reader, the following discussion is matched to the excitation energy within the Kohn-Sham spectrum. The discussion is based on notes by E. Pehlke.^[318]

Let the system at $t = 0$ be in its electronic ground-state. Alternatively, one can assume a system consisting of different subsystems which are well separated and in its electronic ground-state each (e.g. the case of a proton far above a metal surface). The total electronic energy of the combined system can be approximated as the sum of the electronic energy of the subsystems. The corresponding Kohn-Sham ground-state wavefunctions at $t = 0$ are termed $|\varphi_{k,t=0}\rangle$. Then, the system evolves as a function of time due to the atomic motion which induces a time-dependent potential obeying the time-dependent Kohn-Sham equations:

$$\left(-\frac{1}{2}\nabla^2 + v_{\text{eff}}\right)|\Psi_j(t)\rangle = i\frac{\partial}{\partial t}|\Psi_j(t)\rangle, \quad (\text{B.1})$$

This results in time-dependent wavefunctions $|\Psi_j(t)\rangle$. For practicality we choose a discrete set of times t with a set of atomic coordinates $\mathbf{R}(t)$ for which we calculate again the electronic Kohn-Sham ground-state with ground-state Kohn-Sham orbitals $|\varphi_{k,t}\rangle$. These are solutions to the Kohn-Sham equations:

$$\left(-\frac{1}{2}\nabla^2 + v_{\text{eff},t}^0\right)|\varphi_{k,t}\rangle = \varepsilon_{k,t} |\varphi_{k,t}\rangle, \quad (\text{B.2})$$

where

$$v_{\text{eff},t}^0 = v(\mathbf{r}, t) + v_{\text{H}}[n_t^{\text{BO}}](\mathbf{r}) + v_{\text{XC}}[n_t^{\text{BO}}](\mathbf{r}) \quad (\text{B.3})$$

and $\varepsilon_{k,t}$ are the eigenvalues of the electronic ground-state for an atomic geometry $\mathbf{R}(t)$.

The density n_t^{BO} can be calculated by:

$$n_t^{\text{BO}}(\mathbf{r}) = \sum_k' |\varphi_{k,t}(\mathbf{r})|^2 \quad (\text{B.4})$$

The primed sum \sum' refers to a summation over the occupied states. The energy of the electronic ground-state E_t^{BO} can be calculated as:^[178]

$$E_t^{\text{BO}} = \sum_k' \varepsilon_{k,t} - E_{\text{H}}[n_t^{\text{BO}}] + E_{\text{XC}}[n_t^{\text{BO}}] - \int v_{\text{XC}}[n_t^{\text{BO}}] \cdot n_t^{\text{BO}} d^3\mathbf{r} \quad (\text{B.5})$$

The solutions to the time-dependent Kohn-Sham equations $|\Psi_j(t)\rangle$ can be developed in terms of the ground-state Kohn-Sham orbitals for the same atomic geometry at time t , which are the $|\varphi_{k,t}\rangle$:

$$|\Psi_j(t)\rangle = \sum_{k=1}^{\infty} |\varphi_{k,t}\rangle \langle \varphi_{k,t} | \Psi_j(t) \rangle \quad (\text{B.6})$$

And the density $n(\mathbf{r}, t)$ can be written as:

$$n(\mathbf{r}, t) = \sum_j' |\Psi_j(\mathbf{r}, t)|^2 \quad (\text{B.7a})$$

$$= \sum_j' \sum_{k,l=1}^{\infty} \varphi_{k,t}^* \varphi_{l,t} \langle \Psi_j(t) | \varphi_{k,t} \rangle \langle \varphi_{l,t} | \Psi_j(t) \rangle \quad (\text{B.7b})$$

$$= \sum_{k,l=1}^{\infty} \varphi_{k,t}^* \varphi_{l,t} C_{k,l}, \quad (\text{B.7c})$$

where $C_{k,l} := \sum_j' \langle \Psi_j(t) | \varphi_{k,t} \rangle \langle \varphi_{l,t} | \Psi_j(t) \rangle$. The primed sum \sum' refers to a summation over the states which are occupied at $t = 0$.

An energy $E^{\text{TD}}(t)$ can be defined, that employs the adiabatic approximation to the XC-functional:

$$\begin{aligned} E^{\text{TD}}(t) := & \sum_j' \langle \Psi_j(t) | -\frac{1}{2}\nabla^2 | \Psi_j(t) \rangle + E_{\text{H}}[n(\cdot, t)] + E_{\text{xc}}[n(\cdot, t)] \\ & + \int v(\mathbf{r}, t) \cdot n(\mathbf{r}, t) d^3\mathbf{r} \end{aligned} \quad (\text{B.8})$$

At $t = 0$, this energy is equal to the electronic energy of the ground-state system. If the system consists of several subsystems, each in its electronic ground-state, then $E^{\text{TD}}(t = 0)$ is approximately equal to the sum of the electronic energies of the isolated systems (e.g. the electronic energy of a metal surface plus the electronic energy of an ion far above the surface).

As discussed in the beginning of this appendix, when employing Ehrenfest MD simulations, the sum of kinetic energy of the ions and $E^{\text{TD}}(t)$ is constant and in a ground-state DFT calculation, the total energy of the system is—for the exact XC-functional—equal to the ground-state energy of the interacting many body system. Therefore, $E^{\text{TD}}(t)$ can be interpreted as the electronic energy of the time-dependent system.

This means that the electronic excitation energy E_{exc} can be defined as the difference between these two terms, i.e.:

$$E_{\text{exc}} := E^{\text{TD}}(t) - E_t^{\text{BO}} \quad (\text{B.9})$$

This is identical to Equation 3.13.

$E^{\text{TD}}(t)$ shall be expressed in terms of the Kohn-Sham eigenvalues $\varepsilon_{k,t}$ of the ground-state solution to the Kohn-Sham equations for the atomic geometry at time t (Equation B.10b). Therefore, in Equation B.10a a 0 is added to Equation B.8, i.e. the difference between left and right side of Equation B.3:

$$E^{\text{TD}}(t) = \sum_j' \langle \Psi_j(t) | -\frac{1}{2} \nabla^2 + v_{\text{eff},t}^0 | \Psi_j(t) \rangle + E_{\text{H}}[n(\cdot, t)] + E_{\text{xc}}[n(\cdot, t)] - \int v_{\text{H}}[n_t^{\text{BO}}] \cdot n(\mathbf{r}, t) d^3 \mathbf{r} - \int v_{\text{XC}}[n_t^{\text{BO}}] \cdot n(\mathbf{r}, t) d^3 \mathbf{r} \quad (\text{B.10a})$$

$$= \sum_j' \sum_{k=0}^{\infty} \varepsilon_{k,t} |\langle \Psi_j(t) | \varphi_{k,t} \rangle|^2 + E_{\text{H}}[n(\cdot, t)] + E_{\text{xc}}[n(\cdot, t)] - \int v_{\text{H}}[n_t^{\text{BO}}] \cdot n(\mathbf{r}, t) d^3 \mathbf{r} - \int v_{\text{XC}}[n_t^{\text{BO}}] \cdot n(\mathbf{r}, t) d^3 \mathbf{r} \quad (\text{B.10b})$$

Inserting E_t^{BO} (Equation B.5) and $E^{\text{TD}}(t)$ (Equation B.10b) into the definition of E_{exc} (Equation B.9) yields, after reordering:

$$E_{\text{exc}} = \underbrace{\sum_{k=1}^{\infty} \varepsilon_{k,t} \left[\left(\sum_j' |\langle \Psi_j(t) | \varphi_{k,t} \rangle|^2 \right) - \Theta(\varepsilon_{F,t} - \varepsilon_{k,t}) \right]}_{\tilde{E}_{\text{exc}}^{\text{BO}}} + E_{\text{H}}[n(\cdot, t)] + E_{\text{H}}[n_t^{\text{BO}}] - \int v_{\text{H}}[n_t^{\text{BO}}] \cdot n(\mathbf{r}, t) d^3 \mathbf{r} + E_{\text{xc}}[n(\cdot, t)] - E_{\text{xc}}[n_t^{\text{BO}}] - \int v_{\text{XC}}[n_t^{\text{BO}}] \cdot n(\mathbf{r}, t) d^3 \mathbf{r} + \int v_{\text{XC}}[n_t^{\text{BO}}] \cdot n_t^{\text{BO}} d^3 \mathbf{r} \quad (\text{B.11})$$

Note, the $\varepsilon_{F,t}$ term in the Θ function marks the highest occupied energetic level and allows to include the term into the summation. The underbraced term $\tilde{E}_{\text{exc}}^{\text{BO}}$ represents the energy within the spectrum $\delta\Lambda^{\text{BO}}$ (see Equation 3.12).

For further insight into the remaining terms, a Taylor expansion at n_t^{BO} will be performed:

$$\begin{aligned} E_{\text{XC}}[n(\cdot, t)] &\approx E_{\text{XC}}[n_t^{\text{BO}}] + \int v_{\text{XC}}[n_t^{\text{BO}}](\mathbf{r}) \cdot (n(\mathbf{r}, t) - n_t^{\text{BO}}(\mathbf{r})) d^3\mathbf{r} \\ &\quad + \frac{1}{2} \int d^3\mathbf{r} \int d^3\mathbf{r}' \left. \frac{\delta^2 E_{\text{XC}}[n]}{\delta n(\mathbf{r}) \delta n(\mathbf{r}')} \right|_{n=n_t^{\text{BO}}} (n(\mathbf{r}, t) - n_t^{\text{BO}}(\mathbf{r})) \cdot (n(\mathbf{r}', t) - n_t^{\text{BO}}(\mathbf{r}')) \\ &\quad + \dots \end{aligned} \quad (\text{B.12})$$

$$\begin{aligned} E_{\text{H}}[n(\cdot, t)] &\approx E_{\text{H}}[n_t^{\text{BO}}] + \int v_{\text{H}}[n_t^{\text{BO}}](\mathbf{r}) \cdot (n(\mathbf{r}, t) - n_t^{\text{BO}}(\mathbf{r})) d^3\mathbf{r} \\ &\quad + \frac{1}{2} \int d^3\mathbf{r} \int d^3\mathbf{r}' \frac{(n(\mathbf{r}, t) - n_t^{\text{BO}}(\mathbf{r})) \cdot (n(\mathbf{r}', t) - n_t^{\text{BO}}(\mathbf{r}'))}{|\mathbf{r} - \mathbf{r}'|} \\ &\quad + \dots \end{aligned} \quad (\text{B.13})$$

Inserting Equation B.12 and Equation B.13 into Equation B.11 yields:

$$\begin{aligned} E_{\text{exc}} &= \tilde{E}_{\text{exc}}^{\text{BO}} \\ &\quad + \frac{1}{2} \int d^3\mathbf{r} \int d^3\mathbf{r}' \frac{(n(\mathbf{r}, t) - n_t^{\text{BO}}(\mathbf{r})) \cdot (n(\mathbf{r}', t) - n_t^{\text{BO}}(\mathbf{r}'))}{|\mathbf{r} - \mathbf{r}'|} \\ &\quad + \frac{1}{2} \int d^3\mathbf{r} \int d^3\mathbf{r}' \left. \frac{\delta^2 E_{\text{XC}}[n]}{\delta n(\mathbf{r}) \delta n(\mathbf{r}')} \right|_{n=n_t^{\text{BO}}} (n(\mathbf{r}, t) - n_t^{\text{BO}}(\mathbf{r})) \cdot (n(\mathbf{r}', t) - n_t^{\text{BO}}(\mathbf{r}')) \\ &\quad + \dots \end{aligned} \quad (\text{B.14})$$

In case of the simulation of a proton impinging on an Al-metal surface, the term $(n(\mathbf{r}', t) - n_t^{\text{BO}}(\mathbf{r}'))$ does not vanish because the difference of the electronic density around a proton and its 'BO-system' (an H^0) is large. Therefore, the energy $\tilde{E}_{\text{exc}}^{\text{BO}}$, which is the energy within the spectrum $\delta\Lambda^{\text{BO}}$, is not to be interpreted as the excitation energy E_{exc} .

As long as the excitation is delocalized the energy within the spectrum is approximately equal to the excitation energy. This is a necessary condition for the interpretation of $\delta\Lambda^{\text{BO}}$ as an excitation spectrum. Please note that the many-body spectrum may be different from the Kohn-Sham electronic excitation spectrum because Kohn-Sham energies in general differ from quasi particle energies.

The integral terms in Equation B.14 are closely related to the Hartree term and the XC-kernel often discussed in the context of linear response (LR) TDDFT, see e.g. Refs. [222, 316, 317]. Especially against the background of charge transfer excitations, improved approximations like range-separated hybrid functionals for the XC-kernel are being successfully employed in LR calculations.^[317] However, these are numerically extremely demand-

ing exceeding the currently explorable feature space of the here employed TDDFT-MD simulations.

For a general discussion on electronic excitations obtained in TDDFT simulations see e.g. Refs. [222, 319]. For a discussion on charge transfer excitations please refer e.g. to Refs. [317, 320].

This chapter contains additional information for subsection 3.4.3. Here, we estimate the amount of energy deposited into the excitation of plasmons upon impact of the 10 eV proton on the Al_{188} -cluster. We take a two-step approach.

First, we calculate the adsorption spectra of different nanoparticles and compare to reference data where possible. Second, we apply a laser pulse with a frequency relevant to the system for 10 periods and evaluate the time-development of the electric dipole moment in z direction.

1. As a first step, we reproduce the work of Zhang et al.^[321] and Varas et al.^[322] who investigated the adsorption spectra of a spherical Na_{331} (bcc) cluster with an experimental lattice constant of $a = 4.23$ and diameter $2R = 28.8$. Atoms are arranged symmetrical around a central atom. Na atoms were described by norm-conserving Troullier-Martins pseudopotentials with nonlinear core-correction and created with fhi98PP. To obtain adsorption spectra, we calculated with the TDDFT code Octopus the electronic ground-state of the system. Afterwards, the ground-state electronic system is perturbed at $t = 0$ by a delta-kick electric field $\mathbf{E}(\mathbf{r}, t) = \kappa_0 \delta(t) \cdot \mathbf{e}_z$, as implemented within Octopus. Here, we chose $\kappa_0 = 0.005$ a.u., i.e. small enough to ensure a linear response. Kohn-Sham wavefunctions are propagated in time with a time step $\Delta t = 0.06$ au for $T_{\text{max}} = 1200$ au. We chose a grid spacing of 0.5 bohr and a spherical simulation cell with radius 42 bohr.

The dynamical polarizability $\alpha(\omega)$ can then be calculated from the frequency representation of the induced time-dependent density $\delta n(\mathbf{r}, \omega)$:

$$\delta n(\mathbf{r}, \omega) = \int_0^{T_{\text{max}}} \delta n(\mathbf{r}, t) e^{(i\omega - \gamma)t} dt \quad (\text{C.1})$$

$$\alpha(\omega) = -\kappa_0^{-1} \int z \delta n(\mathbf{r}, \omega) d\mathbf{r} \quad (\text{C.2})$$

And the adsorption cross section σ can be calculated as $\sigma = \frac{4\pi\omega}{c} \text{Im}\alpha(\omega)$. We chose $\gamma = 0.1$ eV as a damping frequency.

Results are visualized in Figure C.1 together with the plasmon frequencies of the bulk plasmon ω_B . Values for the surface plasmon $\omega_S = \omega_B/\sqrt{2}$ and the Mie Plasmon $\omega_M = \omega_B/\sqrt{3}$ as obtained from a classical description (i.e. Drude metal) are

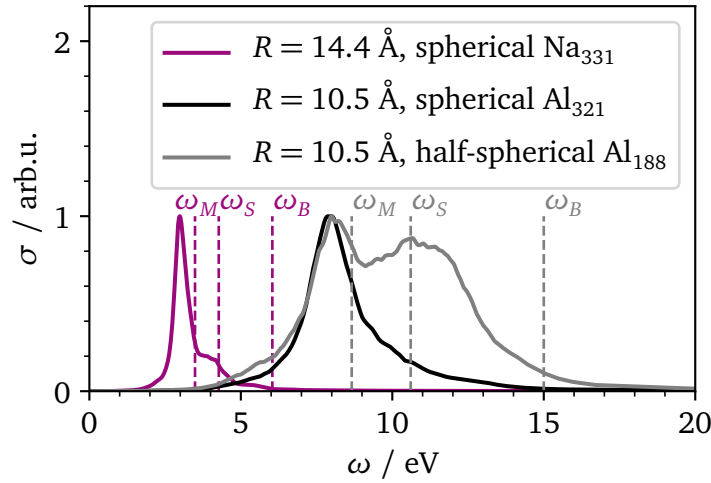


Figure C.1: Absorption cross section σ for a spherical Na_{331} (bcc) cluster, a spherical Al_{321} (fcc) cluster and the half-spherical Al_{188} cluster described in chapter 3. Vertical lines are frequencies $\omega_B^{\text{Na}} = 6.04 \text{ eV}$,^[321] and $\omega_B^{\text{Al}} = 15.0 \text{ eV}$.^[292] Here: $\omega_B = \sqrt{2} \cdot \omega_S = \sqrt{3} \cdot \omega_M$ as obtained in a classical picture.^[323]

additionally shown.^[323] The main plasmonic resonance of the Na_{331} cluster is at $\omega = 2.98 \text{ eV}$, which is the same value as obtained in Refs. [321, 322]. The authors of Ref. [321, 322] also obtained a value for a jellium cluster of $\omega = 3.17 \text{ eV}$. Barbry obtained a similar value in his simulations for a non-spherical and faceted Na_{380} cluster of 3.16 eV for jellium and 3.35 eV for the pseudopotential approach, the energy difference is traced back to the chosen geometry.^[324] For classical optics the main plasmonic resonance is at $\omega = 3.49 \text{ eV} = \omega_B / \sqrt{3}$. The difference was explained by the confining potential at the interface which is softer than in the classical picture, and therefore electronic oscillations are slowed down.^[322]

As a next step, we employ the same methodology to a spherical Al_{321} cluster (identical simulation parameters), see Figure C.1. We obtain a maximum resonance at $\omega = 7.99 \text{ eV}$ (classical optics: $\omega = \omega_B / \sqrt{3} = 8.66 \text{ eV}$). The difference is most probably of the same nature as in case of the Na cluster.

Additionally the adsorption cross section was calculated for the half-spherical Al_{188} cluster, see also Figure C.1 which also shows a main peak at $\omega = 7.99 \text{ eV}$ and a second peak at approximately $\omega = 10.6 \text{ eV}$. The second peak is likely to arise from the surface plasmon because it is located at the expected position. However, due to the very specific geometry of the Al_{188} cluster, the second peak is significantly broadened.

2. In the next step, we excite the spherical Al_{321} cluster and the semi-spherical Al_{188} cluster with a laser of a fixed frequency. The laser pulse is described by an electric field \mathbf{E} , where the x and y components are zero and the z component E_z is described

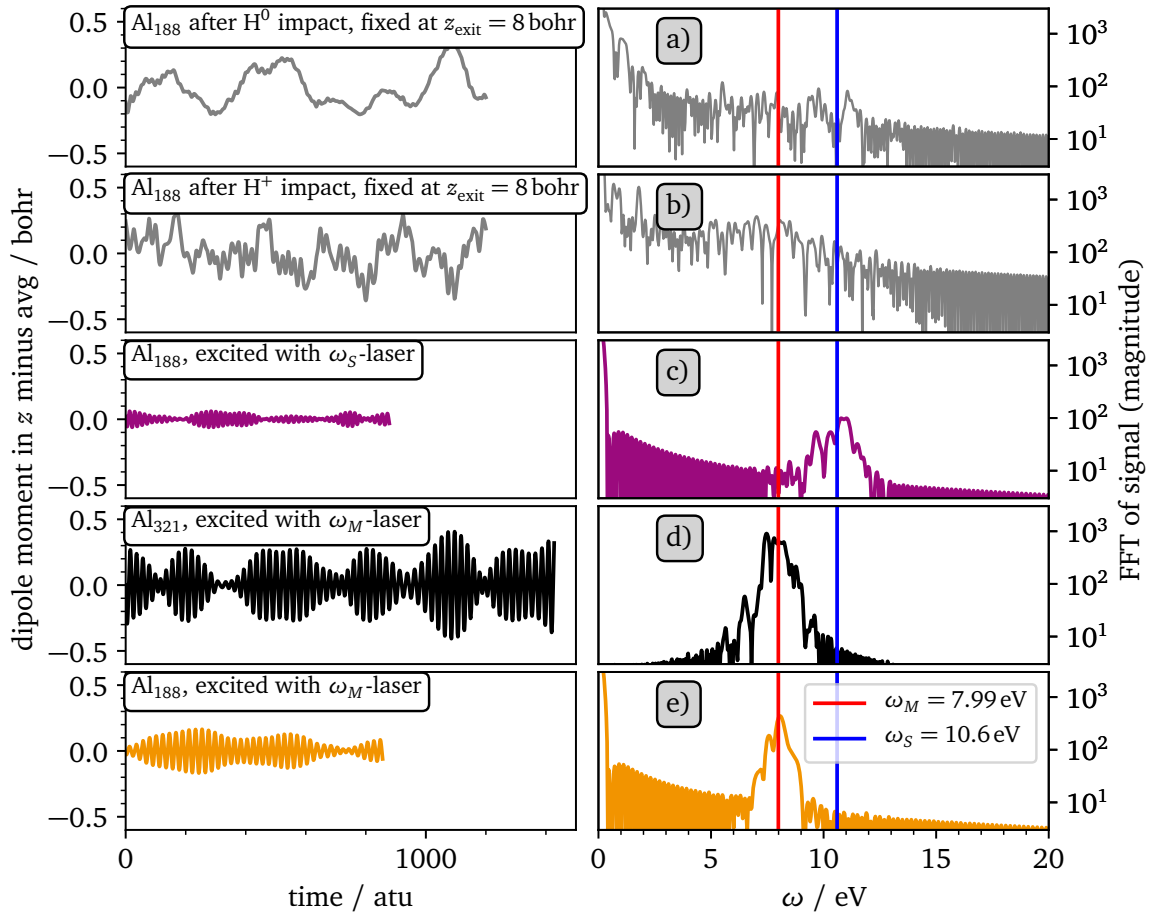


Figure C.2: **Left:** Time development of the electric dipole moment in z direction after different types of excitation. **Right:** Fourier transform of the signal. Details see text.

by the product of the excitation which is described by a function $g(t)$ and an envelope function $f(t)$:

$$E_z(t) = f(t) \cdot g(t) \cdot \Theta(t) \cdot \Theta(2\tau - t) \quad (\text{C.3})$$

$$f(t) = -f_0 \sin\left(\frac{\pi}{2} \frac{t}{\tau}\right) \quad (\text{C.4})$$

$$g(t) = g_0 \cos(\omega \cdot t), \quad (\text{C.5})$$

where Θ is the Heaviside function, $f_0 = 0.02$, $g_0 = 0.1$, $\tau = 5 \cdot \frac{2\pi}{\omega}$, i.e. the laser pulse is zero after 10 periods of excitation ($= 2\tau = 10 \cdot \frac{2\pi}{\omega}$). All values are given in atomic units.

After additional 5 periods have passed and the system is granted sufficient relaxation time, the time-development of the z component of the electric dipole moment is sampled. A visualization of the z component of the electric dipole moment after a total of 15 periods of the laser frequency (10 of which are excitation), is shown in Figure C.2c-e). Peaks of the laser excitation are clearly visible in the Fourier transform of the electric dipole moment in z direction.

Additionally, we perform TDDFT-MD simulations of an H^0 and an H^+ impinging on the Al_{188} cluster with initial kinetic energy $E_{kin}^{init} = 10$ eV at a starting distance of $z = 16$ bohr (identical to the simulations presented in chapter 3). We propagate the projectile towards the surface until an exit distance of $z_{exit} = 8$ bohr is reached. Then, we freeze the atomic geometry and only permit the electronic wavefunctions to develop in time. In this case, we also sample the time-development of the electric dipole moment in z direction which we present in Figure C.2a) and b).

Please note that the energy transfer into the electronic oscillation in Figure C.2c-e) is 0.14 eV, 0.76 eV, and 0.16 eV, respectively. Although the energy transfer into the Al_{321} cluster is comparatively high, the amplitude of the oscillation of the electric dipole moment in z direction that arises from the electronic charge transfer of the 10 eV H^+ projectile is even below the amplitude of the Al_{188} cluster excited with the frequency of the Mie plasmon. Therefore, we infer that the energy transfer into plasmon excitations is of similar magnitude, i.e. in the range of a few 100 meV. This is consistent with the results by Gras-Marti and Echenique^[96] who studied a proton with kinetic energy of 1 keV. They calculated an energy dissipation ΔW during the approach from ∞ to 1 Å above the Al jellium edge of $\Delta W \approx 0.07$ eV. See also section 1.2.

Additionally we show Kohn-Sham electronic excitation spectra $\delta\Lambda^{BO}$ of the clusters after the laser excitation in Figure C.3. The excitation is expected to decay exponentially from the Fermi energy towards both sides of the energy range. Main contributions to a deviation from the 'perfect' exponential curve arise from the finite set of electronic states of the cluster.

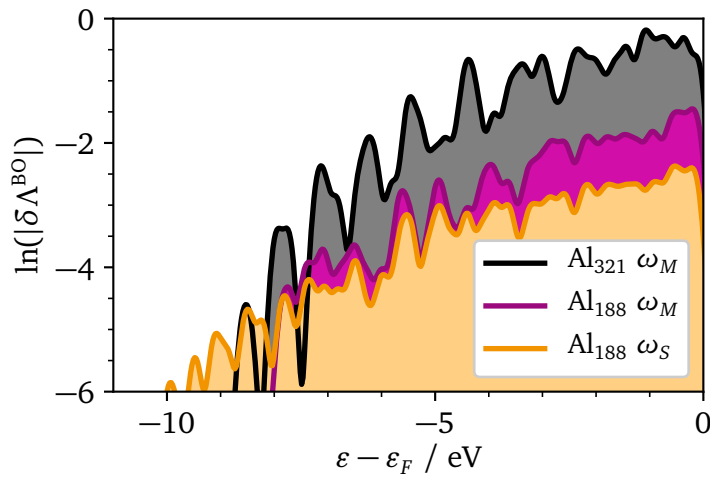


Figure C.3: Kohn-Sham electronic excitation spectrum $\delta\Lambda^{\text{BO}}$ for different geometries after laser excitation with different frequencies $\omega_M = 7.99 \text{ eV}$ or $\omega_S = 10.6 \text{ eV}$. Calculation of spectra according to Equation 3.11. Duration of excitation: 15 periods, afterwards 5 periods relaxation. Here: $\delta\Lambda^{\text{BO}}$ after $t = 20 \cdot$ periods in total.

D.1 Introduction

In subsection 1.1.2 different charge transfer processes were presented. Within the literature, there exists agreement that resonant neutralization can be simulated with the help of TDDFT. A simulation of Auger processes with the help of current implementations of TDDFT is not to be found in the literature. The reason for this failure is unclear, however Nagano et al.^[257] argued, that ‘[...] no Auger emission of electrons is described in the present TDLDA calculation. This may be expected, since the TDLDA is a kind of mean-field theory which does not allow any change of the occupation of the orbitals [...]’.

As introduced in subsection 2.1.3, authors often distinguish between density-functional theory (DFT) and density-functional approximation (DFA), where DFT refers to the exact theory and DFA to the approximations introduced into DFT.^[178,226] See also subsection 2.1.3. The most severe approximation in this context is the XC-functional which in case of realistic material simulations with TDDFT is taken as adiabatic, i.e. memory effects are completely neglected, see also subsection 2.2.4.

As the the Runge-Gross-theorem is derived (with the constraints mentioned in subsection 2.2.1) from the Schrödinger equation, the failure of TDDFT simulations to describe Auger processes is most likely not a failure of TDDFT itself but of the approximation to exchange and correlation. Therefore, discussions regarding Auger effects are rather oriented on DFAs then on DFT itself. The main concern in this context is the lack of memory in currently employed XC-functionals because TDDFT as formulated is an exact theory (under the limitations of the Runge-Gross theorem).

Kapoor^[325] studied autoionization processes and stated: ‘*TDDFT employing known and practicable exchange-correlation potentials does not capture any autoionization dynamics. Approximate exchange-correlation potentials capturing such dynamics would necessarily require memory effects*’. A similar point of view is also found in the work of Lacombe and Maitra.^[326]

In any case, as of today it is not clear what exactly causes the failure of currently employed TDDFT simulations to describe Auger effects.

D.2 Helium Ion and Argon Ion Impinging on Al(111)

| Parameter | Unit | Value |
|----------------------------------|-------------------|--------------|
| Mesh Spacing | bohr | 0.5 |
| XC-Functional | | AGGA-PBE |
| Coulomb Cutoff | | spherical |
| Volume of Simulation Box | bohr ³ | 60 · 60 · 60 |
| Min Distance Atoms to Box Edge | bohr | 12.0 |
| Projectile Starting Distance z | bohr | 16.0 |
| Time Step | atu | 0.02 |

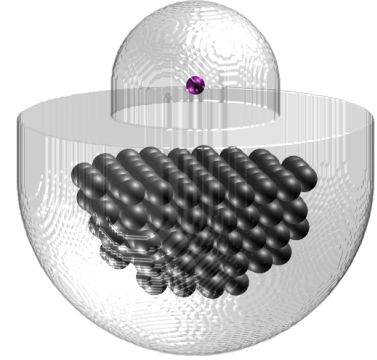


Table D.1: **Left:** Overview of most relevant parameters of the simulations with Ar^+ and He^+ impinging on Al_{188} -cluster. **Right:** Visualization of the employed cluster in its corresponding simulation cell.

In this section, we investigate two different model systems. These are the interaction of an He^+ with an Al_{188} -cluster, and the interaction of an Ar^+ with an Al_{188} -cluster. He^+ and Ar^+ scattering has been discussed in the literature by different authors both, theoretically^[49,52] and experimentally.^[50,51] We chose He^+ and Ar^+ projectiles because of the interesting electronic structure. The tabulated value for the ionization energy of He is 24.6 eV,^[299] and for Ar 15.8 eV.^[299] For both, the affinity level is at above the vacuum energy, i.e. a negative ion is not stable in nature. When approaching the Al_{188} -cluster, even when considering image charge effects, no electronic energy level is to be found between the valence band minimum at $\bar{\Gamma}$ of 10.8 eV below the vacuum energy and the Fermi energy at 4.15 eV below the vacuum energy (see also Table 3.2 on page 50). This means that throughout the entire trajectory, the only charge transfer channel is the Auger neutralization channel (in the simulations presented here, for investigations of the real system we refer to Refs. [49–52]).

Details on the Al-cluster have been discussed in chapter 3. For the generation of the Ar pseudopotential, the following cutoff radii have been chosen: $r_s^{\text{Ar}} = r_p^{\text{Ar}} = 1.426$ bohr, $r_d^{\text{Ar}} = 1.733$ bohr. For the generation of the He pseudopotential $r_s^{\text{He}} = 1.092$ bohr.

The starting configuration was obtained by performing independently a ground-state calculation for the Al_{188} -cluster and for the He^+ or the Ar^+ ion. Afterwards, wavefunctions were copied into identical simulation cells. This procedure is necessary, because in contrast to the simulations with an H^+ ion, the Ar^+ and He^+ ions have still one valence electron (for He^+) or seven valence electrons (for Ar^+). An overview on the computational details can be found in Table D.1.

The velocity at the starting distance of $z_{\text{init}} = 16$ bohr was chosen to coincide with the H^+ simulations of chapter 3, chapter 4 and chapter 5. Due to the different masses between the ions, $E_{\text{kin}}^{\text{init}} = 396.38$ eV (Ar^+) and $E_{\text{kin}}^{\text{init}} = 38.72$ eV (He^+). Please note that the Al atom positions have been kept fixed during the entire trajectory. This is highly artificial. When calculating physical quantities, this approximation has to be treated carefully. Fur-

thermore, the electrons around the Ar^+ ion were boosted with an initial phase factor as described in section E.2.

In Figure D.1 we present the kinetic energy difference upon impact together with the Bader charge of the He and the Ar projectiles. Electronic friction effects are higher for the Ar^+ projectile. This is not to be expected from Equation 1.1, according which $dE/dx \propto v$. As the target materials are identical, the difference may be connected to the higher electron density around the Ar^+ projectile.

Regarding the electronic charge around the projectile, Figure D.1b) shows the Bader charge of the projectile on the exit trajectory with respect to the Al_{188} -cluster. Note that neither the He^+ , nor the Ar^+ carry additional electrons away from the surface. This is not to be expected from experiments and a clear indication, that the current approach is not able to capture Auger effects.

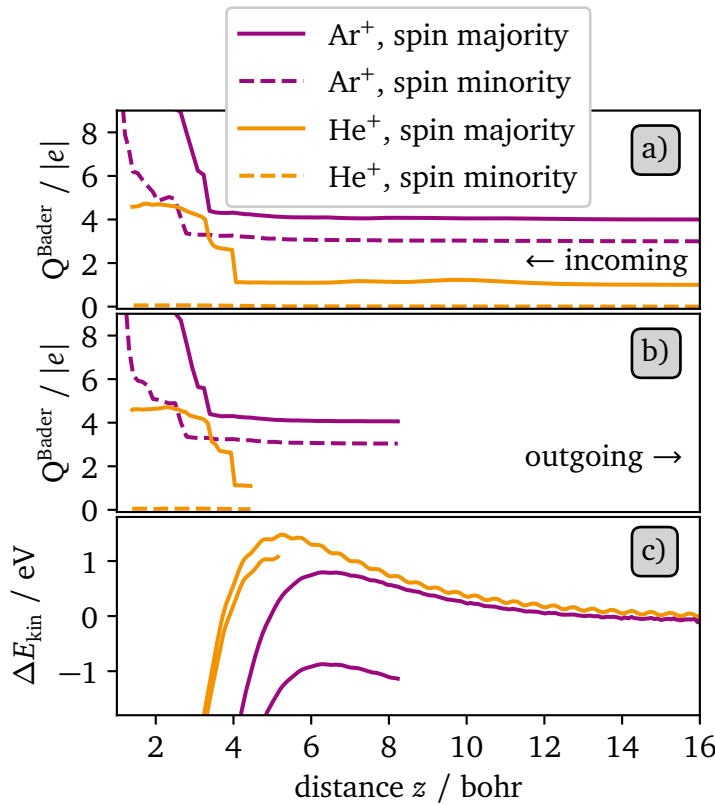


Figure D.1: Bader charge Q^{Bader} for Ar^+ and He^+ impinging on Al_{188} cluster with same velocity as 10 eV proton ($E_{\text{kin}}(\text{Ar}) = 396.38 \text{ eV}$, $E_{\text{kin}}(\text{He}) = 38.72 \text{ eV}$). **a)** incoming trajectory, **b)** outgoing trajectory, **c)** change in kinetic energy with respect to kinetic energy at $z_{\text{init}} = 16 \text{ bohr}$.

E.1 Script for Projecting Wavefunctions

In order to obtain the spectra shown in chapter 3, the (time-dependent, ground-state or frozen-density) Kohn-Sham wavefunctions have to be projected onto (time-dependent, ground-state or frozen-density) Kohn-Sham wavefunctions. The script presented below reads the file of wavefunction Ψ_i and Ψ_j and calculates the scalar product, i.e.:

$$\langle \Psi_i | \Psi_j \rangle \quad (\text{E.1})$$

In the script presented below, one wavefunction is expected to have only real components whereas the other one has a real and an imaginary part. Changes can easily be adapted.

The projection itself was performed using the output data printed by the TDDFT code Octopus in the VTK¹ file format. The script written in the Python programming language is an adapted version of the script developed in our group by R. Kalhöfer:^[328]

Script: Projecting Wavefunctions in VTK file format

```

1  #!/bin/env python3
2  # Scriptname: dot_product_vtk.py
3  # Usage: project wavefunctions
4  # > python dot_product_vtk.py file1 file2
5  # > python dot_product_vtk.py wf1.vtk wf2.vtk
6  # Version: 1
7  # Date: 04/25/2018 15:42
8
9  # import packages
10 from sys import argv
11 from numpy import fromfile
12 import numpy as np
13
14 # open state files
15 def readVTK(name, is_imaginary):
16     state1 = open(name, 'r')
17     # skip the header, i.e.
18     # skip vtk version,
19     # skip octopus info,
20     # skip format,

```

¹Visualization Toolkit ^[327]


```

21     # skip structure,
22     # skip dimension
23     # skip origin
24     for i in range(6):
25         state1.readline()
26
27     # read unit volume
28     # (assuming spacing in x, y and z are
29     # the same)
30     dV = float(state1.readline().split()[1])**3
31
32     # read in number of grid points
33     Np = int(state1.readline().split()[1])
34
35     # skip data type and table
36     for i in range(2):
37         state1.readline()
38
39     # read in real parts
40     re1 = fromfile(state1, dtype='>f8', count=Np)
41
42     # skip blank line, data type and table
43     for i in range(3):
44         state1.readline()
45     # read in imaginary parts if existent
46     if is_imaginary:
47         im1 = fromfile(state1, dtype='>f8', count=Np)
48     state1.close()
49     if is_imaginary: return re1,im1,dV
50     else:           return re1,dV
51
52 # read in files
53 re1,    dV  = readVTK(file1,False)
54 re2,im2,dV  = readVTK(file2,True)
55
56 # calculate and print dot product
57 dotProduct = re2.dot(re1+1j*im1)*dV
58
59 savename='projections.dat'
60 np.savetxt(savename,dotProduct)

```


E.2 Velocity Phase Factor

For an atom moving inside a simulation box that is described by means of TDDFT using Ehrenfest-dynamics the following problem arises: Usually, a ground-state calculation is performed for the system, followed by a time-dependent run where the atoms are given an initial velocity, and wavefunctions are propagated accordingly. The problem that arises in this context is the initial velocity of the electrons located around the projectile. As pointed out by Nagano et al.^[257] and Avendaño-Franco,^[329] in case of a purely local potential, an initial phase factor $\exp(i\mathbf{k} \cdot \mathbf{r})$ has to be applied to the wavefunctions.

To achieve the desired behavior for purely local potentials within the Octopus code, we implemented the initial phase factor and introduced the following variables and their documentation into the Octopus code (not yet available in the public version):

1. The option TDDeltaStrengthMode=kick_orbitals

```
1 Lets you kick those orbitals specified
2 by the block TDKickOrbitals.
```

2. The option TDKickOrbitals

```
1 When this block is set, only specific orbitals are kicked
2 by a kick function. You may want to combine this with
3 the variable TDKickIons. An example call may look like
4 this:
5
6 %TDKickOrbitals
7 yes | yes | no
8 %
9
10 Or in case of a spin polarized calculation:
11
12 %TDKickOrbitals
13 yes | yes | no
14 yes | yes | no
15 %
16
17 Please note: If more columns than orbitals are present,
18 an error message is printed. If less columns than
19 orbitals are present, it will be assumed that the ones
20 that are given are the last orbitals. Each line must
21 have the same number of columns.
```

3. The option TDKickIons

```
1 Lets you decide whether the (Delta-)kick should be
2 applied to the ions as well.
```

Extensions to the case of nonlocal potentials (e.g. nonlocal pseudopotentials) have been discussed e.g. by Castro,^[258] or by Nagano et al.^[257]

BIBLIOGRAPHY

- [1] E. Fitzgerald, *Rubaiyat of Omar Khayyam* (Oxford University Press, Oxford, 2009).
- [2] A. Bogaerts et al., *The 2020 plasma catalysis roadmap*, Journal of Physics D: Applied Physics **53**, 443001 (2020).
- [3] P. Mehta, P. Barboun, D. B. Go, J. C. Hicks, and W. F. Schneider, *Catalysis Enabled by Plasma Activation of Strong Chemical Bonds: A Review*, ACS Energy Letters **4**, 1115 (2019).
- [4] P. F. Williams, ed., *Plasma Processing of Semiconductors* (Springer Netherlands, 1997).
- [5] R. E. Clark and D. H. Reiter, eds., *Nuclear Fusion Research* (Springer Berlin Heidelberg, 2005).
- [6] J. Küppers, *The hydrogen surface chemistry of carbon as a plasma facing material*, Surface Science Reports **22**, 249 (1995).
- [7] L. Gao, X. Shi, and X. Wu, *Applications and challenges of low temperature plasma in pharmaceutical field*, Journal of Pharmaceutical Analysis **11**, 28 (2021).
- [8] T. von Woedtke, S. Reuter, K. Masur, and K.-D. Weltmann, *Plasmas for medicine*, Physics Reports **530**, 291 (2013).
- [9] G. Federici et al., *Plasma-material interactions in current tokamaks and their implications for next step fusion reactors*, Nuclear Fusion **41**, 1967 (2001).
- [10] A. Gorjaev et al., *The upgraded TOMAS device: A toroidal plasma facility for wall conditioning, plasma production, and plasma–surface interaction studies*, Review of Scientific Instruments **92**, 023506 (2021).
- [11] M. Morales-Masis, L. Ding, F. Dauzou, Q. Jeangros, A. Hessler-Wyser, S. Nicolay, and C. Ballif, *Hydrogen plasma treatment for improved conductivity in amorphous aluminum doped zinc tin oxide thin films*, APL Materials **2**, 096113 (2014).
- [12] T. Singh, R. Müller, J. Singh, and S. Mathur, *Tailoring surface states in WO₃ photoanodes for efficient photoelectrochemical water splitting*, Applied Surface Science **347**, 448 (2015).
- [13] E. C. Neyts and A. Bogaerts, *Understanding plasma catalysis through modelling and simulation—a review*, Journal of Physics D: Applied Physics **47**, 224010 (2014).
- [14] A. Bogaerts, T. Kozák, K. van Laer, and R. Snoeckx, *Plasma-based conversion of CO₂: current status and future challenges*, Faraday Discussions **183**, 217 (2015).

- [15] R. Snoeckx and A. Bogaerts, *Plasma technology - a novel solution for CO₂ conversion?*, Chem. Soc. Rev. **46**, 5805 (2017).
- [16] A. Bogaerts, R. Snoeckx, G. Trenchev, and W. Wang, *Modeling for a Better Understanding of Plasma-Based CO₂ Conversion*, Plasma Chemistry and Gas Conversion (2018).
- [17] I. Adamovich et al., *The 2017 Plasma Roadmap: Low temperature plasma science and technology*, Journal of Physics D: Applied Physics **50**, 323001 (2017).
- [18] M. Bonitz et al., *Towards an integrated modeling of the plasma-solid interface*, Frontiers of Chemical Science and Engineering **13**, 201 (2019).
- [19] D. B. Graves and P. Brault, *Molecular dynamics for low temperature plasma-surface interaction studies*, Journal of Physics D: Applied Physics **42**, 194011 (2009).
- [20] W. More, J. Merino, R. Monreal, P. Pou, and F. Flores, *Role of energy-level shifts on Auger neutralization processes: A calculation beyond the image potential*, Phys. Rev. B **58**, 7385 (1998).
- [21] N. Schlünzen, K. Balzer, M. Bonitz, L. Deuchler, and E. Pehlke, *Time-dependent simulation of ion stopping: Charge transfer and electronic excitations*, Contributions to Plasma Physics **59**, e201800184 (2019).
- [22] V. Grill, J. Shen, C. Evans, and R. G. Cooks, *Collisions of ions with surfaces at chemically relevant energies: Instrumentation and phenomena*, Review of Scientific Instruments **72**, 3149 (2001).
- [23] J. Rabalais, *Low Energy Ion-Surface Interactions*, Wiley Series In Ion Chemistry and Physics (Wiley, 1994).
- [24] V. A. Esaulov, "Low Energy Ion Scattering and Recoiling Spectroscopy in Surface Science", in *Surface Science Techniques* (Springer Berlin Heidelberg, 2013), pp. 423–460.
- [25] S. N. Markin, D. Primetzhofer, S. Prusa, M. Brunmayr, G. Kowarik, F. Aumayr, and P. Bauer, *Electronic interaction of very slow light ions in Au: Electronic stopping and electron emission*, Phys. Rev. B **78**, 195122 (2008).
- [26] F. Aumayr and H. Winter, *Inelastic interactions of slow ions and atoms with surfaces*, Nuclear Instruments and Methods in Physics Research Section B: Beam Interactions with Materials and Atoms **233**, 111 (2005).
- [27] V. A. Esaulov, O. Grizzi, L. Guillemot, M. Huels, S. Lacombe, and V. N. Tuan, *An apparatus for multiparametric studies of ion-surface collisions*, Review of Scientific Instruments **67**, 135 (1996).
- [28] S. Wethekam, A. Mertens, and H. Winter, *Survival of He⁺ Ions during Grazing Scattering from a Ag(111) Surface*, Phys. Rev. Lett. **90**, 037602 (2003).
- [29] H. C. Straub, M. A. Mangan, B. G. Lindsay, K. A. Smith, and R. F. Stebbings, *Absolute detection efficiency of a microchannel plate detector for kilo-electron volt energy ions*, Review of Scientific Instruments **70**, 4238 (1999).

- [30] P. Haochang, T. C. M. Horn, and A. W. Kleyn, *Harpooning in Surface Scattering: O_2^- Formation in Collisions of O_2^+ from $\text{Ag}(111)$* , Phys. Rev. Lett. **57**, 3035 (1986).
- [31] B. Willerding, W. Heiland, and K. J. Snowdon, *Neutralization of Fast Molecular Ions H_2^+ and N_2^+ at Surfaces*, Phys. Rev. Lett. **53**, 2031 (1984).
- [32] W. Eckstein, H. Verbeek, and S. Datz, *Backscattering of keV molecular hydrogen ions from Au surfaces*, Applied Physics Letters **27**, 527 (1975).
- [33] H. Akazawa and Y. Murata, *Neutralization of Very-Low-Energy Ions on $\text{Pt}(100)$* , Phys. Rev. Lett. **61**, 1218 (1988).
- [34] H. Sugai, Y. Mitsuoka, and H. Toyoda, *Observation of surface dissociation of low-energy polyatomic ions relevant to plasma processing*, Journal of Vacuum Science and Technology A: Vacuum, Surfaces, and Films **16**, 290 (1998).
- [35] B. Cooper, C. DiRubio, G. Kimmel, and R. McEachern, *Low energy ion-surface interactions*, Nuclear Instruments and Methods in Physics Research Section B: Beam Interactions with Materials and Atoms **64**, 49 (1992).
- [36] M. B. J. Wijesundara, L. Hanley, B. Ni, and S. B. Sinnott, *Effects of unique ion chemistry on thin-film growth by plasma-surface interactions*, Proceedings of the National Academy of Sciences **97**, 23 (2000).
- [37] J. Shen, C. Evans, N. Wade, and R. G. Cooks, *Ion-Ion Collisions Leading to Formation of C-C Bonds at Surfaces: An Interfacial Kolbe Reaction*, Journal of the American Chemical Society **121**, 9762 (1999).
- [38] M. P. Ray, R. E. Lake, S. A. Moody, V. Magadala, and C. E. Sosolik, *A hyperthermal energy ion beamline for probing hot electron chemistry at surfaces*, Review of Scientific Instruments **79**, 076106 (2008).
- [39] M. P. Ray, R. E. Lake, and C. E. Sosolik, *Energy transfer in quasibinary and collective scattering events at a $\text{Ag}(001)$ surface*, Phys. Rev. B **79**, 155446 (2009).
- [40] M. P. Ray, R. E. Lake, L. B. Thomsen, G. Nielson, O. Hansen, I. Chorkendorff, and C. E. Sosolik, *Towards hot electron mediated charge exchange in hyperthermal energy ion-surface interactions*, Journal of Physics: Condensed Matter **22**, 084010 (2010).
- [41] M. L. E. Oliphant, P. B. Moon, and E. Rutherford, *The Liberation of Electrons from Metal Surfaces by Positive Ions*. Proceedings of the Royal Society of London. Series A, Containing Papers of a Mathematical and Physical Character **127**, 388 (1930).
- [42] H. D. Hagstrum, *Theory of Auger Ejection of Electrons from Metals by Ions*, Phys. Rev. **96**, 336 (1954).
- [43] J. Burgdörfer, P. Lerner, and F. W. Meyer, *Above-surface neutralization of highly charged ions: The classical over-the-barrier model*, Phys. Rev. A **44**, 5674 (1991).
- [44] J. Merino, N. Lorente, P. Pou, and F. Flores, *Charge transfer for slow H atoms interacting with Al: Atomic levels and linewidths*, Phys. Rev. B **54**, 10959 (1996).

- [45] J. Merino, N. Lorente, F. Flores, and M. Gusev, *Quantum approach to charge transfer between low energy H^+ ions and Al surfaces*, Nuclear Instruments and Methods in Physics Research Section B: Beam Interactions with Materials and Atoms **125**, 288 (1997).
- [46] J. Merino, N. Lorente, M. Y. Gusev, F. Flores, M. Maazouz, L. Guillemot, and V. A. Esaulov, *Charge transfer of slow H atoms interacting with Al: Dynamical charge evolution*, Phys. Rev. B **57**, 1947 (1998).
- [47] H. S. W. Massey, *The theory of the extraction of electrons from metals by positive ions and metastable atoms*, Mathematical Proceedings of the Cambridge Philosophical Society **26**, 386 (1930).
- [48] S. S. Shekter, J. Exptl. Theor. Phys (U.S.S.R) **7**, 750 (1937).
- [49] A. Iglesias-García, E. A. García, and E. C. Goldberg, *Importance of considering helium excited states in He^+ scattering by an aluminum surface*, Phys. Rev. B **90**, 195416 (2014).
- [50] T. Kravchuk, V. Esaulov, A. Hoffman, and R. Monreal, *He^+ scattering on clean and oxygen covered Al(111)*, Nuclear Instruments and Methods in Physics Research Section B: Beam Interactions with Materials and Atoms **232**, 27 (2005).
- [51] S. Rund, D. Primetzhofer, S. Markin, D. Goebel, and P. Bauer, *Charge exchange of He^+ -ions with aluminium surfaces*, Nuclear Instruments and Methods in Physics Research Section B: Beam Interactions with Materials and Atoms **269**, 1171 (2011).
- [52] E. A. García, N. P. Wang, R. C. Monreal, and E. C. Goldberg, *Interference between resonant and Auger mechanisms for charge-exchange processes near surfaces*, Phys. Rev. B **67**, 205426 (2003).
- [53] A. Arnau et al., *Interaction of slow multicharged ions with solid surfaces*, Surface Science Reports **27**, 113 (1997).
- [54] H. Ryufuku, K. Sasaki, and T. Watanabe, *Oscillatory behavior of charge transfer cross sections as a function of the charge of projectiles in low-energy collisions*, Phys. Rev. A **21**, 745 (1980).
- [55] U. Fano and W. Lichten, *Interpretation of Ar^+ -Ar Collisions at 50 KeV*, Phys. Rev. Lett. **14**, 627 (1965).
- [56] A. Duvenbeck, B. Weidtmann, O. Weingart, and A. Wucher, *Modeling hot-electron generation induced by electron promotion in atomic collision cascades in metals*, Phys. Rev. B **77**, 245444 (2008).
- [57] J. W. Gadzuk, *Resonance-Assisted Hot Electron Femtochemistry at Surfaces*, Phys. Rev. Lett. **76**, 4234 (1996).
- [58] M. Born and R. Oppenheimer, *Zur Quantentheorie der Molekeln*, Annalen der Physik **389**, 457 (1927).
- [59] M. Baer, *Beyond Born-Oppenheimer* (John Wiley & Sons, Inc., 2006).
- [60] H. Ibach, *Physics of Surfaces and Interfaces* (Springer, 2006).

- [61] D. Marx and J. Hutter, *Ab Initio Molecular Dynamics* (Cambridge University Press, 2009).
- [62] A. M. Wodtke, J. C. Tully, and D. J. Auerbach, *Electronically non-adiabatic interactions of molecules at metal surfaces: Can we trust the Born–Oppenheimer approximation for surface chemistry?*, *International Reviews in Physical Chemistry* **23**, 513 (2004).
- [63] J. I. Juaristi, M. Alducin, R. D. Muiño, H. F. Busnengo, and A. Salin, *Role of Electron-Hole Pair Excitations in the Dissociative Adsorption of Diatomic Molecules on Metal Surfaces*, *Phys. Rev. Lett.* **100**, 116102 (2008).
- [64] A. C. Luntz, I. Makkonen, M. Persson, S. Holloway, D. M. Bird, and M. S. Miziański, *Comment on 'Role of Electron-Hole Pair Excitations in the Dissociative Adsorption of Diatomic Molecules on Metal Surfaces'*, *Phys. Rev. Lett.* **102**, 109601 (2009).
- [65] J. I. Juaristi, M. Alducin, R. D. Muiño, H. F. Busnengo, and A. Salin, *Juaristi et al. Reply*: *Phys. Rev. Lett.* **102**, 109602 (2009).
- [66] P. Nordlander and J. C. Tully, *Energy Shifts and Broadening of Excited Hydrogen-Atom Levels in the Vicinity of a Metal Surface*, *Phys. Rev. Lett.* **61**, 990 (1988).
- [67] P. Saalfrank, J. I. Juaristi, M. Alducin, M. Blanco-Rey, and R. D. Muiño, *Vibrational lifetimes of hydrogen on lead films: An ab initio molecular dynamics with electronic friction (AIMDEF) study*, *The Journal of Chemical Physics* **141**, 234702 (2014).
- [68] S. P. Rittmeyer, J. Meyer, J. I. Juaristi, and K. Reuter, *Electronic Friction-Based Vibrational Lifetimes of Molecular Adsorbates: Beyond the Independent-Atom Approximation*, *Phys. Rev. Lett.* **115**, 046102 (2015).
- [69] M. Grottemeyer and E. Pehlke, *Electronic Energy Dissipation During Scattering of Vibrationally Excited Molecules at Metal Surfaces: Ab initio Simulations for HCl/Al(111)*, *Phys. Rev. Lett.* **112**, 043201 (2014).
- [70] M. Timmer and P. Kratzer, *Electron-hole spectra created by adsorption on metals from density functional theory*, *Phys. Rev. B* **79**, 165407 (2009).
- [71] A. M. Wodtke, *Electronically non-adiabatic influences in surface chemistry and dynamics*, *Chemical Society Reviews* **45**, 3641 (2016).
- [72] H. Nienhaus, H. S. Bergh, B. Gergen, A. Majumdar, W. H. Weinberg, and E. W. McFarland, *Electron-Hole Pair Creation at Ag and Cu Surfaces by Adsorption of Atomic Hydrogen and Deuterium*, *Phys. Rev. Lett.* **82**, 446 (1999).
- [73] H. Nienhaus, *Electronic excitations by chemical reactions on metal surfaces*, *Surface Science Reports* **45**, 1 (2002).
- [74] D. Diesing and E. Hasselbrink, *Chemical energy dissipation at surfaces under UHV and high pressure conditions studied using metal–insulator–metal and similar devices*, *Chemical Society Reviews* **45**, 3747 (2016).
- [75] D. J. Auerbach, *Surface Science: Hitting the Surface–Softly*, *Science* **294**, 2488 (2001).

- [76] B. Gergen, *Chemically Induced Electronic Excitations at Metal Surfaces*, Science **294**, 2521 (2001).
- [77] D. A. Kovacs, T. Peters, C. Haake, M. Schleberger, A. Wucher, A. Golczewski, F. Aumayr, and D. Diesing, *Potential electron emission induced by multiply charged ions in thin film tunnel junctions*, Phys. Rev. B **77** (2008).
- [78] S. Meyer, C. Heuser, D. Diesing, and A. Wucher, *Kinetic electronic excitation of solids by fast-particle bombardment*, Phys. Rev. B **78**, 035428 (2008).
- [79] S. Meyer, D. Diesing, and A. Wucher, *Kinetic Electron Excitation in Atomic Collision Cascades*, Phys. Rev. Lett. **93**, 137601 (2004).
- [80] B. Schindler, D. Diesing, and E. Hasselbrink, *Electronically Nonadiabatic Processes in the Interaction of H with a Au Surface Revealed Using MIM Junctions: The Temperature Dependence*, The Journal of Physical Chemistry C **117**, 6337 (2013).
- [81] D. Diesing, D. Kovacs, K. Stella, and C. Heuser, *Characterization of atom and ion-induced 'internal' electron emission by thin film tunnel junctions*, Nuclear Instruments and Methods in Physics Research Section B: Beam Interactions with Materials and Atoms **269**, 1185 (2011).
- [82] S. G. Davison and K. W. Sulston, *Green-Function Theory of Chemisorption* (Springer, 2006).
- [83] R. Monreal and F. Flores, "Charge Exchange Processes in Low Energy Ion-Metal Collisions", in *Theory of the Interaction of Swift Ions with Matter. Part 1*, Vol. 45, Advances in Quantum Chemistry (Academic Press, 2004), pp. 175–199.
- [84] E. G. Lewars, *Computational Chemistry* (Springer, 2011).
- [85] J. F. Ziegler and J. P. Biersack, *The Stopping and Range of Ions in Matter*, Treatise on Heavy-Ion Science, 93 (1985).
- [86] S. Plimpton, *Fast Parallel Algorithms for Short-Range Molecular Dynamics*, Journal of Computational Physics **117**, 1 (1995).
- [87] See the LAMMPS manual: https://lammps.sandia.gov/doc/Intro_overview.html and the Billion atom benchmark <https://lammps.sandia.gov/bench.html>.
- [88] R. Vidal, J. Ferrón, C. Meyer, V. Q. Riascos, and F. Bonetto, *The influence of surface defects on the low energy scattering of Ar ions from a Cu(111) surface*, Surface Science **690**, 121482 (2019).
- [89] P. Kucharczyk, A. Fängerlings, B. Weidtmann, and A. Wucher, *Computer simulation of sputtering induced by swift heavy ions*, Nuclear Instruments and Methods in Physics Research Section B: Beam Interactions with Materials and Atoms **426**, 5 (2018).
- [90] See: <http://www.srim.org/>.

- [91] J. F. Ziegler, M. Ziegler, and J. Biersack, *SRIM – The stopping and range of ions in matter (2010)*, Nuclear Instruments and Methods in Physics Research Section B: Beam Interactions with Materials and Atoms **268**, 1818 (2010).
- [92] E. Fermi and E. Teller, *The Capture of Negative Mesotrons in Matter*, Phys. Rev. **72**, 399 (1947).
- [93] J. Lindhard and M. Scharff, *Energy Dissipation by Ions in the keV Region*, Phys. Rev. **124**, 128 (1961).
- [94] P. M. Echenique, R. M. Nieminen, J. C. Ashley, and R. H. Ritchie, *Nonlinear stopping power of an electron gas for slow ions*, Phys. Rev. A **33**, 897 (1986).
- [95] A. Salin, A. Arnau, P. M. Echenique, and E. Zaremba, *Dynamic nonlinear screening of slow ions in an electron gas*, Phys. Rev. B **59**, 2537 (1999).
- [96] A. Gras-Marti, P. Echenique, and R. Ritchie, *Surface contribution to the energy loss of slow ions*, Surface Science **173**, 310 (1986).
- [97] M. Lindenblatt, E. Pehlke, A. Duvenbeck, B. Rethfeld, and A. Wucher, *Kinetic excitation of solids: The concept of electronic friction*, Nuclear Instruments and Methods in Physics Research Section B: Beam Interactions with Materials and Atoms **246**, 333 (2006).
- [98] M. Persson and B. Hellsing, *Electronic Damping of Adsorbate Vibrations on Metal Surfaces*. Phys. Rev. Lett. **51**, 1395 (1983).
- [99] J. Juaristi, *Energy loss of ions interacting with metal surfaces*, Nuclear Instruments and Methods in Physics Research Section B: Beam Interactions with Materials and Atoms **230**, 148 (2005).
- [100] M. Alducin, R. Díez Muiño, and J. Juaristi, *Non-adiabatic effects in elementary reaction processes at metal surfaces*, Progress in Surface Science **92**, 317 (2017).
- [101] F. J. García de Abajo and P. M. Echenique, *Wake potential in the vicinity of a surface*, Phys. Rev. B **46**, 2663 (1992).
- [102] D. J. Griffiths, *Introduction to Electrodynamics* (Cambridge University Press, 2017).
- [103] A. Liebsch, *Dynamical screening at simple-metal surfaces*, Phys. Rev. B **36**, 7378 (1987).
- [104] S. Andersson and B. N. J. Persson, *Long-Range Scattering of Electrons by Electron-Hole Pair Excitations at Metal Surfaces*, Phys. Rev. Lett. **50**, 2028 (1983).
- [105] H. Winter, *Image charge effects in ion surface scattering*, Journal of Physics: Condensed Matter **8**, 10149 (1996).
- [106] S. C. Lam and R. J. Needs, *First-principles calculations of the screening of electric fields at the aluminium (111) and (110) surfaces*, Journal of Physics: Condensed Matter **5**, 2101 (1993).
- [107] D. M. Newns, *Self-Consistent Model of Hydrogen Chemisorption*, Phys. Rev. **178**, 1123 (1969).

- [108] R. Brako and D. Newns, *Charge exchange in atom-surface scattering: Thermal versus quantum mechanical non-adiabaticity*, Surface Science **108**, 253 (1981).
- [109] J. Geerlings, J. Los, J. Gauyacq, and N. Temme, *Charge transfer in atom-surface collisions. On the validity of the semi-classical approximation*, Surface Science **172**, 257 (1986).
- [110] D. C. Langreth and P. Nordlander, *Derivation of a master equation for charge-transfer processes in atom-surface collisions*, Phys. Rev. B **43**, 2541 (1991).
- [111] M. Pamperin, F. X. Bronold, and H. Fehske, *Many-body theory of the neutralization of strontium ions on gold surfaces*, Phys. Rev. B **91**, 035440 (2015).
- [112] M. Bonitz, K. Balzer, N. Schlünzen, M. R. Rasmussen, and J.-P. Joost, *Ion Impact Induced Ultrafast Electron Dynamics in Finite Graphene-Type Hubbard Clusters*, physica status solidi (b) **256**, 1970028 (2019).
- [113] P. W. Anderson, *Localized Magnetic States in Metals*, Phys. Rev. **124**, 41 (1961).
- [114] T. B. Grimley, *The indirect interaction between atoms or molecules adsorbed on metals*, Proceedings of the Physical Society **90**, 751 (1967).
- [115] W. Brenig and K. Schönhammer, *On the theory of chemisorption*, Zeitschrift für Physik **267**, 201 (1974).
- [116] A. Yoshimori and K. Makoshi, *Time-dependent Newns-Anderson model*, Progress in Surface Science **21**, 251 (1986).
- [117] A. Groß, *Theoretical Surface Science* (Springer Berlin Heidelberg, 2009).
- [118] J. K. Nørskov, F. Studt, F. Abild-Pedersen, and T. Bligaard, *Fundamental Concepts in Heterogeneous Catalysis* (Wiley, New York, 2014).
- [119] R. Brako and D. Newns, *The electron-hole mechanism for sticking of adsorbates: A soluble model*, Solid State Communications **33**, 713 (1980).
- [120] R. Brako and D. M. Newns, *Slowly varying time-dependent local perturbations in metals: a new approach*, Journal of Physics C: Solid State Physics **14**, 3065 (1981).
- [121] A. Iglesias-García, E. A. García, and E. C. Goldberg, *Localized description of surface energy gap effects in the resonant charge exchange between atoms and surfaces*, Journal of Physics: Condensed Matter **23**, 045003 (2010).
- [122] L. Gao et al., *Dynamical resonant neutralization of low-energy Na⁺ ions scattered from Au(111), Pd(111), Cu(111), and Cu(110) surfaces*, Phys. Rev. A **96**, 052705 (2017).
- [123] D. Bird, M. Miziański, M. Lindenblatt, and E. Pehlke, *Electronic excitation in atomic adsorption on metals: A comparison of ab initio and model calculations*, Surface Science **602**, 1212 (2008).
- [124] M. S. Miziański, D. M. Bird, M. Persson, and S. Holloway, *Electronic nonadiabatic effects in the adsorption of hydrogen atoms on metals*, The Journal of Chemical Physics **122**, 084710 (2005).

- [125] M. Pamperin, F. X. Bronold, and H. Fehske, *Ion-induced secondary electron emission from metal surfaces*, Plasma Sources Science and Technology **27**, 084003 (2018).
- [126] A. G. Borisov, A. K. Kazansky, and J. P. Gauyacq, *Finite Time Effect in the Charge Transfer Process during an Ion-Metal Surface Collision*, Phys. Rev. Lett. **80**, 1996 (1998).
- [127] I. K. Gainullin, *Three-dimensional modeling of resonant charge transfer between ion beams and metallic surfaces*, Phys. Rev. A **95**, 052705 (2017).
- [128] I. Gainullin, *Towards quantitative LEIS with alkali metal ions*, Surface Science **677**, 324 (2018).
- [129] I. K. Gainullin, *Theoretical investigation of the ion-induced polarization-charge influence on resonant charge transfer*, Phys. Rev. A **100**, 032712 (2019).
- [130] M. Elstner, D. Porezag, G. Jungnickel, J. Elsner, M. Haugk, T. Frauenheim, S. Suhai, and G. Seifert, *Self-consistent-charge density-functional tight-binding method for simulations of complex materials properties*, Phys. Rev. B **58**, 7260 (1998).
- [131] D. Porezag, T. Frauenheim, T. Köhler, G. Seifert, and R. Kaschner, *Construction of tight-binding-like potentials on the basis of density-functional theory: Application to carbon*, Phys. Rev. B **51**, 12947 (1995).
- [132] G. Seifert, D. Porezag, and T. Frauenheim, *Calculations of molecules, clusters, and solids with a simplified LCAO-DFT-LDA scheme*, International Journal of Quantum Chemistry **58**, 185 (1996).
- [133] B. Hourahine et al., *DFTB+, a software package for efficient approximate density functional theory based atomistic simulations*, The Journal of Chemical Physics **152**, 124101 (2020).
- [134] T. A. Niehaus, D. Heringer, B. Torralva, and T. Frauenheim, *Importance of electronic self-consistency in the TDDFT based treatment of nonadiabatic molecular dynamics*, The European Physical Journal D **35**, 467 (2005).
- [135] J. Jakowski, S. Irle, B. G. Sumpter, and K. Morokuma, *Modeling Charge Transfer in Fullerene Collisions via Real-Time Electron Dynamics*, The Journal of Physical Chemistry Letters **3**, 1536 (2012).
- [136] F. Spiegelman, N. Tarrat, J. Cuny, L. Dontot, E. Posenitskiy, C. Martí, A. Simon, and M. Rapacioli, *Density-functional tight-binding: basic concepts and applications to molecules and clusters*, Advances in Physics: X **5**, 1710252 (2020).
- [137] A. Schleife, E. W. Draeger, V. M. Anisimov, A. A. Correa, and Y. Kanai, *Quantum Dynamics Simulation of Electrons in Materials on High-Performance Computers*, Computing in Science & Engineering **16**, 54 (2014).
- [138] M. A. Zeb, J. Kohanoff, D. Sánchez-Portal, A. Arnau, J. I. Juaristi, and E. Artacho, *Electronic Stopping Power in Gold: The Role of d Electrons and the H/He Anomaly*, Phys. Rev. Lett. **108**, 225504 (2012).

- [139] E. E. Quashie and A. A. Correa, *Electronic stopping power of protons and alpha particles in nickel*, Phys. Rev. B **98**, 235122 (2018).
- [140] M. Lindenblatt and E. Pehlke, *Ab Initio Simulation of the Spin Transition during Chemisorption: H/Al(111)*, Phys. Rev. Lett. **97**, 216101 (2006).
- [141] M. Lindenblatt, J. van Heys, and E. Pehlke, *Molecular dynamics of nonadiabatic processes at surfaces: Chemisorption of H/Al(1 1 1)*, Surface Science **600**, 3624 (2006).
- [142] C. L. Moss, C. M. Isborn, and X. Li, *Ehrenfest dynamics with a time-dependent density-functional-theory calculation of lifetimes and resonant widths of charge-transfer states of Li^+ near an aluminum cluster surface*, Phys. Rev. A **80**, 024503 (2009).
- [143] A. Castro, M. Isla, J. I. Martínez, and J. A. Alonso, *Scattering of a proton with the Li_4 cluster: Non-adiabatic molecular dynamics description based on time-dependent density-functional theory*, Chemical Physics **399**, 130 (2012).
- [144] A. V. Krasheninnikov, Y. Miyamoto, and D. Tománek, *Role of electronic excitation in ion collisions with carbon nanostructures*, Phys. Rev. Lett. **99**, 016104 (2007).
- [145] R. Seraide, M. A. Bernal, G. Brunetto, U. de Giovannini, and A. Rubio, *TDDFT-Based Study on the Proton-DNA Collision*, The Journal of Physical Chemistry B **121**, 7276 (2017).
- [146] S. Bubin, B. Wang, S. Pantelides, and K. Varga, *Simulation of high-energy ion collisions with graphene fragments*, Phys. Rev. B **85**, 235435 (2012).
- [147] S. Zhao, W. Kang, J. Xue, X. Zhang, and P. Zhang, *Comparison of electronic energy loss in graphene and BN sheet by means of time-dependent density functional theory*, Journal of Physics: Condensed Matter **27**, 025401 (2015).
- [148] Z. Wang, S.-S. Li, and L.-W. Wang, *Efficient Real-Time Time-Dependent Density Functional Theory Method and its Application to a Collision of an Ion with a 2D Material*, Phys. Rev. Lett. **114**, 063004 (2015).
- [149] A. Ojanperä, A. V. Krasheninnikov, and M. Puska, *Electronic stopping power from first-principles calculations with account for core electron excitations and projectile ionization*, Phys. Rev. B **89**, 035120 (2014).
- [150] C.-W. Lee and A. Schleife, *Hot-Electron-Mediated Ion Diffusion in Semiconductors for Ion-Beam Nanostructuring*, Nano Letters **19**, 3939 (2019).
- [151] A. Jafarzadeh, K. M. Bal, A. Bogaerts, and E. C. Neyts, *CO_2 Activation on TiO_2 -Supported Cu_5 and Ni_5 Nanoclusters: Effect of Plasma-Induced Surface Charging*, The Journal of Physical Chemistry C **123**, 6516 (2019).
- [152] P. Nordlander and J. C. Tully, *Energy shifts and broadening of atomic levels near metal surfaces*, Phys. Rev. B **42**, 5564 (1990).
- [153] S. A. Deutscher, X. Yang, and J. Burgdörfer, *Atomic resonances of hydrogen near aluminum surfaces: Adiabatic evolution of the ground state*, Phys. Rev. A **55**, 466 (1997).

- [154] A. Borisov, D. Teillet-Billy, and J. Gauyacq, *Energy shift and broadening of H levels in front of a metal surface*, Nuclear Instruments and Methods in Physics Research Section B: Beam Interactions with Materials and Atoms **78**, 49 (1993).
- [155] M. C. Torralba, P. G. Bolcatto, and E. C. Goldberg, *Calculation of ion-surface collisions for a wide range of scattering geometries*, Phys. Rev. B **68**, 075406 (2003).
- [156] K. Snowdon, R. Hentschke, A. Nürmann, W. Heiland, E. Mühling, and W. Eckstein, *Comparison of Auger and resonant transition rates in the hydrogen-metal surface interaction*, Nuclear Instruments and Methods in Physics Research Section B: Beam Interactions with Materials and Atoms **23**, 309 (1987).
- [157] B. Obreshkov and U. Thumm, *H⁻ formation in collisions of hydrogen atoms with Al(100) surfaces*, Phys. Rev. A **87**, 022903 (2013).
- [158] H. Jouin and F. A. Gutierrez, *Threshold effects in surface-plasmon transition rates and neutral fractions for protons traveling near a metallic surface*, Phys. Rev. A **80**, 042901 (2009).
- [159] H. Jouin and F. A. Gutierrez, *Velocity dependence of outgoing neutral fractions for H(1s) and H⁺ beams impinging on Al(111) at grazing incidence*, Phys. Rev. A **84**, 014901 (2011).
- [160] R. Baragiola, E. Alonso, J. Ferron, and A. Oliva-Florio, *Ion-induced electron emission from clean metals*, Surface Science **90**, 240 (1979).
- [161] D. Hasselkamp, S. Hippler, and A. Scharmann, *Ion-induced secondary electron spectra from clean metal surfaces*, Nuclear Instruments and Methods in Physics Research Section B: Beam Interactions with Materials and Atoms **18**, 561 (1986).
- [162] H. Winter and A. Borisov, *Formation of hydrogen atoms in grazing scattering from an aluminum surface*, Nuclear Instruments and Methods in Physics Research Section B: Beam Interactions with Materials and Atoms **115**, 211 (1996).
- [163] H. Nienhaus, R. Zimny, and H. Winter, *Neutralization of fast protons after grazing scattering from Al(111)*, Radiation Effects and Defects in Solids **109**, 1 (1989).
- [164] A. Borisov and H. Winter, *Formation of H- on thin aluminum films*, Nuclear Instruments and Methods in Physics Research Section B: Beam Interactions with Materials and Atoms **115**, 142 (1996).
- [165] M. Okada and Y. Murata, *Scattering of low-energy (10 - 350 eV) light ions from Al(111); neutralization and dissociation*, Journal of Physics: Condensed Matter **9**, 1919 (1997).
- [166] W. Heiland, *Charge exchange processes and surface chemistry*, Surface Science **251-252**, 942 (1991).
- [167] H. Eder, F. Aumayr, P. Berlinger, H. Störi, and H. Winter, *Excitation of plasmons by impact of slow ions on clean mono- and polycrystalline aluminum*, Surface Science **472**, 195 (2001).

- [168] *The Nobel Prize in Chemistry 1998*, Press release. NobelPrize.org. Nobel Media AB 2019. Fri. 24 May 2019.
- [169] T. Fließbach, *Quantenmechanik - Lehrbuch zur Theoretischen Physik III* (Springer Berlin Heidelberg, Wiesbaden, 2018).
- [170] C. David Sherrill and H. F. Schaefer, *The Configuration Interaction Method: Advances in Highly Correlated Approaches*, *Advances in Quantum Chemistry* **34**, 143 (1999).
- [171] W. Kohn, *Nobel Lecture: Electronic structure of matter - wave functions and density functionals*, *Rev. Mod. Phys.* **71**, 1253 (1999).
- [172] L. H. Thomas, *The calculation of atomic fields*, *Mathematical Proceedings of the Cambridge Philosophical Society* **23**, 542 (1927).
- [173] E. Fermi, *Eine statistische Methode zur Bestimmung einiger Eigenschaften des Atoms und ihre Anwendung auf die Theorie des periodischen Systems der Elemente*, *Zeitschrift für Physik* **48**, 73 (1928).
- [174] E. H. Lieb, *Thomas-fermi and related theories of atoms and molecules*, *Reviews of Modern Physics* **53**, 603 (1981).
- [175] P. A. M. Dirac, *Note on Exchange Phenomena in the Thomas Atom*, *Mathematical Proceedings of the Cambridge Philosophical Society* **26**, 376 (1930).
- [176] P. Hohenberg and W. Kohn, *Inhomogeneous Electron Gas*, *Phys. Rev.* **136**, B864 (1964).
- [177] W. Kohn and L. J. Sham, *Self-Consistent Equations Including Exchange and Correlation Effects*, *Phys. Rev.* **140**, A1133 (1965).
- [178] E. Engel and R. M. Dreizler, *Density Functional Theory* (Springer Berlin Heidelberg, 2011).
- [179] J. F. Janak, *Proof that $\partial E / \partial n_i = \epsilon_i$ in density-functional theory*, *Phys. Rev. B* **18**, 7165 (1978).
- [180] S. Hamel, P. Duffy, M. E. Casida, and D. R. Salahub, *Kohn-Sham orbitals and orbital energies: fictitious constructs but good approximations all the same*, *Journal of Electron Spectroscopy and Related Phenomena* **123**, 345 (2002).
- [181] A. D. Becke, *Perspective: Fifty years of density-functional theory in chemical physics*, *The Journal of Chemical Physics* **140**, 18A301 (2014).
- [182] M. A. Marques, M. J. Oliveira, and T. Burnus, *Libxc: A library of exchange and correlation functionals for density functional theory*, *Computer Physics Communications* **183**, 2272 (2012).
- [183] J. P. Perdew and K. Schmidt, *Jacob's ladder of density functional approximations for the exchange-correlation energy*, *AIP Conference Proceedings* **577**, 1 (2001).
- [184] A. D. Becke, *A new mixing of Hartree-Fock and local density-functional theories*, *The Journal of Chemical Physics* **98**, 1372 (1993).

- [185] R. Nagai, R. Akashi, and O. Sugino, *Completing density functional theory by machine learning hidden messages from molecules*, npj Computational Materials **6** (2020).
- [186] R. M. Martin, *Electronic structure: basic theory and practical methods* (Cambridge University Press, Cambridge, New York, 2004).
- [187] D. M. Ceperley and B. J. Alder, *Ground State of the Electron Gas by a Stochastic Method*, Phys. Rev. Lett. **45**, 566 (1980).
- [188] J. P. Perdew and W. Yue, *Accurate and simple density functional for the electronic exchange energy: Generalized gradient approximation*, Phys. Rev. B **33**, 8800 (1986).
- [189] C. Filippi, X. Gonze, and C. Umrigar, “Generalized gradient approximations to density functional theory: comparison with exact results”, in *Recent Developments and Applications of Modern Density Functional Theory*, Vol. 4, edited by J. Seminario, Theoretical and Computational Chemistry (Elsevier, 1996), pp. 295–326.
- [190] J. P. Perdew, J. A. Chevary, S. H. Vosko, K. A. Jackson, M. R. Pederson, D. J. Singh, and C. Fiolhais, *Atoms, molecules, solids, and surfaces: Applications of the generalized gradient approximation for exchange and correlation*, Phys. Rev. B **46**, 6671 (1992).
- [191] J. P. Perdew, K. Burke, and M. Ernzerhof, *Generalized Gradient Approximation Made Simple*, Phys. Rev. Lett. **77**, 3865 (1996).
- [192] A. D. Becke, *Density-functional thermochemistry. III. The role of exact exchange*, The Journal of Chemical Physics **98**, 5648 (1993).
- [193] E. Fermi and E. Amaldi, *Accad. Ital. Rome* **6** (1934).
- [194] J. P. Perdew and A. Zunger, *Self-interaction correction to density-functional approximations for many-electron systems*, Phys. Rev. B **23**, 5048 (1981).
- [195] Y. Zhang and W. Yang, *A challenge for density functionals: Self-interaction error increases for systems with a noninteger number of electrons*, The Journal of Chemical Physics **109**, 2604 (1998).
- [196] M. Lundberg and P. E. M. Siegbahn, *Quantifying the effects of the self-interaction error in DFT: When do the delocalized states appear?*, The Journal of Chemical Physics **122**, 224103 (2005).
- [197] A. Ruzsinszky, J. P. Perdew, G. I. Csonka, O. A. Vydrov, and G. E. Scuseria, *Spurious fractional charge on dissociated atoms: Pervasive and resilient self-interaction error of common density functionals*, The Journal of Chemical Physics **125**, 194112 (2006).
- [198] J. P. Perdew and M. Levy, *Physical Content of the Exact Kohn-Sham Orbital Energies: Band Gaps and Derivative Discontinuities*, Phys. Rev. Lett. **51**, 1884 (1983).
- [199] J. P. Perdew, *Density functional theory and the band gap problem*, International Journal of Quantum Chemistry **28**, 497 (2009).
- [200] J. P. Perdew, R. G. Parr, M. Levy, and J. L. Balduz, *Density-Functional Theory for Fractional Particle Number: Derivative Discontinuities of the Energy*, Phys. Rev. Lett. **49**, 1691 (1982).

- [201] A. Dreuw and M. Head-Gordon, *Failure of Time-Dependent Density Functional Theory for Long-Range Charge-Transfer Excited States: The Zinc bacteriochlorin-Bacteriochlorin and Bacteriochlorophyll-Spheroidene Complexes*, Journal of the American Chemical Society **126**, 4007 (2004).
- [202] M. K. Harbola and V. Sahni, *Quantum-Mechanical Interpretation of the Exchange-Correlation Potential of Kohn-Sham Density-Functional Theory*, Phys. Rev. Lett. **62**, 489 (1989).
- [203] J. D. Talman and W. F. Shadwick, *Optimized effective atomic central potential*, Phys. Rev. A **14**, 36 (1976).
- [204] C.-O. Almbladh and U. von Barth, *Exact results for the charge and spin densities, exchange-correlation potentials, and density-functional eigenvalues*, Phys. Rev. B **31**, 3231 (1985).
- [205] R. van Leeuwen and E. J. Baerends, *Exchange-correlation potential with correct asymptotic behavior*, Phys. Rev. A **49**, 2421 (1994).
- [206] E. Räsänen, S. Pittalis, and C. R. Proetto, *Universal correction for the Becke-Johnson exchange potential*, The Journal of Chemical Physics **132**, 044112 (2010).
- [207] A. D. Becke and E. R. Johnson, *A density-functional model of the dispersion interaction*, The Journal of Chemical Physics **123**, 154101 (2005).
- [208] E. Engel, J. A. Chevary, L. D. Macdonald, and S. H. Vosko, *Asymptotic properties of the exchange energy density and the exchange potential of finite systems: relevance for generalized gradient approximations*, Zeitschrift für Physik D Atoms, Molecules and Clusters **23**, 7 (1992).
- [209] C. Legrand, E. Suraud, and P.-G. Reinhard, *Comparison of self-interaction-corrections for metal clusters*, Journal of Physics B: Atomic, Molecular and Optical Physics **35**, 1115 (2002).
- [210] S. Kümmel and J. P. Perdew, *Optimized effective potential made simple: Orbital functionals, orbital shifts, and the exact Kohn-Sham exchange potential*, Phys. Rev. B **68**, 035103 (2003).
- [211] J. Krieger, Y. Li, and G. Iafrate, *Derivation and application of an accurate Kohn-Sham potential with integer discontinuity*, Physics Letters A **146**, 256 (1990).
- [212] M. M. Rieger and P. Vogl, *Self-interaction corrections in semiconductors*, Phys. Rev. B **52**, 16567 (1995).
- [213] B. Baumeier, P. Krüger, and J. Pollmann, *Self-interaction-corrected pseudopotentials for silicon carbide*, Phys. Rev. B **73**, 195205 (2006).
- [214] E. E. Quashie, B. C. Saha, X. Andrade, and A. A. Correa, *Self-interaction effects on charge-transfer collisions*, Phys. Rev. A **95**, 042517 (2017).
- [215] T. Tsuneda and K. Hirao, *Self-interaction corrections in density functional theory*, The Journal of Chemical Physics **140**, 18A513 (2014).

- [216] O. Gunnarsson, B. I. Lundqvist, and J. W. Wilkins, *Contribution to the cohesive energy of simple metals: Spin-dependent effect*, Phys. Rev. B **10**, 1319 (1974).
- [217] U. v. Barth and L. Hedin, *A local exchange-correlation potential for the spin polarized case. i*, Journal of Physics C: Solid State Physics **5**, 1629 (1972).
- [218] R. O. Jones and O. Gunnarsson, *The density functional formalism, its applications and prospects*, Reviews of Modern Physics **61**, 689 (1989).
- [219] J. Behler, B. Delley, K. Reuter, and M. Scheffler, *Nonadiabatic potential-energy surfaces by constrained density-functional theory*, Phys. Rev. B **75**, 115409 (2007).
- [220] W. Kohn, *Density-functional theory for excited states in a quasi-local-density approximation*, Phys. Rev. A **34**, 737 (1986).
- [221] E. K. U. Gross, L. N. Oliveira, and W. Kohn, *Rayleigh-Ritz variational principle for ensembles of fractionally occupied states*, Phys. Rev. A **37**, 2805 (1988).
- [222] M. A. Marques, N. T. Maitra, F. M. Nogueira, E. Gross, and A. Rubio, eds., *Fundamentals of Time-Dependent Density Functional Theory* (Springer Berlin Heidelberg, 2012).
- [223] M. A. Marques, C. Ullrich, F. Nogueira, A. Rubio, K. Burke, and E. K. U. Gross, eds., *Time-Dependent Density Functional Theory* (Springer Berlin Heidelberg, 2006).
- [224] C. A. Ullrich, *Time-Dependent Density-Functional Theory* (Oxford University Press, 2011).
- [225] E. Runge and E. K. U. Gross, *Density-Functional Theory for Time-Dependent Systems*, Phys. Rev. Lett. **52**, 997 (1984).
- [226] E. Gross and W. Kohn, *Time-Dependent Density-Functional Theory*, Density Functional Theory of Many-Fermion Systems **21**, 255 (1990).
- [227] N. T. Maitra, I. Souza, and K. Burke, *Current-density functional theory of the response of solids*, Phys. Rev. B **68**, 045109 (2003).
- [228] S. Botti, A. Schindlmayr, R. D. Sole, and L. Reining, *Time-dependent density-functional theory for extended systems*, Reports on Progress in Physics **70**, 357 (2007).
- [229] R. van Leeuwen, *Mapping from Densities to Potentials in Time-Dependent Density-Functional Theory*, Phys. Rev. Lett. **82**, 3863 (1999).
- [230] J. K. Dewhurst et. al, See: `elk.sourceforge.net`.
- [231] A. Gulans, S. Kontur, C. Meisenbichler, D. Nabok, P. Pavone, S. Rigamonti, S. Sagmeister, U. Werner, and C. Draxl, *exciting: a full-potential all-electron package implementing density-functional theory and many-body perturbation theory*, Journal of Physics: Condensed Matter **26**, 363202 (2014).
- [232] See: <http://www.flapw.de>.
- [233] N. D. Lang and W. Kohn, *Theory of Metal Surfaces: Work Function*, Phys. Rev. B **3**, 1215 (1971).

- [234] U. von Barth and C. D. Gelatt, *Validity of the frozen-core approximation and pseudopotential theory for cohesive energy calculations*, Phys. Rev. B **21**, 2222 (1980).
- [235] G. B. Bachelet, D. R. Hamann, and M. Schlüter, *Pseudopotentials that work: From H to Pu*, Phys. Rev. B **26**, 4199 (1982).
- [236] N. Troullier and J. L. Martins, *Efficient pseudopotentials for plane-wave calculations*, Phys. Rev. B **43**, 1993 (1991).
- [237] S. G. Louie, S. Froyen, and M. L. Cohen, *Nonlinear ionic pseudopotentials in spin-density-functional calculations*, Phys. Rev. B **26**, 1738 (1982).
- [238] L. Kleinman and D. M. Bylander, *Efficacious Form for Model Pseudopotentials*, Phys. Rev. Lett. **48**, 1425 (1982).
- [239] D. Vanderbilt, *Soft self-consistent pseudopotentials in a generalized eigenvalue formalism*, Phys. Rev. B **41**, 7892 (1990).
- [240] D. R. Hamann, *Optimized norm-conserving Vanderbilt pseudopotentials*, Phys. Rev. B **88**, 085117 (2013).
- [241] M. Schlipf and F. Gygi, *Optimization algorithm for the generation of ONCV pseudopotentials*, Computer Physics Communications **196**, 36 (2015).
- [242] M. Fuchs and M. Scheffler, *Ab initio pseudopotentials for electronic structure calculations of poly-atomic systems using density-functional theory*, Computer Physics Communications **119**, 67 (1999).
- [243] A. Castro, M. A. L. Marques, and A. Rubio, *Propagators for the time-dependent Kohn-Sham equations*, The Journal of Chemical Physics **121**, 3425 (2004).
- [244] A. Gómez Pueyo, M. A. L. Marques, A. Rubio, and A. Castro, *Propagators for the Time-Dependent Kohn-Sham Equations: Multistep, Runge-Kutta, Exponential Runge-Kutta, and Commutator Free Magnus Methods*, Journal of Chemical Theory and Computation **14**, 3040 (2018).
- [245] R. Kosloff, *Time-dependent quantum-mechanical methods for molecular dynamics*, The Journal of Physical Chemistry **92**, 2087 (1988).
- [246] H. O. Wijewardane and C. A. Ullrich, *Real-Time Electron Dynamics with Exact-Exchange Time-Dependent Density-Functional Theory*, Phys. Rev. Lett. **100**, 056404 (2008).
- [247] P. Pechukas and J. C. Light, *On the Exponential Form of Time-Displacement Operators in Quantum Mechanics*, The Journal of Chemical Physics **44**, 3897 (1966).
- [248] J. Van Heys, M. Lindenblatt, and E. Pehlke, *Molecular-dynamics simulations of non-adiabatic processes at surfaces*, Phase Transitions **78**, 773 (2005).
- [249] C. Moler and C. Van Loan, *Nineteen Dubious Ways to Compute the Exponential of a Matrix, Twenty-Five Years Later*, SIAM Review **45**, 3 (2003).
- [250] T. J. Park and J. C. Light, *Unitary quantum time evolution by iterative Lanczos reduction*, The Journal of Chemical Physics **85**, 5870 (1986).

- [251] M. Feit, J. Fleck, and A. Steiger, *Solution of the Schrödinger equation by a spectral method*, Journal of Computational Physics **47**, 412 (1982).
- [252] O. Sugino and Y. Miyamoto, *Density-functional approach to electron dynamics: Stable simulation under a self-consistent field*, Phys. Rev. B **59**, 2579 (1999).
- [253] J. C. Tully, *Molecular dynamics with electronic transitions*, The Journal of Chemical Physics **93**, 1061 (1990).
- [254] J. C. Tully, *Mixed quantum-classical dynamics*, Faraday Discuss. **110**, 407 (1998).
- [255] R. Díez Muiño and H. F. Busnengo, *Dynamics of Gas-Surface Interactions - Atomic-level Understanding of Scattering Processes at Surfaces* (Springer Science and Business Media, Berlin Heidelberg, 2013).
- [256] I. Csizmadia, International Journal of Quantum Chemistry **13**, 159 (1978).
- [257] R. Nagano, K. Yabana, T. Tazawa, and Y. Abe, *Time-dependent mean-field description for multiple charge-transfer processes in Ar^{8+} –Ar collisions*, Phys. Rev. A **62**, 062721 (2000).
- [258] A. Castro Barrigón, “A first-principles time-dependent density functional theory scheme for the computation of the electromagnetic response of nanostructures”, PhD thesis (Universidad de Valladolid, 2004).
- [259] A. Schleife, E. W. Draeger, Y. Kanai, and A. A. Correa, *Plane-wave pseudopotential implementation of explicit integrators for time-dependent Kohn-Sham equations in large-scale simulations*, The Journal of Chemical Physics **137**, 22A546 (2012).
- [260] C. A. Rozzi, D. Varsano, A. Marini, E. K. U. Gross, and A. Rubio, *Exact Coulomb cutoff technique for supercell calculations*, Phys. Rev. B **73**, 205119 (2006).
- [261] M. Frigo and S. G. Johnson, “FFTW: An Adaptive Software Architecture for the FFT”, in Proceedings of the International Conference on Acoustics, Speech, and Signal Processing, Vol. 3 (1998), pp. 1381–1384.
- [262] P. P. Ewald, *Die Berechnung optischer und elektrostatischer Gitterpotentiale*, Annalen der Physik **369**, 253 (1921).
- [263] B. Wood, W. M. C. Foulkes, M. D. Towler, and N. D. Drummond, *Coulomb finite-size effects in quasi-two-dimensional systems*, Journal of Physics: Condensed Matter **16**, 891 (2004).
- [264] M. Leslie and N. J. Gillan, *The energy and elastic dipole tensor of defects in ionic crystals calculated by the supercell method*, Journal of Physics C: Solid State Physics **18**, 973 (1985).
- [265] G. Shaviv and N. J. Shaviv, *Why the Salpeter approximation is not valid in the Sun*, Journal of Physics A: Mathematical and General **36**, 6187 (2003).
- [266] D. Tieleman, S. Marrink, and H. Berendsen, *A computer perspective of membranes: molecular dynamics studies of lipid bilayer systems*, Biochimica et Biophysica Acta (BBA) - Reviews on Biomembranes **1331**, 235 (1997).

- [267] A. Castro, A. Rubio, and M. J. Stott, *Solution of Poisson's equation for finite systems using plane-wave methods*, Canadian Journal of Physics **81**, 1151 (2003).
- [268] M. R. Jarvis, I. D. White, R. W. Godby, and M. C. Payne, *Supercell technique for total-energy calculations of finite charged and polar systems*, Phys. Rev. B **56**, 14972 (1997).
- [269] G. Makov and M. C. Payne, *Periodic boundary conditions in ab initio calculations*, Phys. Rev. B **51**, 4014 (1995).
- [270] M. Marques, *octopus: a first-principles tool for excited electron-ion dynamics*, Computer Physics Communications **151**, 60 (2003).
- [271] A. Castro, H. Appel, M. Oliveira, C. A. Rozzi, X. Andrade, F. Lorenzen, M. A. L. Marques, E. K. U. Gross, and A. Rubio, *octopus: a tool for the application of time-dependent density functional theory*, physica status solidi (b) **243**, 2465 (2006).
- [272] X. Andrade et al., *Time-dependent density-functional theory in massively parallel computer architectures: the octopus project*, Journal of Physics: Condensed Matter **24**, 233202 (2012).
- [273] X. Andrade et al., *Real-space grids and the Octopus code as tools for the development of new simulation approaches for electronic systems*, Physical Chemistry Chemical Physics **17**, 31371 (2015).
- [274] N. Tancogne-Dejean et al., *Octopus, a computational framework for exploring light-driven phenomena and quantum dynamics in extended and finite systems*, The Journal of Chemical Physics **152**, 124119 (2020).
- [275] J. Meister and W. H. E. Schwarz, *Principal Components of Ionicity*, The Journal of Physical Chemistry **98**, 8245 (1994).
- [276] G. Henkelman, A. Arnaldsson, and H. Jónsson, *A fast and robust algorithm for Bader decomposition of charge density*, Computational Materials Science **36**, 354 (2006).
- [277] A. Okabe, B. Boots, K. Sugihara, and S. N. Chiu, *Spatial Tessellations: Concepts and Applications of Voronoi Diagrams* (Wiley, 2000).
- [278] F. Mercier and O. Baujard, "Voronoi diagrams to model forest dynamics in French Guiana", in Proceedings of the 2rd International Conference on GeoComputation (1997), pp. 161–171.
- [279] N. K. Bose and A. K. Garga, *Neural network design using Voronoi diagrams*, IEEE transactions on neural networks **4**, 778 (1993).
- [280] R. F. W. Bader, *Atoms in Molecules: A Quantum Theory* (Clarendon Press, 1994).
- [281] W. Tang, E. Sanville, and G. Henkelman, *A grid-based Bader analysis algorithm without lattice bias*, Journal of Physics: Condensed Matter **21**, 084204 (2009).
- [282] A. H. Larsen et al., *The atomic simulation environment—a Python library for working with atoms*, Journal of Physics: Condensed Matter **29**, 273002 (2017).
- [283] W. Humphrey, A. Dalke, and K. Schulten, *VMD – Visual Molecular Dynamics*, Journal of Molecular Graphics **14**, 33 (1996).

- [284] J. Ahrens, B. Geveci, and C. Law, *ParaView: An End-User Tool for Large Data Visualization*, *Visualization Handbook* (Elsevier, 2005).
- [285] A. Stukowski, *Visualization and analysis of atomistic simulation data with OVITO—the Open Visualization Tool*, *Modelling and Simulation in Materials Science and Engineering* **18**, 015012 (2009).
- [286] J. D. Hunter, *Matplotlib: A 2D graphics environment*, *Computing In Science & Engineering* **9**, 90 (2007).
- [287] Free Software Foundation, See: <https://www.gnu.org/software/bash/>.
- [288] Python Software Foundation, *Python Language Reference*, version 2.7. Available at <http://www.python.org>.
- [289] M. Tafipolsky and R. Schmid, *A general and efficient pseudopotential Fourier filtering scheme for real space methods using mask functions*, *The Journal of Chemical Physics* **124**, 174102 (2006).
- [290] K. Lejaeghere, V. Van Speybroeck, G. Van Oost, and S. Cottenier, *Error Estimates for Solid-State Density-Functional Theory Predictions: An Overview by Means of the Ground-State Elemental Crystals*, *Critical Reviews in Solid State and Materials Sciences* **39**, 1 (2013).
- [291] C. Kittel, *Introduction to Solid State Physics* (Wiley, 1995).
- [292] J. Sprösser-Prou, A. vom Felde, and J. Fink, *Aluminum bulk-plasmon dispersion and its anisotropy*, *Phys. Rev. B* **40**, 5799 (1989).
- [293] A. Kiejna and B. I. Lundqvist, *First-principles study of surface and subsurface O structures at Al(111)*, *Phys. Rev. B* **63** (2001).
- [294] N. E. Singh-Miller and N. Marzari, *Surface energies, work functions, and surface relaxations of low-index metallic surfaces from first principles*, *Phys. Rev. B* **80**, 235407 (2009).
- [295] E. Chulkov, V. Silkin, and P. Echenique, *Image potential states on metal surfaces: binding energies and wave functions*, *Surface Science* **437**, 330 (1999).
- [296] J. Hölzl and F. K. Schulte, *Work function of metals*, *Solid Surface Physics*, 1 (1979).
- [297] G. Lu, D. Orlikowski, I. Park, O. Politano, and E. Kaxiras, *Energetics of hydrogen impurities in aluminum and their effect on mechanical properties*, *Phys. Rev. B* **65**, 064102 (2002).
- [298] R. Stumpf, *H-Induced Reconstruction and Faceting of Al Surfaces*, *Phys. Rev. Lett.* **78**, 4454 (1997).
- [299] R. Gross and A. Marx, *Festkörperphysik* (De Gruyter, Berlin, 2018).
- [300] M. Taylor and P. Nordlander, *Electron tunneling rates between an atom and a corrugated surface*, *Phys. Rev. B* **64**, 115422 (2001).
- [301] V. Q. Riascos, M. Tacca, R. Vidal, C. Gonzalez, E. C. Goldberg, and F. Bonetto, *Band Structure Effects on the Charge Exchange Processes in H^+ Colliding with a Cu(111) Surface*, *The Journal of Physical Chemistry C* **122**, 28192 (2018).

- [302] P. Nordlander and J. Tully, *Lifetimes of excited atoms near metal surfaces*, Surface Science **211-212**, 207 (1989).
- [303] C. Makait, “Vereinfachte Tight-Binding-Modellierung des Ladungstransferprozesses bei Streuung von H^+ an Al”, Bachelor’s Thesis (Christian-Albrechts-Universität zu Kiel, 2018).
- [304] M. E. Gruner and R. Pentcheva, *Dynamics of optical excitations in a Fe/MgO(001) heterostructure from time-dependent DFT*, Phys. Rev. B **99**, 195104 (2019).
- [305] B. Y. Mueller and B. Rethfeld, *Relaxation dynamics in laser-excited metals under nonequilibrium conditions*, Phys. Rev. B **87**, 035139 (2013).
- [306] R. Zimny, Z. Mišković, N. Nedeljković, and L. Nedeljković, *Interplay of resonant and Auger processes in proton neutralization after grazing surface scattering*, Surface Science **255**, 135 (1991).
- [307] A. Schleife, Y. Kanai, and A. A. Correa, *Accurate atomistic first-principles calculations of electronic stopping*, Phys. Rev. B **91**, 014306 (2015).
- [308] M. Berger, J. Coursey, M. Zucker, and J. Chang, *Stopping-Power and Range Tables for Electrons, Protons, and Helium Ions*, see: <https://dx.doi.org/10.18434/T4NC7P>, 1999.
- [309] X. He and J. A. Yarmoff, *Correlated Electron Effects in Low Energy Sr^+ Ion Scattering*, Phys. Rev. Lett. **105**, 176806 (2010).
- [310] X. He and J. Yarmoff, *Measuring correlated-electron effects with low energy alkaline earth ion scattering*, Nuclear Instruments and Methods in Physics Research Section B: Beam Interactions with Materials and Atoms **269**, 1195 (2011).
- [311] H. Shao, P. Nordlander, and D. C. Langreth, *Probing the Highly Correlated Mixed-Valent State via Charge Transfer with Atoms Moving Out from a Surface*, Phys. Rev. Lett. **77**, 948 (1996).
- [312] D. A. Papaconstantopoulos, *Handbook of the Band Structure of Elemental Solids - From $Z = 1$ To $Z = 112$* (Springer, Berlin, Heidelberg, 2014).
- [313] M. Fuchs, Y.-M. Niquet, X. Gonze, and K. Burke, *Describing static correlation in bond dissociation by Kohn–Sham density functional theory*, The Journal of Chemical Physics **122**, 094116 (2005).
- [314] O. Gunnarsson and B. I. Lundqvist, *Exchange and correlation in atoms, molecules, and solids by the spin-density-functional formalism*, Phys. Rev. B **13**, 4274 (1976).
- [315] K. A. H. German, C. B. Weare, and J. A. Yarmoff, *Inner-shell promotions in low-energy Li^+ -Al collisions at clean and alkali-covered Al(100) surfaces*, Phys. Rev. B **50**, 14452 (1994).
- [316] M. Petersilka, U. J. Gossmann, and E. K. U. Gross, *Excitation Energies from Time-Dependent Density-Functional Theory*, Phys. Rev. Lett. **76**, 1212 (1996).
- [317] S. Kümmel, *Charge-Transfer Excitations: A Challenge for Time-Dependent Density Functional Theory That Has Been Met*, Advanced Energy Materials **7**, 1700440 (2017).

- [318] E. Pehlke, Private Communication, 2019.
- [319] G. Onida, L. Reining, and A. Rubio, *Electronic excitations: density-functional versus many-body Green's-function approaches*, Rev. Mod. Phys. **74**, 601 (2002).
- [320] N. T. Maitra, *Charge transfer in time-dependent density functional theory*, Journal of Physics: Condensed Matter **29**, 423001 (2017).
- [321] P. Zhang, J. Feist, A. Rubio, P. García-González, and F. J. García-Vidal, *Ab initio nanoplasmonics: The impact of atomic structure*, Phys. Rev. B **90**, 161407 (2014).
- [322] A. Varas, P. García-González, J. Feist, F. García-Vidal, and A. Rubio, *Quantum plasmonics: from jellium models to ab initio calculations*, Nanophotonics **5**, 409 (2016).
- [323] A. Liebsch, *Electronic Excitations at Metal Surfaces* (Springer US, 1997).
- [324] M. Barbry, "Plasmons in Nanoparticles: Atomistic Ab Initio Theory for Large Systems", https://cfm.ehu.es/view/files/MArc_barbry_2-1.pdf, PhD thesis (Universidad del País Vasco, 2018).
- [325] V. Kapoor, *Autoionization in time-dependent density-functional theory*, Phys. Rev. A **93**, 063408 (2016).
- [326] L. Lacombe and N. T. Maitra, *Developing new and understanding old approximations in TDDFT*, Faraday Discuss. **224**, 382 (2020).
- [327] W. Schroeder, K. Martin, and B. Lorensen, *The Visualization Toolkit - An Object-Oriented Approach to 3D Graphics*, <https://raw.githubusercontent.com/lorensen/VTKExamples/master/src/VTKBookLaTeX/VTKTextBook.pdf>, 2018.
- [328] R. Kalhöfer, Private Communication, 2017.
- [329] G. Avendaño-Franco, "Charge Transfer Process in Atomic Collision from First Principles", <http://hdl.handle.net/2078.1/133573>, PhD thesis (UC Louvain, 2013).
- [330] L. Deuchler and E. Pehlke, *Energy transfer during resonant neutralization of hyperthermal protons at an aluminum surface studied with time-dependent density functional theory*, Phys. Rev. B **102**, 235421 (2020).
- [331] B. Rahn, R. Wen, L. Deuchler, J. Stremme, A. Franke, E. Pehlke, and O. M. Magnussen, *Coadsorbate-Induced Reversal of Solid-Liquid Interface Dynamics*, Angewandte Chemie International Edition **57**, 6065 (2018).

CURRICULUM VITAE

| | |
|-------------------|---|
| Name | Lukas Deuchler |
| Nationality | German |
| 09/2016 – today | PhD Student, CAU Kiel |
| 10/2016 – 12/2016 | Research Stay, Donostia/Spain Nano-bio Spectroscopy Group at the European Theoretical Spectroscopy Facility (ETSF) |
| 04/2014 – 06/2016 | Master Physics, CAU Kiel Final Thesis: <i>DFT Analysis of the Diffusion Mechanism of S Adsorbates on a Br Pre-Covered Cu(100)-Surface</i> |
| 07/2012 – 03/2013 | Exchange Student and Internship, Bariloche/Argentina Instituto Balseiro |
| 09/2010 – 04/2014 | Bachelor Physics, CAU Kiel Final Thesis: <i>Monte Carlo Simulations of Complex Spin Structures in Two Dimensional Systems</i> |
| Publications | |
| 2020 | <i>Energy Transfer During Resonant Neutralization of Hyperthermal Protons at an Aluminum Surface Studied with TDDFT</i> , L. Deuchler and E. Pehlke, Physical Review B 102 , 235421 (2020), Ref. [330] |
| 2019 | <i>Time-dependent simulation of ion stopping: Charge transfer and electronic excitations</i> , N. Schlünzen, K. Balzer, M. Bonitz, L. Deuchler, and E. Pehlke, Contributions to Plasma Physics 59 , e201800184, Ref. [21] |
| 2018 | <i>Coadsorbate-induced reversal of solid-liquid interface dynamics</i> , B. Rahn, R. Wen, L. Deuchler, J. Stremme, A. Franke, E. Pehlke, and O. M. Magnussen, Angewandte Chemie International Edition 57 , 6065, Ref. [331] |

DANKSAGUNG

Ich bedanke mich ganz herzlich bei

- meinem Doktorvater Prof. Dr. Eckhard Pehlke für das spannende Thema der Arbeit, die hervorragende Unterstützung und die intensive Betreuung während der Bearbeitung des Themas,
- bei Dr. Alexandra Dávila López für viele intensive und gewinnbringende Diskussionen,
- den aktuellen sowie ehemaligen Mitgliedern der Arbeitsgruppe von Prof. Pehlke mit denen ich viele anregende Diskussionen genießen konnte: Sönke Buttenschön, Richard Kalhöfer, Mario Santer, Insa Meinke, Reinhold Kaiser, Philip Lauwen, Christopher Makait, Oliver Heyen, Marten Schmidt, Svenja Hövelmann, Mitja Funk und Lea Stankewitz,
- bei Prof. Dr. Michael Bonitz, Dr. Karsten Balzer und Niklas Schlünzen für die anregende Kollaboration,
- bei Prof. Dr. Angel Rubio und Dr. Joaquim Jornet-Somoza für die Betreuung während eines Forschungsaufenthaltes,
- den technisch-administrativen Mitarbeiterinnen und Mitarbeitern Frau Schulz, Herrn Hohmann, Dr. Ludwig, Dr. Balzer und Dr. Knief für ihre Unterstützung,
- bei meinen Freunden und meiner Familie,
- bei all denen, die mir die Ehre erweisen, diese Arbeit zu lesen,
- und insbesondere bei meiner Frau für den unverzichtbaren Rückhalt und die unendliche Motivation.

SELBSTSTÄNDIGKEITSERKLÄRUNG

Ich erkläre gemäß §9 Abs. 7 der *Promotionsordnung (Satzung) der Mathematisch-Naturwissenschaftlichen Fakultät und Technischen Fakultät der Christian-Albrechts-Universität zu Kiel - 2018*, vom 9. August 2018, dass

- die Abhandlung - abgesehen von der Beratung durch meinen Betreuer - nach Inhalt und Form eine eigenständige und nur mit den angegebenen Hilfsmitteln von mir verfasste Arbeit ist,
- die Arbeit weder ganz, noch zum Teil schon einer anderen Stelle im Rahmen eines Prüfungsverfahrens vorgelegen hat, veröffentlicht worden ist oder zur Veröffentlichung eingereicht wurde,
- dass die Arbeit unter Einhaltung der Regeln guter wissenschaftlicher Praxis der Deutschen Forschungsgemeinschaft entstanden ist und
- mir kein akademischer Grad entzogen wurde.

Kiel, den 11. August 2021

[Lukas Deuchler]